

National Centre for Nuclear Research

Grzegorz Żarnecki

Measurement of the charged current  
muon antineutrino single  $\pi^-$   
production cross section at T2K

The thesis written under the supervision of  
**dr hab. Justyna Łagoda**  
(National Centre for Nuclear Research)

Warsaw, February 2022



## Streszczenie

Praca opisuje pomiar podwójnie różniczkowego przekroju czynnego na produkcję pojedynczego  $\pi^-$  w oddziaływaniu  $\bar{\nu}_\mu$  w materiale scyntylacyjnym. Wynik jest przedstawiony w funkcji zmiennych kinematycznych mionu, tj. w pędzie i cosinusie kąta emisji mionu względem osi wiązki neutrin ( $p_\mu, \cos\theta_\mu$ ). Dane pomiarowe zostały zebrane w ND280 - bliskim detektorze eksperymentu T2K - podczas działania wiązki w trybie  $\bar{\nu}_\mu$  w latach 2014-2018. Zgromadzone dane odpowiadają statystyce ok.  $8.46 \times 10^{20}$  protonów na tarczę.

T2K jest eksperymentem neutrinowym z długą bazą, którego głównym celem jest badanie oscylacji neutrin. Pomiar przekrojów czynnych na oddziaływania neutrin w przedziale energii od kilkuset MeV do kilku GeV przyczyniają się do lepszego oszacowania niepewności systematycznych w analizie oscylacyjnej. Produkcja pojedynczego naładowanego pionu jest ważnym kanałem oddziaływania dla tej skali energii.

Selekcja przypadków sygnału opiera się na rekonstrukcji toru  $\mu^+$  i  $\pi^-$  w ND280 z wierzchołkiem oddziaływania w poddetektorze scyntylacyjnym FGD1. Optymalizację selekcji i oszacowanie błędów systematycznych wykonano przy pomocy symulacji Monte Carlo opartych na generatorze NEUT v5.4.0. Do obliczenia przekroju czynnego wzięto strumień neutrin scałkowany po całym przedziale energii. Końcowy wynik podano w ograniczonej przestrzeni fazowej kinematyki wyprodukowanego mionu i pionu. Na podstawie podwójnie różniczkowego przekroju czynnego wyznaczono różniczkowy przekrój czynny w  $p_\mu$  (scałkowany po kącie) oraz w  $\cos\theta_\mu$  (scałkowany po pędzie), a także całkowity przekrój czynny (scałkowany po całej przestrzeni fazowej), który wynosi:

$$\sigma_{total} = (1.002 \pm 0.277[\text{stat+syst}] \pm 0.123[\text{stat}]) \times 10^{-40} \text{ cm}^2 \text{ na nukleon}$$

dla mionu w przedziale  $200 \text{ MeV}/c < p_\mu < 30000 \text{ MeV}/c, \cos\theta_\mu > 0.74$

i pionu w przedziale  $100 \text{ MeV}/c < p_\pi < 3000 \text{ MeV}/c, \cos\theta_\pi > 0.32$ .

Uzyskany wynik jest zgodny z przewidywaniami NEUT v5.4.0 dla produkcji pojedynczego  $\pi^-$ , opartymi na modelu Reina-Sehgala dla oddziaływań rezonansowych i modelu Reina-Sehgala z poprawkami Bergera-Sehgala dla oddziaływań koherentnych. Wynik pomiaru jest wyraźnie niższy od przewidywań GENIE v2.8.0, gdzie poprawki Bergera-Sehgala nie były zastosowane.

# Abstract

The thesis presents the measurement of the double differential cross section for single  $\pi^-$  production in  $\bar{\nu}_\mu$  interaction on scintillating material. The results are reported in muon kinematical variables i.e. momentum and cosine of the muon emission polar angle  $(p_\mu, \cos \theta_\mu)$ . Data for this measurement were collected in T2K near detector ND280 during  $\bar{\nu}_\mu$  beam mode runs from 2014 to 2018. Collected data statistics correspond to about  $8.46 \times 10^{20}$  protons on target.

T2K is a long-baseline neutrino oscillation experiment. Cross section measurements of neutrino interaction in sub-GeV to few GeV energy range allow to constrain the systematic uncertainties in the oscillation analysis. Single charged pion production is a relevant interaction mode at this energy scale.

The signal selection is based on the reconstruction of  $\mu^+$  and  $\pi^-$  tracks in ND280 with the interaction vertex in scintillator subdetector FGD1. Selection optimisation and estimation of the systematic errors are done with Monte Carlo simulations based on NEUT v5.4.0 generator. The cross section is measured as integrated over the energy spectrum of the incident neutrino beam. The final result is reported in the restricted phase-space for muon and pion kinematics. The double differential cross section is used to obtain the differential cross section in  $p_\mu$  (integrated over angle), the differential cross section in  $\cos \theta_\mu$  (integrated over momentum) and the total cross section (integrated over the restricted phase-space), which is found to be:

$$\sigma_{total} = (1.002 \pm 0.277[\text{stat+syst}] \pm 0.123[\text{stat}]) \times 10^{-40} \text{ cm}^2 \text{ per nucleon}$$

for muon with  $200 \text{ MeV}/c < p_\mu < 30000 \text{ MeV}/c$ ,  $\cos \theta_\mu > 0.74$

and pion with  $100 \text{ MeV}/c < p_\pi < 3000 \text{ MeV}/c$ ,  $\cos \theta_\pi > 0.32$ .

This result on single  $\pi^-$  production is in agreement with the nominal NEUT v5.4.0 predictions, which are based on Rein-Sehgal model of resonant interaction and Rein-Sehgal model of coherent interaction with Berger-Sehgal corrections. The measurement is however smaller than GENIE v2.8.0 predictions, were Rein-Sehgal coherent model is used without Berger-Sehgal corrections.

## Acknowledgements

I would like to thank Prof Justyna Łagoda for her supervision, encouragement and support throughout my PhD studies. Many of the opportunities I took wouldn't be possible without her approval and recommendation. I thank also all other members of the Neutrino Warsaw Group - from the very beginning I felt welcome as a member of the team. In particular I want to thank late Prof Maria 'Hula' Szeptycka for reviewing draft of my Thesis and Dr Kasia Kowalik for helping me with highland2 in the early days.

On many levels my work was supported by other members of T2K collaboration. I would like to thank members of former NuMu Working Group, Selection and Detector Systematics Group, Neutrino Interactions Working Group, as well as Late Stage Analyses and Cross Section conveners, in particular Dr Ciro Riccio and Dr Stephen Dolan who helped me a lot with the cross section software tools. I'm also grateful to Prof Jan Sobczyk for reviewing draft of the first chapter of my thesis.

I would also like to thank my family, especially my parents, for their love and unconditional support. No matter what happens I can always count on you. Special thanks go to my sister Dominika, who was my main companion during hard lockdown in 2020 and helped me keep my sanity.

Above all I thank One to Whom I owe everything. None of this work would be possible without His grace. Praise be to God.



# Contents

<b>Introduction</b>	9
<b>1. Neutrino physics</b>	13
1.1. Neutrinos in Standard Model	13
1.1.1. Neutrino helicity	14
1.1.2. Dirac and Majorana neutrinos	15
1.1.3. Neutrino mass	15
1.2. Neutrino Oscillations	16
1.2.1. CP Violation	17
1.2.2. Matter effects	18
1.2.3. Neutrino mass hierarchy	19
1.2.4. Experimental status	19
1.3. Neutrino Interactions	21
1.3.1. CC quasielastic (CCQE) interaction	22
1.3.2. CC resonant (RES) interaction	23
1.3.3. CC deep inelastic scattering (DIS)	24
1.3.4. CC coherent (COH)	25
1.3.5. NC interactions	26
1.3.6. Initial nucleon state	26
1.3.7. MEC interaction and 2p2h effect	27
1.3.8. Final state interactions	27
1.4. Signal definition for the cross section measurement	29
1.5. Differential cross section measurement	30
<b>2. T2K experiment</b>	32
2.1. The neutrino beam	32
2.1.1. Off-axis strategy	34
2.1.2. Flavour content	35
2.2. INGRID <i>on-axis</i> near detector	38

2.3.	ND280 <i>off-axis</i> near detector . . . . .	39
2.3.1.	UA1 magnet and side muon range detector . . . . .	40
2.3.2.	Fine grained detectors . . . . .	41
2.3.3.	Time projection chambers . . . . .	42
2.3.4.	Electromagnetic calorimeters . . . . .	44
2.3.5.	Multi-Pixel Photon Counters . . . . .	45
2.3.6.	Data Acquisition . . . . .	46
2.4.	Super-Kamiokande far detector . . . . .	47
2.5.	Summary of the collected T2K data . . . . .	49
<b>3.</b>	<b>Samples selection for the cross section measurement . . . . .</b>	<b>51</b>
3.1.	Pre-Selection . . . . .	53
3.2.	CC-inclusive . . . . .	57
3.3.	Signal samples selection . . . . .	60
3.3.1.	One Pion Cut . . . . .	60
3.3.2.	One TPC $\pi^-$ sample . . . . .	61
3.3.3.	Z-range cut . . . . .	64
3.3.4.	One FGD $\pi^-$ sample . . . . .	69
3.4.	Efficiency studies . . . . .	74
3.4.1.	Efficiency vs true $\mu^+, \pi^-$ kinematical variables . . . . .	74
3.4.2.	Efficiency vs neutrino energy, $Q^2$ and $W$ . . . . .	78
3.5.	Background samples selection . . . . .	81
3.5.1.	CC-other . . . . .	81
3.5.2.	Reversed Z-range cut . . . . .	85
<b>4.</b>	<b>Systematic uncertainties . . . . .</b>	<b>90</b>
4.1.	Detector systematic uncertainties . . . . .	90
4.1.1.	Variation-like systematics . . . . .	91
4.1.2.	Weight-like systematics . . . . .	93
4.1.3.	Pion secondary interactions . . . . .	101
4.1.4.	Detector systematics overview . . . . .	106
4.2.	Model systematic uncertainties . . . . .	110
4.3.	Flux systematic uncertainty . . . . .	113
<b>5.</b>	<b>Cross section extraction method . . . . .</b>	<b>115</b>
5.1.	Phase-space binning . . . . .	115
5.1.1.	Reconstructed phase-space binning . . . . .	116
5.1.2.	True phase-space binning . . . . .	125

5.2. Likelihood Fitter . . . . .	129
5.2.1. Maximum likelihood method . . . . .	130
5.2.2. Maximum likelihood for binned data . . . . .	130
5.2.3. Likelihood fit implementation . . . . .	132
5.2.4. Cross section calculation and error propagation . . . . .	136
5.3. Fake data studies . . . . .	137
5.3.1. Asimov fit . . . . .	137
5.3.2. Enhanced signal fit . . . . .	142
5.3.3. Statistical and systematic fluctuations . . . . .	147
5.3.4. NEUT to Genie fit . . . . .	148
<b>6. Data results . . . . .</b>	<b>155</b>
6.1. Events distribution in the phase-space . . . . .	155
6.2. Fit output . . . . .	162
6.3. Cross section extraction . . . . .	165
<b>Summary and outlook . . . . .</b>	<b>175</b>
<b>Appendix A . . . . .</b>	<b>178</b>
<b>Appendix B . . . . .</b>	<b>183</b>
<b>Appendix C . . . . .</b>	<b>191</b>
<b>Acronyms . . . . .</b>	<b>192</b>



# Introduction

The existence of neutrino was first proposed in 1930 by Pauli in order to preserve the conservation of energy, momentum and angular momentum in nuclear  $\beta$  decay [1]. Several years later Fermi [2] proposed the theory of  $\beta$  decay which was the first successful use of quantum field theory beyond electromagnetism and an important milestone towards modern description of neutrino interactions with matter. Neutrino interactions were directly observed for the first time in 1956 by Reines and Cowan [3] in the reaction  $\bar{\nu}_e + p \rightarrow e^+ + n$ . Since the antineutrinos from the reactor experiments produced only positrons a new quantum number was introduced for the phenomenological description: the lepton number ( $L_e$ ). Soon it was discovered that there are different neutrino types related to different charged leptons.

Muons were observed in cosmic rays in 1937 by Neddermayer and Anderson [4], Street and Stevenson [5], and Nishina et al. [6]. It was later discovered that pion decays into muon [7] and process  $\pi \rightarrow \mu + \nu$  was proposed as the description [8]. In 1960 Pontecorvo [9] and Schwartz [10] suggested to perform experiment with high energy neutrino beam, originating from pion decays, in order to check whether interactions of such neutrino would result in electron or muon production. In 1962 the experiment in Brookhaven confirmed the existence of muon neutrino [11]. In order to describe all neutrino interactions known at that time the muon lepton number ( $L_\mu$ ) was introduced and separate conservation laws were considered for  $L_\mu$  and  $L_e$ .

Tau was first discovered in 1975 by Perl et al. [12] in the scattering process  $e^+ + e^- \rightarrow \tau^+ + \tau^-$ . The new particle was found to decay in the leptonic modes and thus it was expected to observe associated type of neutrino - tau neutrino  $\nu_\tau$  - which would interact with a conservation of the tau lepton number  $L_\tau$ . First observation of tau neutrino interaction was reported in 2001 by DONUT experiment [13] and later by OPERA [14] and Super-Kamiokande [15]. It is now broadly accepted that neutrinos exist in three flavour states: electron neutrino  $\nu_e$ , muon neutrino  $\nu_\mu$  and tau neutrino  $\nu_\tau$ .

In his original proposition [1] Pauli suggested that the neutrino mass should be of the same order of magnitude as the electron mass, however Fermi [2] and Perrin [16] presented arguments that neutrino should be much lighter than electron or even pos-

sibly massless. Direct determination of the neutrino mass is possible by studying the kinematics of  $\beta$  decay. So far all such measurements are compatible with the hypothesis of a massless neutrino [17]. The indication of a nonzero neutrino mass comes from a very different phenomenon: neutrino oscillations.

Neutrino oscillations is a quantum effect where neutrino of a given flavour  $\nu_\alpha$  propagates over a long distance and is measured as a neutrino of a different flavour  $\nu_\beta$ . It was first considered by Maki et al. [18] for two flavours oscillation  $\nu_e \rightleftharpoons \nu_\mu$ . As described in section 1.2 such transition is possible if a flavour state is a superposition of mass eigenstates. In 1998 Super-Kamiokande experiment provided evidence [19] for neutrino oscillations consistent with the flavour-mass mixing. For the next decades various other experiments confirmed this observation using different neutrino sources [20]-[24].

Neutrino oscillation experiments remain an active area of research with some important questions still to be answered. One of the fundamental problems is a possible violation of the charge-parity symmetry in the neutrino sector which would be manifested in a different oscillation probabilities for neutrinos and antineutrinos propagating in vacuum.

A significant systematic uncertainty source in neutrino oscillation analyses is related to modelling of neutrino interactions in matter. In order to constrain the systematic uncertainty it is necessary to measure various neutrino interaction modes. The goal of this Thesis is the cross section measurement of the charged current  $\bar{\nu}_\mu$  interaction with single  $\pi^-$  production.

## Thesis overview

**Chapter 1** of the thesis presents basic information about neutrinos: their properties within the Standard Model, neutrino oscillations, neutrino interactions with matter. Additionally it provides the motivation for main Author's analysis: cross section measurement of single  $\pi^-$  production in  $\bar{\nu}_\mu$  CC interaction in the scintillator (CH) detector FGD1 (a subsystem of the T2K near detector, ND280). Considered is the double-differential production cross section in outgoing muon momentum  $p_\mu$  and emission angle  $\cos\theta_\mu$ .

**Chapter 2** describes the setup of the T2K experiment: neutrino beam production, basic properties of the beam, features of the detectors with particular focus on near detector ND280 which is used for the cross section measurement. Several ND280 subdetectors and data acquisition system are discussed. Basic information about far

detector Super-Kamiokande is provided as well.

**Chapter 3** covers the basic stage of the cross section measurement i.e. selection of the signal and background samples. Author followed *blind analysis* approach and did not check the selected data event rate until final stages of analysis. The selection strategy was optimised with the dedicated Monte Carlo (MC). A particular focus is given to the so-called Z-range cut, which is a selection criterion based on particles range in matter and is distinct from other ND280 analyses. Selection studies performed by Author include purity and efficiency estimations, and comparison of background samples to simulated background in signal samples.

**Chapter 4** describes the systematic uncertainties relevant for the measurement. That includes detector systematic uncertainties, flux, neutrino interaction modelling and FSI related uncertainties. One of the major systematic uncertainties is related to simulation of secondary pion interactions in the detector. Due to the specific selection strategy Author introduced an innovation in estimation of this effect i.e. dynamic volume of interest.

**Chapter 5** presents the procedure of the cross section extraction based on the likelihood fit method. Signal and background MC samples are simultaneously fitted to measured event rate in order to obtain signal cross section and constrain other processes. The validation of the method with Monte Carlo studies is discussed.

**Chapter 6** presents the final results with unblinded data. Event rates in all analysis samples are shown. Fit results are discussed and the extracted cross section is compared with nominal predictions of NEUT v5.4.0 and GENIE v2.8.0 Monte Carlo.

The main part of the thesis is concluded with **Summary and outlook** of the analysis.

**Appendix A** presents additional efficiency studies related to the Z-range cut.

**Appendix B** describes additional likelihood fit studies. The impact of statistical fluctuations on main fit parameters is described. The fit with unblinded data is presented with one of the analysis samples excluded.

**Appendix C** shows the elemental composition of FGD1 scintillator modules.

In the thesis, Author used standard T2K software packages that provide the tools for accessing Monte Carlo information, propagation of systematic errors and cross section extraction. All the described selection studies, estimation of detector systematic uncertainties, likelihood fit validation studies as well as the innovations mentioned in the overview above were done by Author.

# Chapter 1

## Neutrino physics

### 1.1. Neutrinos in Standard Model

Vast majority of experimental results in the high energy physics can be described with Standard Model of elementary particles, which was developed in the 1970s. According to this model the entire matter is built from a set of particles of spin  $\frac{1}{2}$ , called fermions: six quarks and six leptons (and a corresponding set of antiparticles).

There are three charged leptons: electron  $e^-$ , muon  $\mu^-$ , tau  $\tau^-$  and three leptons with no electric charge called neutrinos  $\nu$ . Each charged lepton is associated with neutrino of a distinct flavour, which is labelled as  $\nu_e, \nu_\mu$  or  $\nu_\tau$ , thus leptons are grouped into three families. (Similarly antiparticles  $e^+, \mu^+, \tau^+$  are associated with  $\bar{\nu}_e, \bar{\nu}_\mu, \bar{\nu}_\tau$ , respectively.) Lepton properties can be described with three lepton flavour numbers  $L_e, L_\mu, L_\tau$ , equal to 1 for a lepton and -1 for an antilepton of the relevant flavour. Lepton flavour numbers are conserved in all known phenomena apart from neutrino oscillations (described in section 1.2). The total lepton number  $L = L_e + L_\mu + L_\tau$  is conserved also in neutrino oscillations.

Neutrinos interact with matter only via weak force which can be described as an exchange of  $W^\pm$  (charged current (CC) interaction) or  $Z^0$  (neutral current (NC) interaction) bosons. Example Feynman diagrams for such interactions are presented in Fig. 1.1. In the left diagram antineutrino of a given flavour  $\bar{\nu}_l$  interacts with proton via exchange of  $W^\pm$  boson. As a result charged lepton  $l^+$  and neutron are produced. This process, called CC quasielastic (CCQE) interaction, is of particular interest in experiments with water Cherenkov detector because the measurement of outgoing  $l^+$  kinematics allows to estimate energy of the incoming  $\bar{\nu}_l$ <sup>1</sup> with quite good accuracy. The identification of neutrino flavour is possible by the identification of  $l^+$  flavour. In right

---

<sup>1</sup>In other detectors calorimetric measurement may give better energy estimation.

diagram antineutrino interacts with proton via exchange of  $Z^0$  boson. The identity of incoming and outgoing particles remains the same. In NC interactions it is not possible to distinguish neutrino flavours.



Figure 1.1: Feynman diagrams of antineutrino  $\bar{\nu}_l$  interaction with proton.

Left: Quasielastic CC interaction. Right: Elastic NC scattering.

### 1.1.1. Neutrino helicity

The weak current couples electrons only to  $\nu_e$ , muons only to  $\nu_\mu$  and taus only to  $\nu_\tau$  [25]:

$$J_\rho^{\text{lep}} = \bar{\psi}_e \gamma_\rho (1 - \gamma_5) \psi_{\nu_e} + \bar{\psi}_\mu \gamma_\rho (1 - \gamma_5) \psi_{\nu_\mu} + \bar{\psi}_\tau \gamma_\rho (1 - \gamma_5) \psi_{\nu_\tau}. \quad (1.1)$$

The presence of chirality operator  $(1 - \gamma_5)$  in formula 1.1 has an important consequence with respect to neutrinos. In the limit of  $m \rightarrow 0$  and  $E \rightarrow |\vec{p}|$  the plane-wave solution to the Dirac equation may be expressed as:

$$\psi_0 = \frac{1}{\sqrt{2}} \begin{pmatrix} \chi \\ \boldsymbol{\sigma} \cdot \hat{\mathbf{p}} \chi \end{pmatrix} \exp(-ip \cdot x), \quad (1.2)$$

where  $\chi$  is the usual two-component Pauli spinor,  $\boldsymbol{\sigma}$  is the Pauli spin vector,  $\hat{\mathbf{p}}$  is the momentum operator scaled by the total fermion momentum  $\mathbf{p}/|\vec{p}|$  and  $\boldsymbol{\sigma} \cdot \hat{\mathbf{p}}$  denotes the helicity operator. From that one can obtain:

$$(1 - \gamma_5) \psi_0 = \begin{cases} \psi_0 & \text{if } \boldsymbol{\sigma} \cdot \hat{\mathbf{p}} \chi = -\chi \\ 0 & \text{if } \boldsymbol{\sigma} \cdot \hat{\mathbf{p}} \chi = \chi \end{cases} \quad (1.3)$$

Neutrino has very small mass and interacts only via the interactions with the chirality operator. This results in neutrinos being observed as particles with left-handed helicity, described by spinor  $\psi_L^{\nu}$ . Similarly antineutrinos are observed as particles with right-handed helicity, described by spinor  $\bar{\psi}_R^{\bar{\nu}}$ . Assuming that neutrino is massless, it has definite helicity states.

### 1.1.2. Dirac and Majorana neutrinos

If neutrino has nonzero mass then it is propagating slower than the speed of light and one can choose the frame of reference where neutrino is right-handed (since the spin projection is invariant under Lorentz transformation) or antineutrino is left-handed. Thus in general there are four spinors:  $\psi_L^\nu$ ,  $\psi_R^\nu$ ,  $\bar{\psi}_L^\nu$ ,  $\bar{\psi}_R^\nu$ .

The Dirac particle and antiparticle of the same helicity are different objects. If  $\psi_{R(L)}^\nu$  is not the same as  $\bar{\psi}_{R(L)}^\nu$  the neutrino is called Dirac neutrino. In such case there are four states of the same mass. Dirac neutrinos have nonzero magnetic and electric dipole moments.

In 1937 Majorana considered idea of particle being identical with its own antiparticle [26]. If  $\psi_{R(L)}^\nu = \bar{\psi}_{R(L)}^\nu$  the neutrino is called Majorana neutrino. In this scenario the CPT operation<sup>2</sup> is equivalent to Lorentz transformation and there are only two states with the same mass. The Majorana neutrinos have zero magnetic and electric dipole moments [27].

There is an important consequence of neutrino being Majorana particle: violation of lepton number. A well-known example of such process is hypothetical neutrinoless double  $\beta$ -decay ( $0\nu\beta\beta$ ):

$${}^A_Z N \rightarrow {}^A_{Z+2} N' + 2e^-.$$

Observation of such events would be an indication that neutrino is Majorana particle however alternative explanations involving new physics are also possible [28]. Currently no experimental evidence of  $0\nu\beta\beta$  decays has been found. Various experiments provide lower limits for nuclei half-lives in this decay mode [29]-[32].

### 1.1.3. Neutrino mass

Neutrino mass may be measured directly by observing  $\beta$ -decays,  $e^\pm$  capture on nuclei, or pion or tau decays. As it will be explained in section 1.2 neutrino flavour states are superposition of mass eigenstates. Thus most recent limits on neutrino masses reported below are to be treated as limitations on the effective masses for a given flavour i.e. average masses in direct measurement:

- $m_{\nu_e}^{eff} < 1.1$  eV (90% CL) as reported by KATRIN [35],
- $m_{\nu_\mu}^{eff} < 190$  keV (90% CL) from  $\pi^- \rightarrow \mu^- + \bar{\nu}_\mu$  (PDG evaluation) [17],
- $m_{\nu_\tau}^{eff} < 18.2$  MeV (95% CL) from  $\tau^- \rightarrow n\pi + \nu_\tau$  as reported by ALEPH [36].

---

<sup>2</sup> The CPT operation (charge conjugation, parity operation and time reversal combined) changes a left-handed particle into a right-handed antiparticle.

The constraints on neutrino mass are also provided indirectly by observation of cosmic microwave background, nuclei half-lives limits for double  $\beta$ -decay and neutrino oscillation experiments. The latter ones don't probe the absolute scale of neutrino mass but allow for precise measurement of a difference of squared mass eigenvalues as explained in the next section.

## 1.2. Neutrino Oscillations

One of the most important fronts in the neutrino physics is studying the phenomenon of neutrino oscillations. The neutrino flavour oscillations were first considered in the 1960s by Maki et al. [18], Gribov and Pontecorvo [37], Bahcall and Frautschi [38]. It is a quantum effect related to the fact that neutrino interacts as a flavour eigenstate ( $\nu_e, \nu_\mu, \nu_\tau$ ) but propagates as a superposition of three mass eigenstates ( $\nu_1, \nu_2, \nu_3$ ) (more precisely - eigenstates of propagation Hamiltonian). Eigenvalues of Hamiltonian for propagation in vacuum are simply:

$$E_i = \sqrt{|\vec{p}|^2 + m_i^2}, \quad (1.4)$$

where  $\vec{p}$  - neutrino momentum,  $m_i$  - mass corresponding to  $i$ -th eigenstate<sup>3</sup>. The flavour-mass mixing is described by Pontecorvo-Maki-Nakagawa-Sakata (PMNS) matrix:

$$|\nu_i\rangle = \sum_{i=1}^3 U_{li}^* |\nu_i\rangle.$$

The PMNS matrix  $U$  is usually parametrised by three mixing angles ( $\theta_{12}, \theta_{13}, \theta_{23}$ ) and CP violation phase  $\delta_{CP}$ :

$$U = \begin{pmatrix} 1 & 0 & 0 \\ 0 & c_{23} & s_{23} \\ 0 & -s_{23} & c_{23} \end{pmatrix} \begin{pmatrix} c_{13} & 0 & s_{13}e^{-i\delta_{CP}} \\ 0 & 1 & 0 \\ -s_{13}e^{i\delta_{CP}} & 0 & c_{13} \end{pmatrix} \begin{pmatrix} c_{12} & s_{12} & 0 \\ -s_{12} & c_{12} & 0 \\ 0 & 0 & 1 \end{pmatrix} \\ = \begin{pmatrix} c_{12}c_{13} & s_{12}c_{13} & s_{13}e^{-i\delta_{CP}} \\ -s_{12}c_{23} - c_{12}s_{13}s_{23}e^{i\delta_{CP}} & c_{12}c_{23} - s_{12}s_{13}s_{23}e^{i\delta_{CP}} & c_{13}s_{23} \\ s_{12}s_{23} - c_{12}s_{13}c_{23}e^{i\delta_{CP}} & -c_{12}s_{23} - s_{12}s_{13}c_{23}e^{i\delta_{CP}} & c_{13}c_{23} \end{pmatrix},$$

where  $s_{ij}$  is  $\sin(\theta_{ij})$  and  $c_{ij}$  -  $\cos(\theta_{ij})$ .

---

<sup>3</sup>Some authors take a different approach and consider states of the same energy  $E$  but with different momenta  $p_i$  given by  $p_i = \sqrt{E^2 - m_i^2}$ . This however leads to the same oscillation probability formulas. See [39].

The probability that a neutrino produced in  $\nu_\alpha$  flavour state will interact as a neutrino in  $\nu_\beta$  state is expressed as:

$$P(\nu_\alpha \rightarrow \nu_\beta) = \delta_{\alpha\beta} - 4 \sum_{i>j} \text{Re}(U_{\alpha i}^* U_{\beta i} U_{\alpha j} U_{\beta j}^*) \sin^2 \left( \Delta m_{ij}^2 \frac{L}{4E} \right) \pm 2 \sum_{i>j} \text{Im}(U_{\alpha i}^* U_{\beta i} U_{\alpha j} U_{\beta j}^*) \sin \left( \Delta m_{ij}^2 \frac{L}{4E} \right), \quad (1.5)$$

where  $\Delta m_{ij}^2 = m_i^2 - m_j^2$  is a difference of squared masses,  $L$  is neutrino propagation distance and  $E$  is neutrino energy<sup>4</sup>. The  $\pm$  sign distinguishes neutrinos and anti-neutrinos.

At this point neutrino oscillations experiments can be categorised into two basic types:

- *Appearance experiment* - aims to observe interactions of  $\nu_\beta$  neutrinos originating from a source of  $\nu_\alpha$  neutrinos ( $\alpha \neq \beta$ ). It probes  $P(\nu_\alpha \rightarrow \nu_\beta)$  probability.
- *Disappearance experiment* - aims to measure neutrinos of the same flavour as produced in a source. It probes  $P(\nu_\alpha \rightarrow \nu_\alpha)$  probability.

Note that neutrino flavour identification is based on identification of the produced charged lepton. Since the charged leptons have different masses the possibility to recognise particular neutrino flavour depends on the energy scale.

### 1.2.1. CP Violation

Charge-parity (CP) symmetry is a symmetry of interaction under the combination of charge conjugation operation C and space inversion P. As indicated by Sakharov [40] the violation of CP symmetry is one of the necessary conditions to explain matter-antimatter asymmetry in the Universe.

If the CP symmetry is violated in neutrino sector the oscillation probability (in vacuum) should be unequal for neutrinos and antineutrinos:  $P(\nu_\alpha \rightarrow \nu_\beta) \neq P(\bar{\nu}_\alpha \rightarrow \bar{\nu}_\beta)$ . The difference between those probabilities is a measure of CP asymmetry and is expressed as:

$$P(\nu_\alpha \rightarrow \nu_\beta) - P(\bar{\nu}_\alpha \rightarrow \bar{\nu}_\beta) = 4 \sum_{i>j} \text{Im}(U_{\alpha i}^* U_{\alpha j} U_{\beta i} U_{\beta j}^*) \sin \left( \Delta m_{ij}^2 \frac{L}{4E} \right). \quad (1.6)$$

Assuming  $\alpha \neq \beta$  the imaginary part of matrix elements' product has the same value for all flavours and  $i, j$  indices (with respect to  $\pm$  sign):

---

<sup>4</sup>In this formula  $E = |\vec{p}|c$ .

$$\text{Im}(U_{\alpha i}^* U_{\alpha j} U_{\beta i} U_{\beta j}^*) = \pm s_{12} c_{12} s_{13} c_{13}^2 s_{23} c_{23} \sin \delta_{CP}.$$

This quantity is often referred to as Jarlskog invariant. By using  $\sin(2\theta) = 2 \sin \theta \cos \theta$  identity it can be written as:

$$J_{CP} = \frac{1}{8} \sin(2\theta_{12}) \sin(2\theta_{13}) \sin(2\theta_{23}) \cos \theta_{13} \sin \delta_{CP}. \quad (1.7)$$

At this point a few remarks can be made:

- To observe CP violation in neutrino sector it is necessary to measure appearance probability of a new flavour  $P(\nu_\alpha \rightarrow \nu_\beta)$ .
- CP violation can occur only if all mixing angles have values different than 0 and  $\frac{n\pi}{2}$ .
- CP symmetry is conserved for  $\delta_{CP} = 0$  or  $\pi$ .
- For the CP violation all mass values must be different. Otherwise the right side of Eq. 1.6 vanishes.

Similarly, Jarlskog invariant can be determined for quark sector as a combination of CKM matrix elements. Jarlskog invariant for quark sector is  $J^q = (3.00_{-0.09}^{+0.15}) \times 10^{-5}$  [33], while for lepton sector the maximal possible value of the Jarlskog invariant ( $J^l = J_{max}^l \sin \delta_{CP}$ ) is  $J_{max}^l = 3.32 \pm 0.08 \times 10^{-2}$  [34]. This indicates that leptonic CP violation can be much more significant than the CP violation in quark sector.

### 1.2.2. Matter effects

The problem of neutrino oscillations in matter was first considered by Wolfenstein [41, 42] and later elaborated by Mikheyev and Smirnov [43]. The oscillations can be discussed in an effective Hamiltonian formalism. In presence of matter the propagation Hamiltonian needs to be modified due to forward neutrino scattering which differs for different neutrino flavours. For all (anti)neutrino flavours NC scattering is possible on  $e^-$ ,  $n$  or  $p$ . However, CC scattering is possible only for  $\nu_e(\bar{\nu}_e)$  on  $e^-$ . Thus the additional term in Hamiltonian must be related to electrons presence:

$$H_{matter} = H_0 \pm \sqrt{2} G_F n_e,$$

where  $H_0$  - Hamiltonian for propagation in vacuum,  $G_F$  - Fermi coupling constant,  $n_e$  - number density of electrons. The  $\pm$  sign distinguishes neutrinos and anti-neutrinos. As a result of modifying Hamiltonian the eigenstates and eigenvalues are also changed. The oscillation formulas can be rewritten in similar form only with new values of the

mixing angles  $\theta_m$  and  $\Delta m_m^2$ . For specific  $n_e$  there is a maximal flavour-mass mixing which leads to significant amplification of oscillation probabilities in matter. This phenomenon is called Mikheyev-Smirnov-Wolfenstein (MSW) effect. In two flavour approximation the oscillations are parametrised with one mixing angle  $\theta$  and one  $\Delta m^2$ . Then the mixing angle in matter  $\theta_m$  can be calculated as:

$$\tan 2\theta_m = \frac{\Delta m^2 \sin 2\theta}{\Delta m^2 \cos 2\theta \mp 2\sqrt{2}G_F n_e E},$$

where  $\theta, \Delta m^2$  - oscillation parameters in vacuum,  $E$  - neutrino energy. The maximal mixing in matter ( $\theta_m = 45^\circ$ ) happens if

$$\Delta m^2 \cos 2\theta = \pm 2\sqrt{2}G_F n_e E, \quad (1.8)$$

which is referred to as resonance condition [44]. Taking into account the MSW effect is particularly important in the explanation of the observed electron neutrino deficit in solar neutrino experiments.

Note that the resonance condition in Eq. 1.8 includes ‘+’ sign for neutrinos and ‘-’ for antineutrinos. Thus the oscillation probabilities in matter are different for neutrinos and antineutrinos even if the CP symmetry is conserved, which must be taken into account in experiments which aim to probe CP violation. The scale of this  $\nu/\bar{\nu}$  difference depends on energy and propagation distance. For more detailed discussion see [45, 46].

### 1.2.3. Neutrino mass hierarchy

There are two possible orderings of neutrino masses: normal hierarchy (NH) with  $m_1 < m_2 < m_3$  and inverted hierarchy (IH) with  $m_3 < m_1 < m_2$  as presented in Fig. 1.2. The sign of  $\Delta m_{21}^2$  is known from studying the MSW effect for solar neutrinos [47].

Current studies indicate that  $|\Delta m_{32}^2| \approx |\Delta m_{13}^2| \gg \Delta m_{21}^2$ . Thus the oscillation experiments might be divided into two groups: those studying oscillations with large  $L/E$  ratio (solar and long baseline reactor neutrinos), sensitive to small  $\Delta m_{21}^2$  and those with smaller  $L/E$  ratio (accelerator, atmospheric and medium baseline reactor neutrinos), sensitive to large  $\Delta m_{32}^2$  and  $\Delta m_{13}^2$ . The small squared mass difference is sometimes called *solar*  $\Delta m_{sol}^2$  and the large one *atmospheric*  $\Delta m_{atm}^2$ .

### 1.2.4. Experimental status

Current determination of oscillation parameters is based on results from various experiments [17] which due to different neutrino sources can be categorised as:

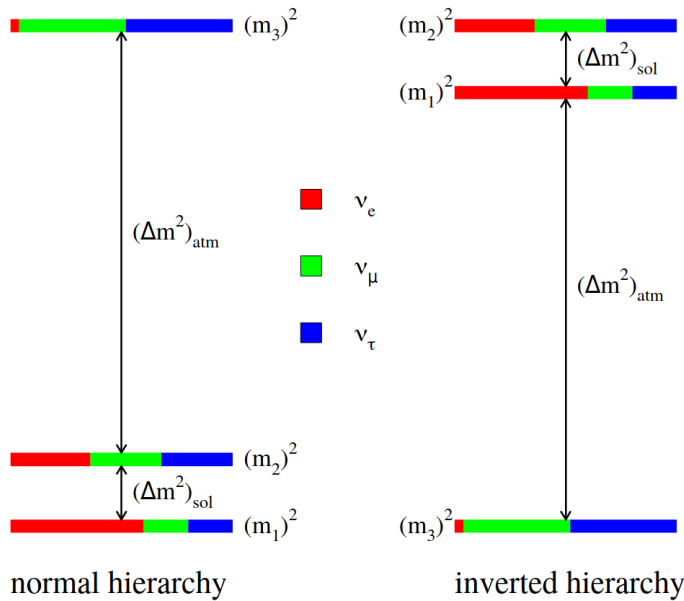


Figure 1.2: Possible mass hierarchies. Colors indicate the flavour composition of mass states in vacuum. Figure taken from [48].

- solar neutrino experiments (e.g. SAGE, Super-Kamiokande, SNO, Borexino), which measure low energy (MeV scale)  $\nu_e$  produced in the core of the Sun. These experiments contribute dominantly to  $\theta_{12}$  determination;
- reactor antineutrino experiments (KamLAND, Daya Bay, RENO, Double Chooz), which detect low energy (MeV scale)  $\bar{\nu}_e$  produced in the fission processes in the nuclear reactors. KamLAND, which uses long baseline, is particularly sensitive to  $\Delta m_{21}^2$ . Other reactor experiments with shorter baseline are more sensitive to  $\theta_{13}$  and  $|\Delta m_{32}^2|$ ;
- atmospheric neutrino experiments (Super-Kamiokande, KM3NeT, IceCube DeepCore), which study neutrinos ( $\nu_{\mu,e}, \bar{\nu}_{\mu,e}$ ) originating from the decays of secondary particles produced in cosmic rays interactions<sup>5</sup> in the Earth's atmosphere. The energy scale for atmospheric neutrinos ranges from sub-GeV to TeV. These experiments are sensitive to  $\theta_{23}$ ,  $|\Delta m_{32}^2|$ ,  $\theta_{13}$  and  $\delta_{CP}$ ;
- accelerator long-baseline experiments (K2K, MINOS, T2K, NOvA), which use primary proton beam to produce secondary particles decaying to muons and neutrinos. This allows to obtain very pure  $\nu_\mu/\bar{\nu}_\mu$  beam at GeV energy scale (see section 2.1 for details). These experiments contribute to determination of  $\theta_{23}$ ,  $|\Delta m_{32}^2|$ ,  $\theta_{13}$  and  $\delta_{CP}$ .

<sup>5</sup>Primary cosmic rays are mostly high energy protons and  $\alpha$  particles.

It is expected that the next generation experiments (DUNE [49], Hyper-Kamiokande [50]) will allow for the definitive confirmation of CP violation (if  $|\sin \delta_{CP}|$  is close enough to 1). Current best fit values of the oscillation parameters are reported in Table 1.1.

Parameter	Best fit
$\Delta m_{21}^2$	$(7.53 \pm 0.18) \times 10^{-5} \text{ eV}^2$
$\Delta m_{32}^2, \text{ NH}$	$(2.453 \pm 0.034) \times 10^{-3} \text{ eV}^2$
$\Delta m_{32}^2, \text{ IH}$	$(-2.546_{-0.040}^{+0.034}) \times 10^{-3} \text{ eV}^2$
$\sin^2 \theta_{12}$	$0.307_{-0.012}^{+0.013}$
$\sin^2 \theta_{23}, \text{ NH}$	$0.547 \pm 0.021$
$\sin^2 \theta_{23}, \text{ IH}$	$0.545 \pm 0.021$
$\sin^2 \theta_{13}$	$0.0218 \pm 0.0007$
$\delta_{CP}$	$(1.36 \pm 0.17)\pi \text{ rad}$

Table 1.1: Best fit values for oscillation parameters as reported in [51].

### 1.3. Neutrino Interactions

Study of neutrino oscillations is based on the measurement of CC interactions due to possibility of flavour identification. Figure 1.3 presents predicted and measured cross section per nucleon divided by neutrino energy for CC muon (anti)neutrino interaction on an isoscalar target. Three main types of interaction are contributing to the total predicted cross section: quasielastic (CCQE), resonant (RES) and deep inelastic scattering (DIS). Those three modes are dominant in different energy regions: CCQE in sub-GeV range, RES in about 1-5 GeV region and DIS in higher energies. This figure doesn't include other interactions such as CC coherent (COH) when neutrino interacts on a nucleus as a whole rather than on a single nucleon, or meson exchange current (MEC) interaction inside nucleus.

T2K experiment, described in Chapter 2, uses NEUT generator [52, 53] to simulate neutrino interactions in the detector. In following subsections most important interaction modes and their implementation in NEUT are discussed in more detail. Only neutrino interactions in nucleus are taken into account since for the T2K energy scale the cross section of neutrino-electron scattering is three orders of magnitude smaller than neutrino-nucleon scattering [54, 55].

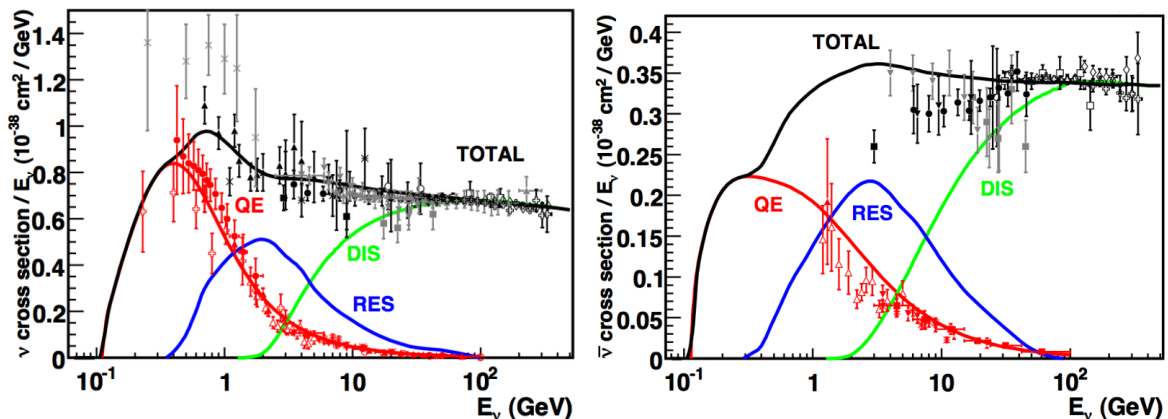


Figure 1.3: Cross section measurements [54] and predictions [56] for different types of charged current interaction as a function of neutrino energy. Left: for muon neutrino. Right: for muon antineutrino. Figure taken from [57]. Note that  $\nu_l$  ( $\bar{\nu}_l$ ) CCQE interaction can occur only on neutron (proton). Thus reported CCQE cross section per nucleon is smaller by a factor of two than cross section per neutron (proton).

### 1.3.1. CC quasielastic (CCQE) interaction

The simplest example of CC neutrino interaction in hadronic matter is the quasielastic interaction on a single nucleon. Due to the electric charge and lepton number conservation neutrino (antineutrino) may interact quasielastically only on neutron (proton):

- $\nu_l + n \rightarrow l^- + p$ ,
- $\bar{\nu}_l + p \rightarrow l^+ + n$  (see Feynman diagram in Fig. 1.1).

The oscillation probabilities on a fixed distance depend on the (anti)neutrino energy  $E_\nu$ . In case of Cherenkov detectors the CCQE channel is crucial for oscillation analysis since the measurement of the charged lepton kinematics allows for a straightforward calculation of neutrino energy. Assuming that an antineutrino  $\bar{\nu}_l$  interacts on a bound proton at rest the antineutrino energy can be estimated as:

$$E_{\bar{\nu}}^{reco} = \frac{m_n^2 - (m_p - E_b)^2 - m_l^2 + 2(m_p - E_b)E_l}{2(m_p - E_b - E_l + p_l \cos \theta_l)}, \quad (1.9)$$

where:  $m_n$  denotes the neutron mass,  $m_p$  is the proton mass,  $E_b$  is the binding energy of the proton inside a nucleus,  $m_l$ ,  $E_l$ ,  $p_l$ ,  $\theta_l$  denote the charged lepton mass, total energy, momentum and emission angle, respectively (in laboratory frame).

The prediction of CCQE cross section on free nucleon is given by Llewellyn-Smith formalism. This description includes several form factors which are functions of four-momentum transfer  $Q^2$ : vector ( $F_1$ ,  $F_2$ ), axial-vector ( $F_A$ ) and pseudoscalar ( $F_M$ )

form factors [58]. Vector form factors can be constrained from electron scattering measurements using conservation of vector current. The axial-vector form factor is assumed to have a dipole form:

$$F_A(Q^2) = \frac{F_A(0)}{\left(1 + Q^2/(M_A^{CCQE})^2\right)^2}, \quad (1.10)$$

where  $F_A(0) = g_A$  is known from nucleon  $\beta$  decay and  $M_A^{CCQE}$  is the axial mass which is determined from neutrino scattering. The pseudoscalar form factor may be expressed using partial conservation axial current as:

$$F_M(Q^2) = \frac{2m_N^2}{m_\pi^2 + Q^2} F_A(Q^2), \quad (1.11)$$

where  $m_N$  is the nucleon mass and  $m_\pi$  is the pion mass.

The Llewellyn-Smith formalism is used in NEUT and many other Monte Carlo generators, however it does not describe interaction on nucleon bound within nucleus. It is necessary to introduce the proper treatment of the initial nucleus state which is discussed in subsection 1.3.6.

### 1.3.2. CC resonant (RES) interaction

If there is enough energy transferred to a nucleon it is possible to produce baryon resonance. The lightest resonance of this kind is  $\Delta$  (central mass 1232 MeV/c<sup>2</sup>), which decays almost exclusively (branching ratio 99.4% [59]) into one nucleon and one pion in time of the order of 10<sup>-23</sup> s. In this case there are four possible (anti)neutrino resonant interactions:

- $\nu_l + p \rightarrow l^- + \Delta^{++}$ ,
- $\nu_l + n \rightarrow l^- + \Delta^+$ ,
- $\bar{\nu}_l + p \rightarrow l^+ + \Delta^0$ ,
- $\bar{\nu}_l + n \rightarrow l^+ + \Delta^-$ .

The Feynman diagram for the latter one, with the subsequent  $\Delta^-$  decay, is presented in Fig. 1.4. The resonant interaction is the main contribution to events with single pion production and is simulated in NEUT generator using the Rein-Sehgal model [66, 67] with form factors proposed by Graczyk-Sobczyk [60]. Resonant interactions in NEUT are described with three parameters: the axial mass  $M_A^{RES}$  and the axial form factor  $C_5^A$  (both introduced by Graczyk-Sobczyk) and the scaling parameter  $I_{1/2}$  of nonresonant background contributing to single pion production (the latter parameter included in the original Rein-Sehgal model).

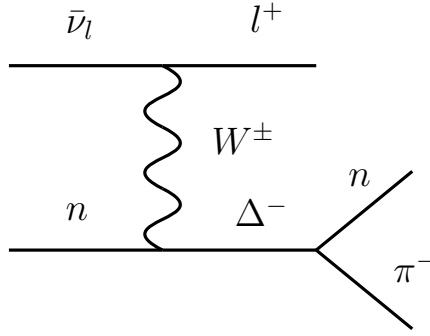


Figure 1.4: Example of  $\bar{\nu}_l$  CC resonant interaction which leads to single charged pion production.

### 1.3.3. CC deep inelastic scattering (DIS)

Deep inelastic scattering is the dominant interaction in the kinematic region of high four-momentum transfer  $Q^2 \gtrsim 1 \text{ GeV}^2/c^2$  and high hadronic invariant mass  $W \gtrsim 2 \text{ GeV}/c^2$ . The squared four-momentum transfer  $Q^2$  in CC neutrino interaction is equal to:

$$Q^2 = 2E_\nu(E_l - p_l \cos \theta) - m_l^2 - m_\nu^2 \approx 2E_\nu(E_l - p_l \cos \theta) - m_l^2$$

where  $\theta_l$  denotes angle between the direction of neutrino propagation and the direction of charged lepton propagation. The hadronic invariant mass  $W$  is equal to:

$$W = \sqrt{M^2 - Q^2 + 2M(E_\nu - E_l)},$$

where  $M$  is the nucleon mass.

An example diagram for CC DIS interaction is presented in Fig. 1.5. For lower energy DIS might result in single pion production and similar experimental signature as RES. For higher energy the production of multiple pions and other particles is likely to occur.

Assuming that the mass of produced lepton  $m_l$  is much smaller than the total lepton energy  $E_l$  the  $Q^2$  value may be approximated as:

$$Q^2 \approx 4E_\nu E_l \sin^2 \left( \frac{\theta_l}{2} \right). \quad (1.12)$$

Events with high energy and high angle lepton tracks are likely to be a signature of CC DIS interactions which are characterised by high  $Q^2$ .

The predicted DIS cross section is described by nucleon structure functions which depend on  $Q^2$  and energy transfer to target nucleon [61]. In case of NEUT generator the nucleon structure functions are taken from the parton distribution functions (PDFs)

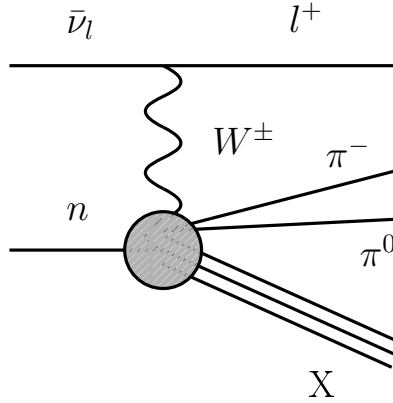


Figure 1.5: Example of  $\bar{\nu}_l$  CC DIS interaction which leads to production of two pions. X indicates any number of additional hadrons.

GRV98 [62] with corrections by Bodek and Yang [63]. Separate parametrisation is applied in NEUT for simulating events in  $1.3 \text{ GeV}/c^2 < W < 2 \text{ GeV}/c^2$  region and  $W > 2 \text{ GeV}/c^2$ . Interactions within these kinematic regions are tagged in NEUT as Multi  $\pi$  and DIS, respectively<sup>6</sup>. The hadronisation is simulated with PYTHIA/JETSET [65] at  $W > 2 \text{ GeV}/c^2$  and an internal NEUT method is applied at lower  $W$ . The latter one uses Andreopoulos-Gallagher-Kehayias-Yang (AGKY) model [64] to describe multiple pion production.

#### 1.3.4. CC coherent (COH)

Coherent neutrino interaction occurs in the kinematic region of small four-momentum transfer. Most CC COH interactions are characterised by forward going lepton tracks which is equivalent to  $Q^2$  below  $\sim 0.1 \text{ GeV}^2/c^2$  (see Eq. 1.12). Neutrino doesn't probe the individual nucleons, but interacts with the nucleus as a whole leaving it in the ground state.

CC coherent interaction next to CC RES and CC DIS contributes significantly to single charged pion production:

- $\nu_l + N \rightarrow l^- + \pi^+ + N$ ,
- $\bar{\nu}_l + N \rightarrow l^+ + \pi^- + N$ .

In the nominal NEUT generator coherent interaction is simulated using the Rein-Sehgal model with correction from Berger-Sehgal [68].

<sup>6</sup> Such nomenclature is somewhat confusing since interactions at  $W > 2 \text{ GeV}/c^2$  may result in multi pion production and there is no strict  $2 \text{ GeV}/c^2$  threshold for neutrino CC DIS.

### 1.3.5. NC interactions

All aforementioned CC processes have analogues in NC neutrino interactions. Neutrino may scatter elastically on a single nucleon (see Fig. 1.1, right diagram), produce a baryonic resonance ( $\nu_l + p \rightarrow \nu_l + \Delta^+$ ), cause a hadronisation via NC DIS or scatter coherently on an entire nucleus with production of single  $\pi^0$  ( $\nu_l + N \rightarrow \nu_l + \pi^0 + N$ ). However due to lack of charged lepton it is impossible to determine the neutrino flavour and from the perspective of long-baseline oscillation experiments NC interactions must be treated as background.

### 1.3.6. Initial nucleon state

In first approximation neutrino interaction in a nucleus can be described on the assumption that nucleons are independent particles in the nuclear potential and neutrino interacts on a single nucleon (impulse approximation). This simplified picture is then corrected by introducing correlations between nucleons. Thus proper initial nucleon state modelling must include Fermi motion (motion of nucleons relative to nucleus as a whole) and bounding energy, and take into account interactions between nucleons.

Each nucleus model determines a spectral function (SF) which is a 2-dimensional probability distribution of nucleon in momentum-binding energy phase space. One of the simplest models - the Relativistic Fermi Gas (RFG) [69] treats nucleons as free particles propagating in a constant nuclear potential. According to Fermi-Dirac statistics nucleons occupy momentum states from the ground state to the state of maximal momentum called Fermi momentum  $p_F$  (for  $^{12}\text{C}$  nucleus  $p_F \approx 230 \text{ MeV}/c$ ) [70].

An improved approach takes nuclear potential as a function of radial coordinate (Local Fermi Gas - LFG) [71]. The nominal NEUT generator uses Benhar SF model, which includes the effect of nucleon-nucleon correlations [72]. For more detailed discussion see [73].

Interactions between nucleons may be described by short-range or long-range correlations. The short-range correlations are related to p-n pairs and can be probed in electron scattering experiments [74]. The long-range correlations correspond to nucleon interacting with the rest of nucleus as a whole and can be described by random phase approximation (RPA) [75]. This technique takes into account the modification of electroweak coupling strength due to the screening in nuclear medium.

### 1.3.7. MEC interaction and 2p2h effect

As it was mentioned, nucleons are not free particles within the nucleus potential but they are interacting with one another. In particular it is possible to consider pair of correlated nucleons, which exchange virtual meson. Neutrino can interact with such pairs and it is referred to as meson exchange current (MEC) interaction. MEC is the dominant source of *2 particles - 2 holes* (2p2h) effect, which refers to neutrino interacting with a correlated pair of nucleons, ejecting both out of the nucleus [76, 77, 78]. In the nominal NEUT generator the Nieves model is used to simulate 2p2h effect [79]. The 2p2h cross section for the Nieves model is presented in Fig. 1.6 in the true three-momentum transfer  $q_3$  and true energy transfer  $q_0$  phase-space. Next to MEC interactions the region of nucleon-nucleon correlations (NN) can be distinguished where the neutrino interactions are described by different Feynman diagrams.

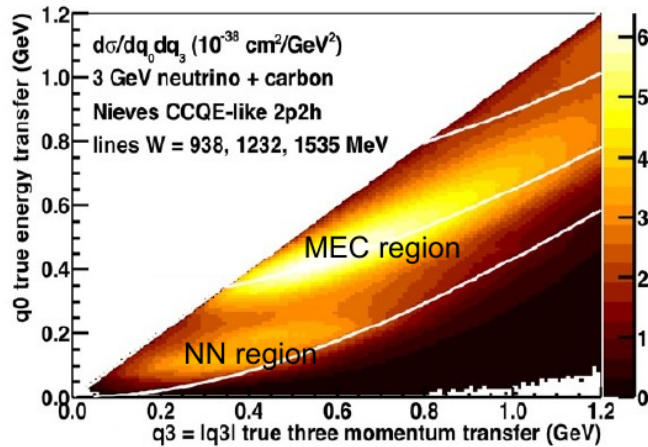


Figure 1.6: The 2p2h cross section in the  $q_3, q_0$  phase-space. Image taken from [80].

### 1.3.8. Final state interactions

In the previous subsections several types of neutrino-nucleus interactions were discussed. At the nuclear level the generated events are simulated with the impulse approximation approach in two stages:

1. Neutrino interacts on a single nucleon or on a pair inside a nucleus.
2. Produced particles propagate through nuclear matter.

Different interactions often result in different particles emitted out of the nucleus. The multiplicity and types of those particles determines so-called *final state topology* or simply *topology*. Relation between the neutrino interaction mode and topology is not

straightforward due to possibility that particles will reinteract within the nucleus they were produced in. These are so-called *final state interactions* (FSI) which are simulated for hadrons only (as leptons are less likely to reinteract). Examples of FSI are:

- absorption of a pion produced in RES interaction,
- quasi-elastic pion scattering,
- scattering of a nucleon which participated in CCQE interaction,
- pion production caused by hadrons reinteraction,
- charge exchange interaction e.g.  $\pi^- + p \rightarrow \pi^0 + n$ .

In NEUT generator the cascade model is used to simulate pion, nucleon and kaon FSI. A hadron is treated as classical object propagating inside the nucleus in finite steps. At each step there is a probability of undergoing several types of interaction. For low momentum pions ( $p_\pi < 500$  MeV/c) the probabilities of quasi-elastic interaction, single charge exchange and absorption are obtained with the tables computed from the Oset et al. model [81]. For high momentum pions ( $p_\pi > 500$  MeV/c) the calculation of the interaction probabilities is based on  $\pi^\pm$  scattering cross section data compiled by the Particle Data Group [82]. To prevent discontinuities, these two approaches are matched in the  $400 \text{ MeV}/c < p_\pi < 500 \text{ MeV}/c$  region [83]. NEUT FSI modelling is parametrised by a set of scaling factors, which correspond to different pion interactions: inelastic scattering, pion production, pion absorption and charge exchange.

FSI processes may impact the kinematics of produced particles and the final state topology. Despite that effect, in general the multiplicity of outgoing leptons and pions can be used to categorise topology in relation to mode of neutrino interaction as presented in Table 1.2.

topology	dominant interaction
1 $\mu^+$ + 0 $\pi$	$\bar{\nu}_\mu$ CCQE
1 $\mu^+$ + 1 $\pi$	$\bar{\nu}_\mu$ CC RES or COH
1 $\mu^+$ + multiple $\pi$	$\bar{\nu}_\mu$ CC DIS
0 $l^\pm$ + multiple $\pi$	NC DIS

Table 1.2: Examples (non-exhaustive) of the final state topology and the corresponding dominant mode of neutrino interaction. Nucleon multiplicity is not taken into account here.

## 1.4. Signal definition for the cross section measurement

One of the major sources of systematic uncertainties in the oscillation analysis is related to the cross section of neutrino interactions. Thus, precise measurements of different interaction channels are needed to constrain these uncertainties.

The total event rate for  $\nu_\beta$  neutrino interactions in a certain process  $i$  may be expressed as:

$$R_i = \sum_\alpha \int_{E_\nu} \phi_\alpha(E_\nu) \times \sigma_{\beta,i}(E_\nu) \times \epsilon(E_\nu) \times N \times P(\nu_\alpha \rightarrow \nu_\beta) dE_\nu,$$

where  $\phi_\alpha(E_\nu)$  is the neutrino  $\nu_\alpha$  flux as a function of the neutrino energy  $E_\nu$ ,  $\sigma_{\beta,i}$  is the cross section for  $\nu_\beta$  interaction in  $i$ -th interaction mode,  $\epsilon$  is the detector efficiency,  $N$  is the number of targets and  $P(\nu_\alpha \rightarrow \nu_\beta)$  is the oscillation probability.

The main objective of the analysis presented in this thesis is the cross section measurement of  $\bar{\nu}_\mu$  CC interaction with single  $\pi^-$  production in the off-axis near detector (ND280) of the T2K experiment. Cross section is reported for interactions in the scintillator (hydrocarbon) subdetector FGD1 (an ND280 subsystem). The signal is defined as a topology with a single  $\mu^+$  and  $\pi^-$  and no other mesons in the final state (i.e. exiting the nucleus):

$$\bar{\nu}_\mu + A \rightarrow \mu^+ + \pi^- + A' + X,$$

where  $A, A'$  denotes nucleus before and after the interaction, and  $X$  indicates arbitrary number of free nucleons in the final state. The signal topology will be tagged in this thesis as  $\bar{\nu}_\mu$  **CC1 $\pi^-$  topology**. In case of  $\pi^-$  being not identified in the experiment  $\bar{\nu}_\mu$  CC1 $\pi^-$  topology contributes to the background in CC quasi-elastic sample used in the far detector for oscillation analysis and thus its modelling needs to be constrained by dedicated measurement. Another major goal of the cross section studies is validation of neutrino interaction models.

Currently there is one published measurement of the  $\bar{\nu}_\mu$  CC1 $\pi^-$  cross section on hydrocarbon [84] (which is the main component of FGD1) in the  $\bar{\nu}_\mu$  energy range 1.5 to 10 GeV and one published measurement of the same topology on liquid argon for antineutrinos at a mean energy of 3.6 GeV [85]. Result presented in this thesis provides additional information by probing antineutrino interactions at lower energy range of about 0.5 to 1.5 GeV.

The measurement is reported in the restricted phase-space of ( $\mu^+, \pi^-$ ) kinematical variables because of the requirements for the selection efficiency and signal event rate outside of this region (as shown in subsection 3.4.1):

- $p_\mu > 200$  MeV/c - low selection efficiency below this threshold (see Fig. 3.16).
- $\cos\theta_\mu > 0.74$  and  $\cos\theta_\pi > 0.32$  - low selection efficiency for high angles (see Fig. 3.16 and 3.17).
- $100 \text{ MeV}/c < p_\pi < 3000 \text{ MeV}/c$  - low selection efficiency for events with  $p_\pi < 100$  MeV/c; for  $p_\pi > 3000$  MeV/c region the contribution of signal events is negligible (see Fig. 3.17).

## 1.5. Differential cross section measurement

In general, it is desirable to measure the differential cross section in as many observables as possible. It is favoured to measure considered cross section as N-dimensional differential rather than several 1D differential distributions. However, the number of bins is limited by the statistics of selected sample (if the binning is too fine the cross section per bin becomes very sensitive to statistical fluctuations). In the described  $\bar{\nu}_\mu$  CC1 $\pi^-$  cross section measurement the exact data event rate was not checked until final stages of analysis<sup>7</sup>. Strategy for the measurement was based on MC predictions from NEUT version 5.4.0 normalised to collected data sample of  $8.5 \times 10^{20}$  protons on target (POT). Based on MC simulations around 650-700 selected events were expected.

The cross section is measured as integrated over the energy spectrum of the incident neutrino beam, double-differential cross section  $\frac{d^2\sigma}{dp_\mu d\cos\theta_\mu}$  in  $\mu^+$  kinematic variables: momentum and cosine of the angle of the outgoing  $\mu^+$  with respect to Z axis (longitudinal detector axis, parallel to the beam axis). The benefit of using these variables is that:

- Theoretical calculation of charged lepton kinematics depends only on initial neutrino energy and four-momentum transfer. Thus it is essentially model-independent.
- Muon kinematical variables are directly observed in the experiment. Therefore the estimation of the variables of interest depends only on the detector model.

The goal of this analysis is to report cross section in *true* physical variables while in the experiment only *reconstructed* variables are observed. This approach is called *unfolding method*<sup>8</sup>. Ultimately the result is reported **in the restricted phase-space** (see section 1.4) as:

- Cross section in 29 bins of 2D phase-space:  $p_\mu, \cos\theta_\mu$ ,

---

<sup>7</sup>Such approach is sometimes called *blind analysis*.

<sup>8</sup>Alternative approach is called *forward folding* when the cross section is reported in reconstructed variables.

- Cross section in 16 bins of 2D phase-space:  $p_\mu, \cos\theta_\mu$  (coarse binning),
- Cross section in 4  $p_\mu$  bins (integrated over angle),
- Cross section in 4  $\cos\theta_\mu$  bins (integrated over momentum),
- Total cross section integrated over the restricted phase-space.

# Chapter 2

## T2K experiment

The T2K experiment [86] is a long baseline neutrino oscillation experiment located in Japan, using a  $\nu_\mu$  or  $\bar{\nu}_\mu$  beam generated at an accelerator complex. The beam energy spectrum is peaked at 600 MeV, where mostly CCQE and resonant interactions occur. The oscillation parameters are studied by measuring neutrino interactions in the near detector complex (where  $\frac{L}{E}$  ratio is small and probability of flavour transition is negligible) and in the far detector (where  $\frac{L}{E}$  ratio corresponds to maximal  $P(\nu_\mu \rightarrow \nu_e)$ ). In addition to the oscillation analysis the T2K experiment has a wide program of neutrino interaction cross section measurements at the near detector complex [87].



Figure 2.1: View of T2K layout.

### 2.1. The neutrino beam

The neutrino beam in T2K experiment is produced in the J-PARC facility. The scheme of the beam production is presented in Fig. 2.2. The primary beamline consists of three

accelerators, which prepare an intense proton beam. The first stage is a linear accelerator, where  $H^-$  ions are accelerated to 180 MeV and converted into a proton beam by charge-stripping foils. Then protons reach the rapid-cycling proton synchrotron, where they are accelerated to 3 GeV and finally enter the main ring synchrotron (MR), where they reach energy of 30 GeV.

The beam is produced in spills. Each spill lasts about  $5 \mu\text{s}$  and the time between two consecutive spills is approximately 2.5 s. A spill has the structure of eight bunches, with each bunch lasting 58 ns and pause between bunches lasting 582 ns. Due to narrow bunch width it is unlikely to have background from non-beam interactions coinciding with the beam.

The proton beam power was increasing throughout the T2K data taking history. (See section 2.5 for details.) The data sets relevant for Author’s analysis were collected with the beam power varying from approximately 200 kW to 500 kW.<sup>1</sup>

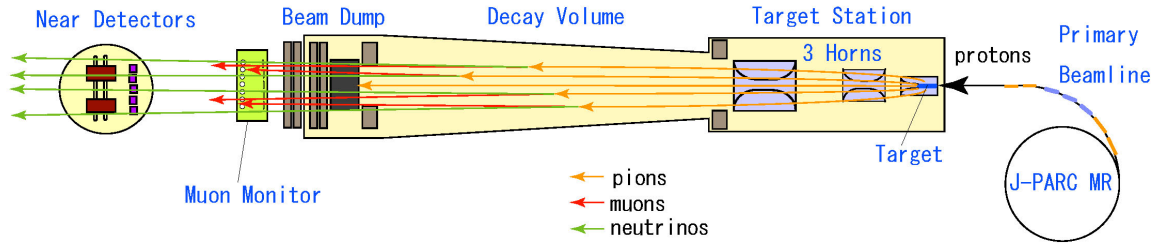


Figure 2.2: Schematic drawing of neutrino production beamline (not to scale).

The proton beam is directed onto a graphite target, which has a shape of a rod of length 91.4 cm and diameter 2.6 cm. In the proton interactions with target several types of mesons are produced, mostly pions [88]. Those secondary particles propagate in the magnetic field produced by 3 magnetic horns [89]. The T2K horns consist of aluminum conductors, which have coaxial structure. The target is inserted inside the inner conductor of the most upstream horn (see Fig. 2.3). The magnetic field is optimized to focus pions of a chosen charge in the decay volume. The horns work at the pulsed current of 250 kA resulting in a magnetic field up to 1.7 T.

The direction of the current powering the magnets may be reversed and thus setup may work in two modes: Forward Horn Current (FHC) when mostly  $\pi^+$  are focused and Reversed Horn Current (RHC) when  $\pi^-$  are focused. Then in the decay volume pions decay into muons and neutrinos:

<sup>1</sup>This change in beam power doesn’t have any significant impact on the measurement in the near detectors. The dedicated pile-up systematic uncertainty is included in the analysis.

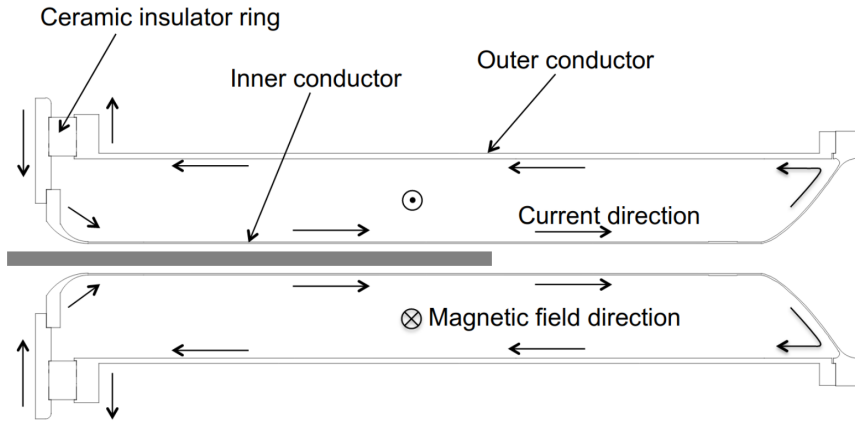


Figure 2.3: Cross-section of the most upstream magnetic horn. Directions of current and magnetic field are shown. The proton beam enters from the left. The inner conductor diameter is 5.4 cm, the outer conductor diameter is 40 cm and the entire horn is 1.5 m long. Grey field indicates approximate location of the target. Figure adapted from [89].

$$\begin{aligned}
 \pi^+ &\rightarrow \mu^+ + \nu_\mu \\
 \pi^- &\rightarrow \mu^- + \bar{\nu}_\mu
 \end{aligned}
 \tag{2.1}$$

Hence, effectively FHC works as neutrino beam mode and RHC as antineutrino beam mode.

Pions which did not yet decay and other hadrons are then stopped in the beam dump. Muon monitor, installed behind the beam dump, measures the direction and intensity of high energy muons, which allows for indirect monitoring of neutrino beam. Neutrinos propagate further underground to the near detectors: ND280 and INGRID, which are located 280 meters from the target.

### 2.1.1. Off-axis strategy

T2K is historically the first *off-axis* neutrino experiment. The far detector and one of the near detectors are measuring neutrinos emitted at an angle  $2.5^\circ$  from the proton beam axis. The energy spectrum of such neutrinos is much more narrow than for neutrinos emitted parallel to the proton beam (which are referred to as *on-axis* neutrino beam). This is a kinematical effect related to the decay of the parent particle [90]. For the dominant charged pion decay ( $\pi \rightarrow \mu\nu_\mu$ ) the neutrino energy in the laboratory frame (LAB)  $E_\nu$  may be expressed as:

$$E_\nu = \frac{E_\nu^*}{\gamma_\pi(1 - \beta_\pi \cos \theta)}, \quad (2.2)$$

where  $\gamma_\pi$  and  $\beta_\pi$  are usual Lorentzian factors calculated for pion in LAB,  $\theta$  is the angle of neutrino emission in LAB and  $E_\nu^*$  is the neutrino energy in the pion rest frame (so for a given decay channel  $E_\nu^* = \text{const.}$ ). The relation between neutrino energy  $E_\nu$  and pion-parent energy  $E_\pi$  in LAB is visualised in Fig. 2.4 for several  $\theta$  values. The neutrino energy  $E_\nu$  is weakly dependent on  $E_\pi$  and for each *off-axis* angle there is a maximal accessible neutrino energy. Thus, pions in a broad energy range contribute to a narrow peak of neutrino energy.

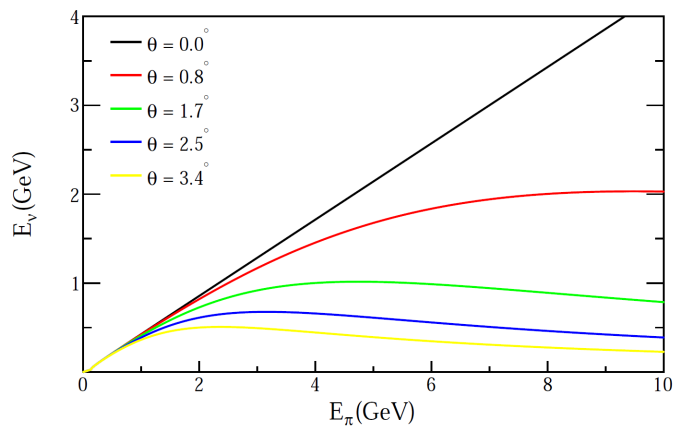


Figure 2.4: Relation between neutrino energy  $E_\nu$  and decaying pion energy  $E_\pi$  for different *off-axis* angles of neutrino propagation. Figure taken from [91].

Narrow  $E_\nu$  spectrum enhances sensitivity to oscillation effect at the far detector as presented in Fig. 2.5. (The fact that  $E_\nu$  distribution reaches beyond 1 GeV is due to kaon decays - see next subsection.) Additionally this strategy decreases contribution of non-quasielastic neutrino interactions and intrinsic  $\nu_e$  background. Change of the *off-axis* angle by 1 mrad ( $0.057^\circ$ ) corresponds to relative neutrino energy peak change  $\delta E_\nu/E_\nu \sim 2\%$ . Thus it is important to monitor precisely direction of the beam.

### 2.1.2. Flavour content

The charged pion decays are predominant source of neutrinos, but other particles also contribute. Table 2.1 presents different channels of parent-particles decays. Next to pions kaons are the lightest mesons and thus are also often produced in the proton beam interaction with the target. The mass of a kaon is roughly 3.5 times bigger than pion mass, which results in higher energy of emitted neutrino. Heavier mesons might also be produced, but they rarely decay with neutrino emission and their contribution is negligible.

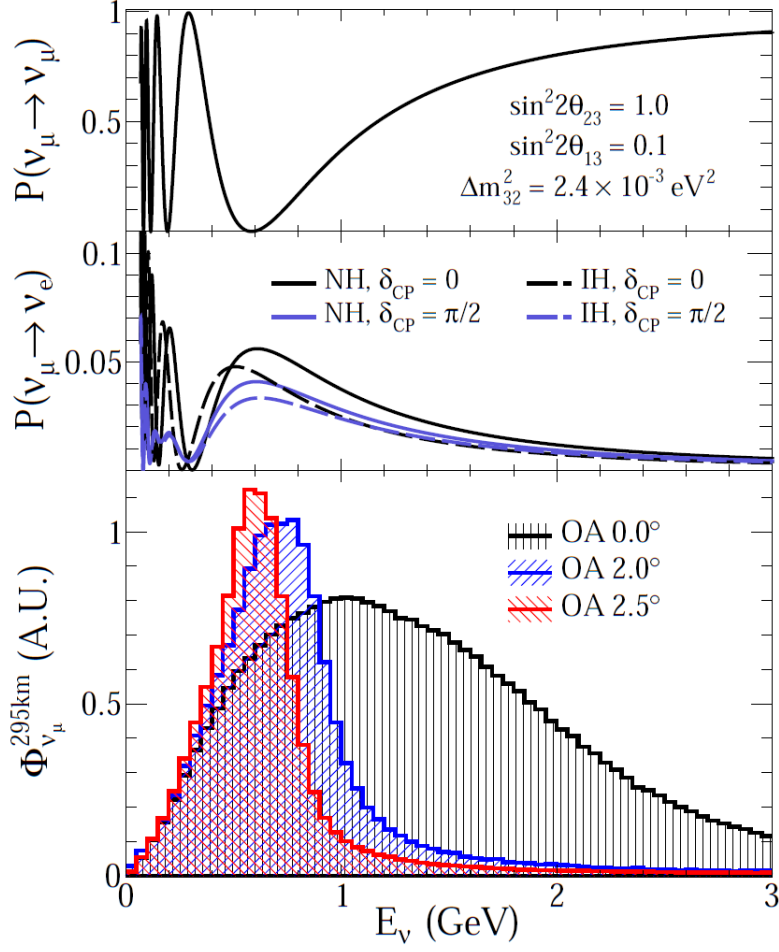


Figure 2.5: Top: Muon neutrino disappearance probability. Middle: Electron appearance probability for different mass hierarchy and  $\delta_{CP}$  hypotheses. Bottom: Beam flux at T2K far detector as a function of neutrino energy.

Channel	Branching ratio (%)
$\pi^+ \rightarrow \mu^+ \nu_\mu$	99.9877
$\pi^+ \rightarrow e^+ \nu_e$	$1.23 \times 10^{-4}$
$K^+ \rightarrow \mu^+ \nu_\mu$	63.55
$K^+ \rightarrow \pi^0 \mu^+ \nu_\mu$	3.353
$K^+ \rightarrow \pi^0 e^+ \nu_e$	5.07
$K_L^0 \rightarrow \pi^- \mu^+ \nu_\mu$	27.04
$K_L^0 \rightarrow \pi^- e^+ \nu_e$	40.55
$\mu^+ \rightarrow e^+ \bar{\nu}_\mu \nu_e$	100

Table 2.1: Decay channels of neutrino parent-particles. Decays for negative particles are charge-symmetrical.

In Figure 2.6 the simulated beam flux at the *off-axis* near detector ND280 is shown as a function of neutrino energy. The peak of the distribution is around 600 MeV. Plots present the contributions of different neutrino flavours for FHC (neutrino beam mode) and RHC (antineutrino beam mode). In case of FHC mode the  $\nu_\mu$  flux is significantly bigger than background flavours flux in the entire range of considered energy (except  $E_\nu < 100$  MeV, but such events aren't probed in the experiment). On the other hand for RHC mode the  $\bar{\nu}_\mu$  flux at high energies is comparable with the so-called “wrong-sign” background i.e.  $\nu_\mu$  flux.

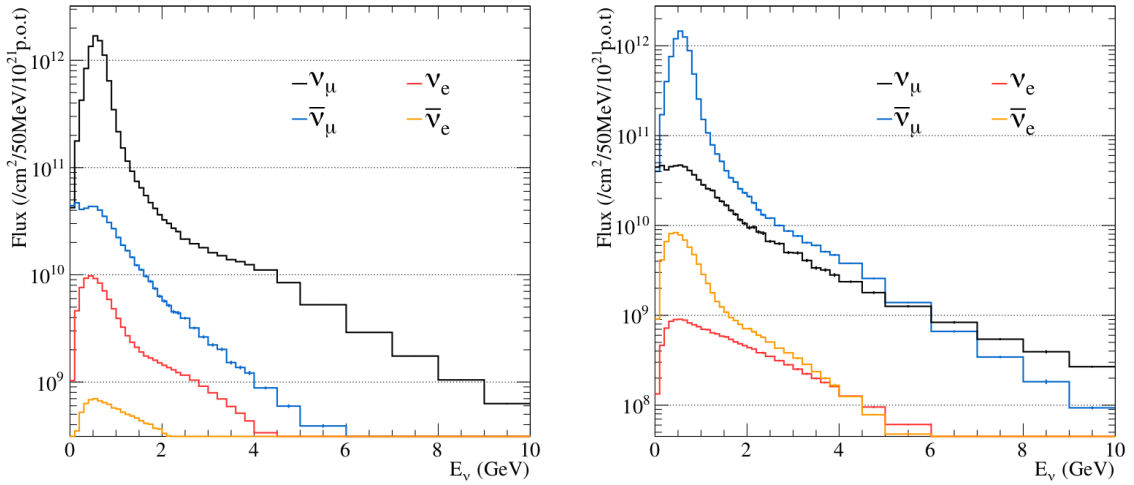


Figure 2.6: Simulated T2K flux at ND280. Neutrino type composition is shown. Left:  $\nu_\mu$  beam mode. Right:  $\bar{\nu}_\mu$  beam mode.

Such asymmetry may be understood intuitively as the neutrino beam production begins with the proton beam interacting with matter. Protons and target nuclei are positively charged and thus more positive secondary particles are produced than negative ones, in particular more  $\pi^+$ 's than  $\pi^-$ 's, which decays contribute to the  $\nu_\mu$  and  $\bar{\nu}_\mu$  flux, respectively. As a result, the “wrong-sign” flux contamination is more significant in the RHC mode than in the FHC, even though magnetic horns are supposed to suppress such background. This effect is more relevant for high energies, since high energy pions are more forward-going and more likely to travel through the central area of magnetic horn where there is no magnetic field. Thus they are not defocused and reach the decay volume.

This asymmetry is enhanced in the measurement by the fact that CC interaction cross-section is higher for neutrinos than anti-neutrinos (see Fig. 2.7). Thus the measurement of CC  $\bar{\nu}_\mu$  interactions in the detector is more encumbered by the CC  $\nu_\mu$  background than the other way around.

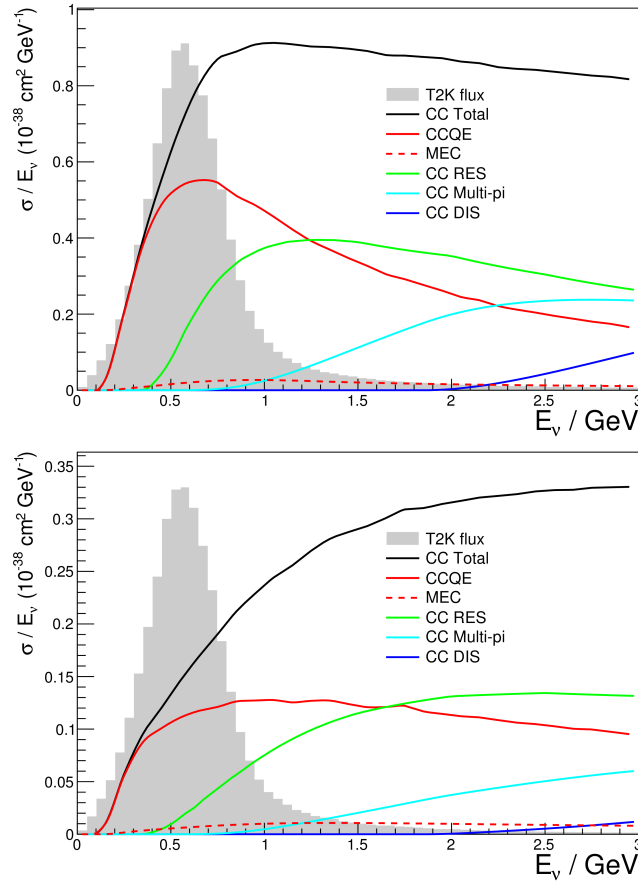


Figure 2.7: Top: (Bottom:) The  $\nu_\mu$  ( $\bar{\nu}_\mu$ ) cross-sections calculated in NEUT generator as a function of  $E_\nu$ , shown with the  $\nu_\mu$  ( $\bar{\nu}_\mu$ ) flux (gray shape) for the T2K  $\nu_\mu$  ( $\bar{\nu}_\mu$ ) beam mode.

## 2.2. INGRID *on-axis* near detector

The Interactive Neutrino GRID (INGRID) [92] is a cross-shaped *on-axis* near detector, which task is to monitor precisely the direction, profile and intensity of the neutrino beam. The collected statistics is enough to provide daily measurements. The beam center is determined with an accuracy better than 10 cm, which corresponds to 0.4 mrad.

The detector is composed of 16 Fe/scintillator modules and one scintillator module (see Fig. 2.8). Fe/scintillator modules are built of interleaved 9 iron target plates and 11 tracking scintillator planes. Each tracking plane consists of two scintillator layers and each layer has 24 scintillator bars. Two consecutive layers are oriented perpendicular to each other, which allows for 3D track reconstruction. The additional scintillator module, called the Proton Module, consists only of scintillator planes and is located in front of the central INGRID module. It provides additional information about low energy particles produced in neutrino interactions which would not be reconstructed in Fe/scintillator module.

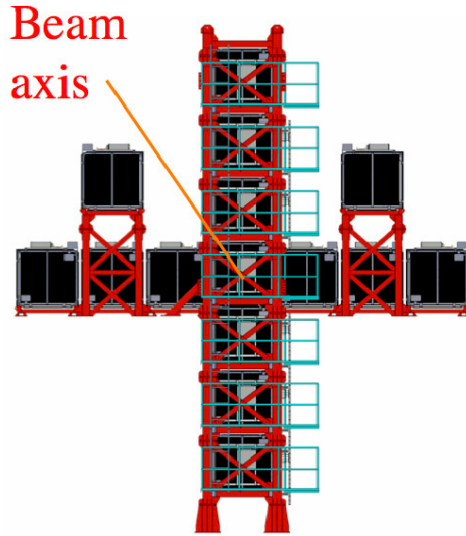


Figure 2.8: *On-axis* near detector INGRID.

The energy loss  $dE/dx$  is measured using the charge deposition in a scintillator corrected by the track length. It allows to distinguish muons and pions from protons. For the sub-GeV muons the momentum is estimated from the range of the track in the Proton Module or the standard INGRID module behind the Proton Module.

### 2.3. ND280 *off-axis* near detector

ND280 (Fig. 2.9) is a multipurpose detector used to constrain the *off-axis* flux and neutrino interaction model, and to measure cross-sections for various (anti)neutrino interaction channels. The magnetic field of 0.2 T provided by refurbished UA1 magnet allows for distinction of negative and positive particles and momentum measurement.

The most inner parts of ND280 are P $\emptyset$ D (upstream  $\pi^0$  detector built of scintillator, water, brass and lead layers [93]) and tracker, which allows for precise CC interaction measurements that support the oscillation analysis. The tracker consists of two scintillator Fine Grained Detectors (FGDs) [94] and three gaseous Time Projection Chambers (TPCs) [95]. FGDs serve as the interaction targets and provide tracking of low energy particles. TPCs allow for particle identification via energy loss  $dE/dx$  measurement and provide good track momentum reconstruction.

Both P $\emptyset$ D and tracker are surrounded by Electromagnetic Calorimeters (ECals) [96]. The Downstream ECal, P $\emptyset$ D and tracker are mounted inside a metal frame structure, called the *basket*.

Additionally, the magnet is equipped with Side Muon Range Detector (SMRD) [97] that detects muons traveling at high angles with respect to the beam direction.

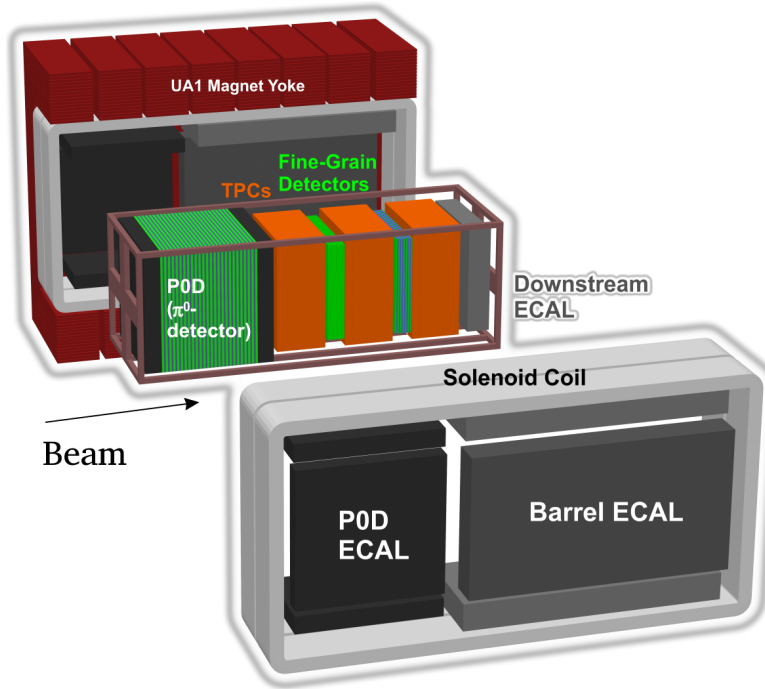


Figure 2.9: *Off-axis* near detector ND280 (exploded view).

For reconstruction of events measured in the ND280 a three-dimensional right-handed Cartesian coordinate system is introduced where  $Z$  axis is parallel to the beam axis and  $Y$  axis points “up” in vertical direction.

The analyses presented in this Thesis are based on antineutrino interactions in the tracker and thus the  $P0D$  will not be described in details. However, a more extensive description of ECals and SMRD is included since the track reconstruction in those subdetectors is relevant for the signal selection in the presented cross-section measurement.

### 2.3.1. UA1 magnet and side muon range detector

Magnet for ND280 is a reused unit from CERN experiments UA1 and NOMAD [98]. It consists of an aluminium coil, cooled by water, and return iron yoke, which surrounds ND280 in order to contain the magnetic field inside the detector. The magnet has external dimensions of  $7.6 \text{ m} \times 5.6 \text{ m} \times 6.1 \text{ m}$ , with inner volume dimensions of  $7 \text{ m} \times 3.5 \text{ m} \times 3.6 \text{ m}$ . The total yoke weight is 850 t. The coil is built of aluminium bars of  $5.45 \text{ cm} \times 5.45 \text{ cm}$  cross-section with a central 23 mm diameter hole for water to flow. Two halves of magnet yoke are installed on movable carriages, which allows for ‘opening’ of ND280. The magnet provides dipole magnetic field of 0.2 T perpendicular to neutrino beam axis. Inside the yoke gaps side muon range detector (SMRD) modules are mounted.

SMRD system consists of 440 scintillator modules: 192 horizontally oriented and 248 vertically oriented. The external dimensions of the SMRD modules are adapted to the dimensions of the yoke gaps and measure to  $955 \text{ mm} \times 686 \text{ mm} \times 9 \text{ mm}$  for horizontal and  $955 \text{ mm} \times 892 \text{ mm} \times 9 \text{ mm}$  for vertical modules (with the last dimension pointing radially outward). Each module is built of 4 to 5 scintillator counters. A single counter is built of a polystyrene-based scintillator slab, serpentine-routed wavelength shifting (WLS) fiber and a Multi-Pixel Photon Counter (MPPC). SMRD performs three main functions. Firstly, it allows for the momentum measurement of muons emitted at high angles (with respect to the neutrino beam) with short or no track segment in the TPC<sup>2</sup>. Secondly, it provides cosmic muons trigger for calibration purposes. Thirdly, it is used to detect background particles entering ND280 from outside or originating from interactions of beam neutrinos in the magnet yoke.

### 2.3.2. Fine grained detectors

Two fine grained detectors (FGDs) provide target mass for neutrino interaction and track charged particles coming from the interaction vertex. Upstream FGD (FGD1) consists of layers of polystyrene scintillator bars oriented alternately in horizontal X and vertical Y directions, allowing 3D track reconstruction. Each pair of layers constitute XY module. Due to such bars arrangement the FGD track reconstruction works well for forward going particles (along Z axis) but is of worse quality for high angle tracks. FGD provides also the measurement of energy loss in the scintillator which in case of fully contained tracks can be used for particle identification as explained in subsection 3.3.4. Most neutrino interactions in FGD1 happen on carbon nuclei. Downstream FGD (FGD2) has similar structure, but scintillator layers are interleaved with water layers, which allows for cross-section measurement on water.

Each FGD (see Fig. 2.10) has dimensions  $2300 \text{ mm} \times 2400 \text{ mm} \times 365 \text{ mm}$  and provides 1.1 tons of target material. Scintillator bars have dimensions  $9.61 \text{ mm} \times 9.61 \text{ mm} \times 1864.3 \text{ mm}$ . FGD1 consists of 5760 scintillator bars, divided into 15 XY modules, each with 192 bars horizontally oriented and 192 bars vertically oriented, while FGD2 consists of 7 such XY modules, with water layers 2.5 cm wide. Each scintillator bar has a hole in the middle for a WLS fibre. One end of the fibre is connected to MPPC photodetector and the second is coated by aluminium to form a mirror and amplify the signal.

Calibration of the photodetectors response is done with a LED light injection sys-

---

<sup>2</sup>Usually the reconstructed track crosses several subdetectors. Term *segment* means part of the reconstructed track corresponding to a given subdetector.

tem. There is one LED for each MMPC which flashes near the end of the WLS fibre opposite the MPPC. Additionally the LED system allows to detect mechanical glitches such as breaks in the fiber or bad fiber-MPPC connection.

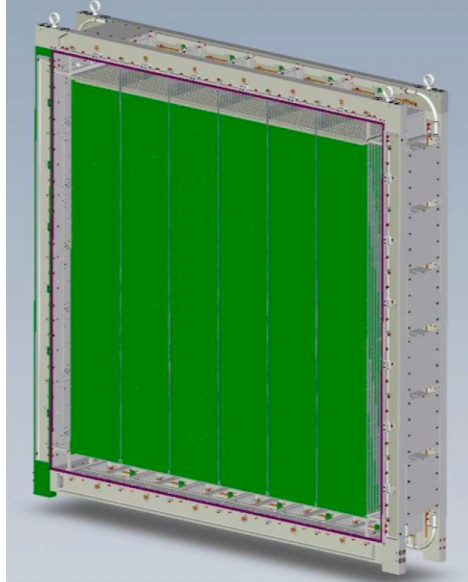


Figure 2.10: Schematic view of an FGD subdetector without the front cover. XY modules (green) are mounted perpendicularly to the neutrino beam direction. Figure taken from [86].

### 2.3.3. Time projection chambers

Three time projection chambers (TPCs) perform several crucial functions in the near detector. Firstly, they provide excellent 3D tracking of charged particles (with the spatial resolution of the order of 1 mm), which allows for determination of number and orientation of particles propagating through the detector. This is a basis for selecting different types of neutrino interactions. Secondly, the tracks curvature in the magnetic field allows for charge identification and momentum measurement of the particle. The accuracy of charge identification depends on the precision of momentum measurement. For particle's momentum around 1 GeV/c the precision of momentum measurement is approximately 10% and over 99% of tracks have correctly identified charge. This quality becomes worse for higher momenta. For particle's momentum around 5 GeV/c (10 GeV/c) the precision of momentum measurement is approximately 25% (60%) and about 97% (90%) of tracks have correctly identified charge. Thirdly, TPCs allow for particle identification based on energy loss  $dE/dx$  measurement (see Fig. 2.11). Resolution of the deposited energy for minimum ionizing particles is approximately 7.8%.

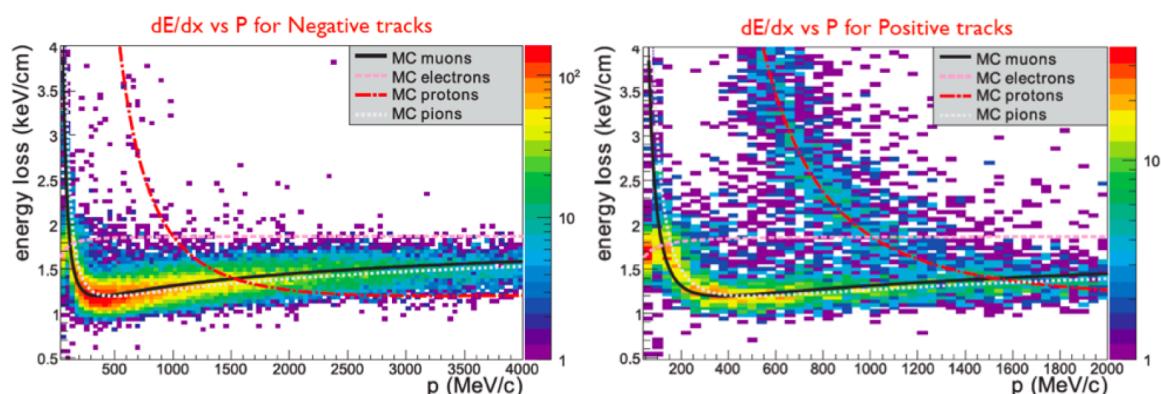


Figure 2.11: Energy loss  $dE/dx$  in TPC versus momentum. Left: Negatively charged particles. Right: Positively charged particles. The lines correspond to the estimated average energy loss for a specific particle. Plots taken from [99].

Each of three time projection chambers (TPCs) has dimensions of  $2.3 \text{ m} \times 2.4 \text{ m} \times 1 \text{ m}$  and consists of the inner box, containing argon-based drift gas and outer box containing  $\text{CO}_2$  as an insulating gas. The electric field is applied from a central cathode to anodes at both sides of the TPC. When a charged particle propagates through the TPC, it ionises gas and ionisation electrons drift to an anode. At each side of the TPC chamber there are 12 MicroMEGAS modules, which amplify the signal before sending it to Data Acquisition system. Each MicroMEGAS module is divided into 1728 pads arranged in 48 rows and 36 columns. Each pad has dimensions of  $7 \text{ mm} \times 9.8 \text{ mm}$  and all are aligned in YZ plane.

The distinct element of MicroMEGAS is a thin metallic micromesh which divides the volume into two regions: drift volume and amplification gap ( $100 \mu\text{m}$  thin). Within the amplification gap the electric field is stronger by two orders of magnitude with respect to the drift volume. Thus, when ionisation electrons drift towards the readout plane and reach the amplification gap they are accelerated and strip off other  $e^-$  from gas molecules. As a result, an avalanche is created and the signal is amplified. Figure 2.12 presents simplified TPC scheme and principle of MicroMEGAS operation.

The photoelectron calibration system was included in the T2K TPCs design. The central copper cathode in each TPC has a set of aluminium targets on its surface. A laser produces  $266 \text{ nm}$  light which is focused into quartz fibers and transported to defocusing optical modules in the inner box. Flashing a diffuse  $266 \text{ nm}$  light on the cathode causes photoelectric effect on aluminium surface but not on copper. This results in a very specific pattern of photoelectrons emitted from the cathode. The distortion of the control pattern in MicroMEGAS signal allows to measure distortions of the electron drift due to inhomogeneity of the electric and magnetic field inside TPC.

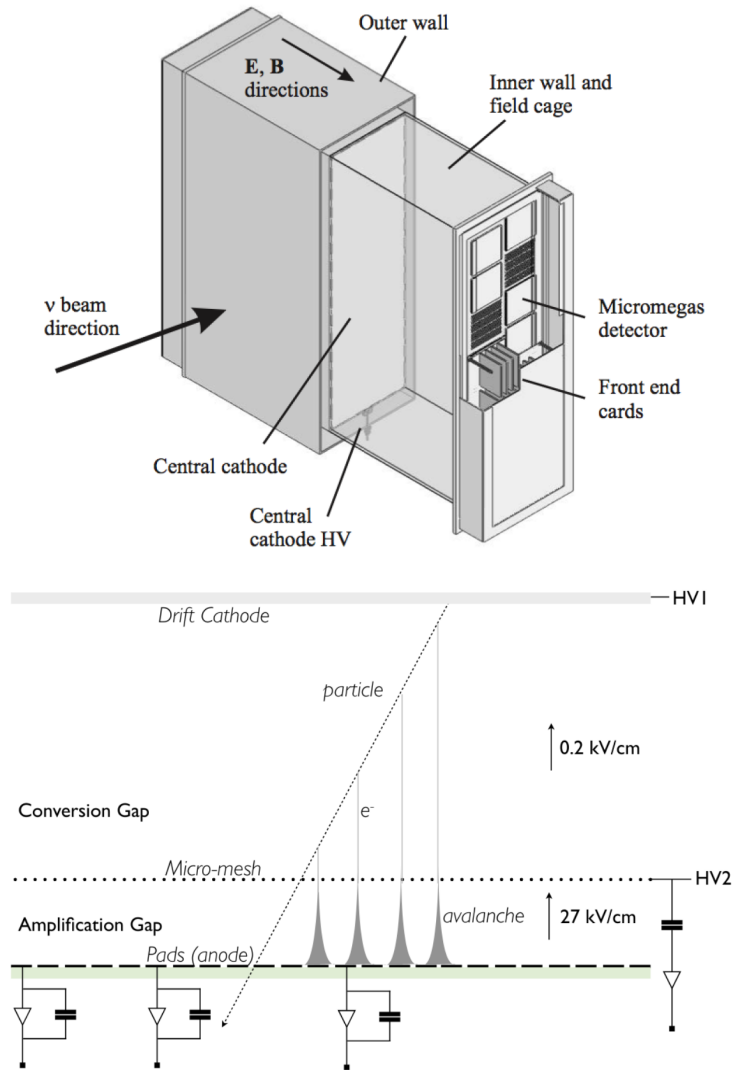


Figure 2.12: Top: Simplified cut-away drawing of the TPC taken from [101]. Bottom: Principle of TPC readout with MicroMegas usage. Figure taken from [102].

### 2.3.4. Electromagnetic calorimeters

ND280 ECal is an electromagnetic calorimeter surrounding inner subdetectors (P $\phi$ D, FGDs, TPCs), designed for measurement of energy and direction of photons, mostly from  $\pi^0$  decays. It provides supplementary information to the tracker and is used to improve separation of electrons, muons and pions, in addition to the TPC particle identification. ECal modules are based on a similar technology as FGDs. They use layers of plastic scintillator bars as an active material interleaved with lead sheets. The bars have a  $4 \text{ cm} \times 1 \text{ cm}$  cross section and differ in length for different modules. The scintillation light is read by one or two MPPCs, depending on the bar length.

There are 13 ECal modules of three types: 6 Barrel-ECal modules surrounding the tracker volume on its four sides along Z axis (beam direction), one downstream module

(Ds-ECal) covers downstream exit of the tracker volume and 6 PØD-ECal modules surround PØD detector on its four sides along Z axis. Ds-ECal is mounted inside the basket containing inner ND280 subdetectors. Other 12 ECal modules are affixed to the magnet yoke. The arrangement of the ECal modules is presented in Fig. 2.9.

Ds-ECal consists of 34 scintillator-lead layers (1.75 mm lead sheet in each layer). This corresponds to  $10.6 X_0^3$  ( $\sim 1\lambda_I^4$ ). In each layer there are 50 scintillator bars of 2.04 m length. The orientation alternates between X and Y axis in consecutive layers. Each Barrel-ECal module consists of 31 scintillator-lead layers, corresponding to  $9.7 X_0$ . In the side modules there are 16 layers with 2.28 m long scintillator bars in Y-direction and 15 layers with 3.84 m long bars in Z-direction. In the four top and bottom modules there are 16 layers with 1.52 m long bars in X-direction and 15 layers with 3.84 m long bars in Z-direction. PØD-ECal modules have coarser granularity and consist of 6 scintillation-lead layers with 4 mm lead sheet and 2.34 m long scintillator bars per layer layer. All bars are oriented parallel to the beam. PØD-ECal is used to tag muons and photons which exited PØD without reconstruction.

### 2.3.5. Multi-Pixel Photon Counters

One of the most common devices in the ND280 and INGRID detectors are Multi-Pixel Photon Counters (MPPCs), which transform light signal from scintillator detectors into electric impulse. They were chosen for use in the near detector complex since they can operate within magnetic field, unlike photomultiplier tubes. MPPCs are used in all subdetectors except the TPC. Examples of MPPCs are presented in Fig. 2.13.

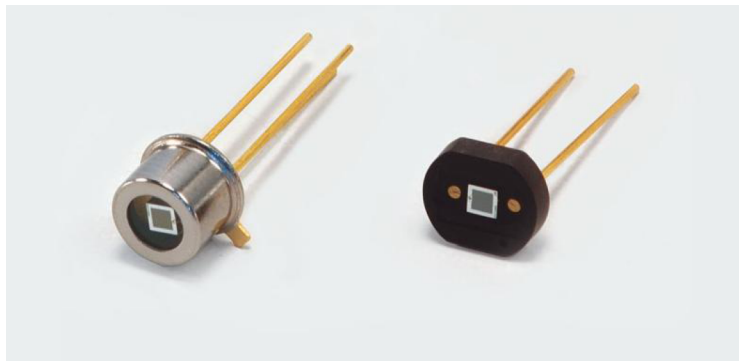


Figure 2.13: A Multi-Pixel Photon Counter (MPPC). Image taken from [103].

A single MPPC used in ND280 has a sensitive area of  $1.3 \times 1.3 \text{ mm}^2$  and is composed of a grid of 667 photodiode pixels. Each pixel is designed to operate above its

<sup>3</sup> $X_0$  (radiation length) is defined as the distance after which an electron beam has  $1/e$  of its initial energy.

<sup>4</sup> $\lambda_I$  (interaction length) is defined as the mean free path of a particle before interacting.

breakdown voltage  $V_{bd}$  (approximately 70 V) and produces an avalanche of electrons if hit by a photon. Thus an MPPC gives the single photon counting capability. The total signal is a summed contribution from all pixels that fire when a light signal is detected in the MPPC. The photoelectron gain per pixel is of the order of  $10^6$ . The exact gain rate depends on the operating voltage  $V_{op}$  (usually 1-2 V above  $V_{bd}$ ) and temperature (thus regular recalibration is needed during data taking).

Overall 64,000 MPPCs were produced for the T2K experiment [104]. A detailed study of the MPPCs performance can be found in [105].

### 2.3.6. Data Acquisition

The ND280 Data Acquisition System (DAQ) [106, 107] consists of a number of modules which provide readout and control of the subdetectors. The architecture of DAQ system electronics is presented in Fig. 2.14.

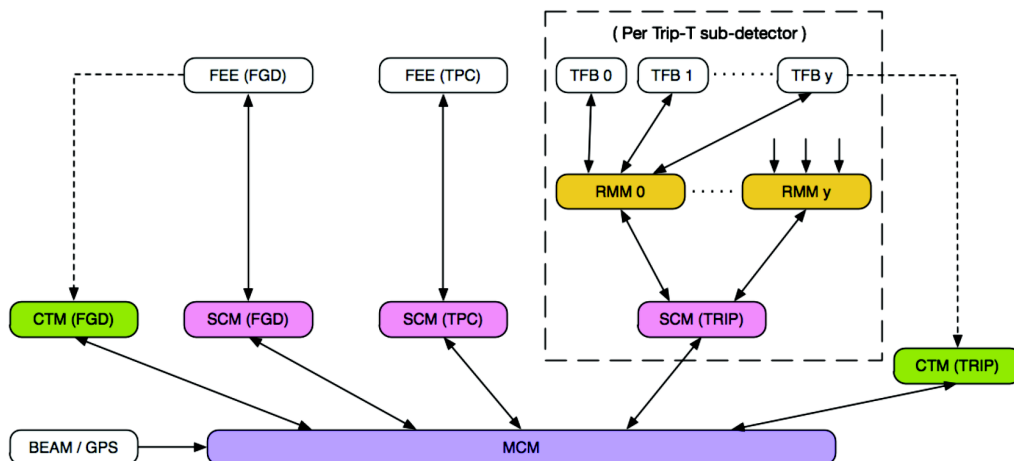


Figure 2.14: The scheme of the T2K ND280 DAQ electronics. Figure taken from [106]. Abbreviations explained in the text.

As described in the previous subsection the scintillator bars in ND280 are read out by MPPC photo-sensors. With the exception of the FGD front-end electronics, all MPPCs are conjoined with the Trip-t Front-End Boards (TFBs). Each TFB works with up to 64 MPPC sensors. Readout Merger Modules allow for control and readout from up to 48 TFBs per RMM and provide the communication interface with ND280 DAQ.

The Front-End Electronics (FEE) for the FGD system [94] resides in 24 minicrates per each FGD. Each minicrate in FGD1 (FGD2) contains four (two) Front-End Boards (FEBs) that power the MPPCs and also digitize the MPPC signal. Data from each

minicrate are read out and sent over optical fiber link to Data Collector Cards installed outside the magnet.

The FEE for the TPC system [95] has the same building block for each MicroMEGAS. Each block consists of six Front-End Cards (FECs) and one Front-End Mezzanine (FEM). The FEM board aggregates the data from the FECs, reduces the raw data event size and sends the remaining data to the Data Concentrator Card.

The accelerator beam spill is produced every 2.5 seconds and each spill consists of eight 58 ns long bunches. The physics occupancy is therefore low. Trip-t operation is synchronized to the bunch structure, while FGD and TPC read out is active for the entire spill. This allows for the identification of Michel electrons which are delayed due to the decay time of the muon.

The Master Clock Module (MCM) coordinates the clock and trigger for the readout system. It provides a high precision 100 MHz clock, which is obtained from the GPS reference system shared with the neutrino beamline. The MCM also sets readout triggers, which are assigned to the front-end electronics.

Each subdetector has the Slave Clock Module (SCM), which receives clock and trigger signals from the MCM. The SCM may be switched to a local clock and trigger module, which allows stand-alone operation of each sub-system.

The Cosmic Trigger Module receives cosmic trigger signals from the TFBs and from the FGD front-end electronics. Certain logical combinations of the trigger signals are signatures of coincidences that represent cosmic tracks crossing the various subdetectors.

## 2.4. Super-Kamiokande far detector

T2K far detector Super-Kamiokande (SK) is a 50 kt water Cherenkov detector, localised in the old zinc mine under mount Ikeno, 295 km from the beam production target in J-PARC. The detector is shielded by 1000 m of rocks (2700 m water equivalent) to reduce cosmic rays background rate by about 5 orders of magnitude with respect to the Earth surface. Over 20 years of operation SK obtained results in the field of atmospheric, solar and accelerator neutrino oscillations ([108]-[111]) as well as the world-leading limit on the proton life-time [112].

Figure 2.15 presents the diagram of the detector. Cylindric SK cavity is 41 m high and 39 m wide, filled with 50 kt of ultra-pure water. It is divided in to two regions. The Inner Detector (ID) is 36.2 m high and 33.8 m wide and its walls are covered with  $\sim 11000$  inward-facing 50 cm photomultiplier tubes (PMTs). This corresponds to 40% coverage of the ID surface. Surrounding the ID is the Outer Detector (OD)

which is cylindrical space of 2m radial width. On its walls the OD is equipped with 1885 outward-facing 20 cm PMTs, which are used to tag particles entering or exiting the ID.

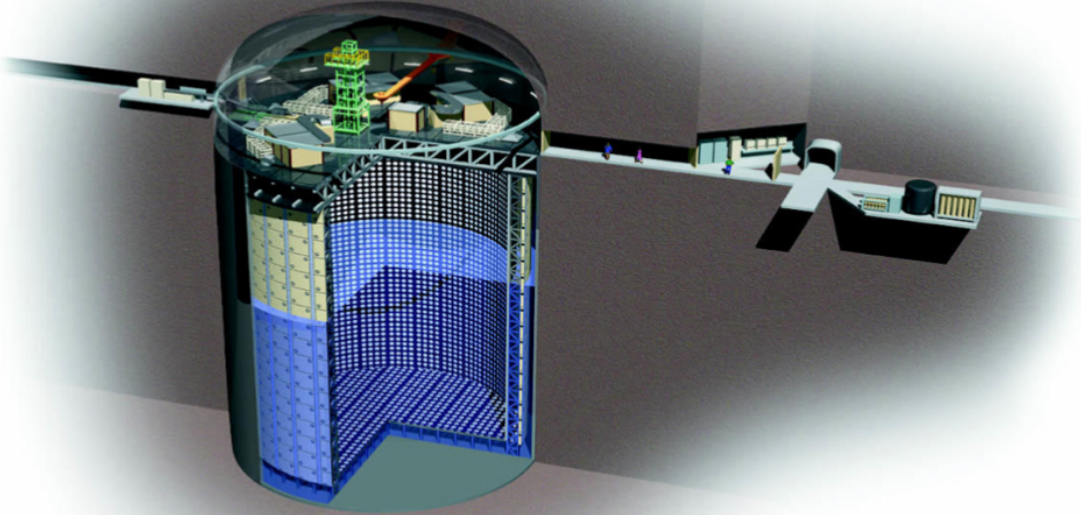


Figure 2.15: Diagram of the far detector Super-Kamiokande.

Water Cherenkov detectors use Cherenkov light [113] to detect charged particles produced in neutrino CC interactions. When a charged particle propagates faster than the speed of light in a medium, it polarizes molecules of the medium, which then turn back to the ground state, emitting radiation (i.e. Cherenkov light). Cherenkov threshold (minimal energy for causing Cherenkov radiation) is given by:

$$E = \frac{mc^2}{\sqrt{1 - (1/n)^2}}, \quad (2.3)$$

where  $m$  is the particle mass and  $n$  is the refractive index of the medium (1.33 for water). Thus heavier particles must have higher energy to be detected.

Emitted light forms coherent cone-like wave front with opening angle:

$$\cos\theta = \frac{1}{\beta n}, \quad (2.4)$$

where  $\beta = v/c$ . For ultra-relativistic particles  $\beta \approx 1$  and  $\theta \approx 42^\circ$  in water. When particles propagate through the water tank, they cause emission of Cherenkov radiation

until their energy drops below the threshold. As a result PMTs on SK walls detect ring-like light signal.

The measurement of  $\nu_\mu$  disappearance or  $\nu_e$  appearance is based on a particle identification (PID) used to separate electrons and muons in SK. Due to the large mass muon direction is hardly affected by multiple scattering in water, which results in a clear, sharp ring of PMT hits on the SK wall. Electrons however are easily scattered inside the detector and tend to induce electromagnetic showers, which create multiple Cherenkov rings in slightly different directions. This is detected by PMTs as a “fuzzy” ring pattern. Figure 2.16 presents an example of SK event displays with  $\mu$ -like and e-like rings.

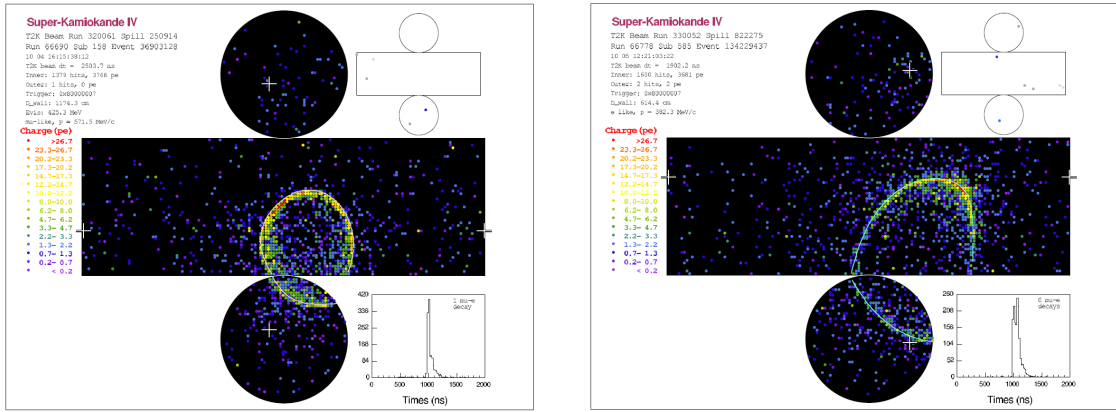


Figure 2.16: Data event display in Super-Kamiokande. Left:  $\mu$ -like event. Right:  $e$ -like event.

Since 2020 SK operates with Gadolinium dissolved in water. Gadolinium nucleus is characterised by a large cross-section for neutron capture. When falling back to the ground state Gd nucleus emits 8 MeV  $\gamma$  approximately 30  $\mu$ s after the neutron capture. Sensitivity to this signal is expected to improve the efficiency of antineutrino detection ( $\bar{\nu}_l + p \rightarrow l^+ + n$ ) [114].

## 2.5. Summary of the collected T2K data

T2K experiment started collecting good quality data in January 2010. Figure 2.17 summarises 10 years of data taking. Blue line presents growth of the total number of protons on target (POT). Red (violet) line corresponds to the accumulated data in neutrino (antineutrino) beam mode. The total good quality data statistics is equivalent to  $3.64059 \times 10^{21}$  POT with  $1.99006 \times 10^{21}$  POT for neutrino (FHC) beam mode and  $1.65053 \times 10^{21}$  POT for antineutrino (RHC) beam mode. Data relevant for the

analysis presented in this thesis was collected in RHC runs 5-9 and corresponds to  $0.84599 \times 10^{21}$  POT (which is smaller than nominal POT for RHC runs due to failures in ND280 operation). Red (violet) dots in the plot show the proton beam power in FHC (RHC) mode. The beam power was gradually increasing through the last 10 years and reached maximum of 522.627 kW in the early 2020. The rate of accumulating POT is proportional to the proton beam power.

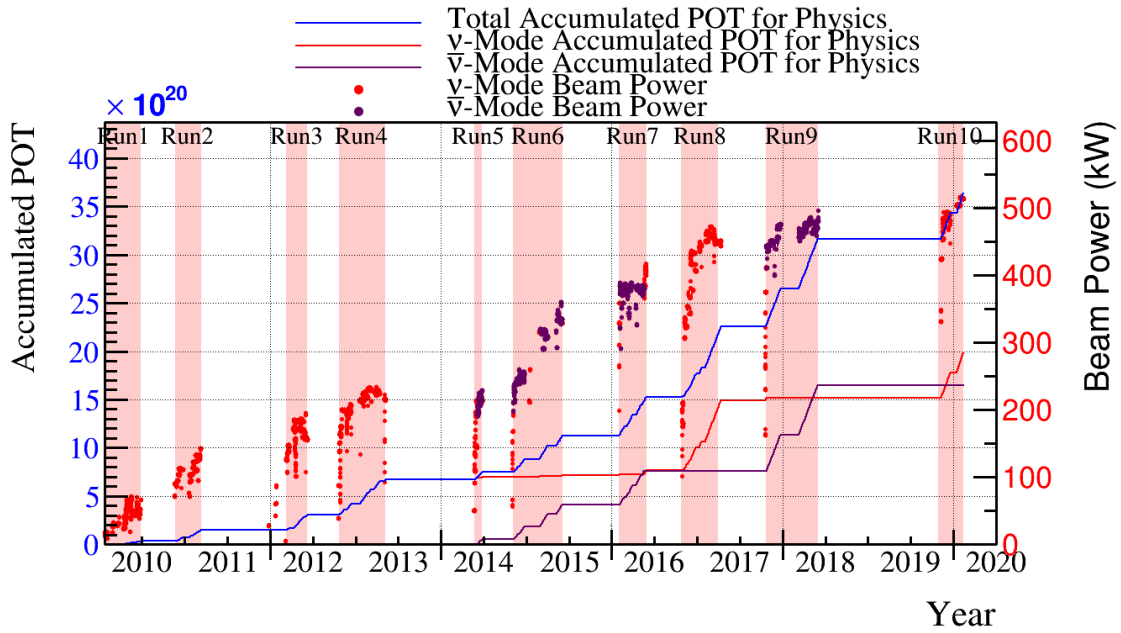


Figure 2.17: Accumulated data statistics (lines) and proton beam power (dots) for all T2K runs.

# Chapter 3

## Samples selection for the cross section measurement

The main objective of Author's PhD research was the cross-section measurement of  $\bar{\nu}_\mu$  CC interaction in FGD1 subdetector with single charged pion production. FGD1 consists mostly of scintillator material which is hydrocarbon. As explained in Chapter 1 the signal is defined as events with a single  $\mu^+$  and  $\pi^-$  and no other mesons emitted in the final state (i.e. exiting the nucleus):

$$\bar{\nu}_\mu + N \rightarrow \mu^+ + \pi^- + N' + X,$$

where  $X$  indicates any number of free nucleons exiting the nucleus. By definition **only interactions within FGD1 fiducial volume are treated as signal**. The measurement is based on data collected in  $\bar{\nu}_\mu$  beam mode (RHC) runs (5-7 and 9, see Fig. 2.17) and corresponding MC samples.

In general, the flux integrated cross section may be expressed as:

$$\sigma^{signal} = \frac{N^{signal}}{\epsilon \cdot \Phi \cdot T}, \quad (3.1)$$

where  $N^{signal}$  - number of selected signal events,  $\epsilon$  - selection efficiency,  $\Phi$  - integrated flux,  $T$  - number of target nucleons. In case of differential cross-section it is:

$$\left( \frac{d\sigma^{signal}}{dx} \right)_i = \frac{N_i^{signal}}{\epsilon_i \cdot \Phi \cdot T \cdot \Delta x_i}, \quad (3.2)$$

where  $x$  is the phase-space variable (such as the particle momentum), index  $i$  indicates a given bin of the phase space,  $\epsilon_i$  denotes selection efficiency within that bin and  $\Delta x_i$  is the bin width. The crucial point of the measurement is the estimation of  $N_i^{signal}$  - number of signal events in a given bin. In case of presented analysis this was done by binned likelihood fit method, which is described in details in section 5.2.

The first stage of the cross section measurement is creating the selection of the signal samples and the background samples (sidebands). The signal samples are used to estimate the signal event rate while the purpose of the sidebands is to provide constraints on the background processes. The selection studies for the presented work were based on MC samples produced with NEUT generator and corresponding to  $\bar{\nu}_\mu$  beam mode runs 5+6+7+9. **Unless stated otherwise, all plots in this chapter were generated for those MC samples** and normalised to collected data statistics corresponding to  $8.46 \times 10^{20}$  POT.

The basic figure of merit that is checked when studying the signal selection's performance is the product of purity and efficiency. Purity  $\mathbf{p}$  is defined as the fraction of events with true signal topology in the selected sample:

$$\mathbf{p} = \frac{S}{N}, \quad (3.3)$$

where  $S$  is the number of selected signal events,  $N$  - the number of all selected events. Efficiency is defined as the ratio of signal events that were successfully selected to all signal events that were present in the detector  $S_{all}$ :

$$\epsilon = \frac{S}{S_{all}} \quad (3.4)$$

A short motivation for using  $\mathbf{p} \times \epsilon$  as the figure of merit is given below.

The expected number of signal events  $\langle S \rangle$  in the measurement may be expressed as:

$$\langle S \rangle = \epsilon \cdot \Phi \cdot T \cdot \sigma_S,$$

where  $\epsilon$  is the selection efficiency,  $\Phi$  - neutrino flux,  $T$  - number of targets,  $\sigma_S$  - signal cross section. In the signal region a certain number of background events  $\langle B \rangle$  is expected as well. Thus, the expected total number of measured events  $\langle N \rangle$  is given by:

$$\langle N \rangle = \langle S \rangle + \langle B \rangle.$$

The signal cross-section may be extracted in the measurement as:

$$\sigma_{meas} = \frac{N - \langle B \rangle}{\epsilon \cdot \Phi \cdot T}.$$

Assuming that the *expected* number of background events is known very well i.e. its uncertainty is small compared to the statistical error on the number of signal events, the statistical error of the cross-section is given by:

$$\delta\sigma_{meas} = \frac{\sqrt{N}}{\epsilon \cdot \Phi \cdot T}.$$

Thus, the expected statistical error is:

$$\langle \delta\sigma_{meas} \rangle = \frac{\sqrt{\langle N \rangle}}{\epsilon \cdot \Phi \cdot T}.$$

The expected total number of events may be expressed as:

$$\langle N \rangle = \frac{\langle S \rangle}{\mathbf{p}}.$$

Thus, the expected statistical error is:

$$\langle \delta\sigma_{meas} \rangle = \frac{\sqrt{\frac{\langle S \rangle}{\mathbf{p}}}}{\epsilon \cdot \Phi \cdot T} = \frac{\sqrt{\frac{\epsilon \cdot \Phi \cdot T \cdot \sigma_S}{\mathbf{p}}}}{\epsilon \cdot \Phi \cdot T} = \sqrt{\frac{\sigma_S}{\mathbf{p} \cdot \epsilon \cdot \Phi \cdot T}}.$$

In the denominator of the final expression the product of purity and efficiency  $\mathbf{p} \cdot \epsilon$  appears. Optimizing this quantity leads to minimal expected statistical error of the measured cross-section. This is the key motivation for choosing such figure of merit. For more detailed discussion see [115].

The reported cross section is double-differential in  $\mu^+$  kinematical variables: momentum and cosine of the angle of the outgoing  $\mu^+$  with respect to Z axis (longitudinal detector axis). Two signal samples and two background samples are selected for the measurement and used simultaneously in the likelihood fit described in section 5.2. The signal samples provide sensitivity to  $\bar{\nu}_\mu$  CC1 $\pi^-$  topology, while the background samples allow to constrain other processes. All samples are based on reconstruction of  $\mu^+$  candidate and share basic selection criteria described in sections 3.1 and 3.2. Further selection of the signal and background samples is described in sections 3.3 and 3.5, respectively. The efficiency studies for the signal samples are presented in section 3.4 and Appendix A.

### 3.1. Pre-Selection

Samples selection is based on event signature in tracker, which is the inner part of ND280. An example of event display in the detector is presented in Fig. 3.1. Initial cuts (so-called pre-selection), which are common among many T2K analyses, are presented in this subsection.

1. **Event quality** cut - Event is within the beam bunch time window and has good data quality flags. Data quality flags depend on factors such as the subdetectors performance in a given period of data taking.<sup>1</sup> For the Monte Carlo samples data quality is always good.

---

<sup>1</sup>Author was responsible for setting FGD data quality flags for run 10.

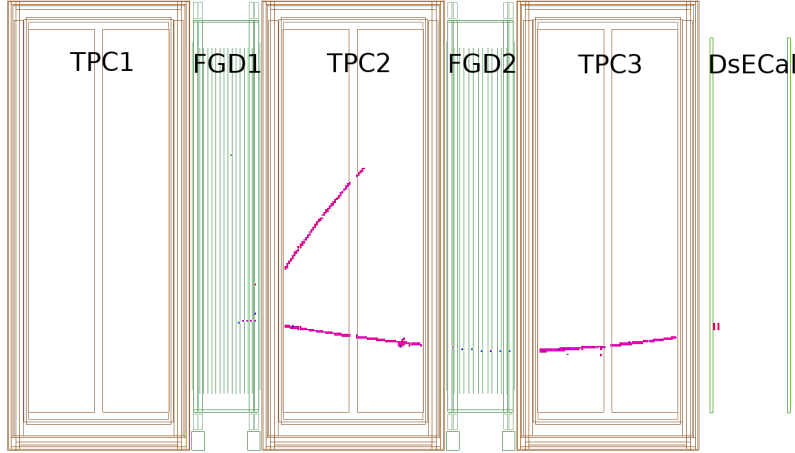


Figure 3.1: Data event display in tracker region of ND280. Neutrino beam enters from left. The interaction happens in FGD1, a positively charged particle penetrates TPC2, FGD2 and TPC3 and reaches DsECal. A negatively charged particle exits TPC2.

2. **Total multiplicity** cut - There must be at least one reconstructed track in the TPC2 (nearest subdetector downstream of FGD1) with more than 18 TPC clusters<sup>2</sup>. The choice of such cut threshold is based on MC studies of the momentum reconstruction resolution (see Fig. 3.2).

3. **Quality and fiducial volume** cut - The highest momentum positive track (HMPT) must have more than 18 TPC clusters. It also must originate in the FGD1 fiducial volume (FV)<sup>3</sup>. FV corresponds to the central 182 scintillator bars in the X and Y layers. Each layer consists of 192 scintillator bars (see subsection 2.3.2) so 5 bars on both ends of each layer are excluded. Additionally, the most upstream XY module is not included in the FV. The goal of this cut is to exclude neutrino interactions outside of FGD1.

4. **TPC1 veto** - This cut aims to remove tracks entering the FGD1 FV from the upstream side of the detector. The highest momentum track other than HMPT is taken into account. If such track starts more than 150 mm upstream from the HMPT's start position and contains a TPC1 segment, it is likely a signature of a particle entering FGD1 from the upstream ND280 region and the event is rejected.

5. **External FGD1** cut - Rejection of external background from the two most downstream layers of FGD1. This cut is applied to reject events with mis-reconstructed

<sup>2</sup>A cluster consists of coincided signals from neighbouring pads in a MicroMEGAS column.

<sup>3</sup>In ND280 coordinate system FGD1 FV dimensions are:  $|X| < 874.51$  mm,  $|Y-55| < 874.51$  mm, and  $136.875 < Z < 446.955$  mm.

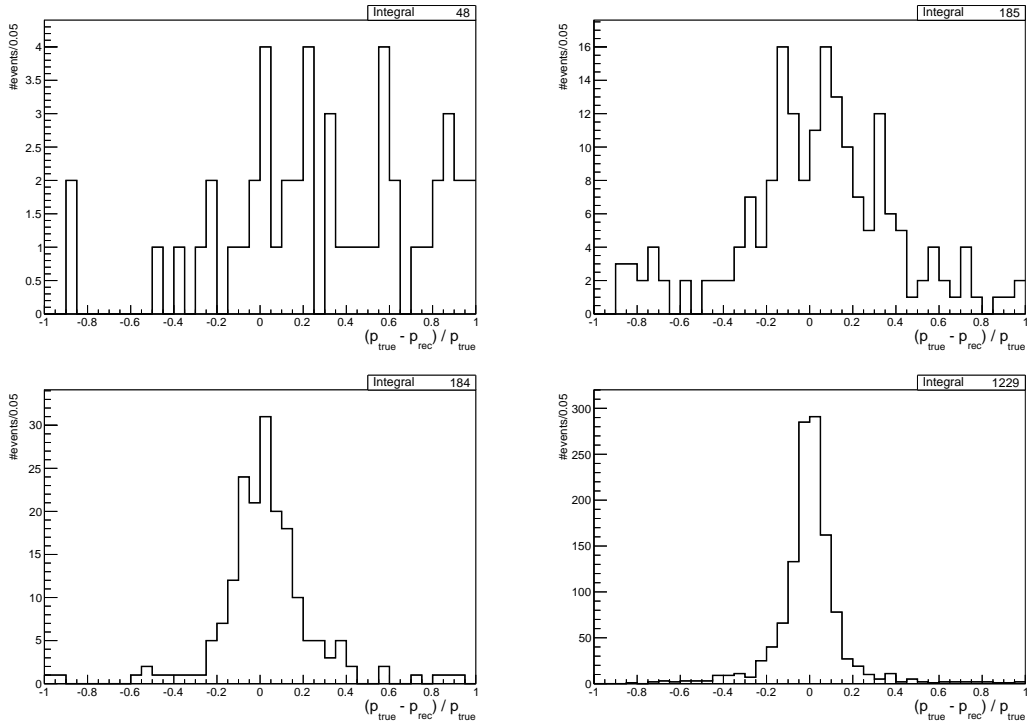


Figure 3.2: Distribution of the momentum reconstruction resolution  $(p_{true} - p_{rec})/p_{true}$  for TPC2 tracks with different number of clusters. **Plots drawn for MC subsample corresponding to  $5 \times 10^{19}$  POT.** Top left: Tracks with 10-18 TPC2 clusters. Top right: Tracks with 19-36 TPC2 clusters. Bottom left: Tracks with 37-54 TPC2 clusters. Bottom right: Tracks with more than 54 TPC2 clusters.

tracks, that were split into a track fully contained in FGD1 and a track starting in the last layers of FGD1 and traversing TPC2.

For the preselected sample the signal  $\bar{\nu}_\mu$  CC1 $\pi^-$  selection efficiency  $\epsilon = 78.8\%$  and purity  $\mathbf{p} = 6.44\%$ . In each event selected with the aforementioned cuts the highest momentum positive track is treated as a  $\mu^+$  candidate<sup>4</sup>. The distributions of kinematical variables of those candidates in the MC sample are presented in Fig. 3.3. About 45% of the candidates correspond to true  $\mu^+$  tracks and the dominant background are proton tracks - approximately 32%. In the low momentum region the dominant background are  $e^\pm$  tracks. The *no truth* category in the legend refers to MC events with reconstructed track, but no true particle assigned to it. The rate of such events is below 0.01% in the overall sample. The particles classified as *other* are mostly  $K^\pm$ .

<sup>4</sup>About 84% of events in the preselected sample have exactly one reconstructed positive track crossing TPC. MC studies indicate that reconstructed second highest momentum positive tracks (SHMPTs) rarely correspond to true  $\mu^+$  (about 8% of SHMPTs). Thus such tracks are not treated as  $\mu^+$  candidates.

The true identity composition of the  $\mu^+$  candidates is summarized in Table 3.1 (*no truth* events neglected) - the low momentum region  $p_\mu < 500$  MeV/c is distinguished since in the CC-inclusive selection the additional cut is applied there (related to energy loss  $dE/dx$  in TPC).

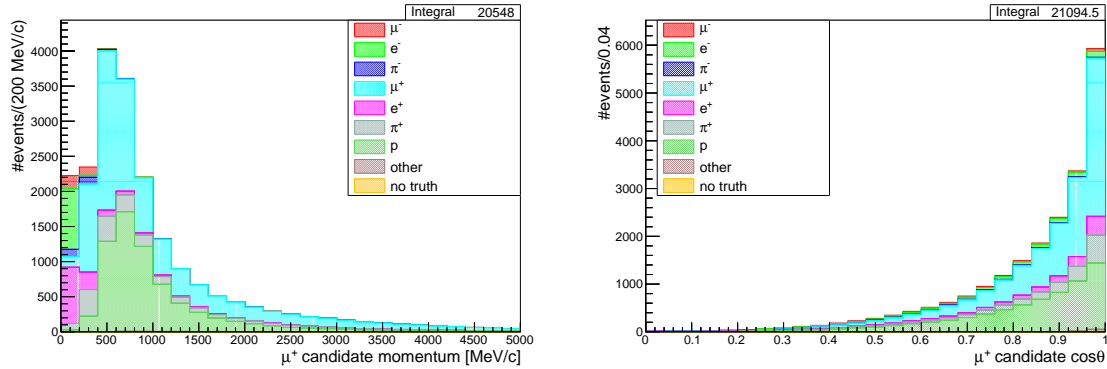


Figure 3.3: **Pre-Selection.** MC distribution of reconstructed kinematic variables (left - momentum, right -  $\cos\theta$ ) of the reconstructed  $\mu^+$  candidate. Colors indicate the true identity of the candidate.

particle	fraction of $\mu^+$ candidates in pre-selected sample	
	whole sample	$p_\mu < 500$ MeV/c
$\mu^-$	1.9%	4.8%
$e^-$	4.4%	13.8%
$\pi^-$	1.1%	3.2%
$\mu^+$	45%	39%
$e^+$	6.4%	17%
$\pi^+$	8.9%	10.2%
p	31.8%	11.8%
other	0.4%	0.1%

Table 3.1: **Pre-Selection.** Proportions of true  $\mu^+$  candidates' identities in the MC sample.

Table 3.2 presents the true final state topology composition of the preselected sample (*no truth* events neglected). Abbreviation  $\bar{\nu}_\mu$  CC0 $\pi$  indicates  $\bar{\nu}_\mu$  charged current interactions with  $\mu^+$  and no mesons in the final state. The signal topology with  $\mu^+$ ,  $\pi^-$  and no other mesons in the final state is referred to as  $\bar{\nu}_\mu$  CC1 $\pi$ . Abbreviation  $\bar{\nu}_\mu$  CC-other indicates any other  $\bar{\nu}_\mu$  CC interactions with  $\mu^+$  in the final state. Although the measurement is done for  $\bar{\nu}_\mu$  beam mode the beam is contaminated with  $\nu_\mu$ . This results in significant  $\nu_\mu$  CC interactions background. Another major background source

is due to out of fiducial volume (OOFV) interactions, especially for events with low  $\mu^+$  candidate momentum.

true topology	fraction of events in pre-selected sample	
	whole sample	$p_\mu < 500 \text{ MeV}/c$
$\bar{\nu}_\mu \text{ CC}0\pi$	33.7%	30.9%
$\bar{\nu}_\mu \text{ CC}1\pi$	6.4%	4.9%
$\bar{\nu}_\mu \text{ CC-other}$	5.4%	2.4%
NC (flavour blind)	9.2%	6.4%
CC $\nu_\mu$ background	20.4%	9.5%
CC $\nu_e + \bar{\nu}_e$ background	1.8%	1.4%
Out of Fiducial Volume (OOFV)	22.9%	44.5%

Table 3.2: **Pre-Selection.** Proportions of true final state topology in the MC sample. The  $\bar{\nu}_\mu$  CC topologies are categorized with respect to mesons multiplicity (abbreviations explained in the text).

## 3.2. CC-inclusive

In order to select a sample of  $\bar{\nu}_\mu$  CC interactions additional criteria are used to identify  $\mu^+$  with better purity. This sample is also referred to as CC-inclusive, since the selection is not based on all reconstructed tracks but on the properties of  $\mu^+$  candidate. Additional cuts use TPC particle identification (PID), which was already developed and applied in other T2K analyses [116]. The measured energy loss  $C_T^{meas}$  is compared with the expected loss  $C_T^{exp}(i)$  for a given particle hypothesis  $i$  ( $i = \mu, e, \pi, p$ ) by calculating the pull variable:

$$\delta(i) = \frac{C_T^{meas} - C_T^{exp}(i)}{\sigma^{exp}(i)}, \quad (3.5)$$

where  $\sigma^{exp}(i)$  is the deposited energy resolution. The pull variable  $\delta(i)$  is calculated for each TPC segment of the track. In general a  $\mu^+$  candidate may have one TPC segment (in TPC2) or two segments (in TPC2 and TPC3). The probability density functions are calculated using  $\delta(i)$ :

$$P_i = \frac{1}{\sqrt{2\pi}\sigma^{exp}(i)} \exp \left[ - \sum_j^{\text{TPC}j} \frac{\delta_j(i)^2}{2} \right], \quad (i = \mu, e, \pi, p), \quad (3.6)$$

where  $j$  indicates the  $j$ -th TPC segment.

The  $i$  particle likelihood is defined as:

$$L_i = \frac{P_i}{P_\mu + P_e + P_\pi + P_p}, \quad (i = \mu, e, \pi, p). \quad (3.7)$$

Additionally, the MIP-likelihood is defined as:

$$L_{MIP} = \frac{L_\mu + L_\pi}{1 - L_p}. \quad (3.8)$$

For selecting  $\mu^+$  candidates a combination of cuts on  $L_{MIP}$  and  $L_\mu$  likelihoods is used. The first cut is applied for low momentum tracks and rejects  $e^\pm$  background:

$$L_{MIP} > 0.9 \quad \text{if } p < 500 \text{ MeV}/c. \quad (3.9)$$

The second cut ( $L_\mu > 0.1$ ) reduces proton and some of  $\pi^+$  background from neutrino CC interactions. The distributions of  $L_{MIP}$  and  $L_\mu$  are shown in Fig. 3.4 .

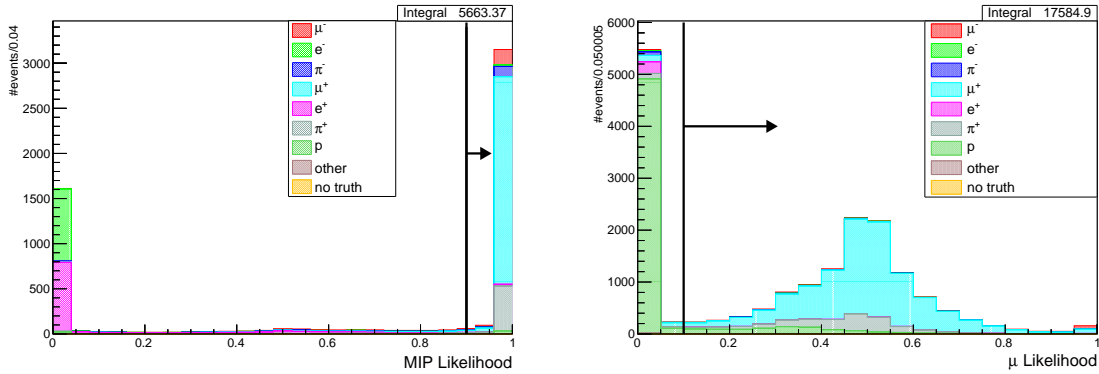


Figure 3.4: Left: MIP-likelihood  $L_{MIP}$  distribution for  $p < 500$  MeV/c. Right: Muon-likelihood  $L_\mu$  distribution for events satisfying  $L_{MIP}$  cut. Colors indicate the true identity of the candidate.

The described criteria increase significantly the purity of the selected  $\mu^+$  candidates. In  $\bar{\nu}_\mu$  CC-inclusive sample, about 74.9% of  $\mu^+$  candidates correspond to true  $\mu^+$  tracks (for pre-selected sample that was 45%). The distributions of kinematical variables of those candidates in MC sample are presented in Fig. 3.5. The true identity composition of the  $\mu^+$  candidates is summarized in Table 3.3.

Table 3.4 presents the true final state topology composition of the  $\bar{\nu}_\mu$  CC-inclusive sample. Thanks to better  $\mu^+$  identification the OOFV background was reduced by a factor of 3 and contribution of all  $\bar{\nu}_\mu$  CC topologies increased with respect to the preselected sample. The signal selection efficiency  $\epsilon = 69.8\%$  and purity  $\mathbf{p} = 9.86\%$ .

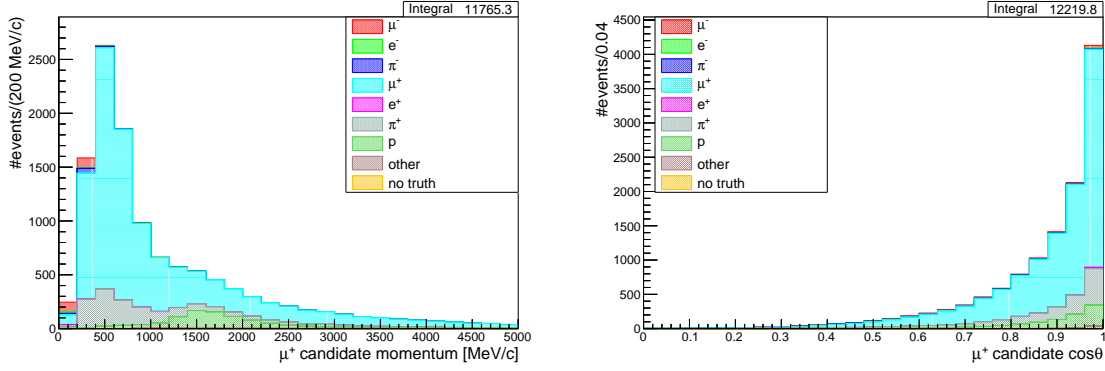


Figure 3.5: **CC-inclusive selection.** MC distribution of reconstructed kinematic variables (left - momentum, right -  $\cos\theta$ ) of the reconstructed  $\mu^+$  candidate. Colors indicate the true identity of the candidate.

particle	fraction of $\mu^+$ candidates in CC-inclusive sample
$\mu^-$	2.1%
$e^-$	0.3%
$\pi^-$	0.7%
$\mu^+$	74.9%
$e^+$	0.4%
$\pi^+$	13.4%
p	7.7%
other	0.5%

Table 3.3: **CC-inclusive selection.** Proportions of true  $\mu^+$  candidates' identities in the MC sample.

true topology	fraction of events in CC-inclusive sample
$\bar{\nu}_\mu$ CC0 $\pi$	55.5%
$\bar{\nu}_\mu$ CC1 $\pi$	9.9%
$\bar{\nu}_\mu$ CC-other	8.3%
NC (flavour blind)	4.4%
CC $\nu_\mu$ background	14.9%
CC $\nu_e + \bar{\nu}_e$ background	0.7%
Out of Fiducial Volume (OOFV)	6.5%

Table 3.4: **CC-inclusive selection.** Proportions of true final state topologies in the MC sample.

### 3.3. Signal samples selection

#### 3.3.1. One Pion Cut

An additional cut is used to select the sample with single negative pion ( $CC1\pi^-$ ). This selection step uses particle signatures both in TPC and FGD. The TPC is used to reconstruct charged pions, electrons and positrons. These secondary tracks are required to start in the FGD1 FV and have more than 18 clusters in the TPC. The TPC particle identification is based, as described in the previous section, on the energy loss  $dE/dx$  measurement. The FGD is used to identify Michel electrons and FGD-contained pion tracks.

The one pion cut rejects events with:

- $\pi^+$  track reconstructed in TPC ,
- $e^\pm$  track reconstructed in TPC - such signature likely indicates  $\pi^0$  decay,
- Michel electron (ME) - found by searching for delayed signals in FGD1 due to the decay time of the muon ( $2.19 \mu s$ ). The ME delayed signal must be outside of the beam bunch window and is required to have at least 7 hits in FGD1 [117]. ME is more likely to originate from  $\pi^+$  decay chain rather than from  $\pi^-$  decay chain, since  $\pi^-$  is more likely to be absorbed by positively charged nuclei.<sup>5</sup>

Events with any aforementioned signature contribute to one of the sidebands (CC-other), which is described in section 3.5.1.

The one pion cut selects events which contribute to two signal samples:

- one  $\pi^-$  track reconstructed in TPC2, originating in FGD1 - **CC1TPC $\pi^-$  signal sample**

or

- no  $\pi^-$  track reconstructed in TPC2 and one pion track fully contained in FGD1 - **CC1FGD $\pi^-$  signal sample**

The  $CC1\pi^-$  sample consists mostly of events with reconstructed TPC  $\pi^-$  (92%). Events with FGD-contained pion constitute about 8% of the sample. These two topologies are then treated as a separate samples.<sup>6</sup>

---

<sup>5</sup>ME originates from decay of  $\mu^\pm$  which originates from  $\pi^\pm$  decay. For CC-inclusive sample a reconstructed ME originates approximately 2 times more often from  $\pi^+$  decay chain than from  $\pi^-$ .

<sup>6</sup>There is no strict condition on the starting point of  $\pi^-$  candidate track  $\mathbf{x}_\pi$  with respect to the starting point of  $\mu^+$  candidate track  $\mathbf{x}_\mu$ . A minor improvement of the selection purity (by 1-2%) is possible by applying a cut on the distance between  $\mathbf{x}_\pi$  and  $\mathbf{x}_\mu$ . Such cut however would require the introduction of an additional detector systematic uncertainty and thus it is not used.

### 3.3.2. One TPC $\pi^-$ sample

First signal sample consists of events that satisfy the one pion cut and contain a reconstructed TPC  $\pi^-$  track. Some features of the CC1TPC $\pi^-$  sample are studied here. The distributions of the reconstructed momentum  $p_\mu$  and  $\cos\theta_\mu$  of the  $\mu^+$  candidate are shown in Fig. 3.6. Colors indicate the true identity of the candidate particle. One can see that there are three major components: true  $\mu^+$  (37%), misidentified  $\pi^+$  (43.8%) and misidentified protons (16.8%).

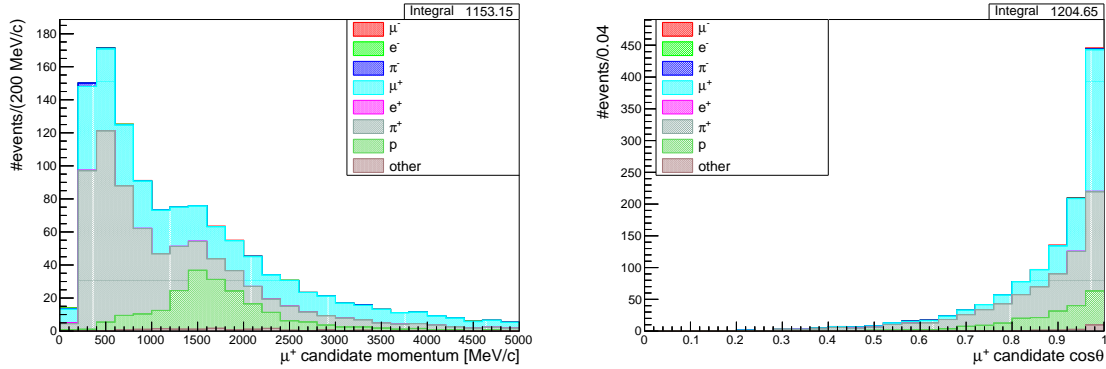


Figure 3.6: **CC1TPC $\pi^-$  signal selection.** MC distribution of reconstructed kinematic variables (left - momentum, right -  $\cos\theta$ ) of the reconstructed  $\mu^+$  candidate. Colors indicate the true identity of the candidate.

The distributions of the reconstructed momentum  $p_\pi$  and  $\cos\theta_\pi$  of the TPC  $\pi^-$  candidate are presented in Fig. 3.7. There are two major components: true  $\pi^-$  (43.3%) and misidentified  $\mu^-$  (55.1%). The true identities of the  $\mu^+$  and  $\pi^-$  candidates are summarized in Tables 3.5 and 3.6.

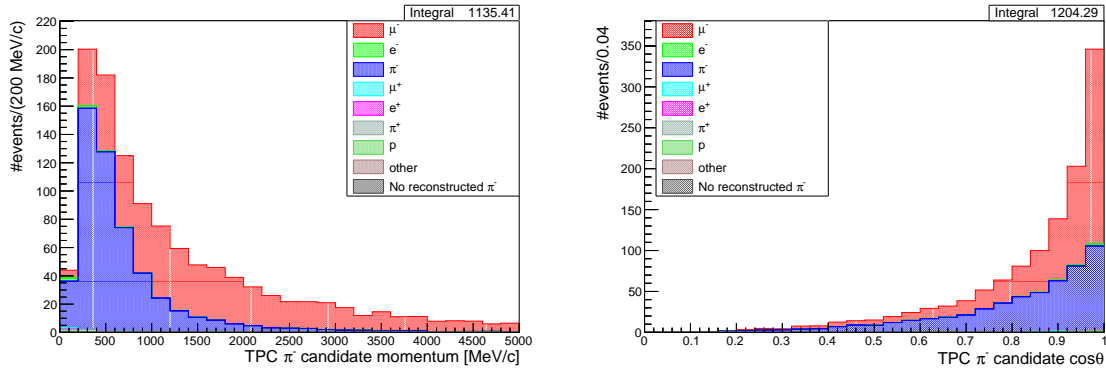


Figure 3.7: **CC1TPC $\pi^-$  signal selection.** MC distribution of reconstructed kinematic variables (left - momentum, right -  $\cos\theta$ ) of the reconstructed TPC  $\pi^-$  candidate. Colors indicate the true identity of the candidate.

particle	fraction of the candidates in CC1TPC $\pi^-$ sample	
	$\mu^+$ candidate	TPC $\pi^-$ candidate
$\mu^-$	0.4%	55.1%
$e^-$	0.1%	0.6%
$\pi^-$	0.3%	43.3%
$\mu^+$	37%	0.2%
$e^+$	0.2%	0.1%
$\pi^+$	43.8%	0.3%
p	16.8%	0.4%
other	1.4%	0.1%

Table 3.5: **CC1TPC $\pi^-$  signal selection.** Proportions of true  $\mu^+$  and  $\pi^-$  candidates' identities in the MC sample.

$\mu^+$ candidate	TPC $\pi^-$ candidate	fraction of the events in CC1TPC $\pi^-$ sample
$\mu^+$	$\pi^-$	33.4%
$\mu^+$	$\mu^-$	2.7%
$\pi^+$	$\pi^-$	6.0%
$\pi^+$	$\mu^-$	37.5%
p	$\pi^-$	3.2%
p	$\mu^-$	13.4%
other		3.8%

Table 3.6: **CC1TPC $\pi^-$  signal selection.** True identities of the candidates' pairs.

One can see that a significant fraction of the reconstructed muons (pions) are in fact misidentified hadrons (muons) of the same charge. This is mostly due to the neutrino background in the nominally anti-neutrino beam as can be seen in Table 3.7. The CC1TPC $\pi^-$  signal sample is designed to select  $\bar{\nu}_\mu$  CC interaction with  $\mu^+\pi^-$  in the final state, but the background  $\nu_\mu$  CC interaction with  $\pi^+\mu^-$  in the final state may be easily confused with the signal. The purity of the CC1TPC $\pi^-$  sample is 27.8% and  $\nu_\mu$  CC1 $\pi^+$  background contributes to 27.3% of the events. The purity of the sample is smaller than the fraction of events with correctly identified  $\mu^+\pi^-$  pair (Table 3.6) due to  $\bar{\nu}_\mu$  CC-other topology where lepton and charged pion were correctly identified, but other mesons were not reconstructed. For analogous reason there are more selected events with misidentified  $\pi^+\mu^-$  particles than  $\nu_\mu$  CC1 $\pi^+$  events. Note that the contribution of  $\nu_\mu$  CC-other topology (22.5%) is significantly bigger than the contribution of  $\bar{\nu}_\mu$  CC-other (7.4%). The key difference is in neutral meson production in resonant interactions. Consider  $\nu_\mu(\bar{\nu}_\mu)$  CC1 $\pi^0$  topology (a subset of  $\nu_\mu(\bar{\nu}_\mu)$  CC-other). It may be produced via  $\Delta$  resonance:

$$\begin{aligned}\nu_\mu + \text{n} &\rightarrow \mu^- + \Delta^+ \rightarrow \mu^- + \pi^0 + \text{p}, \\ \bar{\nu}_\mu + \text{p} &\rightarrow \mu^+ + \Delta^0 \rightarrow \mu^+ + \pi^0 + \text{n}.\end{aligned}$$

topology	fraction of the CC1TPC $\pi^-$ sample
$\bar{\nu}_\mu$ CC0 $\pi$	0.6%
$\bar{\nu}_\mu$ CC1 $\pi^-$	27.8%
$\bar{\nu}_\mu$ CC-other	7.4%
NC (flavour blind)	6.8%
$\nu_\mu$ CC0 $\pi$	5.1%
$\nu_\mu$ CC1 $\pi^+$	27.3%
$\nu_\mu$ CC-other	22.5%
CC $\nu_e + \bar{\nu}_e$	0.2%
Out of Fiducial Volume (OOFV)	2.3%

Table 3.7: **CC1TPC $\pi^-$  signal selection.** Proportions of true final state topologies in the MC sample. The  $\nu_\mu$  CC topologies are categorized with respect to mesons multiplicity in similar manner as  $\bar{\nu}_\mu$  topologies. The CC0 $\pi$  topologies correspond to the final state without any mesons. The  $\nu_\mu$  CC1 $\pi^+$  ( $\bar{\nu}_\mu$  CC1 $\pi^-$ ) topology refers to the final state with single  $\pi^+$  ( $\pi^-$ ) and no other mesons. The  $\nu_\mu(\bar{\nu}_\mu)$  CC-other topology indicates the final state with multiple mesons or a single meson different than  $\pi^+$  ( $\pi^-$ ).

The  $\nu_\mu$  CC1 $\pi^0$  topology may be misidentified as signal if  $\pi^0$  remains undetected,  $\mu^-$  is misidentified as  $\pi^-$  candidate and proton is in proper kinematic range to be selected as  $\mu^+$  candidate. On the other hand for  $\bar{\nu}_\mu$  CC1 $\pi^0$  topology there's no negative particle in the final state and thus it is very unlikely to be selected in the CC1TPC $\pi^-$  sample.

For the presented sample the signal selection efficiency  $\epsilon = 19.4\%$  and purity  $\mathbf{p} = 27.8\%$ .

### 3.3.3. Z-range cut

An additional cut is introduced in order to suppress neutrino background in the CC1TPC $\pi^-$  sample. Since pions and protons interact via strong force, their range in matter is on average significantly smaller than muons range for similar momentum. Also, most of the  $\mu^+/\pi^-$  reconstructed tracks are not emitted at a large angle with respect to the detector Z-direction (which is almost parallel to the off-axis neutrino beam direction at ND280). Therefore the Z-coordinate of the ending point of the reconstructed track (called also *ending Z-position of a track*) is a fair estimation of the particle range in ND280. Ending Z-position of the reconstructed  $\mu^+$  and TPC  $\pi^-$  tracks is presented in Fig. 3.8. Colors indicate the true identity of the reconstructed particle.

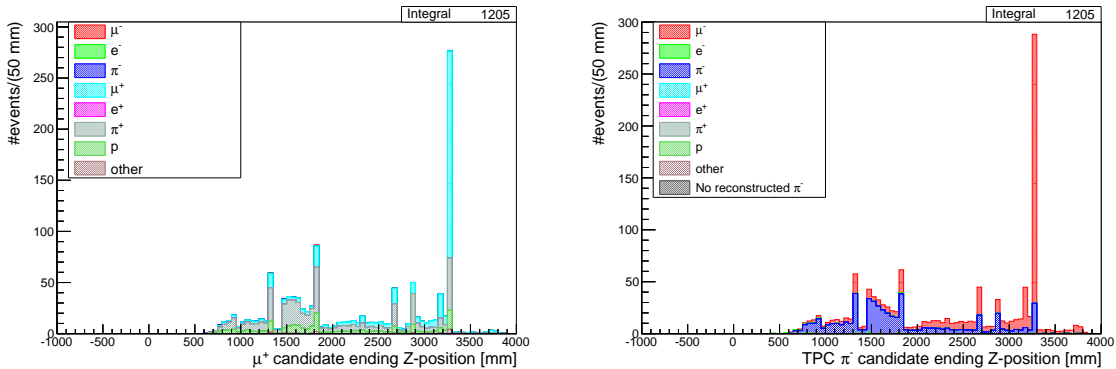


Figure 3.8: **CC1TPC  $\pi^-$  signal selection.** MC distribution of the ending Z-position of the reconstructed particle track (left:  $\mu^+$  candidate, right: TPC  $\pi^-$  candidate). Colors indicate the true identity of the candidate.

The distribution of the ending Z-position has several peaks which indicate the boundaries of the ND280 subdetectors. The (0, 0, 0) point in the ND280 coordinate system is located inside TPC1. The first peak near  $Z = 1300$  mm corresponds to tracks ending at the downstream wall of TPC2. The second peaked region is in the range of  $1500 \text{ mm} < Z < 1800 \text{ mm}$ . It corresponds to tracks ending in FGD2. Another peak around  $Z = 2700$  mm corresponds to tracks ending at the downstream wall of TPC3.

The region of  $2800 \text{ mm} < Z < 3300 \text{ mm}$  corresponds to Downstream ECal, with the highest peak corresponding to particles that reached the most downstream point in the ECal and left the detector. Tracks with  $Z > 3300 \text{ mm}$  have ending point in the SMRD (part of the SMRD protrudes downstream with respect to the ECal).

True  $\mu^\pm$ 's tend to have more downstream ending  $Z$ -position than true  $\pi^\pm$ 's. Therefore, by looking at the difference of ending  $Z$ -position of  $\mu^+/\pi^-$  candidates it should be possible to distinguish signal  $\bar{\nu}_\mu \text{ CC}1\pi^-$  topology from  $\nu_\mu \text{ CC}1\pi^+$  background. The distribution of the difference of ending  $Z$ -position ( $Z_\mu - Z_\pi$ ) is shown in Fig. 3.9 with colors indicating the true topology. For the signal  $\text{CC}1\pi^-$  events the  $(Z_\mu - Z_\pi)$  is usually positive, while for the  $\text{CC}1\pi^+$  background it is much more often negative.

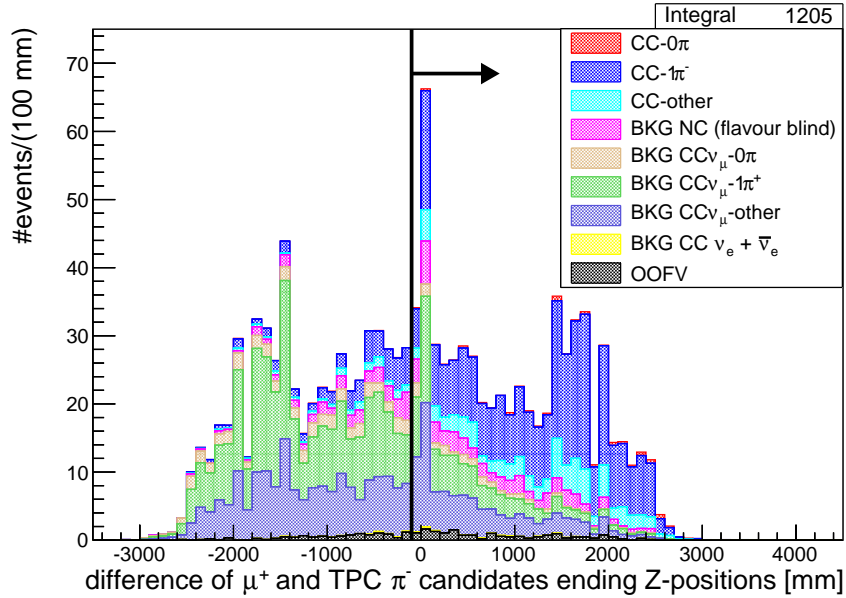


Figure 3.9: **CC1TPC $\pi^-$  signal selection.** MC distribution of the difference of the ending  $Z$ -positions of the reconstructed  $\mu^+$  and TPC  $\pi^-$  tracks. Colors indicate the true topology of the event.

The proposed  $Z$ -range cut selects events with a TPC  $\pi^-$  track and  $Z_\mu - Z_\pi > -10 \text{ cm}$ . The events which do not satisfy this condition constitute one of the sidebands (**Reversed  $Z$ -range background sample**) described in section 3.5.2.

The  $(-10) \text{ cm}$  threshold was chosen to optimise the product of selection efficiency and purity. The selection performance for different threshold values is presented in Fig. 3.10. The optimal selection is for the threshold values around zero. However there is an important reason for not letting this constant to be exactly zero. It was checked for FHC beam mode runs that there is a discrepancy between MC and data in  $(Z_\mu - Z_\pi)$  distribution around  $0 \text{ cm}$  (Fig. 3.11). The cut on that variable should be applied in

region where MC agrees with data. Otherwise it would introduce discrepancy between MC predicted event rate and actual data event rate in the selected sample.

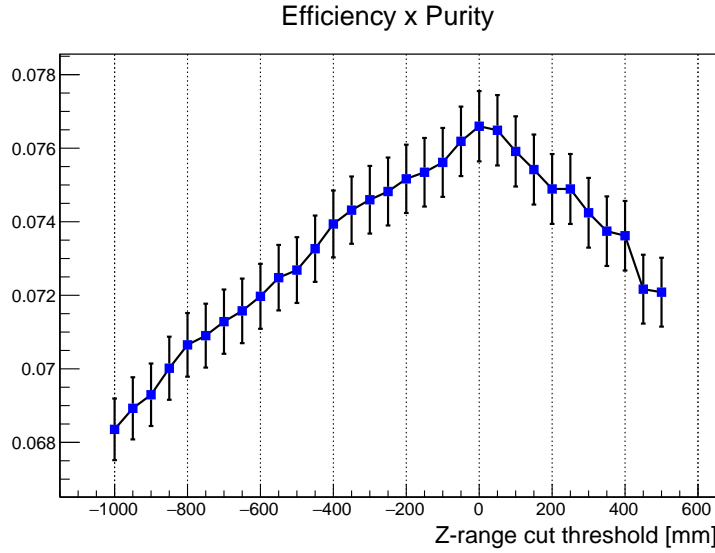


Figure 3.10: Product of the efficiency and purity for different threshold values in the Z-range cut.

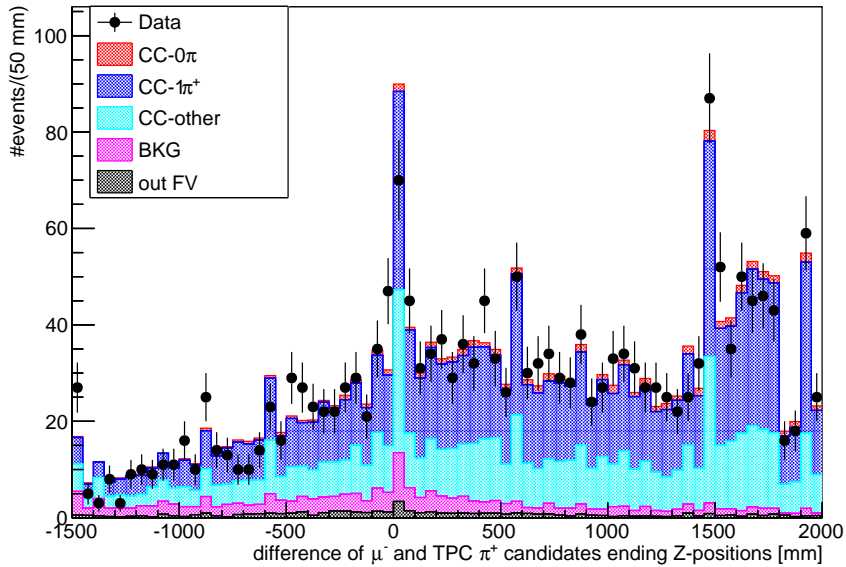


Figure 3.11: **Monte Carlo and data distribution for  $\nu_\mu$  beam mode runs 2-4.** Distribution of the difference of the ending Z-positions of the reconstructed  $\mu^-$  and  $\pi^+$  tracks for  $\nu_\mu$  CC1 $\pi^+$  sample. Colors indicate the true topology of the event.

The Z-range cut impact on the topology composition of the sample is presented in Table 3.8. With the Z-range cut applied all background CC  $\nu_\mu$  topologies are signifi-

cantly suppressed and the purity of CC1TPC $\pi^-$  signal sample is increased from 27.8% to 45.4%. Quite contrary for the region with reversed Z-range cut, where over 80% of events are CC  $\nu_\mu$  interactions.

topology	fraction of the sample	
	CC1TPC $\pi^-$ signal sample	Reversed Z-range cut sideband
$\bar{\nu}_\mu$ CC0 $\pi$	1.1%	0.1%
$\bar{\nu}_\mu$ CC1 $\pi^-$	45.4%	8.2%
$\bar{\nu}_\mu$ CC-other	11.8%	2.4%
BKG NC (flavour blind)	7.8%	5.6%
BKG $\nu_\mu$ CC0 $\pi$	2.6%	7.9%
BKG $\nu_\mu$ CC1 $\pi^+$	13%	43.3%
BKG $\nu_\mu$ CC-other	15.5%	30.3%
BKG CC $\nu_e + \bar{\nu}_e$	0.3%	0.2%
OOFV	2.6%	1.9%

Table 3.8: Proportions of true final state topologies in the CC1TPC $\pi^-$  signal sample (Z-cut applied) and the Reversed Z-range cut background sample.

With the Z-range cut applied in the CC1TPC $\pi^-$  signal sample, the selection efficiency of the true  $\bar{\nu}_\mu$  CC1 $\pi^-$  signal didn't decrease much and the product of efficiency and purity increased as shown in Table 3.9. The distributions of reconstructed kinematical variables of the  $\mu^+$  and  $\pi^-$  candidates are presented in Fig. 3.12. The true identities of the  $\mu^+$  and  $\pi^-$  candidates are summarized in Tables 3.10 and 3.11. The purity of particle identification significantly increased with respect to the selection without Z-range cut (compare with 3.5): for  $\mu^+$  from 37% to 59.3%, for  $\pi^-$  from 43.3% to 66.1%. As can be seen in Table 3.11 the Z-range cut successfully discriminates events with a pair of true  $\mu^-$  misidentified as  $\pi^-$  and true hadron misidentified as  $\mu^+$ .

$\bar{\nu}_\mu$ CC1TPC $\pi^-$ selection	w/o Z-range cut	with Z-range cut
purity	$(27.8 \pm 0.4)\%$	$(45.4 \pm 0.5)\%$
efficiency	$(19.4 \pm 0.3)\%$	$(16.7 \pm 0.2)\%$
efficiency $\times$ purity	$0.0539 \pm 0.0005$	$0.0756 \pm 0.0009$

Table 3.9: Impact of the Z-range cut on CC1TPC $\pi^-$  signal selection.

The contribution of each channel of neutrino interaction in the selected sample is summarized in Table 3.12. The biggest contribution to the signal events is due to the  $\bar{\nu}_\mu$  CC resonant interaction (RES - 73.4%). Two other major components are  $\bar{\nu}_\mu$  CC coherent interaction (COH - 20.4%) and  $\bar{\nu}_\mu$  CC deep inelastic scattering (DIS - 6.1%).

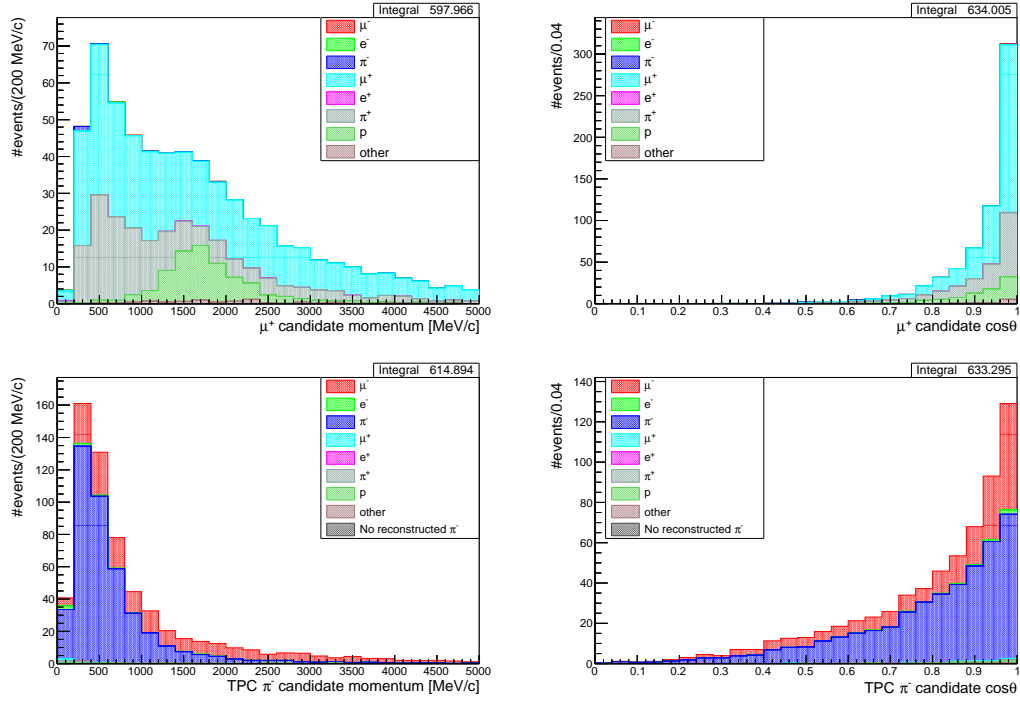


Figure 3.12: **CC1TPC $\pi^-$  signal sample with Z-range cut.** MC distribution of reconstructed kinematic variables (left - momentum, right -  $\cos\theta$ ) of reconstructed candidate (top:  $\mu^+$ , bottom: TPC  $\pi^-$ ). Colors indicate the true identity of the candidate.

particle	fraction of the candidates in CC1TPC $\pi^-$ sample	
	$\mu^+$ candidate	TPC $\pi^-$ candidate
$\mu^-$	0.3%	31.2%
$e^-$	0.1%	0.9%
$\pi^-$	0.3%	66.1%
$\mu^+$	59.3%	0.4%
$e^+$	0.1%	0.1%
$\pi^+$	26.7%	0.5%
p	11.8%	0.7%
other	1.4%	0.1%

Table 3.10: True identities of the candidates in the **CC1TPC $\pi^-$  sample** (with Z-range cut).

$\mu^+$ candidate	TPC $\pi^-$ candidate	fraction of the events in CC1TPC $\pi^-$ sample	
		with Z-range cut	w/o Z-range cut
$\mu^+$	$\pi^-$	54.7%	33.4%
$\mu^+$	$\mu^-$	2.9%	2.7%
$\pi^+$	$\pi^-$	6.8%	6.0%
$\pi^+$	$\mu^-$	19.4%	37.5%
p	$\pi^-$	3.9%	3.2%
p	$\mu^-$	7.8%	13.4%
other		4.5%	3.8%

Table 3.11: True identities of the candidates' pairs in **CC1TPC $\pi^-$  sample** (with and without Z-range cut).

channel	sel. w/o Z-cut	sel. with Z-cut	sel. with Z-cut, <b>true signal events</b>
CCQE	0.5%	0.9%	0.2%
2p2h	0.1%	0.2%	0.02%
RES	20.6%	34.3%	73.4%
DIS	8.5%	13.6%	6.1%
COH	6%	9.2%	20.4%
NC	6.8%	7.8%	-
$\nu_\mu$ CC	55%	31%	-
CC $\nu_e + \bar{\nu}_e$	0.2%	0.3%	-
OOFV	2.3%	2.6%	-

Table 3.12: Contribution of true channels of interaction in the **CC1TPC $\pi^-$  sample** w/o and with Z-range cut applied.

### 3.3.4. One FGD $\pi^-$ sample

The second signal sample consists of events that satisfy the one pion cut and have FGD1-contained  $\pi^-$  track, i.e. track satisfying FGD PID condition with no segments in other subdetectors.

Particle identification method in FGD, which was optimised in other T2K analysis [118], is based on measured energy loss  $E$  and track length in the FGD. It is reliable only for particles stopping in the detector. Figure 3.13-left presents MC distribution of  $E$  versus track length in FGD1. Colors correspond to different particle identity. For a given particle hypothesis  $i$  ( $i = \text{muon, pion or proton}$ ) the expected deposited energy  $E_i(x)$  and resolution  $\sigma_i(x)$  are calculated as a function of measured track length  $x$ . The FGD pull variable is calculated as:

$$\delta(i) = \frac{E - E_i(x)}{\sigma_i(x)} \quad (3.10)$$

Distribution of  $\delta(i)$  for pion hypothesis is shown in Fig. 3.13-right.

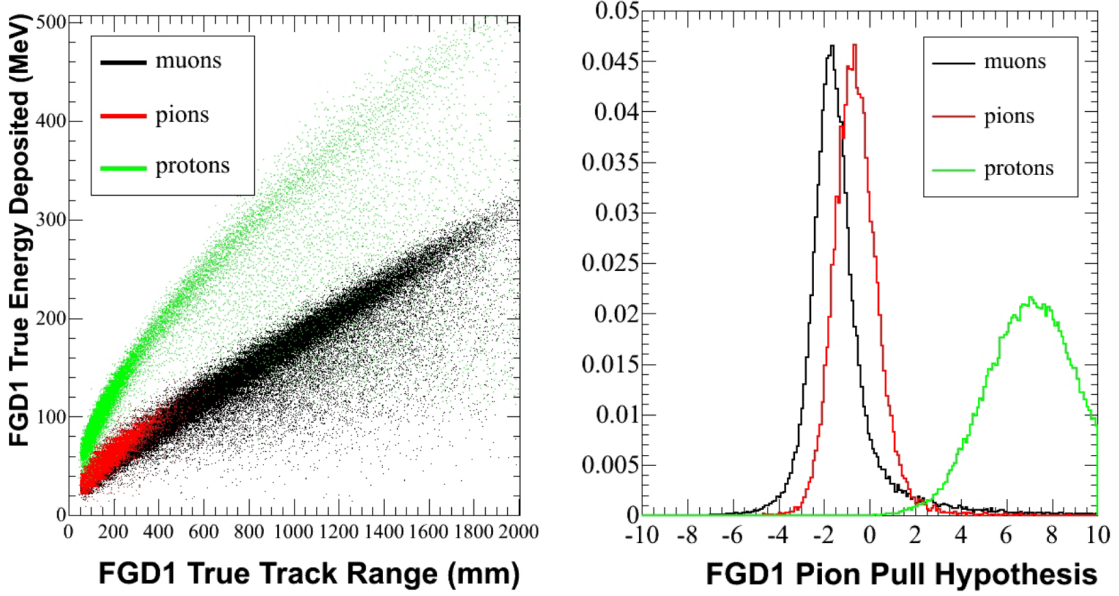


Figure 3.13: Left: MC distribution of the true energy deposition vs true track range for protons, muons and pions in FGD1. Right: MC distribution of the pull variable for pion hypothesis. Plots taken from [118].

An FGD-contained track is identified as pion if:

$$-2 < \delta(\pi) < 2.5. \quad (3.11)$$

Additionally, a cut on the track direction is applied:  $|\cos \theta_\pi| < 0.3$  in order to exclude high angle tracks which cross few FGD layers.

After describing criteria imposed on the FGD1-contained track the kinematical properties of the sample are studied here. The distributions of reconstructed momentum  $p_\mu$  and  $\cos \theta_\mu$  of the  $\mu^+$  candidate are shown in Fig. 3.14. Colors indicate the true identity of the candidate particle. Majority of  $\mu^+$  candidates are true  $\mu^+$  (80.6%), while misidentified particles are mostly  $\pi^+$  (9.1%) and protons (4.8%).

For TPC tracks the momentum is estimated by fitting helix to the reconstructed track. FGD-contained tracks are too short to obtain precise momentum measurement this way. Instead, the momentum reconstruction is based on the energy loss measured in FGD, which is taken as an estimation of the kinetic energy of the particle stopping in FGD. The distributions of reconstructed momentum  $p_\pi$  and  $\cos \theta_\pi$  of the FGD  $\pi^-$  candidate are shown in Fig. 3.15. Colors indicate the true identity of the candidate

particle. The distribution of reconstructed  $\cos\theta_\pi$  has a peak at the threshold value 0.3 and overall most FGD  $\pi^-$  candidates are high angle tracks. This could be expected, since forward going particles are more likely to reach TPC2 and result in TPC  $\pi^-$  candidates. Majority of FGD-contained  $\pi^-$  tracks are true  $\pi^-$  (65.8%). The identities of the  $\mu^+$  and  $\pi^-$  candidates are summarized in Tables 3.13 and 3.14.

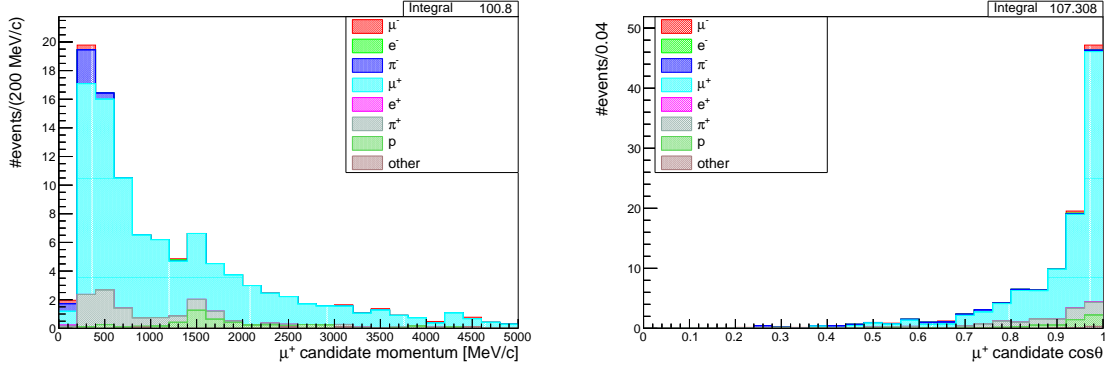


Figure 3.14: **CC1FGD $\pi^-$  signal selection.** MC distribution of reconstructed kinematic variables (left - momentum, right -  $\cos\theta$ ) of the reconstructed  $\mu^+$  candidate. Colors indicate the true identity of the candidate.

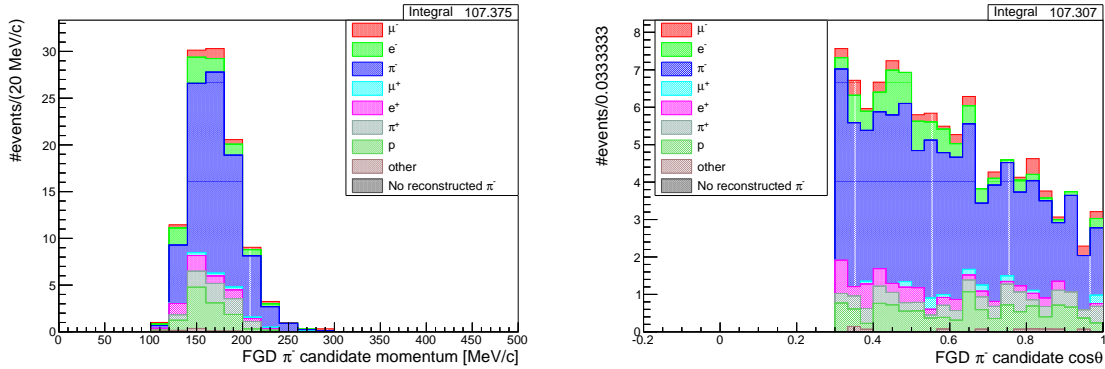


Figure 3.15: **CC1FGD $\pi^-$  signal selection.** MC distribution of reconstructed kinematic variables (left - momentum, right -  $\cos\theta$ ) of the reconstructed FGD  $\pi^-$  candidate. Colors indicate the true identity of the candidate.

The true topology composition of the CC1FGD $\pi^-$  sample is presented in Tab. 3.15. The signal events constitute 57.6% of the sample. The selection efficiency is 3.6%. (Joint efficiency in both signal samples is 20.2%).

The contribution of each channel of neutrino interactions in the selected sample is summarized in Table 3.16. Vast majority of signal events originate from the  $\bar{\nu}_\mu$  CC resonant interaction (RES - 91.6%).

particle	fraction of the candidates in CC1FGD $\pi^-$ sample	
	$\mu^+$ candidate	FGD $\pi^-$ candidate
$\mu^-$	1.7%	3.3%
$e^-$	0.1%	7.9%
$\pi^-$	3.1%	65.8%
$\mu^+$	80.6%	1.3%
$e^+$	0.2%	5%
$\pi^+$	9.1%	6.4%
p	4.8%	10.2%
other	0.5%	0.7%

Table 3.13: True identities of the candidates in the **CC1FGD $\pi^-$  sample**.

$\mu^+$ candidate	FGD $\pi^-$ candidate	fraction of the events in CC1FGD $\pi^-$ sample
$\mu^+$	$\pi^-$	58.1%
$\mu^+$	$\pi^+$	2.6%
$\mu^+$	p	7.7%
$\mu^+$	$e^-$	6.1%
$\mu^+$	$e^+$	3.8%
$\pi^+$	$\pi^-$	2.8%
$\pi^+$	$\pi^+$	2.4%
$\pi^+$	$\mu^-$	1.4%
$\pi^+$	$e^-$	1%
$\pi^+$	p	1%
p	$\pi^-$	1.6%
p	$\pi^+$	1%
p	p	0.8%
other		9.8%

Table 3.14: True identities of the candidates' pairs in **CC1FGD $\pi^-$  signal sample**.

topology	fraction of the $\text{CC1FGD}\pi^-$ sample
$\bar{\nu}_\mu$ CC0 $\pi$	7.2%
$\bar{\nu}_\mu$ CC1 $\pi^-$	57.6%
$\bar{\nu}_\mu$ CC-other	13.8%
NC (flavour blind)	6.9%
$\nu_\mu$ CC0 $\pi$	0.4%
$\nu_\mu$ CC1 $\pi^+$	2.5%
$\nu_\mu$ CC-other	3%
CC $\nu_e + \bar{\nu}_e$	0.6%
Out of Fiducial Volume (OOFV)	8%

Table 3.15: Proportions of true final state topologies in the  $\text{CC1FGD}\pi^-$  sample.

channel	sel. $\text{CC1FGD}\pi^-$	sel. $\text{CC1FGD}\pi^-$ , true $\text{CC1}\pi^-$ topology
CCQE	3.9%	0.4%
2p2h	1.9%	0.1%
RES	61.8%	91.6%
DIS	8%	2.5%
COH	3.1%	5.4%
NC	6.9%	-
$\nu_\mu$ CC	5.9%	-
CC $\nu_e + \bar{\nu}_e$	0.6%	-
OOFV	8%	-

Table 3.16: Contribution of true channels of interaction in the  $\text{CC1FGD}\pi^-$  sample.

## 3.4. Efficiency studies

An important check of the selection are efficiency studies. When performing differential cross-section measurement as a function of a variable  $x$ , the efficiency should not change rapidly as a function of  $x$ . Otherwise, a model dependency related to  $x$  modelling is introduced. In this section efficiency studies for various variables are presented. Kinematical observables of muon and pion are taken into account as well as neutrino energy, four-momentum transfer and hadronic invariant mass.

### 3.4.1. Efficiency vs true $\mu^+, \pi^-$ kinematical variables

Efficiency as a function of true  $\mu^+$  momentum/ $\cos\theta$  is presented in Fig. 3.16 for both signal samples. In the efficiency plots also the distributions of true kinematical variables are included to show statistics available in MC sample (non-normalised to data POT). The red line corresponds to all signal events while green line corresponds to signal events in the selected sample. **Note that bins have different widths to present efficiency without large statistical errors and in each bin the absolute event rate is reported.** Analogical plots for true  $\pi^-$  are presented in Fig. 3.17. Vast majority of true  $\pi^-$  have momentum below 1 GeV/c, while roughly half of true  $\mu^+$  have momentum above that value. In the signal topology leptons are also much more forward-going than pions.

As can be seen in Fig. 3.16 for both signal samples the efficiency is rapidly increasing in low  $\mu^+$  momentum region and above  $\sim 500$  MeV/c it is changing more slowly. This is related to the fact that efficiency of TPC track reconstruction decreases for low particle momentum. The efficiency is gradually increasing with  $\cos\theta_\mu$ . Both those features are common also for other ND280 analyses (see [99, 100]).

In Fig. 3.17 the selection efficiency for CC1TPC $\pi^-$  signal sample changes in similar way for pion kinematics as for muon kinematics in Fig. 3.16. Quite contrary for CC1FGD $\pi^-$  signal sample where efficiency is the highest around pion momentum  $p_\pi = 200$  MeV/c and for high angle pion tracks around  $\cos\theta_\pi = 0.4$ . This behaviour is expected since high momentum pions are likely to escape FGD and not be reconstructed as FGD-contained tracks. Similarly forward-going pions are likely to reach downstream TPC. For very high angle tracks pions are crossing few scintillator layers in FGD and thus are less likely to be reconstructed.

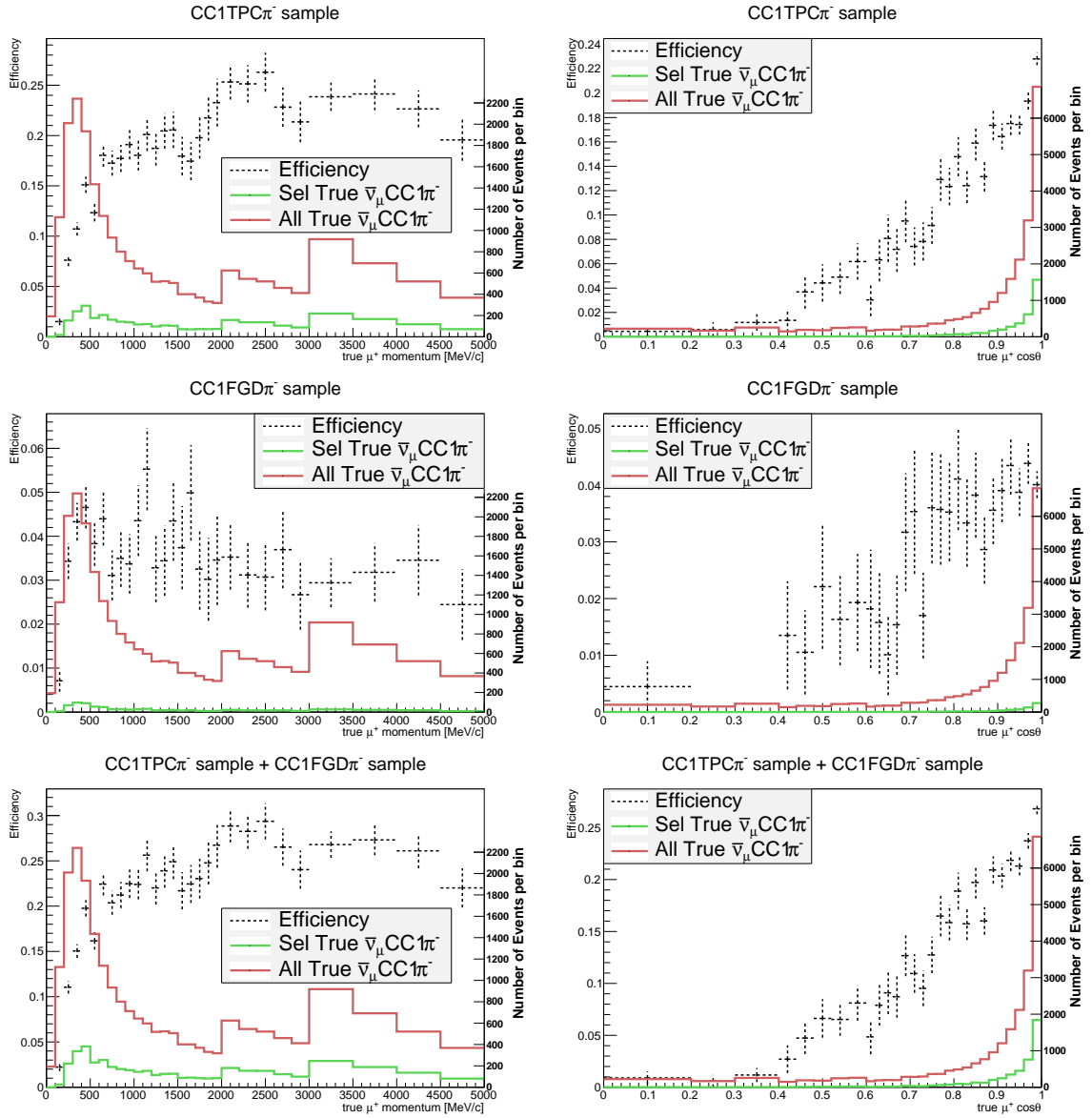


Figure 3.16: Selection efficiency in true kinematic variables (left - momentum, right -  $\cos\theta$ ) of true  $\mu^+$ . Top: CC1TPC $\pi^-$  sample. Middle: CC1FGD $\pi^-$  sample. Bottom: Both signal samples.

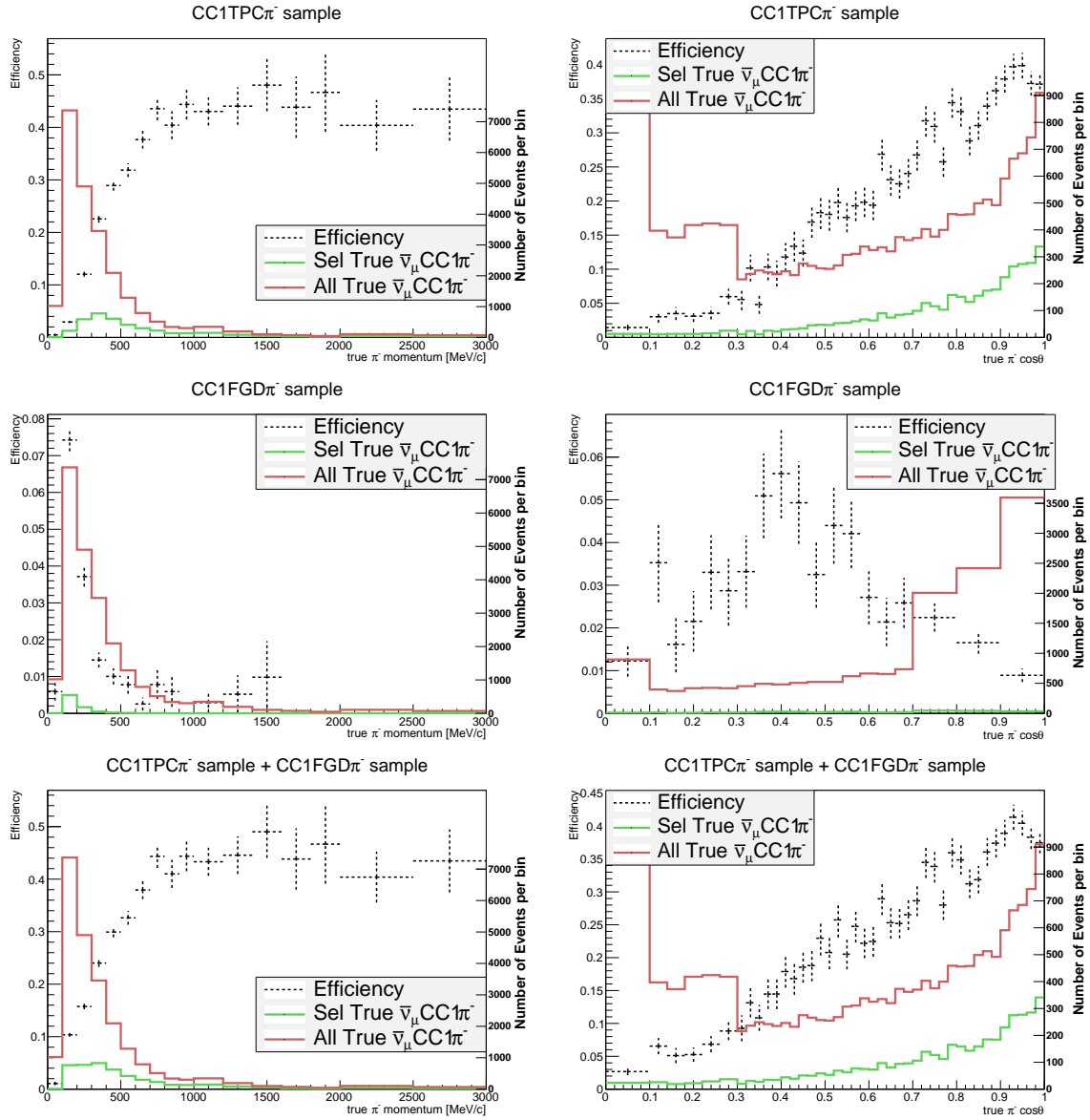


Figure 3.17: Selection efficiency in true kinematic variables (left - momentum, right -  $\cos\theta$ ) of true  $\pi^-$ . Top: CC1TPC $\pi^-$  sample. Middle: CC1FGD $\pi^-$  sample. Bottom: Both signal samples.

As already mentioned in section 1.4, due to small efficiency in some kinematical regions it was decided to use restricted phase space for the cross-section measurement and consider only events with  $p_\mu > 200$  MeV/c,  $\cos\theta_\mu > 0.74$ ,  $p_\pi > 100$  MeV/c and  $\cos\theta_\pi > 0.32$ . Additionally, an upper limit for  $p_\pi$  is applied due to low signal contribution:  $p_\pi < 3000$  MeV/c.

The selection should avoid cuts that introduce a model dependency. The Z-range cut may seem to be dubious for that matter due to modelling of pion kinematics. There is no strict condition put on kinematic variables but after all the ending position of the track surely is impacted by particle's momentum and initial angle of the track. To check the magnitude of this impact more detailed efficiency studies were done. Selections with and without Z-range cut are compared by plotting the ratio of **true CC1 $\pi^-$  topology** events which are selected with Z-range cut to those that were selected by the CC1TPC $\pi^-$  selection without Z-range cut (Fig. 3.18). This ratio is labelled in the plots as the 'Z-cut survival ratio'.

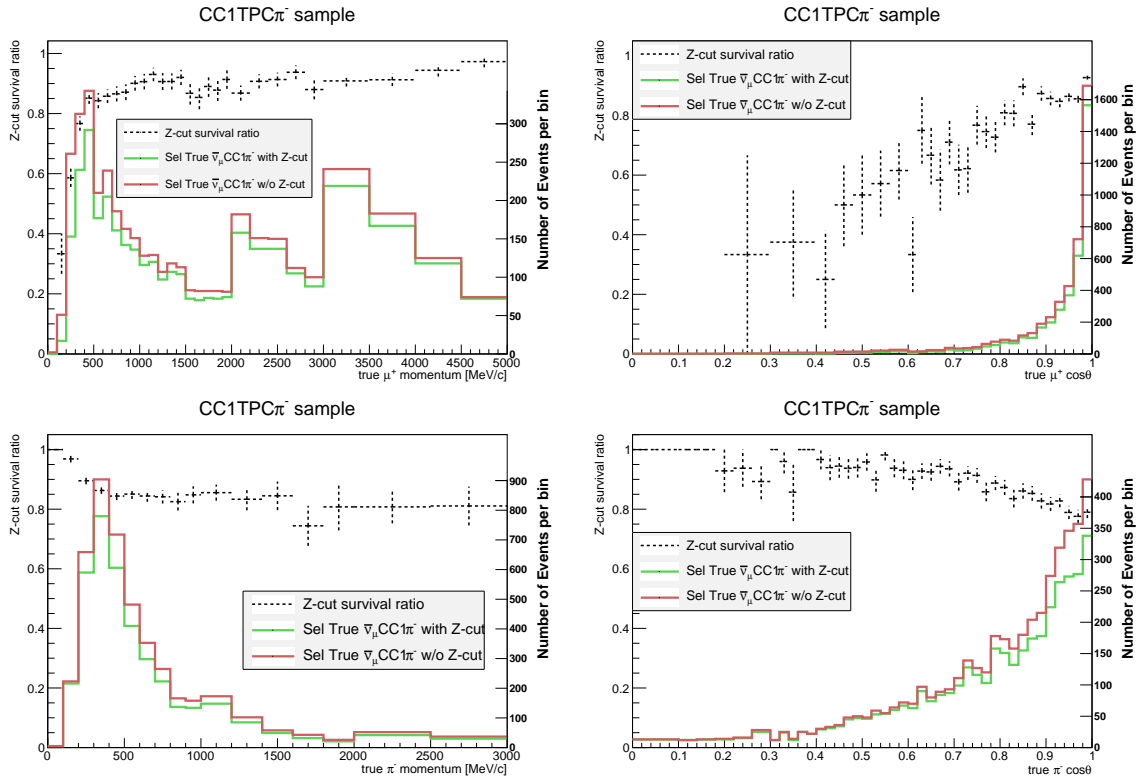


Figure 3.18: Impact of the Z-range cut on the selection efficiency - ratio of number of signal events selected in CC1TPC $\pi^-$  sample with Z-range cut to those selected in the CC1TPC $\pi^-$  without Z-range cut. Distribution in true kinematic variables (left - momentum, right -  $\cos\theta$ ) of true particles (top:  $\mu^+$ , bottom:  $\pi^-$ ).

In case of true  $\mu^+$  momentum the Z-range cut decreases the efficiency significantly

in the first three bins (0-300 MeV/c). For bigger momenta the ratio of events surviving the Z-range cut is higher and quite flat. The cross section will not be reported for events with  $p_{\mu \text{ true}} < 200$  MeV/c due to the phase-space restriction. For true  $\mu^+ \cos\theta_{\mu \text{ true}}$  this ratio is growing with  $\cos\theta_{\mu \text{ true}}$ , which makes sense, as tracks with small  $\theta$  are forward-going and more likely to have further ending Z-position. It must be noted that most events populate the region of  $\cos\theta_{\mu \text{ true}} > 0.8$  (89.6% of all signal events - prior to the Z-range cut), where this ratio is high and rather flat.

When it comes to true  $\pi^-$  momentum the ratio is very high for small momenta, which is expected, since such pion tracks will not have large range in matter and Z-range cut will be easily satisfied. The ratio decreases at first, but in the range 300-1600 MeV/c is flat. For true  $\pi^- \cos\theta_{\pi \text{ true}}$  the ratio is smoothly decreasing, since forward-going pions have further ending Z-position. In conclusion, the Z-range cut doesn't impact significantly the selection efficiency within the restricted phase-space.

### 3.4.2. Efficiency vs neutrino energy, $Q^2$ and $W$

Efficiency studies were also performed for other variables: true neutrino energy  $E_\nu$ , four-momentum transfer squared  $Q^2$  and hadronic invariant mass  $W$ . In this case only signal events within the restricted phase-space (defined in previous subsection) were taken into account. A rapid efficiency variations in  $E_\nu$ ,  $Q^2$  and  $W$  might suggest that there is a model dependency in the selection.

In Fig. 3.19 the selection efficiency and the survival ratio of the Z-range cut are presented as a function of the true  $\bar{\nu}_\mu$  energy  $E_\nu$ . For the CC1TPC $\pi^-$  signal sample the efficiency is increasing with the neutrino energy till about 1000 MeV/c and becomes flatter for higher energy. Such tendency is to be expected - the selection requires reconstruction of both  $\mu^+$  and  $\pi^-$  tracks and the efficiency of track reconstruction is smaller for low momentum particle. This feature is not observed for the Z-cut survival ratio which is quite flat for the entire  $E_\nu$  phase-space. The shape of the efficiency is quite different for the CC1FGD $\pi^-$  sample than for the CC1TPC $\pi^-$  sample. In the bottom left plot the efficiency is highest for small  $E_\nu$  and is characterised by a distinct peak around 500 MeV. For events with small  $E_\nu$  the momentum of produced  $\pi^-$  is low and thus  $\pi^-$  is less likely to escape FGD1 and more likely to be reconstructed as an FGD1-contained track. The peak in the efficiency for this sample is not problematic since for the joint samples the efficiency is more flat.

In Fig. 3.20 the selection efficiency and the survival ratio of the Z-range cut are presented as a function of the true four-momentum transfer  $Q^2$ . For the CC1TPC $\pi^-$  signal sample the efficiency is rather flat in the whole plotted  $Q^2$  range. The Z-cut

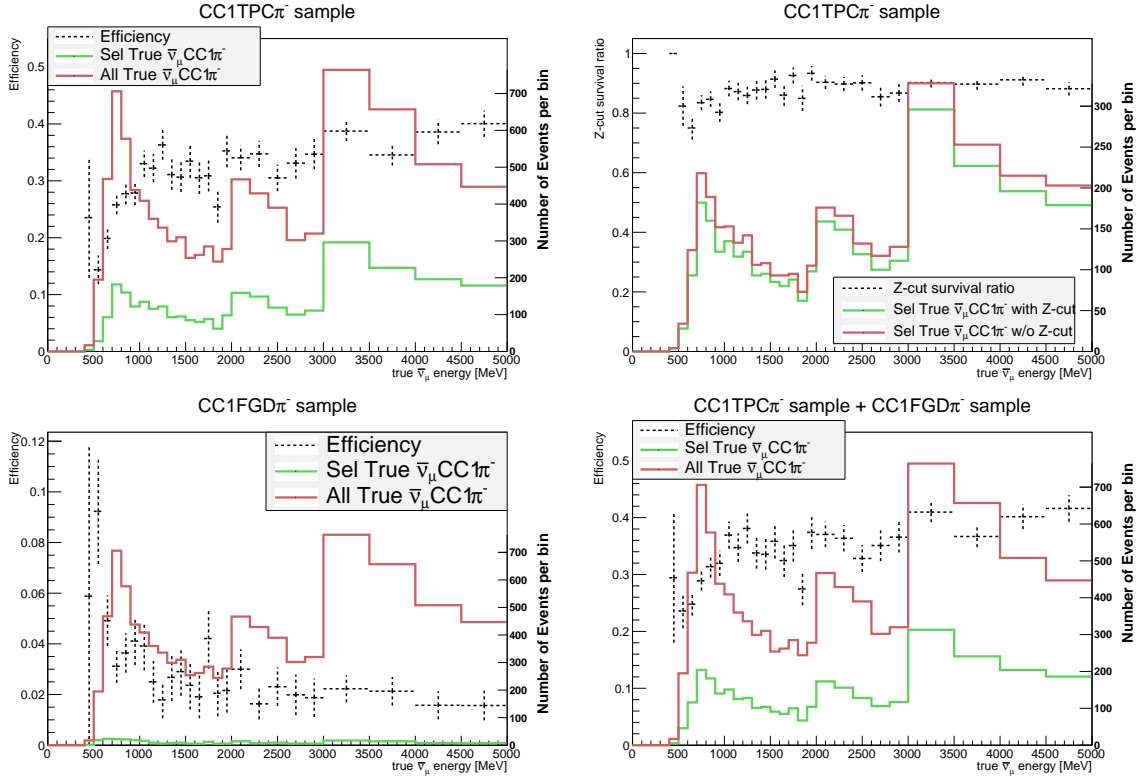


Figure 3.19: **Top left:** CC1TPC $\pi^-$  sample. Selection efficiency versus true  $\bar{\nu}_\mu$  energy. **Top right:** CC1TPC $\pi^-$  sample. Survival ratio of the Z-range cut versus true  $\bar{\nu}_\mu$  energy. **Bottom left:** CC1FGD $\pi^-$  sample. Selection efficiency versus true  $\bar{\nu}_\mu$  energy. **Bottom right:** joint signal samples. Selection efficiency versus true  $\bar{\nu}_\mu$  energy.

survival ratio is very flat for the entire  $Q^2$  phase-space. For the CC1FGD $\pi^-$  sample the efficiency is decreasing with the higher  $Q^2$  values. This is due to the fact that in the events with higher four-momentum transfer the produced pion is more forward-going and hence more likely to reach TPC rather than be reconstructed as an FGD-contained track. For the joint samples the efficiency is more flat.

In Fig. 3.21 the selection efficiency and the survival ratio of the Z-range cut are presented as a function of the true hadronic invariant mass  $W$ . The peak in the signal events distribution between 1200 and 1300 MeV/ $c^2$  is due to the  $\Delta$  resonance (1232 MeV/ $c^2$ ). For the CC1TPC $\pi^-$  signal sample the efficiency is increasing with the  $W$  from 1000 MeV/ $c^2$  till 1400 MeV/ $c^2$ . For the CC1FGD $\pi^-$  signal sample the tendency is quite opposite. This is due to the fact that small  $W$  results in a low momentum pion. Low momentum results in worse efficiency of TPC pion track reconstruction however increases the chance for reconstructing pion as an FGD-contained track. The Z-cut survival ratio is quite flat for the entire  $W$  phase-space.

In conclusion, the efficiency plots are relatively flat for the considered variables

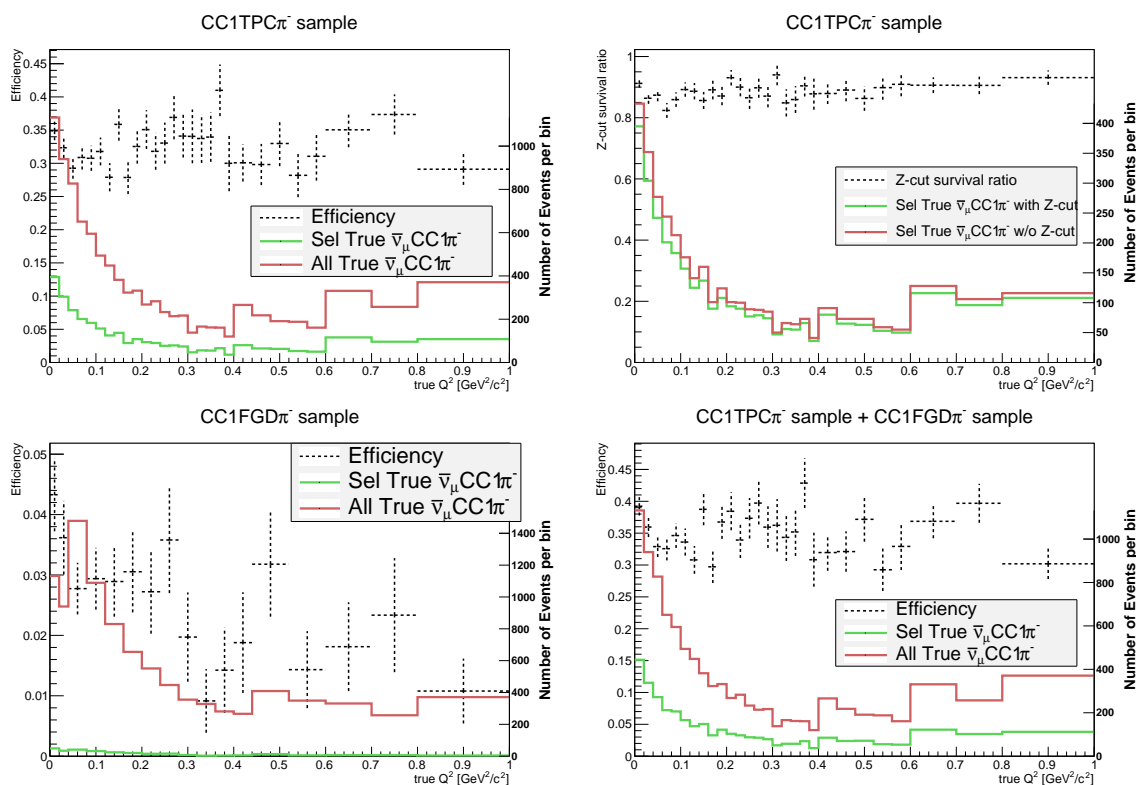


Figure 3.20: **Top left:** CC1TPC $\pi^-$  sample. Selection efficiency versus true four-momentum transfer  $Q^2$ . **Top right:** CC1TPC $\pi^-$  sample. Survival ratio of the Z-range cut versus true four-momentum transfer  $Q^2$ . **Bottom left:** CC1FGD $\pi^-$  sample. Selection efficiency versus true four-momentum transfer  $Q^2$ . **Bottom right:** joint signal samples. Selection efficiency versus true four-momentum transfer  $Q^2$ .

except for the low  $\bar{\nu}_\mu$  energy and low hadronic invariant mass regions where produced particles are characterised by low momenta. The selection criterion specific for Author's analysis i.e. the Z-range cut impacts the efficiency acceptably. Additional efficiency studies related to the Z-range cut are presented in Appendix A.

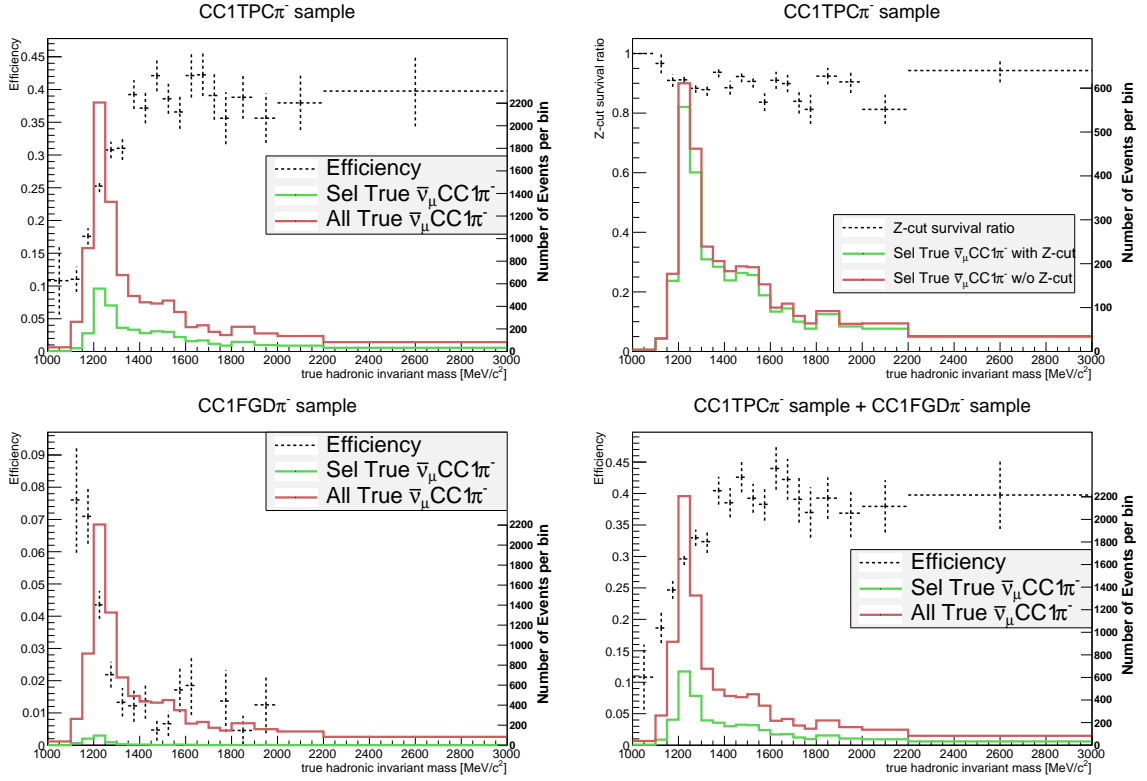


Figure 3.21: **Top left:** CC1TPC $\pi^-$  sample. Selection efficiency versus true hadronic invariant mass  $W$ . **Top right:** CC1TPC $\pi^-$  sample. Survival ratio of the Z-range cut versus true hadronic invariant mass  $W$ . **Bottom left:** CC1FGD $\pi^-$  sample. Selection efficiency versus true hadronic invariant mass  $W$ . **Bottom right:** joint signal samples. Selection efficiency versus true hadronic invariant mass  $W$ .

### 3.5. Background samples selection

Joint signal samples contain about 53% of background events. The detailed background topology composition of the joint signal samples is presented in Table 3.17. These are mostly events with multiple pions that were misidentified or not reconstructed or CC  $\nu_\mu$  interactions. In order to constrain the background content two sidebands are chosen: CC-other sample and reversed Z-range cut sample.

#### 3.5.1. CC-other

CC-other is a subset of  $\bar{\nu}_\mu$  CC-inclusive sample selected with cuts described in subsection 3.2. Additional CC-other cut uses information about reconstructed TPC tracks, Michel Electrons (ME) and FGD-contained pions, which must satisfy any of the conditions explained in subsection 3.3.1. The cut selects events with:

- $\geq 1 e^\pm$  in TPC (55.6% of all CC-other events)

- $\geq 1 \pi^+$  in TPC (30.8% of all CC-other events)
- $> 1 \pi^-$  in TPC (13.2% of all CC-other events)
- $1 \pi^-$  in TPC + at least 1 FGD-contained  $\pi^-$  (1.9% of all CC-other events)
- $\geq 1$  ME (24.3% of all CC-other events)

Conditions above are not mutually exclusive and thus reported proportions do not sum to 100%.

The distributions of reconstructed momentum  $p_\mu$  and  $\cos\theta_\mu$  of the reconstructed  $\mu^+$  candidate are presented in Fig. 3.22. Colors indicate the true identity of the candidate particle. Similarly to the signal sample, there are three major components but in different proportions: true  $\mu^+$  (29.8%), misidentified  $\pi^+$  (33.8%) and misidentified protons (23.9%). Low momentum  $\mu^-$  are mostly high angle or backward-going tracks originating from out of fiducial volume (OOFV) background.

The true identity of the  $\mu^+$  candidates and true topology of the events are summarized in Table 3.18. The sidebands shouldn't have much contribution of the true signal. This condition is satisfied as CC-other sample contains only 6.1% of the true CC1 $\pi^-$  topology.

It is important to use sidebands with a similar phase-space coverage as the background in the signal region. The distributions of reconstructed  $p_\mu$  and  $\cos\theta_\mu$  for the

topology	fraction of the background	detailed topology
$\bar{\nu}_\mu$ CC0 $\pi$	3.7%	
$\bar{\nu}_\mu$ CC-other	22.9%	$\bar{\nu}_\mu$ CC1 $\pi^0$ 2%
		$\bar{\nu}_\mu$ CC-other w/o $\pi^0$ 8.8%
		$\bar{\nu}_\mu$ CC-other with $\pi^0$ 12%
NC (flavour blind)	14.5%	
$\nu_\mu$ CC0 $\pi$	4.4%	
$\nu_\mu$ CC1 $\pi^+$	21.7%	
$\nu_\mu$ CC-other	25.9%	$\nu_\mu$ CC1 $\pi^0$ 2.5%
		$\nu_\mu$ CC-other w/o $\pi^0$ 10%
		$\nu_\mu$ CC-other with $\pi^0$ 13.4%
CC $\nu_e + \bar{\nu}_e$	0.5%	
OOFV	6.4%	

Table 3.17: Proportions of true final state topologies in the joint signal samples background.

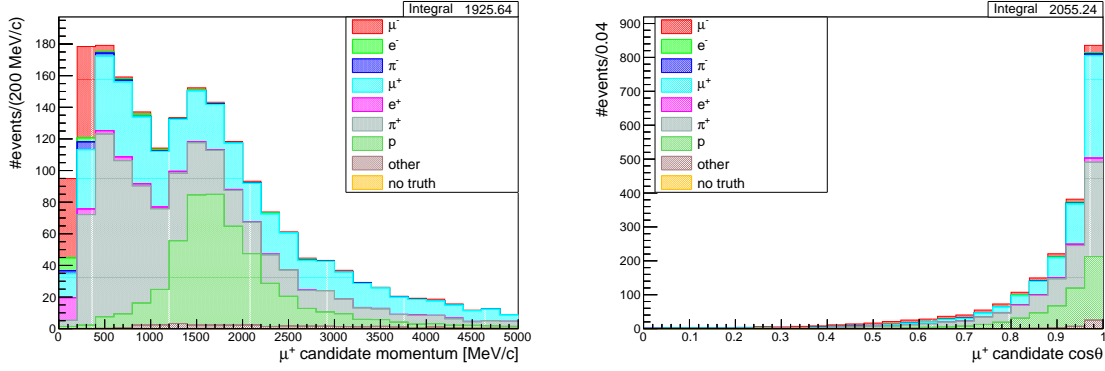


Figure 3.22: **CC-other background selection.** MC distribution of reconstructed kinematic variables (left - momentum, right -  $\cos\theta$ ) of the reconstructed  $\mu^+$  candidate. Colors indicate the true identity of the candidate.

particle	fraction of $\mu^+$ candidates	topology	fraction of the CC-other sample
$\mu^-$	7.1%	$\bar{\nu}_\mu$ CC0 $\pi$	5%
$e^-$	1%	$\bar{\nu}_\mu$ CC1 $\pi^-$	6.1%
$\pi^-$	0.9%	$\bar{\nu}_\mu$ CC-other	18.8%
$\mu^+$	29.8%	NC (flavour blind)	8.4%
$e^+$	1.6%	$\nu_\mu$ CC0 $\pi$	0.8%
$\pi^+$	33.8%	$\nu_\mu$ CC1 $\pi^+$	7.2%
p	23.9%	$\nu_\mu$ CC-other	38.4%
other	1.8%	CC $\nu_e + \bar{\nu}_e$	3.2%
		OOFV	12.1%

Table 3.18: **CC-other selection.** Proportions of true  $\mu^+$  candidates' identities and true final state topologies in the MC sample.

CC-other sample and background events in the joint signal samples are compared in Fig. 3.23. There is a very good agreement between those two. The only serious discrepancy is in the region of  $p_\mu < 200$  MeV/c, but it is excluded from the restricted phase-space.

The sideband and the background in the joint signal samples were also compared with respect to several other variables. In Fig. 3.24 the distributions of true positive MIP particle kinematics are presented. This particle identity is assigned in a following way: if there is a true  $\mu^+$  in the event then it is treated as the positive MIP, else if there is a true  $\pi^+$  then it is taken as the positive MIP. If there's no true  $\mu^+/\pi^+$  the event is omitted. The agreement between the CC-other sideband and background events in the joint signal samples is very good in this case.

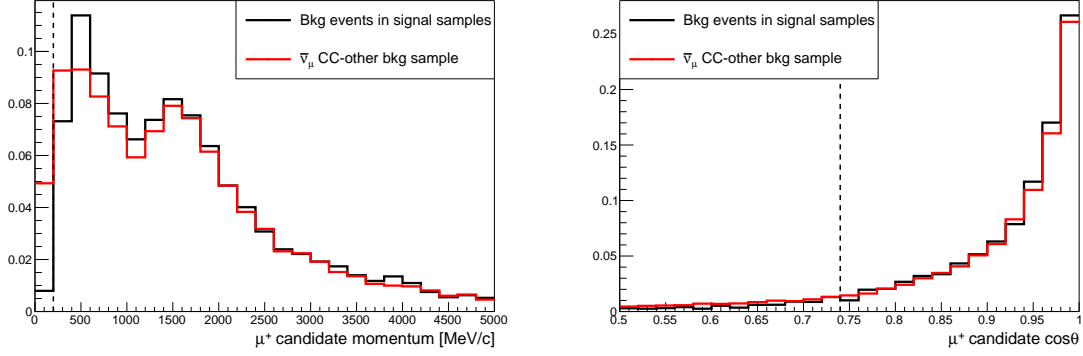


Figure 3.23: MC distribution of reconstructed kinematic variables (left - momentum, right -  $\cos \theta$ ) of reconstructed  $\mu^+$  candidate for CC-other sample and background events in the joint signal samples. Vertical dashed lines indicate the phase-space restrictions:  $p_\mu > 200$  MeV/c,  $\cos \theta_\mu > 0.74$ .

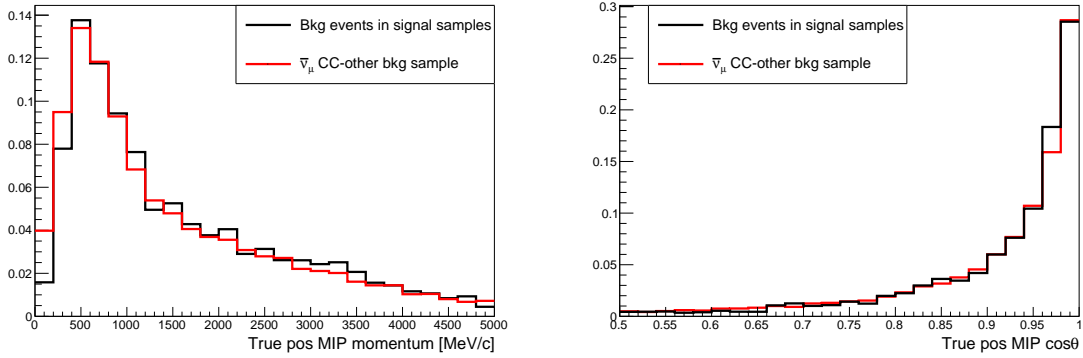


Figure 3.24: Distribution of true kinematic variables (left - momentum, right -  $\cos \theta$ ) of true positive MIP particle for CC-other sample and background events in the joint signal samples.

In similar way one can choose true negative MIP particle in the event as true  $\mu^-/\pi^-$ . The distributions of true negative MIP kinematics are presented in Fig. 3.25. The agreement between the sideband and the signal sample background is not as good as for positive MIP kinematics. In particular the peak in momentum distribution appears to be shifted by 200 MeV/c. However this discrepancy is not critical, because the differential cross-section will be reported in positive particle ( $\mu^+$ ) kinematical variables.

The comparison of CC-other sideband and joint signal samples background for distributions of neutrino energy  $E_\nu$ , four-momentum transfer squared  $Q^2$  and hadronic invariant mass  $W$  are presented in Fig. 3.26. Despite discrepancies for low  $E_\nu$  and low  $Q^2$  regions the general shape of these distributions is similar for both samples.

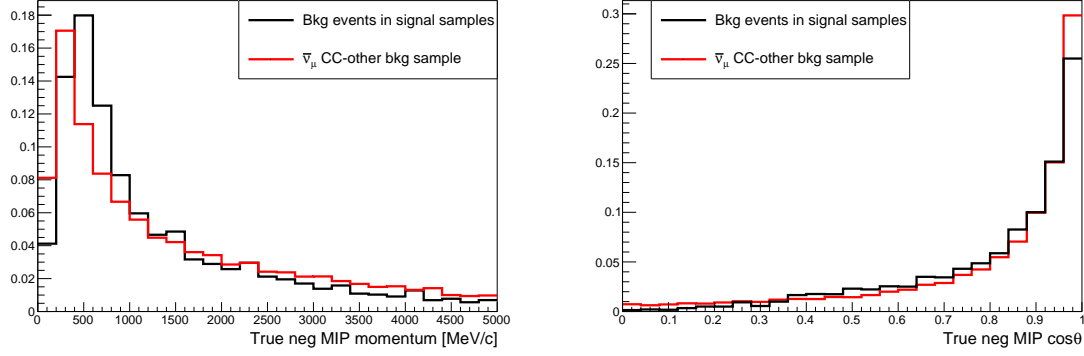


Figure 3.25: Distribution of true kinematic variables (left - momentum, right -  $\cos\theta$ ) of true negative MIP particle for CC-other sample and background events in the joint signal samples.

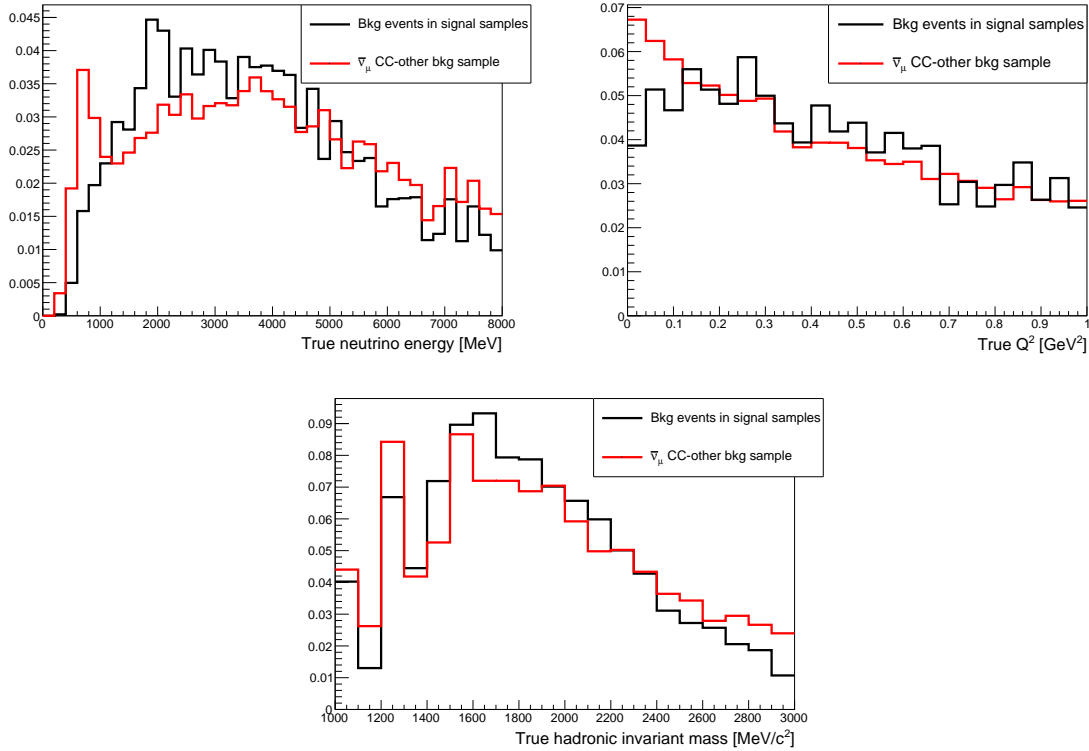


Figure 3.26: Distribution of true variables (top left:  $E_\nu$ , top right:  $Q^2$ , bottom: hadronic invariant mass  $W$ ) for CC-other sample and background events in the joint signal samples.

### 3.5.2. Reversed Z-range cut

Reversed Z-range cut sample is a subset of  $\bar{\nu}_\mu$  CC1 $\pi^-$  sample with cuts described in section 3.3.1. Additional reversed Z-range cut is applied, which selects events with:

- TPC  $\pi^-$  track and  $Z_\mu - Z_\pi < -10$  cm,

where  $Z_{\mu/\pi}$  is the Z-coordinate of the end point of the  $\mu^+/\pi^-$  candidate track. The distributions of reconstructed momentum and  $\cos\theta$  of the reconstructed  $\mu^+$  candidate for this sample are presented in Fig. 3.27. Colors indicate the true identity of the candidate. Similarly as for previously discussed samples, there are three major components: misidentified  $\pi^+$  (62.9%), misidentified protons (22.3%) and true  $\mu^+$  (12.3%).

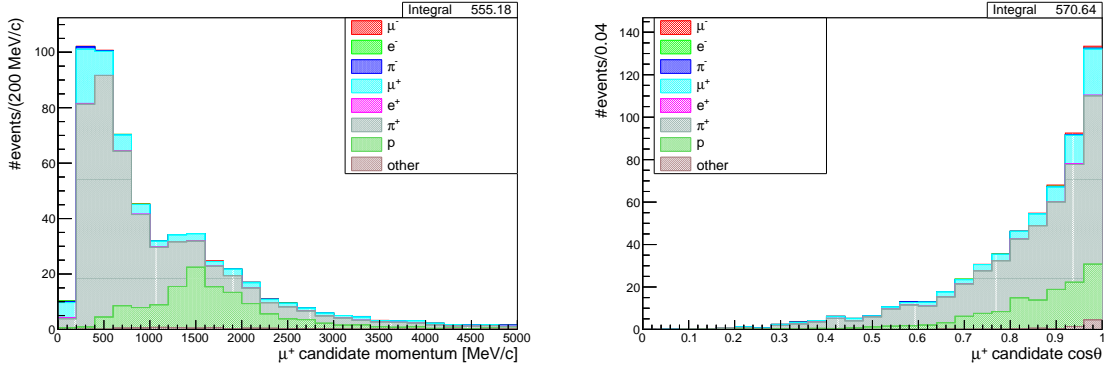


Figure 3.27: **Reversed Z-range cut background selection.** MC distribution of reconstructed kinematic variables (left - momentum, right -  $\cos\theta$ ) of reconstructed  $\mu^+$  candidate. Colors indicate true identity of the candidate.

In Fig. 3.28 there are distributions of reconstructed momentum  $p_\pi$  and  $\cos\theta_\pi$  for the reconstructed TPC  $\pi^-$  candidates. There are two major components: misidentified  $\mu^-$  (81.5%) and true  $\pi^-$  (18%). The true identities of the  $\mu^+$  and  $\pi^-$  candidates are summarized in Table 3.19.

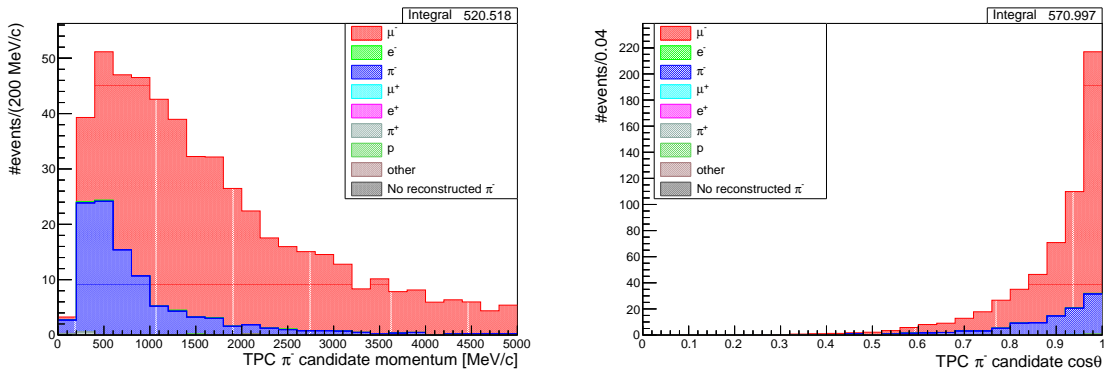


Figure 3.28: **Reversed Z-range cut background selection.** MC distribution of reconstructed kinematic variables (left - momentum, right -  $\cos\theta$ ) of reconstructed  $\mu^+$  candidate. Colors indicate true identity of the candidate.

One can see that most of the reconstructed  $\mu^+$  ( $\pi^-$ ) candidates are in fact misidentified  $\pi^+$  ( $\mu^-$ ). This is a result of a significant contribution of  $\nu_\mu$  CC interaction with

particle	fraction of the candidates in reversed Z-range cut sideband	
	$\mu^+$ candidate	TPC $\pi^-$ candidate
$\mu^-$	0.5%	81.5%
$e^-$	0.1%	0.1%
$\pi^-$	0.4%	18%
$\mu^+$	12.3%	0.1%
$e^+$	0.2%	0 %
$\pi^+$	62.9%	0.2%
p	22.3%	0.1%
other	1.3%	0.1%

Table 3.19: True identities of the candidates in the **reversed Z-range cut CC1 $\pi^-$  background sample**.

$\pi^+\mu^-$  in the final state (CC1 $\pi^+$  topology), which constitutes 43.3% of this sideband. The true topology composition of the sample is summarized in Table 3.20. Reversed Z-range cut sideband contains 8.2% of the true CC1 $\pi^-$  topology.

topology	fraction of the reversed Z-range cut sideband
$\bar{\nu}_\mu$ CC0 $\pi$	0.1%
$\bar{\nu}_\mu$ CC1 $\pi^-$	8.2%
$\bar{\nu}_\mu$ CC-other	2.4%
NC (flavour blind)	5.6%
$\nu_\mu$ CC0 $\pi$	7.9%
$\nu_\mu$ CC1 $\pi^+$	43.3%
$\nu_\mu$ CC-other	30.3%
CC $\nu_e + \bar{\nu}_e$	0.2%
OOFV	1.9%

Table 3.20: **Reversed Z-range cut background selection**. Proportions of true final state topologies in the reversed Z-range cut sideband.

The phase-space coverage of the reversed Z-range cut sideband was compared with the background in the joint signal samples for several variables: reconstructed  $p_\mu$  and  $\cos\theta_\mu$  (Fig. 3.29), true positive MIP particle kinematics (Fig. 3.30), true negative MIP particle kinematics (Fig. 3.31), neutrino energy  $E_\nu$ , four-momentum transfer squared  $Q^2$  and hadronic invariant mass  $W$  (Fig. 3.32).

In general the phase-space coverage of the reversed Z-range cut sideband is less similar to background in the signal region than the CC-other sideband is. When it

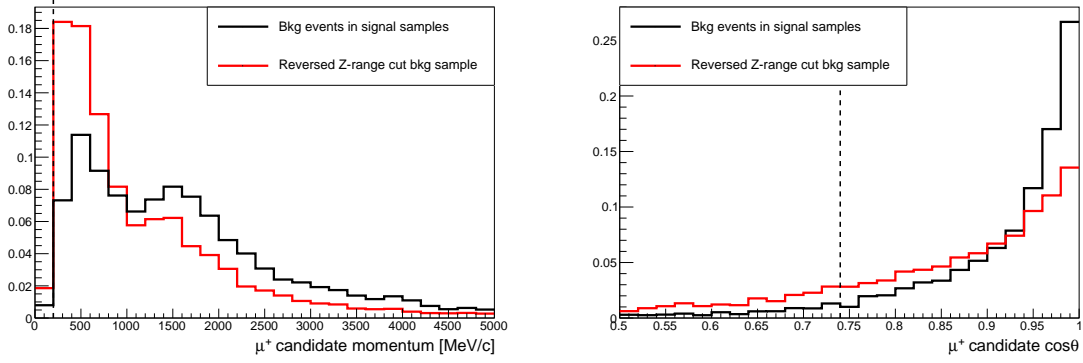


Figure 3.29: Distribution of reconstructed kinematic variables (left - momentum, right -  $\cos\theta$ ) of reconstructed  $\mu^+$  candidate for reversed Z-range cut sideband and background events in the joint signal samples. Vertical dashed lines indicate the phase-space restrictions:  $p_\mu > 200$  MeV/c,  $\cos\theta_\mu > 0.74$ .

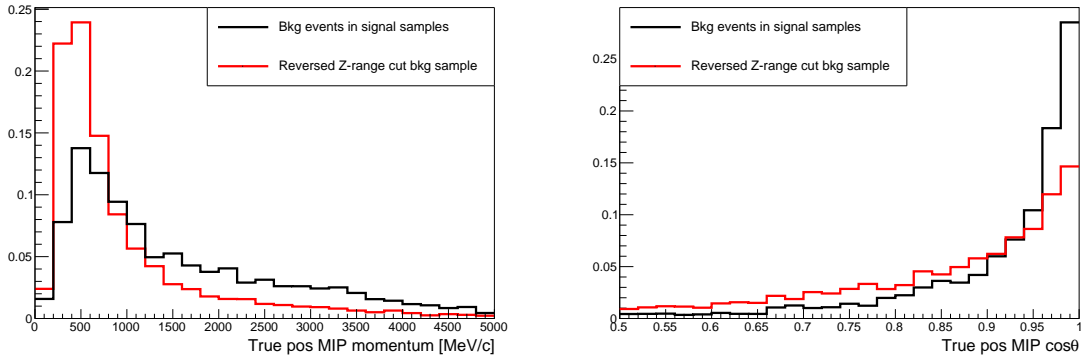


Figure 3.30: Distribution of true kinematic variables (left - momentum, right -  $\cos\theta$ ) of true positive MIP particle for reversed Z-range cut sideband and background events in the joint signal samples.

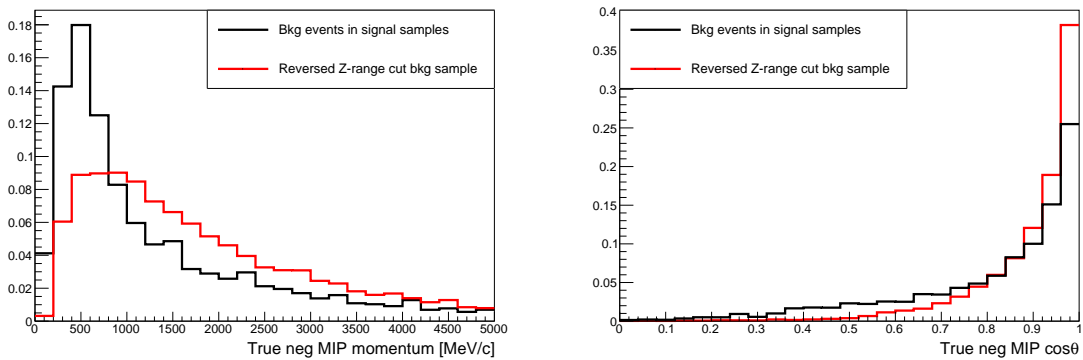


Figure 3.31: Distribution of true kinematic variables (left - momentum, right -  $\cos\theta$ ) of true negative MIP particle for reversed Z-range cut sideband and background events in the joint signal samples.

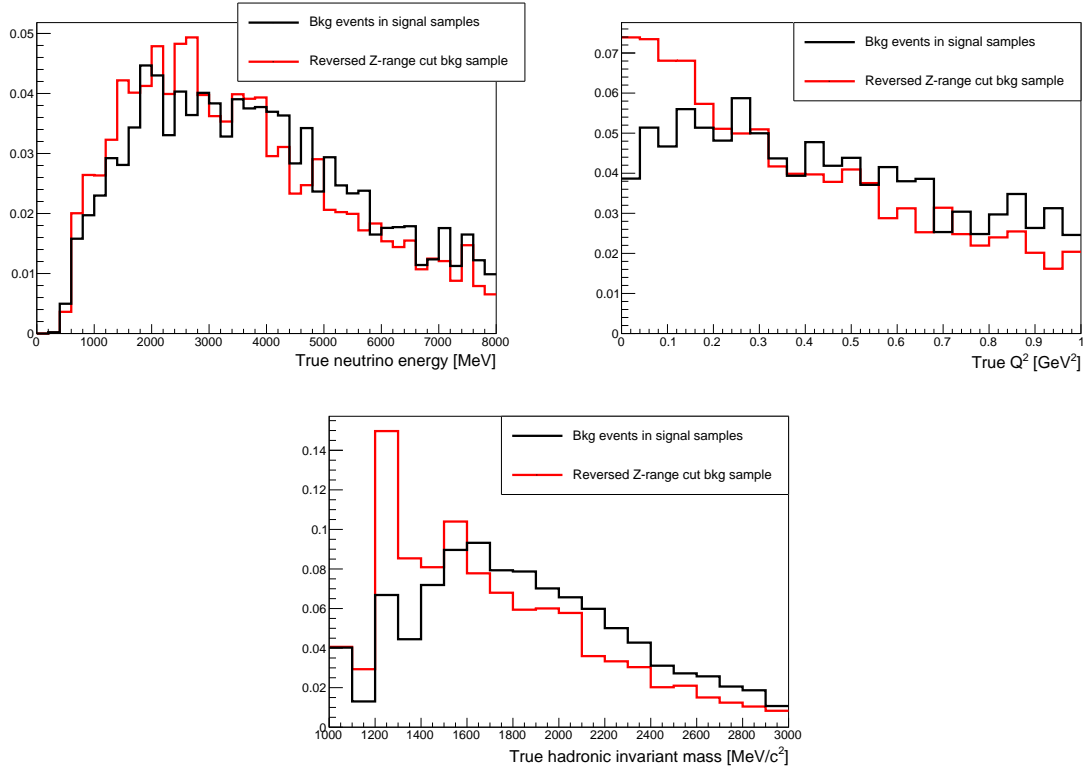


Figure 3.32: Distribution of true variables (top left:  $E_\nu$ , top right:  $Q^2$ , bottom: hadronic invariant mass  $W$ ) for reversed Z-range cut sideband and background events in the joint signal samples.

comes to reconstructed  $\mu^+$  and true positive MIP kinematics the reversed Z-range cut sideband has more low momentum and high angle tracks than the background, while for true negative MIP kinematics it is the other way around. This difference is to some extent expected since one is taking into account mostly background events in CC1TPC $\pi^-$  signal sample (which pass the Z-range cut) and compare them with events that fail to satisfy it. The Z-range cut performance depends to some extent on particles' kinematics as has been shown for signal events in Fig. 3.18. (For additional Z-range cut studies see Appendix A).

The agreement between the sideband and the signal sample background is quite good for neutrino energy  $E_\nu$ , however one can see discrepancies for low  $Q^2$  and  $W$  distribution - the peak around the  $\Delta$  resonance (1232  $\text{MeV}/c^2$ ) is clearly more significant for the reversed Z-range cut sideband than for the background. Despite this fact it was decided to keep this sideband in the analysis in order to avoid potential model dependency introduced by the Z-range cut. If, for any reason, data distribution in  $Z_\mu - Z_\pi$  (Fig. 3.9) is substantially different than MC then the total number of events passing and not passing the cut still will be correctly constrained in the measurement.

# Chapter 4

## Systematic uncertainties

Event rate in the selected samples is impacted by various systematic effects. In this chapter estimation of the related systematic uncertainties is discussed. All relevant systematic uncertainties for  $\bar{\nu}_\mu\text{CC}1\pi^-$  cross section measurement can be divided into three basic types: Detector-related uncertainties, Flux uncertainties and Monte Carlo model uncertainties.

### 4.1. Detector systematic uncertainties

Information presented in this section is mostly based on methods developed by the T2K collaboration [117]-[120]. Author's original input was the modification of pion secondary interactions systematic with dynamic volume of interest (subsection 4.1.3) as well as identification of all relevant systematic effects for the analysis and estimation of the corresponding errors.

The detector systematic effects are propagated within highland2 framework<sup>1</sup> with so-called *toy experiments*. There are two general strategies used:

- Variation method - in each event and each toy experiment certain observables (such as measured energy loss) are modified, which may impact the result of the selection cuts. Thus the number of selected events in the sample may differ for different toy experiments. Variation method is used when a systematic effect impacts continuous observables. It is straightforward to interpret however requires a lot of computational power since the selection is repeated multiple times.
- Weight method - each event in the sample is characterised by an array of systematic weights  $w[\textit{toy}]$  corresponding to all toy experiments. The number of events

---

<sup>1</sup> Highland (high level analysis at the near detector) consists of a set of tools created for all analyses at ND280.

selected in the sample remains the same, but the assigned integral is different for each toy experiment. Weight-like systematics can be further divided into two types which differ with respect to the weight calculation method:

- Efficiency-related systematics - weight method is used to estimate systematic effects which impact discrete observables (such as the reconstructed subdetector track segment).
- Normalisation systematics - weight method is used to estimate systematic effects which do not impact any specific observable but are expected to impact the event rate.

The details of the application of those methods for relevant detector systematic effects are discussed in the subsections below. In most cases the systematic effects are probed with the dedicated Monte Carlo and data control samples in which a given effect is more significant than in the analysis samples.

#### 4.1.1. Variation-like systematics

In this subsection the first three considered systematics ( $\vec{B}$  field distortion, momentum resolution, momentum scale) are related to the track momentum reconstruction. Fourth systematic (TPC PID) is crucial for the selection in all analysis samples. Those four systematics are propagated for all tracks which start in FGD and cross downstream TPC. Fifth discussed systematic (FGD PID) is relevant only for tracks fully contained in FGD.

##### $\vec{B}$ field distortion

When a charged particle enters the TPC, it ionises gas and ionisation electrons drift to the anode. In the nominal track reconstruction it is assumed that the magnetic field  $\vec{B}$  is parallel to the electric field  $\vec{E}$  and thus electrons drift along the field lines. As explained in subsection 2.3.3 TPCs are equipped with the photoelectron calibration system which allows to measure distortions of the electron drift due to inhomogeneities of  $\vec{B}$  and  $\vec{E}$  fields. That in turn allows to estimate so-called *empirical correction* on the track's momentum. This is not included in the eventual momentum reconstruction, but is used to calculate the systematic uncertainty related to the B-field distortion. In each toy experiment the track momentum is varied as:

$$p^{toy} = p^{nominal} + (p^{nominal} - p^{corrected}) \times \beta(toy),$$

where  $\beta(toy)$  is a random factor following the uniform distribution in range (0, 1).

### Momentum resolution

This uncertainty is related to TPC momentum reconstruction resolution. The value of the reconstructed momentum for a global track (i.e. track with FGD and TPC segments) depends on whether the particle is assumed to propagate forward or backward. Thus every track is characterised by reconstructed transverse momentum (with respect to  $\vec{B}$  field direction) for nominal and flipped propagation direction  $p_T^{nominal}, p_T^{flipped}$  as well as true transverse momentum  $p_T^{true}$  (known for Monte Carlo).

The momentum resolution was studied with Monte Carlo and data control samples consisting of muon tracks passing through several TPCs and FGDs. The reconstructed inverse transverse momentum in each TPC segment  $p_T^{-1}$  was checked and the difference in this variable between neighbouring TPCs' (corrected by energy loss in FGD between TPCs)  $\Delta p_T^{-1}$  was calculated. The distributions of  $\Delta p_T^{-1}$  for Monte Carlo and data were characterised by different standard deviation  $\sigma_{\Delta p_T^{-1}}$ . This difference can be minimised by smearing momentum of all MC tracks as:

$$(p_T^{-1})^{smeared} = (p_T^{true})^{-1} + \left( (p_T^{nominal})^{-1} - (p_T^{true})^{-1} \right) \times (1 + \gamma_i),$$

where  $\gamma_i$  is a smearing factor for  $i$ -th bin of transverse momentum  $p_T$ . Values of smearing factors are of the order of 0.1 to 0.3. A conservative error 0.1 is assigned to each smearing factor  $\gamma_i$ . This smearing based on control samples studies is also applied as a reconstruction correction in Author's analysis. For the systematic propagation in each toy experiment inverse transverse momentum  $(p_T^{-1})^{toy}$  is varied as:

$$(p_T^{-1})^{toy} = (p_T^{true})^{-1} + \left( (p_T^{-1})^{smeared} - (p_T^{true})^{-1} \right) \times \left( 1 + 0.1 \frac{\alpha(toy)}{2} \right),$$

where 0.1 factor is related to error on  $\gamma_i$  and  $\alpha(toy)$  is a random number following the normal distribution  $N(0, \sqrt{2})$  (the same  $\alpha(toy)$  value is used for all events in a given toy experiment). Based on  $(p_T^{-1})^{toy}$  the global reconstructed momentum  $p^{toy}$  and momenta assigned to each TPC segment are recalculated.

### Momentum scale

The strength of the magnetic field in ND280 was measured with a Hall probe in 2009 before installing all subdetectors. The uncertainty of this measurement results in 0.57% relative error on the momentum scale. In each toy experiment the reconstructed momentum for a global track is varied according to this error as:

$$p^{toy} = p^{nominal} (1 + 0.0057 \times \alpha'(toy)),$$

where  $\alpha'(toy)$  is a random number following the normal distribution  $N(0, 1)$ .

## TPC PID

Particle identification in TPC is based on the measurement of energy loss  $dE/dx$ . The selection cuts use likelihood variables, which are calculated from pull variables  $\delta(i)$  and deposited energy resolutions  $\sigma^{exp}(i)$  for a given particle hypothesis  $i$  as explained in subsection 3.2. The distributions of pull variables for dedicated Monte Carlo and data control samples were fitted to Gaussian in specific momentum bins.

The proton sample was extracted from beam events in FHC mode. It consisted of events with the highest momentum positive track of momentum between 300 MeV/c and 1.1 GeV/c, depositing large energy loss in TPC (see Fig. 2.11) and starting in FGD FV. To evaluate systematic effect for pions and muons the *sand muon*<sup>2</sup> control sample was used. The systematic is not propagated for electron-like pulls thus no electron control sample was needed.

Two quantities are calculated in order to propagate the systematic uncertainty: the difference between the mean values of pull distributions in data and Monte Carlo and the ratio of the standard deviations of pull distributions (data over Monte Carlo). In each toy experiment for every track and in each TPC segment the measured energy loss  $C_T^{meas}$  is varied, which alters the values of pull and likelihood variables (Eq. 3.5-3.7).

## FGD PID

Particle identification in FGD is based on the measurement of deposited energy as explained in subsection 3.3.4. It is particularly important for CC1FGD $\pi^-$  sample selection where the event signature includes a charged pion track contained in FGD. The selection cut uses the pull variable  $p_\pi$  defined in Eq. 3.10. The pull distributions differ between dedicated Monte Carlo and data control samples. In each toy experiment the pull variables  $p_i$  are varied analogously to how energy loss is varied in TPC PID systematic.

### 4.1.2. Weight-like systematics

Weight-like systematics can be divided into two groups: efficiency-related and normalisation systematics. The weight calculation for all efficiency-related systematics is done in analogous way. In this subsection efficiency effects are introduced first and then the relevant weight calculation method is explained. First four efficiency-related systematics (charge identification, TPC track reconstruction, TPC cluster reconstruc-

---

<sup>2</sup>When the (anti)neutrino from the beam interacts outside of the ND280 the produced muon is referred to as *sand muon*. They may enter the ND280 from the upstream side.

tion, TPC-FGD matching) are relevant for all tracks starting in FGD and crossing downstream TPC and thus are propagated for all events in all analysis samples. Other efficiencies are taken into account only for events with specific characteristics: true track starting in FGD, crossing TPC and reaching ECal (TPC-ECal matching), true track fully contained in FGD (FGD hybrid track reconstruction) or true Michel Electron (ME tagging).

Afterwards normalisation systematics are discussed. First three of them (out of fiducial volume background, pile-up, FGD mass) are relevant for all events in all analysis samples. The systematics related to proton/pion secondary interactions (SI) are propagated only for specific events with true proton/pion tracks. The pion SI systematic is described in details in a separate subsection 4.1.3 since it is the leading detector systematic effect for this analysis.

### Charge identification efficiency

The charge sign of a particle is deduced from the curvature of a TPC track. It may be misidentified especially in case of very energetic particles whose tracks in the magnetic field are nearly straight lines. In order to estimate the probability  $P_{mis}$  of charge misidentification the dedicated data control sample was used with tracks crossing all three TPCs. The probability that the identified charge has the same sign in all TPCs can be expressed as:

$$P_{same} = (1 - P_{mis})^3 + P_{mis}^3.$$

Thus  $P_{mis}$  can be calculated as:

$$P_{mis} = \frac{1}{2} \left( 1 - \sqrt{\frac{4P_{same} - 1}{3}} \right).$$

In this approach it is assumed that the three TPC segments of the global track correspond to one particle. The charge ID efficiency is taken as  $\varepsilon = 1 - P_{mis}$ . This quantity is computed in track momentum bins for data control sample and corresponding Monte Carlo.

### TPC track reconstruction efficiency

The TPC track reconstruction efficiency describes the probability that a charged particle propagating through TPC results in a reconstructed TPC track segment. To study the efficiency in a given TPC the dedicated data control sample with so-called *reference tracks* was used i.e. with track segments in subdetectors surrounding given TPC. For

example to study efficiency in TPC1 events with reference tracks in P $\bar{O}$ D and TPC2 were chosen. Results of these checks are presented in Table 4.1. It was found that the reconstruction efficiency does not depend on momentum, angle or length of the track and it is not decreased by the presence of a second track in the same TPC [119].

	TPC1	TPC2	TPC3
$\epsilon_{data}$	$99.9^{+0.1\%}_{-0.1\%}$	$99.7^{+0.2\%}_{-0.7\%}$	$99.3^{+0.5\%}_{-0.9\%}$
$\epsilon_{MC}$	$99.6^{+0.2\%}_{-0.3\%}$	$99.5^{+0.3\%}_{-0.4\%}$	$99.8^{+0.1\%}_{-0.2\%}$

Table 4.1: TPC track reconstruction efficiency for ND280 TPCs [119].

### TPC cluster reconstruction efficiency

In order to select a muon candidate the quality cut is applied on a reconstructed TPC track segment - it must contain at least 19 clusters in MicroMegas columns (see subsection 3.1). A failure in reconstructing one or more clusters may reduce the number of muon candidates in a sample. The TPC cluster reconstruction efficiency  $\epsilon_{cluster}$  describes a probability that a single cluster in a relevant MicroMega column is found when a charged particle passes through the TPC. In order to study this quantity control samples with muon-like tracks crossing entire length or height of TPC were used. For efficiency  $\epsilon_{cluster} = 100\%$  such tracks should contain all 72 vertical or 288 horizontal clusters. This however is not always the case and the actual efficiency is computed from the distribution of cluster multiplicity per through-going track. The efficiency  $\epsilon_{cluster}$  is found to be of the order of 99.5%. The difference between data and MC in the clusters multiplicity distribution is used to compute the systematic uncertainty.

### TPC-FGD matching efficiency

In the presented analysis as in multiple other ND280 analyses the main object of interest is the reconstructed muon track, which is required to originate in FGD fiducial volume and have a TPC segment. Thus it is essential in global track reconstruction to match FGD and TPC track segments. The so-called *basic matching efficiency* describes the probability that reconstructed track segments in FGD and in downstream TPC which belong to one particle are reconstructed as parts of one global track. For studying this systematic the control sample with muon-like tracks crossing two consecutive TPCs was chosen. For all events both in data and MC such tracks had the FGD segment as well. Thus the basic efficiency is 100%. However, such approach is

insensitive to the limited FGD fiducial volume. If the global reconstructed track starts in FGD FV but the true track vertex is out of FV then the CC-inclusive sample is contaminated with background. Thus the so-called *complete matching efficiency* is defined by the probability of matching FGD-TPC track to the upstream TPC track with reconstructed hits in the most upstream FGD XY module. The complete TPC-FGD matching efficiency is equal to  $99.979 \pm 0.004\%$  in data and  $99.98 \pm 0.004\%$  in MC for reconstructed momenta above 200 MeV/c, and  $99.35 \pm 0.13\%$  in data and  $99.71 \pm 0.06\%$  in MC for reconstructed momenta below 200 MeV/c.

### TPC-ECal matching efficiency<sup>3</sup>

The Z-range cut (described in subsection 3.3.3) is used to split sample with  $\mu^+, \pi^-$  tracks into CC1TPC $\pi^-$  signal sample and Reversed Z-range cut background sample. For this cut the variable of interest is the ending Z-position of the reconstructed track and thus matching TPC-ECal track segments (in particular TPC3-DsECal segments) becomes crucial for classifying an event as signal or background<sup>4</sup>.

The efficiency discussed in this paragraph was measured separately for TPC3-DsEcal and TPC-BarrelEcal matching. The control sample used for this study consisted of muon-like tracks which originate from FGD FV and appear to enter an ECal module (for example a forward-going track which reaches the downstream side of TPC3 is expected to enter DsEcal).

### FGD hybrid track reconstruction efficiency

The FGD hybrid track reconstruction efficiency is related to tracks that are fully contained in FGD. Thus it is crucial systematic for CC1FGD $\pi^-$  sample selection where the event signature includes a charged pion track contained in FGD. The study of this efficiency was done for FGD-contained tracks which are accompanied by FGD-TPC matched muon candidate tracks. Those FGD-contained tracks are called *hybrid* since they were generated in Geant Particle Gun (as pions and protons) and added to the muon track vertices in the real data and MC events. Data-hybrid and MC-hybrid samples were then reprocessed in order to repeat the track reconstruction. The fraction of events with at least one successfully reconstructed FGD-contained track was taken as the efficiency. In general it was lower for events with pion (proton) and muon pro-

---

<sup>3</sup> This systematic is not propagated for CC1FGD $\pi^-$  signal sample and CC-other background sample since TPC-ECal matching plays no role in events selection there.

<sup>4</sup>In CC1TPC $\pi^-$  signal sample 54% of  $\mu^+$  candidates tracks cross TPC3 and DsEcal. Similarly in Reversed Z-range cut background sample 51% of  $\pi^-$  candidates tracks cross TPC3 and DsEcal.

pagating in similar direction since pion (proton) FGD hits were often assigned to the muon track. The difference between data-hybrid and MC-hybrid efficiency is used to compute the systematic uncertainty.

### Michel Electron tagging efficiency

A low momentum charged pion, which is not reconstructed as a track, may decay within FGD1 volume with subsequent  $\mu^\pm$  decay and  $e^\pm$  appearance. Produced  $e^\pm$  is referred to as Michel electron (ME) and its signature is a delayed signal in FGD1 as explained in subsection 3.3.1. The ME tagging efficiency describes a probability that true ME is successfully identified in FGD1 where pion decay occurred. The control sample used for studying this efficiency consisted of cosmic muon tracks stopping in FGD1 [121]. The efficiency is found to be  $58.6 \pm 5.5\%$  for data and  $61.9 \pm 1.1\%$  for MC [122]. The difference between these values is used to compute the systematic uncertainty.

### Weight calculation for efficiency-related effects

In case of efficiency systematics the weights are calculated in a following way:

- In each momentum (or other relevant variable) bin the ratio  $R^{CS} = \varepsilon_{data}^{CS} / \varepsilon_{MC}^{CS}$  **for control sample** is calculated. Both data and MC efficiencies have certain statistical errors  $\delta_{data}^{CS}, \delta_{MC}^{CS}$ . The statistical error on the ratio is:

$$\delta_{stat}^2 = (R^{CS})^2 \left( \frac{(\delta_{data}^{CS})^2}{(\varepsilon_{data}^{CS})^2} + \frac{(\delta_{MC}^{CS})^2}{(\varepsilon_{MC}^{CS})^2} \right).$$

- The difference  $(R^{CS} - 1)$  is taken as a conservative estimation of the systematic error on the ratio.
- Both statistical and systematic errors are included to calculate the total error on the ratio:

$$\delta_{RCS} = \sqrt{\delta_{stat}^2 + (R^{CS} - 1)^2}$$

- **For the analysis samples** in each toy experiment the predicted efficiency in data is taken as  $R^{CS}$  (for the relevant phase-space bin) and varied as:

$$\varepsilon_{data}^{toy} = R^{CS} + \delta_{RCS} \times \alpha(toy),$$

where  $\alpha(toy)$  is a random factor following the normal distribution  $N(0, 1)$ .

- For each relevant true track or ME which was correctly reconstructed or identified the weight

$$w_{eff}^{obj} = \frac{\varepsilon_{data}^{toy}}{\varepsilon_{MC}}$$

is assigned. For each object that was not correctly reconstructed the weight is taken as:

$$w_{ineff}^{obj} = \frac{1 - \varepsilon_{data}^{toy}}{1 - \varepsilon_{MC}}.$$

- The systematic weight for the event is calculated as the product of all weights assigned to relevant true objects:

$$w^{toy} = \prod_{obj} w^{obj},$$

where  $w^{obj} = w_{eff}^{obj}$  if the object was correctly reconstructed and  $w^{obj} = w_{ineff}^{obj}$  for failed reconstruction.

### Out of Fiducial Volume background

Despite dedicated fiducial volume cut which aims to select  $\bar{\nu}_\mu$  interactions within FGD1 FV (see subsection 3.1) certain amount of selected events originate from (anti)neutrino interactions outside of FGD1 FV. Those out of fiducial volume (OOFV) events can be divided into 9 categories:

- Interactions within FGD1 but out of FGD1 FV;
- Interactions in the tracker dead material upstream or downstream of FGD1;
- Neutral hadrons originating from outside the tracker (which may be identified as fake neutrino interaction);
- Backward-going tracks which end in FGD1;
- High angle tracks entering FGD1. In this case tracks are usually poorly reconstructed and TPC-FGD matching may fail;
- Double skipped layers. If the FGD1 track segment lacks two most upstream layers hits the matching with upstream TPC1 is not possible. This may happen if the particle is propagating through the dead material between scintillator bars for tracks at a small angle with respect to the beam direction.
- Last module failure. Sometimes the TPC track segment is poorly reconstructed in  $x$  coordinate due to a time off-set in the TPC drift velocity. Then the TPC-FGD matching is based only on YZ projection hits and the reconstructed track starts in the most downstream FGD module;
- Hard elasting muon scattering in FGD. Probability of such process is modelled in Geant4;

- Bad first hit in the TPC-FGD matching. The algorithm matching FGD hits to the TPC track may pick a poor hit to start the extrapolation in the downstream to upstream direction. As a result the matching may stop within the FGD FV.

To estimate the OOFV systematic uncertainty two contributions are combined: rate uncertainty and reconstruction uncertainty.

For categories with initial neutrino interactions outside the tracker 20% uncertainty has been assigned to the event rate which corresponds to two factors: uncertainty on neutrino interaction cross sections on iron and lead, and data-MC discrepancy for  $\nu_\mu$  CC interactions in the SMRD.

For categories where OOFV event is selected in FGD FV due to a reconstruction flaw the reconstruction uncertainty is included (i.e. uncertainty on the probability of misreconstruction). For almost all categories this uncertainty is up to 40% except of high angle tracks category where the reconstruction uncertainty is set to 150% (a conservative estimation based on a control sample with high angle FGD-triggered cosmics).

In each toy experiment two independent weights are calculated:

$$w_{rate} = 1 + 0.2 \times \alpha(toy),$$

$$w_{reco} = 1 + \sigma_i \times \alpha(toy),$$

where  $w_{rate}$  corresponds to rate uncertainty,  $w_{reco}$  corresponds to reconstruction uncertainty,  $\sigma_i$  is the reconstruction uncertainty for a given category  $i$ , and  $\alpha(toy)$  is a random number following the normal distribution  $N(0,1)$ . The total systematic weight assigned to the event  $w_{toy}$  is calculated as:

$$w_{toy} = w_{rate} \times w_{reco}.$$

If  $w_{toy}$  happens to be negative it is set to zero.

### Pile-up

The TPC1 veto is applied in the preselection (subsection 3.1) in order to exclude sand muons from the CC-inclusive sample. This however comes at cost because  $\bar{\nu}_\mu$  CC interaction in FGD1 FV may coincide with a sand muon crossing TPC1 and get excluded from the analysis sample. Since the nominal Monte Carlo does not include sand muons<sup>5</sup> each MC event must be reweighted by the factor:

$$w_{pileup} = (1 - C_s),$$

---

<sup>5</sup>For technical reasons sand muons are simulated separately from neutrino interactions inside the detector.

where  $C_s$  correction can be calculated with a separate sand muon MC sample as:

$$C_s = \frac{NTPC_s}{POT_s} \times \frac{POT}{8 nSpills},$$

where  $NTPC_s$  is the number of TPC1 events in the sand muon MC sample,  $POT_s$  is the POT rate for the sand muon MC sample,  $POT$  is the POT rate for a data sample and  $nSpills$  is the number of spills in a data sample. Factor 8 in the denominator corresponds to the number of bunches per spill. Since the beam intensity was increasing throughout T2K history the  $C_s$  correction is calculated separately for each data set.

The systematic uncertainty on pile-up correction is evaluated from a data-MC difference  $\Delta_{data:MC}$  in the number of TPC1 events per bunch (with the sand muon MC contribution added to the nominal MC). The uncertainty  $\sigma_{pileup}$  is taken as the larger number among  $\Delta_{data:MC}$  and  $0.3 \times C_s$ . Factor 0.3 corresponds to conservative 30% uncertainty in the sand muon simulation for antineutrino beam mode. In each toy experiment the systematic weight is calculated as:

$$w_{toy} = 1 - C_s - \sigma_{pileup} \times \alpha(toy),$$

where  $\alpha(toy)$  is a random number following the normal distribution  $N(0, 1)$ .

### FGD mass

The event rate of (anti)neutrino interactions in FGD1 fiducial volume is proportional to the number of nuclei targets which in turn is proportional to the mass of FGD XY modules. Thus the uncertainty related to the XY modules mass is equivalent to the uncertainty of the total event rate in the nominal Monte Carlo, and is of the order of 0.6% [117]. In each toy experiment the systematic weight is calculated as:

$$w_{toy} = 1 + 0.006 \times \alpha(toy),$$

where  $\alpha(toy)$  is a random number following the normal distribution  $N(0, 1)$ .

### Proton secondary interactions

Since  $\mu^+$  candidates are sometimes misidentified protons the additional uncertainty related to proton secondary interactions (SI) must be included. Additionally,  $\mu^+$  candidate must be the highest momentum positive track (see subsection 3.1). The systematic related to proton SI is propagated only if:

- true proton was reconstructed as  $\mu^+$  candidate
- **or** there was a true proton in the event with true momentum higher than reconstructed  $\mu^+$  momentum.

In the latter case the reconstruction of proton track and momentum is crucial for the selection result and thus proton SI must be taken into account. The cross section for inelastic proton-nucleus interaction<sup>6</sup> is varied with conservative 10% error assigned. For each proton which undergoes an inelastic interaction the following weight is assigned:

$$w_{proton}^{toy} = \exp\left(\frac{\sigma^{nominal} - \sigma^{toy}}{\sigma^{nominal}}\right) \times \frac{\sigma^{toy}}{\sigma^{nominal}},$$

where  $\sigma^{nominal}$  is the nominal inelastic interaction cross section and  $\sigma^{toy}$  is varied cross section value in a given toy experiment. The systematic weight assigned to the event is calculated as the product of all proton weights:

$$w^{toy} = \prod_{proton} w_{proton}^{toy}.$$

### 4.1.3. Pion secondary interactions

The systematic uncertainty related to charged pion secondary interactions (pion SI) is the leading detector systematic in  $\bar{\nu}_\mu \text{CC}1\pi^-$  cross section measurement. Secondary interactions are defined as the interactions outside the nucleus pion was produced in. Each event has assigned a systematic weight depending on the parametrisation based on cross-sections for specific secondary interaction modes. Following types of interaction are crucial in the weight calculation:

- charged pion absorption in a nucleus,
- charge exchange:  $\pi^\pm + N \rightarrow \pi^0 + N'$ ,
- quasielastic charged pion scattering: the pion interacts inelastically and exactly one pion of the same type exits the interaction.

In each toy experiment the cross-sections for aforementioned modes are varied. Other types of interaction (such as elastic scattering or pion decay) are used in event simulation but they are not varied in toy experiments.

The systematic weight is calculated in a following way:

1. Consider a true charged pion in the event. Divide its trajectory into *steps*. Division depends on track properties, usually it is around 10-20 steps.
2. Each step has a momentum dependent probability of interaction  $P(\text{int})$  and probability of no interaction  $P(\text{NI})$ . Those probabilities depend on cross-sections.

---

<sup>6</sup>Inelastic hadronic proton interaction in Geant4 refers to any process other than fission, elastic scattering or proton capture.

3. The probability of a given trajectory  $P_{traj}$  is calculated as the product of step probabilities:

$$P_{traj} = \prod_{step} P_{step},$$

where  $P_{step} = P(\text{int})$  or  $P(\text{NI})$  depending on whether there was an interaction at a given trajectory step or not.

4. The probability of the event  $P_{evt}$  is calculated as the product of  $P_{traj}$  for all true  $\pi^\pm$  trajectories.
5. The weight  $w_{syst}$  for the toy experiment is calculated as the ratio of the  $P_{evt}$  with a given toy parametrisation to the  $P_{evt}$  with the default parametrisation:

$$w_{syst}[toy] = \frac{P_{evt}^{toy}}{P_{evt}^{def}}.$$

In general not all pion interactions occurring in the detector are important but only those which might alter the selection result. This concern is addressed by defining the **volume of interest (VOI)** which covers only that part of the detector which is crucial for the selection. VOI is used to put certain restrictions on which pion interactions are relevant for the weight calculation. Firstly, pion trajectory must originate in VOI. Secondly, only those trajectory steps which are within VOI are used for the calculation of  $P_{traj}$ .

### Dynamic VOI

For the presented analysis the calculation of pion SI weights was done with a significant innovation. In highland2 the volume of interest (VOI) in which pion hadronic interactions and decays are taken into account is by default set to joint volume of FGD1 and upstream part of TPC2. This was sufficient in old T2K analyses, since the selection of  $\mu/\pi$  requires that track originates in FGD and has a TPC segment. However, in the presented analysis Author introduced the Z-range cut which is based on the ending position of reconstructed  $\mu^+/\pi^-$  tracks. Hadronic interactions in the subdetectors downstream of TPC2 might alter the ending Z-position of the track and thus it becomes necessary to expand VOI for CC1TPC $\pi^-$  signal sample and reversed Z-range cut background sample.

The X and Y boundaries of VOI are kept the same as in older analyses, however the downstream Z boundary  $Z_{VOI}^{max}$  depends on the properties of reconstructed tracks in the event. This may be divided into 5 cases which are described in the paragraphs below. If in any of these cases  $Z_{VOI}^{max} < 57.6$  cm it is adjusted to  $Z_{VOI}^{max} = 57.6$  cm so

that VOI always includes FGD1 and upstream part of TPC2. Maximal possible VOI corresponds to joint FGD1+TPC2+FGD2+TPC3+DsECal volume and its boundary  $Z_{VOI}^{max} = 327.3$  cm. (Approximately 75% of true pions in presented analysis samples have reconstructed ending position within such volume.) For CC1FGD $\pi^-$  signal sample and CC-other background sample VOI modification is not necessary and it is limited to default boundaries.

1. CC1TPC $\pi^-$  signal sample with  $\mu^+$  candidate not being true  $\pi^\pm$  and reaching DsECal downstream wall (or ending less than 10 cm before that position). In this case only the impact of pion SI on  $\pi^-$  candidate track reconstruction was considered. It does not matter where  $\pi^-$  candidate ends - the Z-range cut is always satisfied. Thus VOI may be limited to the standard setting, which in ND280 coordinate system corresponds to  $Z_{VOI}^{max} = 57.6$  cm. The distributions of the reconstructed tracks ending Z-positions for this case are presented in Fig. 4.1.

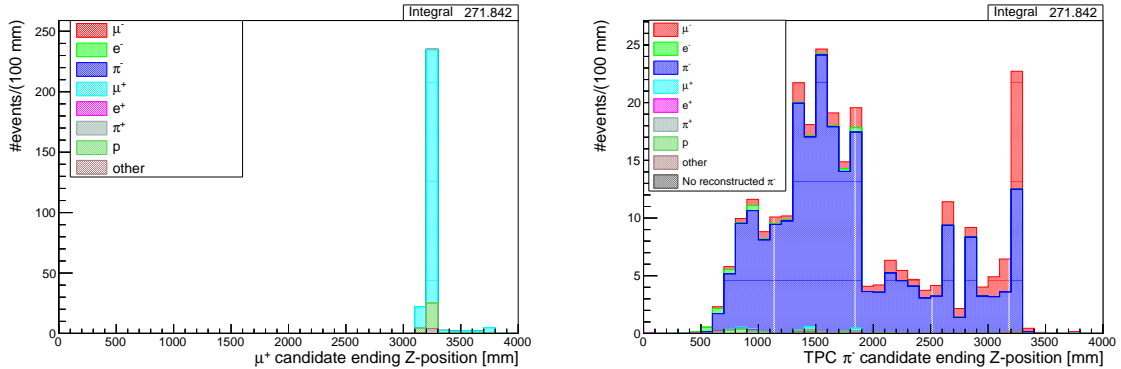


Figure 4.1: **Case 1:** CC1TPC $\pi^-$  signal sample with  $\mu^+$  candidate not being true  $\pi^\pm$  and reaching DsECal downstream wall (or ending less than 10 cm before that position).  $Z_{VOI}^{max} = 57.6$  cm. Left: Distribution of the ending Z-position of the reconstructed  $\mu^+$  candidate track which corresponds mostly to true  $\mu^+$ . Right: Distribution of the ending Z-position of the reconstructed  $\pi^-$  candidate track which corresponds mostly to true  $\pi^-$ . Colors indicate the true identity of the candidate.

- CC1TPC $\pi^-$  signal sample with  $\mu^+$  candidate not being true  $\pi^\pm$  and ending more than 10 cm upstream from DsEcal downstream wall. In this case only the impact of pion SI on  $\pi^-$  candidate track reconstruction was considered. Due to the Z-range cut  $\pi^-$  candidate ending position must satisfy inequality:  $Z_\pi < Z_\mu + 10$  cm. Hypothetically, lack of pion SI could lead to  $\pi^-$  candidate track having bigger Z-range than this threshold. Thus the entire region up to  $Z_\mu + 10$  cm must be treated as VOI. Hence  $Z_{VOI}^{max} = Z_\mu + 10$  cm. The distributions of the reconstructed tracks ending Z-positions for this case are presented in Fig. 4.2.

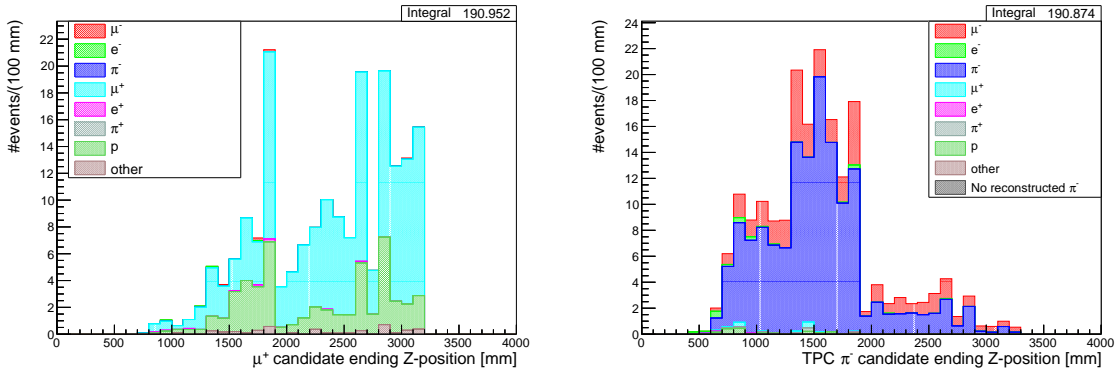


Figure 4.2: **Case 2:** CC1TPC $\pi^-$  signal sample with  $\mu^+$  candidate not being true  $\pi^\pm$  and ending more than 10 cm upstream from DsEcal downstream wall.  $Z_{VOI}^{max} = Z_\mu + 10$  cm. Left: Distribution of the ending Z-position of the reconstructed  $\mu^+$  candidate track which corresponds mostly to true  $\mu^+$ . Right: Distribution of the ending Z-position of the reconstructed  $\pi^-$  candidate track which corresponds mostly to true  $\pi^-$ . Colors indicate the true identity of the candidate.

- CC1TPC $\pi^-$  signal sample with  $\mu^+$  candidate being true  $\pi^\pm$ . In most events ( $\sim 70\%$ ) other reconstructed tracks don't correspond to true pions. Thus only the impact of pion SI on  $\mu^+$  candidate track reconstruction was considered. To pass the Z-range cut the  $\mu^+$  candidate track ending position must satisfy condition:  $Z_\mu > Z_\pi - 10$  cm. Therefore pion SI were included up to  $Z_\pi - 10$  cm. What happens in more downstream part of the  $\mu^+$  candidate track does not impact the selection. Hence  $Z_{VOI}^{max} = Z_\pi - 10$  cm. The distributions of the reconstructed tracks ending Z-positions for this case are presented in Fig. 4.3.
- Reversed Z-range cut background sample with  $\pi^-$  candidate being true  $\pi^\pm$ . In most events ( $\sim 75\%$ ) other reconstructed tracks do not correspond to true pions. Thus only the impact of pion SI on  $\pi^-$  candidate track reconstruction was considered. To pass the reversed Z-range cut the  $\pi^-$  candidate track ending position

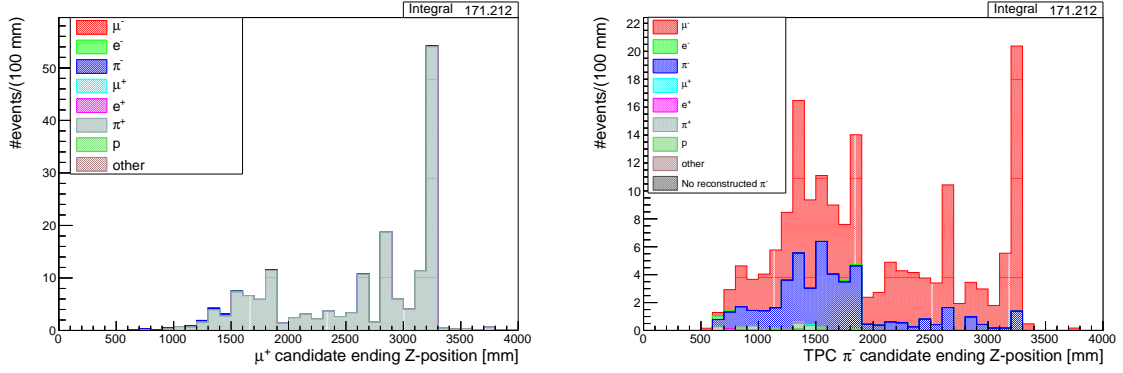


Figure 4.3: **Case 3:** CC1TPC $\pi^-$  signal sample with  $\mu^+$  candidate being true  $\pi^\pm$ .  $Z_{VOI}^{max} = Z_\pi - 10$  cm. Left: Distribution of the ending Z-position of the reconstructed  $\mu^+$  candidate track which corresponds almost exclusively to true  $\pi^+$ . Right: Distribution of the ending Z-position of the reconstructed  $\pi^-$  candidate track which corresponds mostly to misidentified  $\mu^-$ . Colors indicate the true identity of the candidate.

must satisfy condition:  $Z_\pi \geq Z_\mu + 10$  cm. Therefore we only have to include pion SI up to  $Z_\mu + 10$  cm. What happens in more downstream part of the  $\pi^-$  candidate track does not impact the selection. Hence  $Z_{VOI}^{max} = Z_\mu + 10$  cm. The distributions of the reconstructed tracks ending Z-positions for this case are presented in Fig. 4.4.

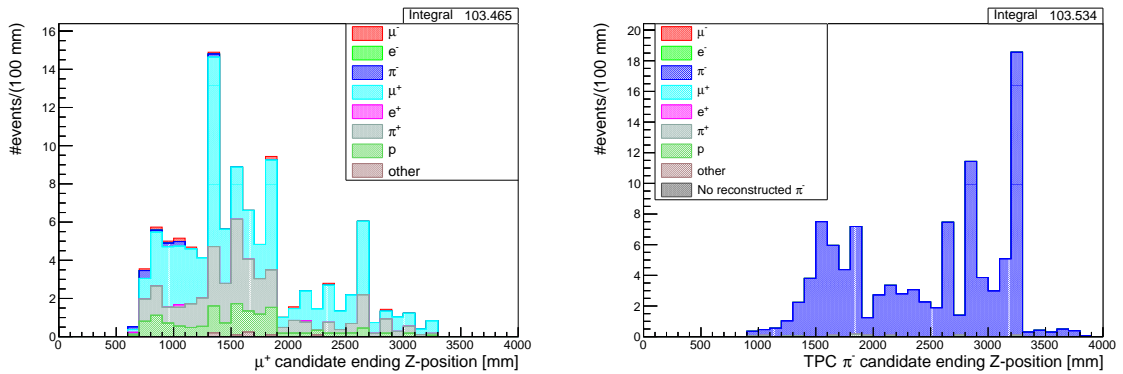


Figure 4.4: **Case 4:** Reversed Z-range cut background sample with  $\pi^-$  candidate being true  $\pi^\pm$ .  $Z_{VOI}^{max} = Z_\mu + 10$  cm. Left: Distribution of the ending Z-position of the reconstructed  $\mu^+$  candidate track which corresponds mostly to true  $\mu^+$ . Right: Distribution of the ending Z-position of the reconstructed  $\pi^-$  candidate track which corresponds almost exclusively to true  $\pi^-$ . Colors indicate the true identity of the candidate.

5. Reversed Z-range cut background sample with  $\pi^-$  candidate not being true  $\pi^\pm$ . In this scenario only the impact of pion SI on  $\mu^+$  candidate track reconstruction was considered (if  $\mu^+$  candidate happens to be true pion). Due to reversed Z-range cut the  $\mu^+$  candidate ending position must satisfy inequality:  $Z_\mu \leq Z_\pi - 10$  cm. Hypothetically, lack of pion SI could lead to  $\mu^+$  candidate track having bigger Z-range than this threshold. Thus  $Z_{VOI}^{max} = Z_\pi - 10$  cm. The distributions of the reconstructed tracks ending Z-positions for this case are presented in Fig. 4.5.

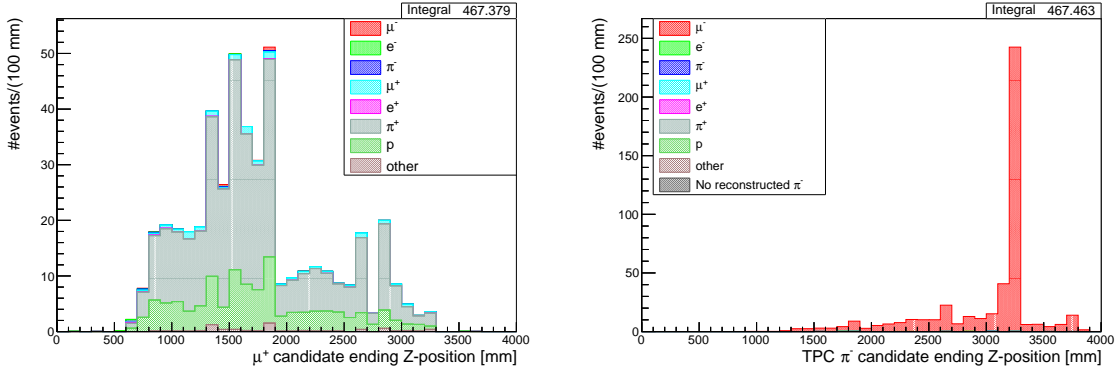


Figure 4.5: **Case 5:** Reversed Z-range cut background sample with  $\pi^-$  candidate not being true  $\pi^\pm$ .  $Z_{VOI}^{max} = Z_\pi - 10$  cm. Left: Distribution of the ending Z-position of the reconstructed  $\mu^+$  candidate track which corresponds mostly to misidentified  $\pi^+$ . Right: Distribution of the ending Z-position of the reconstructed  $\pi^-$  candidate track which corresponds almost exclusively to misidentified  $\mu^-$ . Colors indicate the true identity of the candidate.

#### 4.1.4. Detector systematics overview

In order to estimate the total detector systematic uncertainty all aforementioned systematic effects are combined and 500 toy experiments are thrown. In each toy experiment the propagation of systematic effects results in an event rate  $N^{toy}$  selected in a sample, different than the event rate  $N^{nominal}$  in the nominal selection. The systematic error is calculated as a standard deviation of the  $(N^{nominal} - N^{toy})$  distribution:

$$\sigma = \sqrt{\frac{1}{T} \sum_{toy=1}^T (N^{nominal} - N^{toy})^2},$$

where  $T$  denotes the number of toy experiments. The relative error is taken as:

$$\sigma^{relative} = \frac{\sigma}{N^{nominal}}.$$

In each toy experiment event has a total systematic weight  $w_{toy}^{total}$  assigned which is the product of all systematic weights calculated for specific systematic effects. The uncertainties for the selection within the restricted phase-space<sup>7</sup> are presented in Table 4.2. The weight systematics for specific effects are reported for toy experiment in  $0 < w^{toy} < 2$  range and the total systematic error is reported for  $0 < w_{total}^{toy} < 3$  range. Such conditions exclude no more than 2% of toys with the most extreme weights. For all samples the leading uncertainty is related to pion secondary interactions.

systematic	type	relative error [%]			
		CC1TPC $\pi^-$	CC1FGD $\pi^-$	Reversed Z-cut	CC-other
B-field distortions	variation	0.098	0.053	0.047	0.046
momentum resolution	variation	0.189	0.156	0.212	0.151
momentum scale	variation	0.049	0.037	0.189	0.013
TPC PID	variation	0.902	0.528	1.025	0.584
FGD PID	variation	0.010	0.552	0.011	0.007
charge ID efficiency	weight	0.249	0.097	0.258	0.140
TPC track efficiency	weight	1.142	0.267	0.934	0.261
TPC-FGD matching efficiency	weight	0.228	0.073	0.175	0.108
TPC cluster efficiency	weight	0.011	0.000	0.011	0.030
FGD hybrid track efficiency	weight	0.067	0.681	0.098	0.189
Michel electron	weight	0.137	0.083	0.275	0.019
OOFV background	weight	0.112	0.243	0.093	0.350
pile-up	weight	0.114	0.112	0.116	0.116
FGD mass	weight	0.579	0.564	0.581	0.565
SI pion	weight	4.292	14.16	6.183	2.333
SI proton	weight	0.190	0.022	0.430	0.484
TPC-ECal matching efficiency	weight	1.500	-	0.853	-
TOTAL detector systematic		5.157	15.01	7.029	2.505

Table 4.2: Detector systematic uncertainties related to all signal and background samples selection. **Restricted kinematical phase-space.**

The measured cross section is reported as a double differential in  $\mu^+$  kinematic variables. In general, the scale of the detector systematic uncertainty may vary for

<sup>7</sup>The restriction on reconstructed pion momentum ( $100 \text{ MeV}/c < p_{\pi \text{ reco}} < 3000 \text{ MeV}/c$ ) is applied both for TPC and FGD  $\pi^-$  candidates. Technically an additional systematic should be used for the momentum reconstruction in FGD. However, in the MC studies all  $\pi^-$  candidates in CC1FGD $\pi^-$  sample satisfy even stronger restriction:  $105 \text{ MeV}/c < p_{\pi \text{ reco}} < 300 \text{ MeV}/c$ . Thus potential event migration out of the phase-space is considered to be a negligible effect.

different phase-space regions. The total relative error is presented as a function of  $\mu^+$  candidate kinematical variables: reconstructed momentum (Fig. 4.6) and reconstructed  $\cos\theta$  (Fig. 4.7) including events within and beyond the restricted phase-space. Note that each bin corresponds to a certain subsample selected with additional cut on a variable:  $x_{min} < x < x_{max}$ . Such phase-space region is populated with  $N_{bin}$  events. Thus the uncertainty reported in this bin is calculated as a standard deviation of the  $(N_{bin}^{nominal} - N_{bin}^{toy})$  distribution. Additionally, in toy experiments the reconstructed  $\mu^+$  candidate momentum might be altered (due to B-field distortions, momentum resolution or momentum scale systematic propagation) and events might migrate to different momentum bins which increases the relative error per bin. This is the reason why in Fig. 4.6 the relative error increases in high momentum  $p_{\mu reco}$  region for all analysis samples.

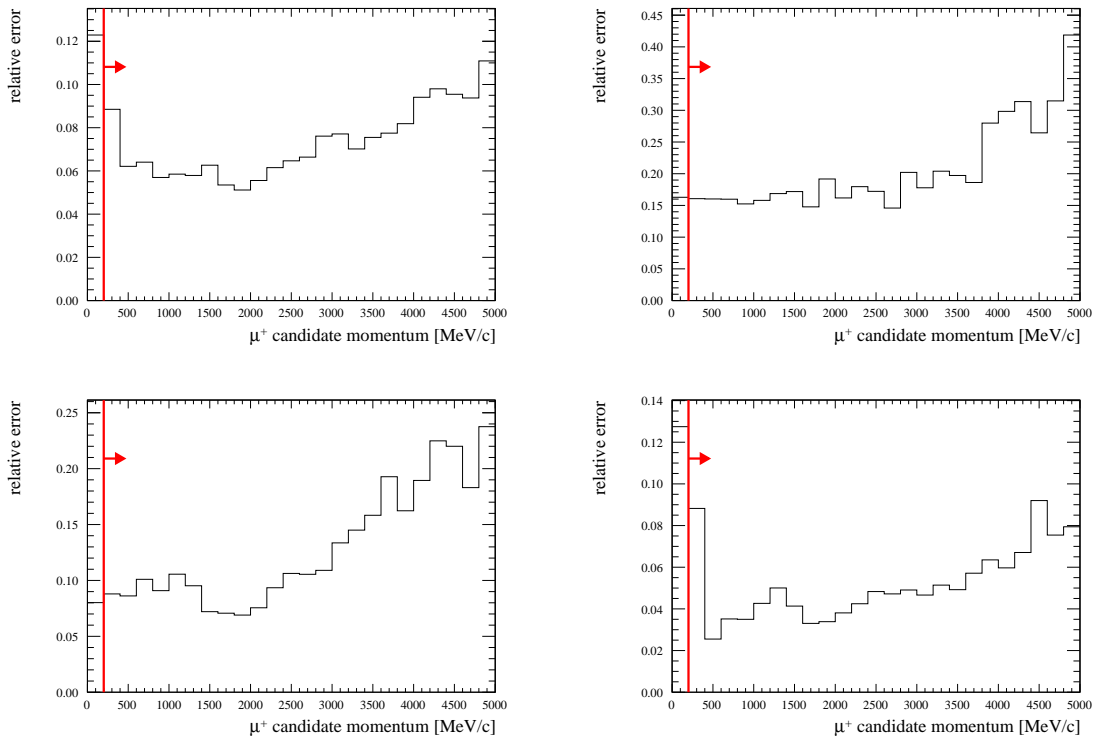


Figure 4.6: Distribution of total relative error as a function of  $\mu^+$  candidate momentum. Top left: CC1TPC $\pi^-$  signal sample. Top right: CC1FGD $\pi^-$  signal sample. Bottom left: Reversed Z-range cut background sample. Bottom right: CC-other background sample. Red line indicates the phase-space restriction:  $p_{\mu reco} > 200$  MeV/c.

As can be seen in Fig. 4.7 in case of CC1FGD $\pi^-$  signal sample and Reversed Z-range cut background sample the scale of total relative error does not depend on reconstructed  $\mu^+$  candidate  $\cos\theta$ . It is quite different for CC1TPC $\pi^-$  signal sample and CC-other background sample where the total relative error is significantly higher for events with high angle  $\mu^+$  tracks. In case of CC1TPC $\pi^-$  sample this is mostly result of pion SI systematic error - high angle  $\mu^+$  tracks rarely reach DsECal downstream wall and thus the conditions to use limited VOI are not satisfied (see description of Fig. 4.1 in subsection 4.1.3). In case of CC-other sample this feature is caused by OOFV systematic error.

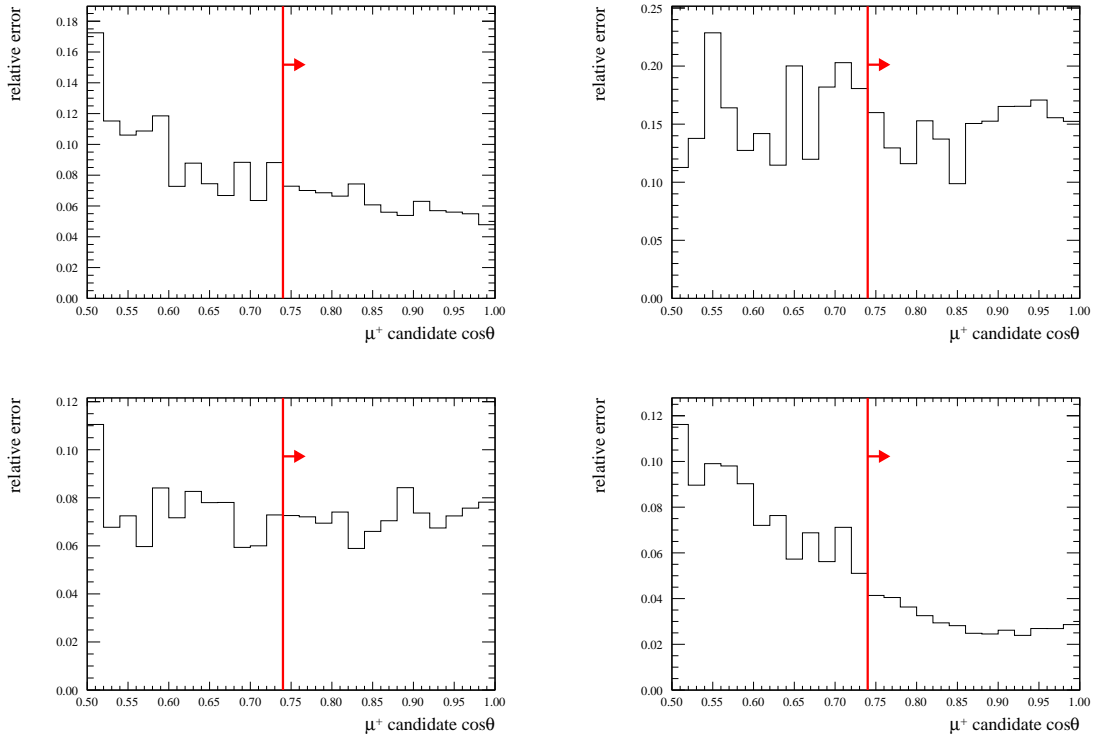


Figure 4.7: Distribution of total relative error as a function of  $\mu^+$  candidate  $\cos\theta$ . Top left: CC1TPC $\pi^-$  signal sample. Top right: CC1FGD $\pi^-$  signal sample. Bottom left: Reversed Z-range cut background sample. Bottom right: CC-other background sample. Red line indicates the phase-space restriction:  $\cos\theta_{\mu reco} > 0.74$ .

The detector systematic covariance matrix is presented in Fig. 5.8, p. 135, after the phase space binning is defined for all analysis samples.

## 4.2. Model systematic uncertainties

Uncertainty on selected event rate arises not only from detector systematic effects but also from imperfect modelling of neutrino interactions. Predictions of the nominal NEUT Monte Carlo are parametrised with a set of quantities enumerated in Table 4.3. Prior values and errors assigned to these parameters are based on recommendations of T2K Neutrino Interactions Working Group [80, 123, 124]. The corresponding covariance matrix is presented in Fig. 4.8. A brief description of the parameters is given in the paragraphs below.

Parameter Name	Abbreviation	Prior	Error
MACCQE	$M_A^{CCQE}$	1.21 GeV/c <sup>2</sup>	0.05 GeV/c <sup>2</sup>
MEC_C	$MEC_C$	1	1
MEC_C_SHAPE	$MEC_C^{shape}$	1	1
CA5	$C_5^A$	1.01	0.15
MARES	$M_A^{RES}$	0.95 GeV/c <sup>2</sup>	0.16 GeV/c <sup>2</sup>
I12RES	$I_{1/2}$	1.3	0.3
DIS_BY_corr	$DIS_{BY\ corr}$	1	0.5
MultiPi_BY	$MultiPi_{BY}$	1	0.5
MultiPi_Xsec_AGKY	$MPiXsecAGKY$	1	0.5
FSI_INEL_LO	$FSI_{INEL}^{LO}$	1	0.29
FSI_INEL_HI	$FSI_{INEL}^{HI}$	1.8	0.47
FSI_PI_PROD	$FSI_{PI\ PROD}$	1	1.1
FSI_PI_ABS	$FSI_{PI\ ABS}$	1.1	0.31
FSI_CEX_LO	$FSI_{CEX}^{LO}$	1	0.44
FSI_CEX_HI	$FSI_{CEX}^{HI}$	1.8	0.28
CCDIS_NORM	$CCDIS_{norm}$	1	0.5
CCMULTIPI	$CCMULTIPI$	1	0.5
CCCOH	$CCCOH$	1	0.3
NCCOH	$NCCOH$	1	0.3
NCOTH	$NCOTH$	1	0.3
CCNUE	$CCNUE$	1	0.03

Table 4.3: Model nuisance parameters. Prior values and errors.

### CCQE axial mass

As explained in subsection 1.3.1 the prediction of CCQE cross section is described with a set of form factors. Two of them: axial-vector ( $F_A$ ) and pseudoscalar ( $F_M$ ) form factors depend on axial mass  $M_A^{CCQE}$  (see equations 1.10-1.11).

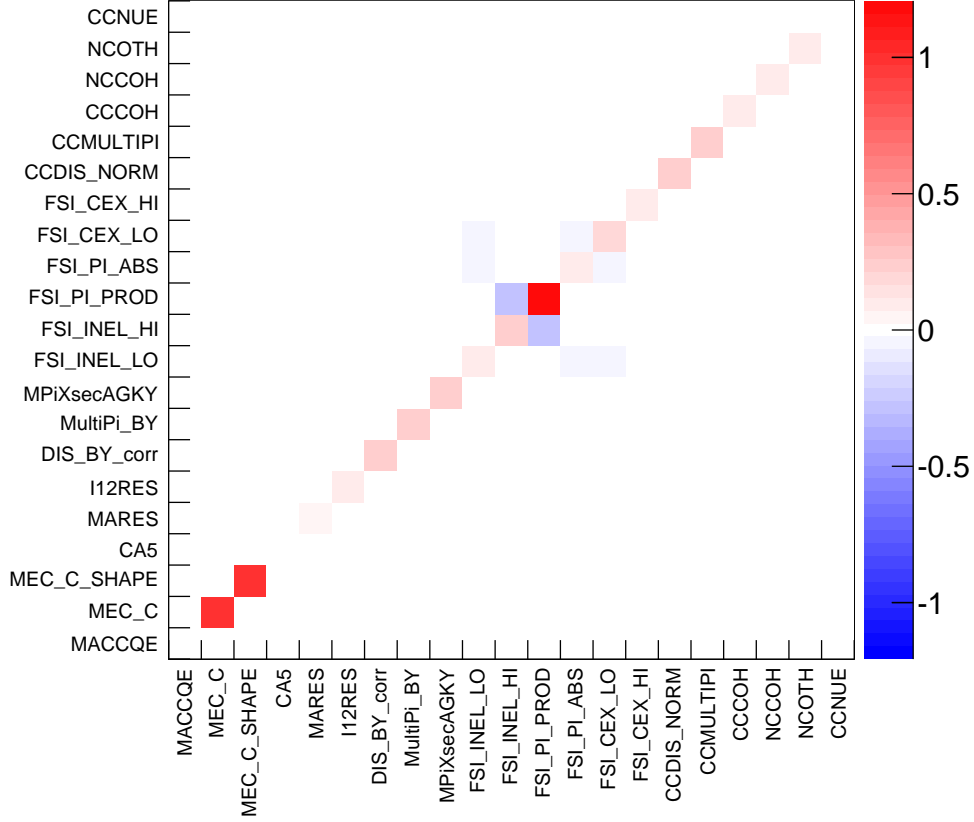


Figure 4.8: Input model nuisance parameters covariance matrix.

### MEC on carbon

Meson exchange current (MEC) interaction is described in subsection 1.11. Two separate parameters are used to characterise MEC interactions on carbon which is the dominant component of FGD1 material. First parameter  $MEC_C$  is a normalisation of all MEC interactions on carbon. Second parameter  $MEC_C^{shape}$  is introduced due to the fact that 2p2h interaction can generally occur in two regions of  $q_3, q_0$  phase-space: MEC region and nucleon-nucleon correlations NN region (see Fig. 1.6 in subsection 1.3.7).  $MEC_C^{shape}$  affects the differential 2p2h cross-section in terms of muon kinematics while keeping the total 2p2h normalisation at each neutrino energy fixed. The nominal value 1 of this parameter corresponds to only MEC region being taken into account.

### Resonant interaction parameters

As explained in subsection 1.3.2 the resonant interactions in NEUT Monte Carlo generator are described with three parameters: the axial mass  $M_A^{RES}$ , the axial form factor  $C_5^A$  and the scaling parameter  $I_{1/2}$  of nonresonant background contributing to single pion production.

### Deep inelastic scattering parameters

DIS interaction and its treatment in NEUT is described in subsection 1.3.3. Two basic DIS parameters are normalising factors:  $CCMULTIPI$  and  $CCDIS_{norm}$  which scale DIS in two hadronic invariant mass regions  $W$  ( $1.3 \text{ GeV}/c^2 < W < 2 \text{ GeV}/c^2$  and  $W > 2 \text{ GeV}/c^2$ , respectively). Other two parameters ( $MultiPi_{BY}$ ,  $DIS_{BY\ corr}$ ) are related to Bodek-Yang (BY) corrections applied to GRV98 PDFs. The uncertainty of these corrections is parametrised as the difference between cross section obtained with the GRV98 PDFs with BY modifications and cross section obtained with the unmodified GRV98. This parametrisation is applied separately in two hadronic invariant mass regions. The last DIS parameter is  $MPiXsecAGKY$  which plays significant role only for low  $W$  region. It is introduced due to AGKY model of multiple pion production which has been implemented in NEUT.

### Neutrino-nucleus coherent interaction parameters

Single pion production might occur in coherent neutrino interaction on nucleus.  $CCCOH$  parameter scales the CC coherent single charged pion production total cross section.  $NCCOH$  parameter scales the NC coherent single  $\pi^0$  production total cross section.

### $\nu_e, \bar{\nu}_e$ interactions normalisation

All CC  $\nu_e$  and CC  $\bar{\nu}_e$  interactions are additionally scaled by a single normalisation parameter:  $CCNUE$ .

### NC other normalisation

$NCOTH$  parameter scales all NC interactions other than single pion production. That includes mostly NC DIS.

### Final state interactions parameters

Importance of the final state interactions (FSI) is explained in subsection 1.3.8. Six parameters are introduced to scale probabilities of different FSI processes. They are summarised in Table 4.4.

Name	Description	Momentum region (MeV/c)
$FSI_{INEL}^{LO}$	Quasielastic pion scattering (low energy)	$< 500$
$FSI_{INEL}^{HI}$	Quasielastic pion scattering (high energy)	$> 400$
$FSI_{CEX}^{LO}$	Single charge exchange (low energy)	$< 500$
$FSI_{CEX}^{HI}$	Single charge exchange (high energy)	$> 400$
$FSI_{PI\ PROD}$	Pion production	$> 400$
$FSI_{PI\ ABS}$	Pion absorption	$< 500$

Table 4.4: FSI parameters.

### 4.3. Flux systematic uncertainty

As explained in the beginning of Chapter 3, the cross section is extracted for a certain neutrino flux. Thus the flux systematic uncertainty must be included in the error propagation of the cross section. The T2K beam group provides flux covariance matrices for various (anti)neutrino flavours both for near and far detector. For Author's analysis the relevant information is about  $\nu_\mu$ ,  $\bar{\nu}_\mu$ ,  $\nu_e$  and  $\bar{\nu}_e$  flux at near detector ND280 for RHC runs. The corresponding covariance matrix is presented in Fig. 4.9. Flux is divided into 5  $\nu_\mu$ , 11  $\bar{\nu}_\mu$ , 2  $\nu_e$  and 1  $\bar{\nu}_e$  energy regions which are reported explicitly in Table 4.5.

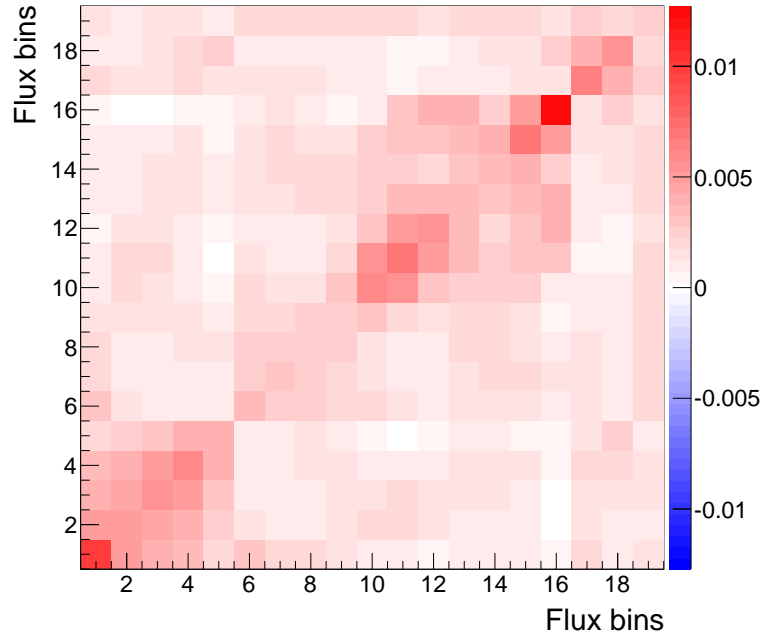


Figure 4.9: Normalised covariance matrix for  $\nu_\mu$ ,  $\bar{\nu}_\mu$ ,  $\nu_e$  and  $\bar{\nu}_e$  flux.

Bin index	$E$ min [GeV]	$E$ max [GeV]	flavour
1	0	0.7	$\nu_\mu$
2	0.7	1	$\nu_\mu$
3	1	1.5	$\nu_\mu$
4	1.5	2.5	$\nu_\mu$
5	2.5	30	$\nu_\mu$
6	0	0.4	$\bar{\nu}_\mu$
7	0.4	0.5	$\bar{\nu}_\mu$
8	0.5	0.6	$\bar{\nu}_\mu$
9	0.6	0.7	$\bar{\nu}_\mu$
10	0.7	1	$\bar{\nu}_\mu$
11	1	1.5	$\bar{\nu}_\mu$
12	1.5	2.5	$\bar{\nu}_\mu$
13	2.5	3.5	$\bar{\nu}_\mu$
14	3.5	5	$\bar{\nu}_\mu$
15	5	7	$\bar{\nu}_\mu$
16	7	30	$\bar{\nu}_\mu$
17	0	2.5	$\nu_e$
18	2.5	30	$\nu_e$
19	0	30	$\bar{\nu}_e$

Table 4.5: Flux binning in (anti)neutrino energy.

# Chapter 5

## Cross section extraction method

The differential cross section is extracted with the binned likelihood fit method. The nominal Monte Carlo is parametrised and fitted to data, with some parameters corresponding to the signal cross section. The first crucial step in this procedure is a choice of binning in which predicted MC event rate is compared with data and a choice of binning in which the cross-section will be reported. It is described in details in section 5.1. The principles of the likelihood fit method, its implementation, necessary input and cross section calculation are discussed in section 5.2. The method is validated in fake data studies presented in section 5.3.

### 5.1. Phase-space binning

The main result of presented analysis is the double-differential cross-section  $\frac{d^2\sigma}{dp_\mu d\cos\theta_\mu}$  in  $\mu^+$  kinematic variables. Thus a suitable 2D binning must be chosen - it is important to take into account such factors as available statistics, resolution of kinematic variables reconstruction and signal selection efficiency.

In this analysis the cross-section will be reported in true physical variables. What is measured directly in a detector are reconstructed variables. Therefore, one can think of a *true phase-space* and a *reconstructed phase-space* with *true bins* and *reco bins*, respectively. In general, the *true* and *reco binning* might be different. The differential cross-section in the  $i$ -th bin of a *true phase-space* is proportional to the number of selected signal events  $N_i$  in this bin. The relation with *reco bins* may be expressed as:

$$\frac{d\sigma}{dx_i} \sim N_i = \sum_j^{\text{recobins}} N_j t_{ij}^{\text{det}},$$

where  $N_j$  is the number of selected signal events in the  $j$ -th *reco bin* and  $t_{ij}^{\text{det}}$  - the transfer matrix (known from the nominal MC).

### 5.1.1. Reconstructed phase-space binning

In this subsection the *reco binning* choice for all signal and background samples is discussed. The crucial point is to consider data statistics available in the experiment. For very small statistics the data in a given bin may fluctuate to zero, which could drive to unphysical result. The expected number of data events  $\mu_{MC}$  in a *reco bin* is the event rate predicted in Monte Carlo and normalised to data POT. Assuming Poisson distribution the probability of getting 0 data events is:

$$P_0(\mu_{MC}) = e^{-\mu_{MC}}$$

For this analysis it was decided that in each *reco bin* such probability should be below  $10^{-5}$ , which means that in each bin  $\mu_{MC}$  has to be greater than 11.5.

At first the optimization of the *reco binning* for CC1TPC $\pi^-$  signal sample will be presented. A starting point was to choose a 2D binning that would allow for straightforward cross-section projection from 2D distribution to two 1D distributions. Such binning should be *regular* i.e. form a grid  $n \times m$ , which is projected to  $n$  bins in one dimension or  $m$  bins in other dimension.

These conditions - a *regular* binning with  $\mu_{MC} > 11.5$  - led to initial binning pattern that was a foundation for both *true* and *reconstructed phase-space binning*. It is presented in Table 5.1.

This initial binning has quite different event rate in different bins as can be seen in Fig. 5.1. It is possible to split initial pattern into finer *reco binning* for the CC1TPC $\pi^-$  signal sample and still satisfy condition for  $\mu_{MC} > 11.5$  in each *reco bin*. Additionally, out of phase-space (OOPS) bins must be included. The final *reco binning* scheme for the CC1TPC $\pi^-$  signal sample is presented in Tables 5.2-5.3 and in Fig. 5.2. Altogether there are 31 bin within the restricted phase-space and 4 OOPS bins:

- $p_{\mu \text{ reco}} < 200 \text{ MeV}/c$ ,
- $p_{\mu \text{ reco}} > 30000 \text{ MeV}/c$ ,
- $\cos\theta_{\mu \text{ reco}} < 0.74$ ,
- bad  $\pi^-$  kinematics bin (i.e.  $p_{\pi \text{ reco}} < 100 \text{ MeV}/c$ ,  $p_{\pi \text{ reco}} > 3000 \text{ MeV}/c$  or  $\cos\theta_{\pi \text{ reco}} < 0.32$ ).

For events with the bad  $\pi^-$  kinematics  $\cos\theta_{\mu \text{ reco}}$  was artificially set to  $> 1$  to assign them to the last of the OOPS bins in order to treat them separately in 2-dimensional binning scheme.

$p_\mu$ min [MeV/c]	$p_\mu$ max [MeV/c]	$\cos\theta_\mu$ min	$\cos\theta_\mu$ max
200	500	0.74	0.88
500	800	0.74	0.88
800	1100	0.74	0.88
1100	30000	0.74	0.88
200	500	0.88	0.94
500	800	0.88	0.94
800	1100	0.88	0.94
1100	30000	0.88	0.94
200	500	0.94	0.97
500	800	0.94	0.97
800	1100	0.94	0.97
1100	30000	0.94	0.97
200	500	0.97	1
500	800	0.97	1
800	1100	0.97	1
1100	30000	0.97	1

Table 5.1: **Initial binning.** A regular pattern allows for simple projection into two 1D distributions.

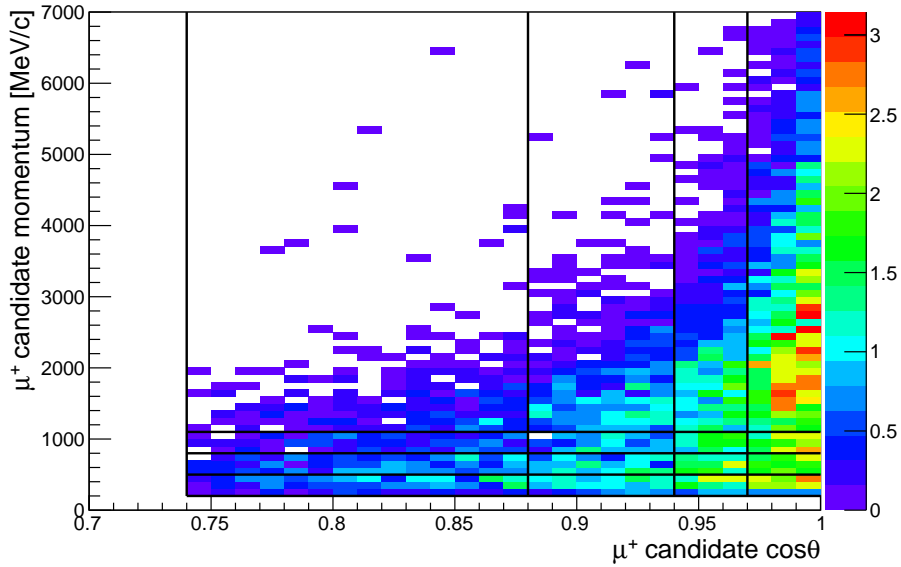


Figure 5.1: **CC1TPC $\pi^-$  signal selection.** Event rate distribution in restricted reconstructed phase-space:  $p_{\mu reco}$  versus  $\cos\theta_{\mu reco}$ . Black lines mark the initial binning scheme.

$p_{\mu \text{ reco}} \text{ min [MeV/c]}$	$p_{\mu \text{ reco}} \text{ max [MeV/c]}$	$\cos\theta_{\mu \text{ reco}} \text{ min}$	$\cos\theta_{\mu \text{ reco}} \text{ max}$
200	500	0.74	0.88
500	800	0.74	0.88
800	1100	0.74	0.88
1100	1500	0.74	0.88
1500	30000	0.74	0.88
200	500	0.88	0.94
500	800	0.88	0.94
800	1100	0.88	0.94
1100	1500	0.88	0.94
1500	2000	0.88	0.94
2000	30000	0.88	0.94
200	500	0.94	0.97
500	800	0.94	0.97
800	1100	0.94	0.97
1100	1500	0.94	0.97
1500	2000	0.94	0.97
2000	2500	0.94	0.97
2500	30000	0.94	0.97
200	500	0.97	1
500	800	0.97	1
800	1100	0.97	1
1100	1500	0.97	1
1500	2000	0.97	0.99
2000	2500	0.97	0.99
2500	3500	0.97	0.99
3500	5000	0.97	0.99
5000	30000	0.97	1
1500	2000	0.99	1
2000	2500	0.99	1
2500	3500	0.99	1
3500	5000	0.99	1

Table 5.2: *Reco binning for CC1TPC $\pi^-$  signal sample (part 1).*

$p_{\mu \text{ reco}}$ min [MeV/c]	$p_{\mu \text{ reco}}$ max [MeV/c]	$\cos\theta_{\mu \text{ reco}}$ min	$\cos\theta_{\mu \text{ reco}}$ max
0	200	-1	1
200	30000	-1	0.74
30000	$10^6$	-1	1
0	$10^6$	1	3

Table 5.3: **Reco binning for CC1TPC $\pi^-$  signal sample** (part 2 - OOPS bins). The last OOPS bin corresponds to events with bad pion kinematics (see explanation in the text).

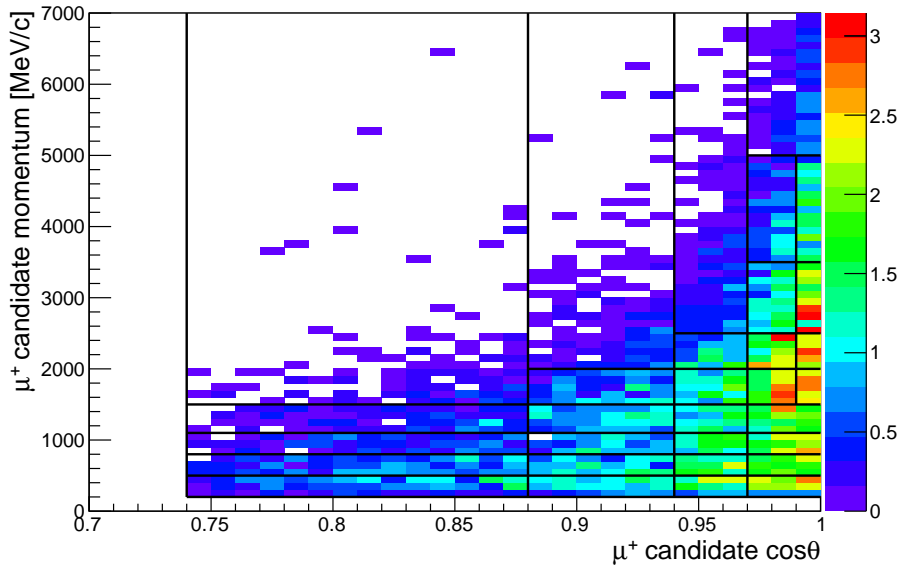


Figure 5.2: **CC1TPC $\pi^-$  signal selection.** Event rate distribution in restricted reconstructed phase-space:  $p_{\mu \text{ reco}}$  versus  $\cos\theta_{\mu \text{ reco}}$ . Black lines mark the eventual reco binning scheme for CC1TPC $\pi^-$  signal sample.

The second signal sample - CC1FGD $\pi^-$  - has much smaller statistics and thus a coarser binning has to be applied. The binning scheme for that sample is presented in Table 5.4 and in Fig. 5.3 (in order to better visualise the difference in statistics between selected samples the same color scale is used as in Fig. 5.2). Altogether there are 5 bins within the restricted phase-space. Each of those bins corresponds to a group of merged reco bins from CC1TPC $\pi^-$  signal sample binning. Additional 4 OOPS bins are the same for both signal samples.

$p_{\mu \text{ reco}} \text{ min [MeV/c]}$	$p_{\mu \text{ reco}} \text{ max [MeV/c]}$	$\cos\theta_{\mu \text{ reco}} \text{ min}$	$\cos\theta_{\mu \text{ reco}} \text{ max}$
200	30000	0.74	0.88
200	1100	0.88	0.97
1100	30000	0.88	0.97
200	1500	0.97	1
1500	30000	0.97	1
0	200	-1	1
200	30000	-1	0.74
30000	$10^6$	-1	1
0	$10^6$	1	3

Table 5.4: **Reco binning** for **CC1FGD $\pi^-$**  signal sample. The last OOPS bin corresponds to events with bad pion kinematics.

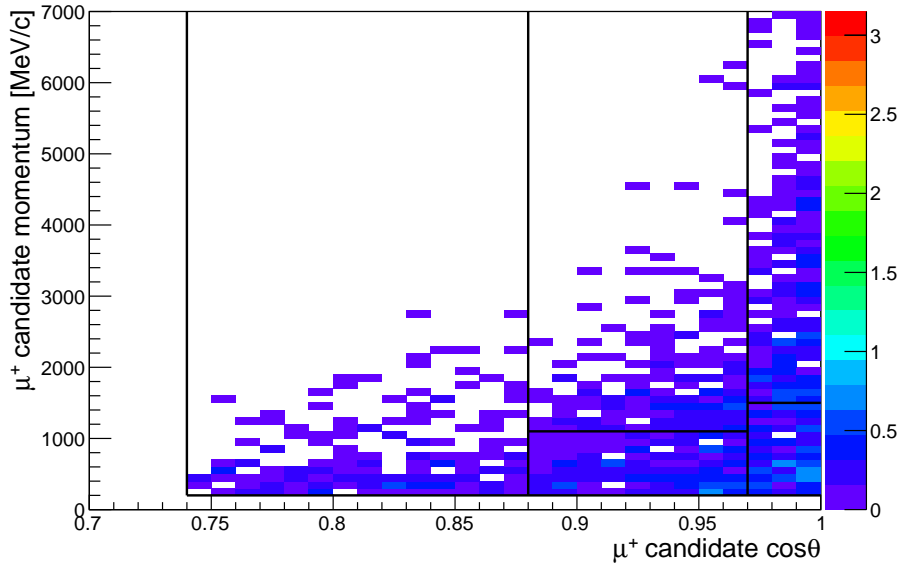


Figure 5.3: **CC1FGD $\pi^-$**  signal selection. Event rate distribution in restricted reconstructed phase-space:  $p_{\mu \text{ reco}}$  versus  $\cos\theta_{\mu \text{ reco}}$ . Black lines mark the eventual reco binning scheme for CC1FGD $\pi^-$  signal sample.

The *reco binning* for the Reversed Z-range cut background sample is presented in Table 5.5 and in Fig. 5.4. The  $\mu^+$  candidate is mostly a misidentified  $\pi^+$  from  $\nu_\mu$  CC background. Thus, the kinematical distributions of  $\mu^+$  candidate are quite different than for the signal samples and the binning scheme must correspond to that. In particular, for  $\cos\theta_{\mu reco} > 0.97$  region there are only 4 bins in this background sample, while for CC1TPC $\pi^-$  signal sample the event rate was sufficient to divide that part of phase-space into 13 bins. Altogether for Reversed Z-range cut background sample there are 18 *reco bins* plus 4 OOPS bins.

$p_{\mu reco}$ min [MeV/c]	$p_{\mu reco}$ max [MeV/c]	$\cos\theta_{\mu reco}$ min	$\cos\theta_{\mu reco}$ max
200	500	0.74	0.82
500	800	0.74	0.82
800	1100	0.74	0.88
1100	1500	0.74	0.88
1500	30000	0.74	0.88
200	500	0.82	0.88
500	800	0.82	0.88
200	500	0.88	0.94
500	800	0.88	0.94
800	1500	0.88	0.94
1500	30000	0.88	0.94
200	800	0.94	0.97
800	1500	0.94	0.97
1500	30000	0.94	0.97
200	800	0.97	1
800	1500	0.97	1
1500	2500	0.97	1
2500	30000	0.97	1
0	200	-1	1
200	30000	-1	0.74
30000	$10^6$	-1	1
0	$10^6$	1	3

Table 5.5: ***Reco binning*** for the Reversed Z-range cut background sample. The last OOPS bin corresponds to events with bad pion kinematics.

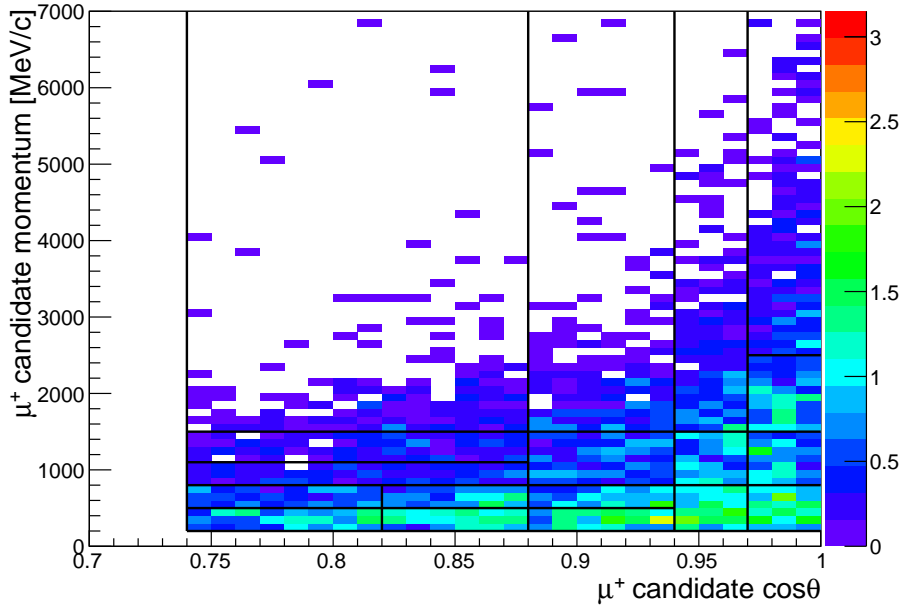


Figure 5.4: **Reversed Z-range cut background selection.** Event rate distribution in restricted *reconstructed phase-space*:  $p_{\mu reco}$  versus  $\cos\theta_{\mu reco}$ . Black lines mark the eventual *reco binning* scheme for Reversed Z-range cut background sample.

The CC-other background sample has the biggest statistics and therefore the proposed binning is much finer than for other samples as can be seen in Fig. 5.5. Altogether

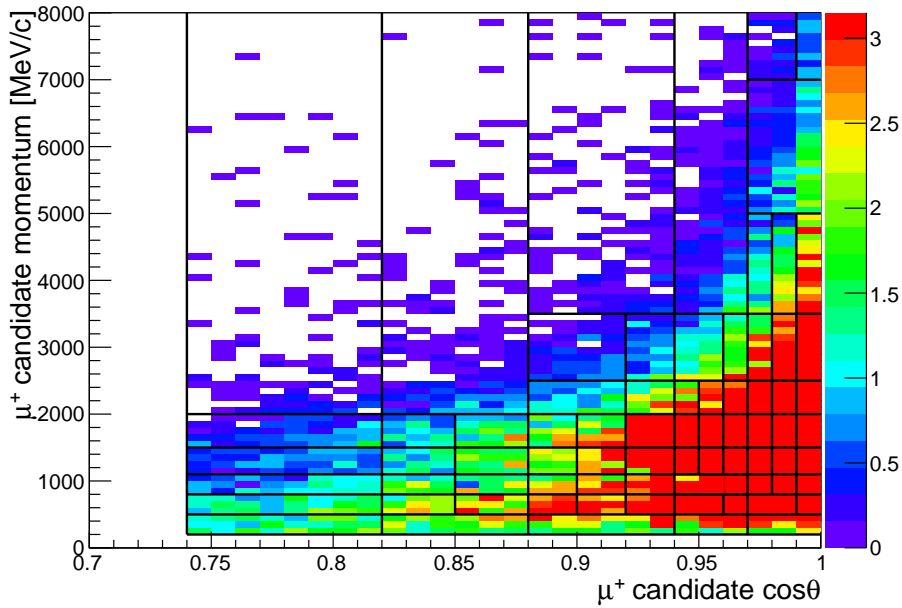


Figure 5.5: **CC-other background selection.** Event rate distribution in restricted *reconstructed phase-space*:  $p_{\mu reco}$  versus  $\cos\theta_{\mu reco}$ . Black lines mark the eventual *reco binning* scheme for CC-other background sample.

there are 74 *reco bins* plus 3 OOPS bins - there is no separate bin for events with bad  $\pi^-$  kinematics. Lack of restrictions on  $\pi^-$  candidate kinematics is due to the CC-other selection cuts, which don't require presence of  $\pi^-$  candidate in the first place. *Reco binning* for CC-other background sample is presented in Tables 5.6-5.8.

$p_{\mu \text{ reco}}$ min [MeV/c]	$p_{\mu \text{ reco}}$ max [MeV/c]	$\cos\theta_{\mu \text{ reco}}$ min	$\cos\theta_{\mu \text{ reco}}$ max
200	500	0.74	0.82
500	800	0.74	0.82
800	1100	0.74	0.82
1100	1500	0.74	0.82
1500	2000	0.74	0.82
2000	30000	0.74	0.82
200	500	0.82	0.88
500	800	0.82	0.85
800	1100	0.82	0.85
1100	1500	0.82	0.85
1500	2000	0.82	0.85
2000	30000	0.82	0.88
500	800	0.85	0.88
800	1100	0.85	0.88
1100	1500	0.85	0.88
1500	2000	0.85	0.88
200	500	0.88	0.94
500	800	0.88	0.9
800	1100	0.88	0.9
1100	1500	0.88	0.9
1500	2000	0.88	0.9
2000	2500	0.88	0.92
2500	3500	0.88	0.92
3500	30000	0.88	0.94
500	800	0.9	0.92
800	1100	0.9	0.92
1100	1500	0.9	0.92
1500	2000	0.9	0.92

Table 5.6: *Reco binning* for CC-other background sample (part 1).

$p_{\mu \text{ reco}} \text{ min [MeV/c]}$	$p_{\mu \text{ reco}} \text{ max [MeV/c]}$	$\cos\theta_{\mu \text{ reco}} \text{ min}$	$\cos\theta_{\mu \text{ reco}} \text{ max}$
500	800	0.92	0.94
800	1100	0.92	0.94
1100	1500	0.92	0.94
1500	2000	0.92	0.94
2000	2500	0.92	0.94
2500	3500	0.92	0.94
200	500	0.94	0.97
500	800	0.94	0.96
800	1100	0.94	0.97
1100	1500	0.94	0.95
1500	2000	0.94	0.95
2000	2500	0.94	0.95
2500	3500	0.94	0.96
3500	30000	0.94	0.97
1100	1500	0.95	0.96
1500	2000	0.95	0.96
2000	2500	0.95	0.96
500	800	0.96	0.97
1100	1500	0.96	0.97
1500	2000	0.96	0.97
2000	2500	0.96	0.97
2500	3500	0.96	0.97
200	500	0.97	1
500	800	0.97	0.99
800	1100	0.97	0.98
1100	1500	0.97	0.98
1500	2000	0.97	0.98
2000	2500	0.97	0.98
2500	3500	0.97	0.98
3500	5000	0.97	0.98
5000	7000	0.97	1
7000	30000	0.97	0.99

Table 5.7: *Reco binning* for CC-other background sample (part 2).

$p_{\mu \text{ reco}} \text{ min [MeV/c]}$	$p_{\mu \text{ reco}} \text{ max [MeV/c]}$	$\cos\theta_{\mu \text{ reco}} \text{ min}$	$\cos\theta_{\mu \text{ reco}} \text{ max}$
800	1100	0.98	0.99
1100	1500	0.98	0.99
1500	2000	0.98	0.99
2000	2500	0.98	0.99
2500	3500	0.98	0.99
3500	5000	0.98	0.99
500	800	0.99	1
800	1100	0.99	1
1100	1500	0.99	1
1500	2000	0.99	1
2000	2500	0.99	1
2500	3500	0.99	1
3500	5000	0.99	1
7000	30000	0.99	1
0	200	-1	1
200	30000	-1	0.74
30000	$10^6$	-1	1

Table 5.8: *Reco binning* for CC-other background sample (part 3).

### 5.1.2. True phase-space binning

As it was already mentioned, the differential cross-section will be reported in true  $\mu^+$  kinematical variables:  $p_{\mu \text{ true}}$  and  $\cos\theta_{\mu \text{ true}}$ . One of the important conditions for the *true phase-space binning* is that each bin range  $[x_{\text{true}}^{\text{min}}, x_{\text{true}}^{\text{max}}]$  should correspond to similar range  $[x_{\text{reco}}^{\text{min}}, x_{\text{reco}}^{\text{max}}]$  in the *reco phase-space*. Initially, the *true phase-space binning* was set to be identical with the *reco binning* for CC1TPC $\pi^-$  signal sample. Such binning scheme however was not entirely satisfying with respect to *true-reco* correspondence and several *true bins* were merged. Additionally, the distribution of the signal selection efficiency in each *true bin* should be possibly flat. These conditions are discussed in paragraphs below. The eventual *true phase-space binning* is presented in Table 5.9. Altogether there are 29 bins within the restricted phase-space and 3 OOPS bins. In this case there is no need for separate OOPS bin for  $p_{\mu \text{ true}} > 30 \text{ GeV/c}$ , since there are no such events. Similarly to *reco binning*, events with bad true  $\pi^-$  kinematics have  $\cos\theta_{\mu \text{ true}} > 1$  artificially assigned in order to treat them separately in 2D binning scheme.

If the *true phase-space* binning is too fine the detector smearing will lead to strong

Bin index	$p_{\mu \text{ true}} \text{ min [MeV/c]}$	$p_{\mu \text{ true}} \text{ max [MeV/c]}$	$\cos\theta_{\mu \text{ true}} \text{ min}$	$\cos\theta_{\mu \text{ true}} \text{ max}$
1	200	500	0.74	0.88
2	500	800	0.74	0.88
3	800	1100	0.74	0.88
4	1100	30000	0.74	0.88
5	200	500	0.88	0.94
6	500	800	0.88	0.94
7	800	1100	0.88	0.94
8	1100	1500	0.88	0.94
9	1500	30000	0.88	0.94
10	200	500	0.94	0.97
11	500	800	0.94	0.97
12	800	1100	0.94	0.97
13	1100	1500	0.94	0.97
14	1500	2000	0.94	0.97
15	2000	2500	0.94	0.97
16	2500	30000	0.94	0.97
17	200	500	0.97	1
18	500	800	0.97	1
19	800	1100	0.97	1
20	1100	1500	0.97	1
21	1500	2000	0.97	0.99
22	2000	2500	0.97	0.99
23	2500	3500	0.97	0.99
24	3500	5000	0.97	0.99
25	5000	30000	0.97	1
26	1500	2000	0.99	1
27	2000	2500	0.99	1
28	2500	3500	0.99	1
29	3500	5000	0.99	1
30	0	200	-1	1
31	200	30000	-1	0.74
32	0	30000	1	3

Table 5.9: *True binning* for  $CC1\pi^-$  signal events. Last OOPS bin corresponds to events with bad pion kinematics.

correlations between *true bins* (since neighbouring *true bins* would correspond to roughly the same region in *reconstructed phase-space*<sup>1</sup>). In order to avoid this a good rule of thumb is to check that for each  $p_{\mu \text{ true}}$  ( $\cos\theta_{\mu \text{ true}}$ ) bin its width is bigger than RMS of  $p_{\mu \text{ reco}} - p_{\mu \text{ true}}$  ( $\cos\theta_{\mu \text{ reco}} - \cos\theta_{\mu \text{ true}}$ ) distribution. The results of such check are presented in Table 5.10. Each bin is wider than the corresponding “Reco – True” RMS for both  $\mu^+$  momentum and  $\cos\theta$ . It must be noted that in some cases single events with bad variable reconstruction were omitted in RMS calculation - those events always constituted less than 2% of event rate in a considered bin.

Another important feature of the *true phase-space binning* is an uniform distribution of the signal selection efficiency in each bin. In the top plot of Fig. 5.6 the selection efficiency for the restricted phase-space is presented. The contribution of signal events from both signal and background samples is considered. The signal events distribution prior to selection is presented in the bottom plot (the nominal MC event rate is shown, not normalised to data POT). One can see that within most bins the efficiency distribution is rather uniform, with the exception of high angle region. A basic solution to improve this feature would be to divide considered bins into smaller ones, but in the presented case this cannot be achieved due to the limited statistics.

---

<sup>1</sup>Consider an extreme example of two true momentum bins: 999-1000 MeV/c and 1000-1001 MeV/c. If the momentum reconstruction resolution is 10% then both bins would correspond to roughly the same range of 900-1100 MeV/c in reconstructed momentum.

Bin index	Bin width [MeV/c]	RMS	
		$p_{\mu \text{ reco}} - p_{\mu \text{ true}}$ [MeV/c]	Bin width ( $\cos\theta$ )
1	300	76.6	0.14
2	300	79.1	0.14
3	300	227	0.14
4	28900	514	0.14
5	300	56	0.06
6	300	48.5	0.06
7	300	225	0.06
8	400	246	0.06
9	28500	445	0.06
10	300	39.8	0.03
11	300	75.8	0.03
12	300	109	0.03
13	400	199	0.03
14	500	345	0.03
15	500	350	0.03
16	27500	1490	0.03
17	300	19	0.03
18	300	90.6	0.03
19	300	67.2	0.03
20	400	181	0.03
21	500	353	0.02
22	500	389	0.02
23	1000	649	0.02
24	1500	1300	0.02
25	25000	3210	0.03
26	500	266	0.01
27	500	484	0.01
28	1000	719	0.01
29	1500	1120	0.01

Table 5.10: **True binning for CC1 $\pi^-$  signal events.** Comparison of bin width and RMS “Reco – True” for  $\mu^+$  kinematical variables.

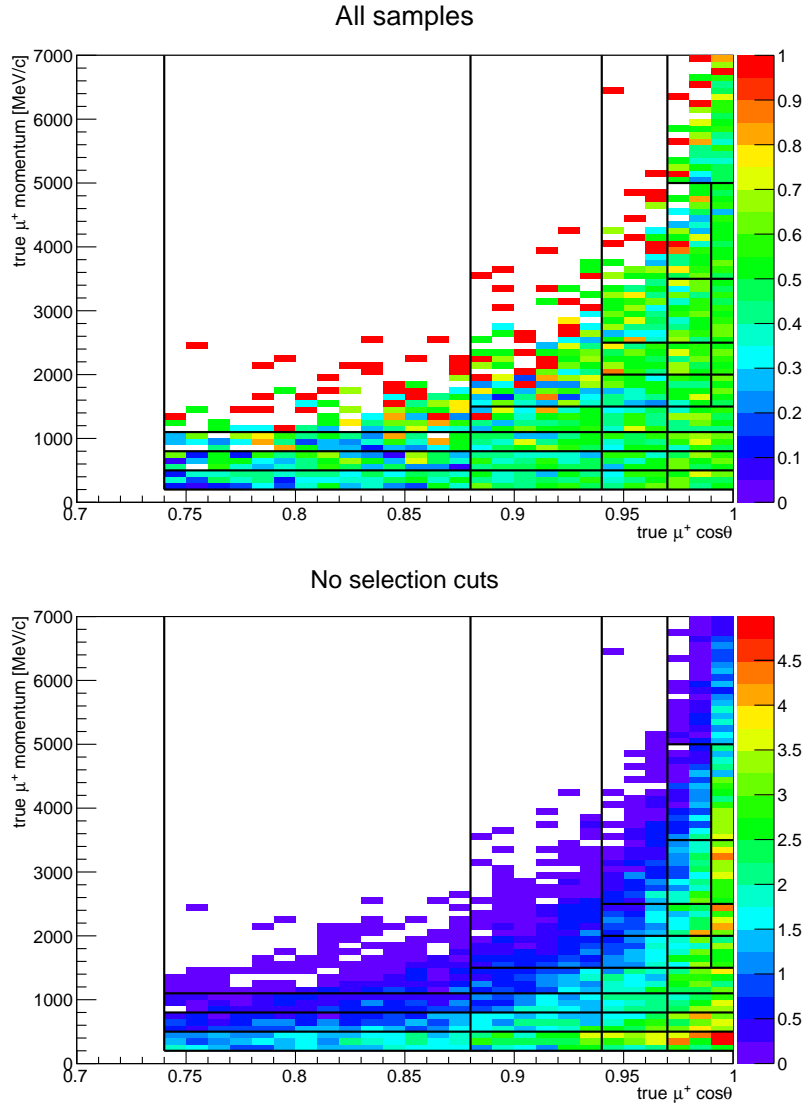


Figure 5.6: Top: Efficiency distribution in *true restricted phase-space*:  $p_{\mu \text{ true}}$  vs.  $\cos\theta_{\mu \text{ true}}$ . Black lines mark the eventual *true binning* scheme. Contributions of all signal and background samples are included. Bottom: Signal events distributions in *true restricted phase-space* prior to any selection cut.

## 5.2. Likelihood Fitter

In the presented analysis the cross section is extracted by the likelihood fit method. The general description of this approach is given in subsections 5.2.1-5.2.2. The software tool applied for the fit is *Super-xslhFitter* [129] (later referred to as the Fitter) developed by Andrew Cudd and used also in other T2K analyses. The Fitter performs two major operations: it fits MC distribution to data (subsection 5.2.3) and extracts the cross section with properly propagated error (subsection 5.2.4).

### 5.2.1. Maximum likelihood method

Consider a probability density function (p.d.f.)  $f(x; \theta)$  which describes the distribution of a certain variable  $x$  and is parametrised with a set of parameters  $\theta$ . Suppose that the exact values of some parameters are unknown and one wants to estimate them by comparing the distribution predicted by  $f(x; \theta)$  with the real data. This can be done with the maximum likelihood fit method.

Consider  $n$  measurements of  $x$ :  $x_1, x_2, \dots, x_n$ . The probability for the  $i$ -th measurement to be in the range  $[x_i, x_i + dx_i]$  is  $f(x_i; \theta)dx_i$ . If each measurement is independent then the probability of obtaining a given set of  $n$  results is expressed as:

$$P(x_i \text{ in } [x_i, x_i + dx_i] \text{ for all } i) = \prod_{i=1}^n f(x_i; \theta)dx_i.$$

If the form of p.d.f. and parameters' values are accurate the above quantity should be high for the measured data. Inversly, if the parameters' values are not accurate this probability should be low. Note that  $dx_i$  forms do not depend on the parameters  $\theta$  and hence the same argumentation can be applied to the following quantity:

$$L(\theta) = \prod_{i=1}^n f(x_i; \theta),$$

which is called the likelihood function [125]. The best estimation of parameters  $\theta$  corresponds to the maximal value of  $L(\theta)$ . It is often more convenient to use logarithm of the likelihood function. Since logarithm is a monotonically increasing function, finding the maximal value of  $\log L(\theta)$  is equivalent to finding maximal  $L(\theta)$ . The advantage of this approach is that instead of optimising the product one can optimise the sum. Thus one can express the log-likelihood function as:

$$\log L(\theta) = \sum_{i=1}^n \log f(x_i; \theta).$$

### 5.2.2. Maximum likelihood for binned data

In case of large data samples, including  $\log f(x_i; \theta)$  for all measurement results would make the log-likelihood function difficult to calculate. Instead, one can divide the phase-space into  $N$  bins and take into account the entries rate  $n_j$  per  $j$ -th bin. In each bin the expected entries rate is:

$$\nu_j(\theta) = n_{tot} \int_{x_j^{min}}^{x_j^{max}} f(x; \theta)dx,$$

where  $n_{tot}$  is the total number of all entries,  $x_j^{min}$  and  $x_j^{max}$  are limits of the  $j$ -th bin. One can think of a single measurement of an  $N$ -dimensional vector  $\mathbf{n} = (n_1, \dots, n_N)$  which is represented as a histogram. For such measurement the p.d.f. is obtained from a multinomial distribution:

$$F(\mathbf{n}; \boldsymbol{\nu}) = \frac{n_{tot}!}{n_1! \dots n_N!} \left( \frac{\nu_1}{n_{tot}} \right)^{n_1} \dots \left( \frac{\nu_N}{n_{tot}} \right)^{n_N},$$

where  $\boldsymbol{\nu} = (\nu_1(\theta), \dots, \nu_N(\theta))$  and the probability to be in bin  $j$  is the ratio of the expected entries rate  $\nu_j$  to the total number of entries  $n_{tot}$ .

Additionally, one can treat the total number of entries  $n_{tot}$  as a Poisson distributed random variable with mean  $\nu_{tot}$ . In such case the expected entries rate in  $j$ -th bin is expressed as:

$$\nu_j(\nu_{tot}, \theta) = \nu_{tot} \int_{x_j^{min}}^{x_j^{max}} f(x; \theta) dx$$

and the p.d.f. is the product of Poisson and multinomial distributions:

$$F(\mathbf{n}; \boldsymbol{\nu}) = \frac{\nu_{tot}^{n_{tot}} e^{-\nu_{tot}}}{n_{tot}!} \frac{n_{tot}!}{n_1! \dots n_N!} \left( \frac{\nu_1}{\nu_{tot}} \right)^{n_1} \dots \left( \frac{\nu_N}{\nu_{tot}} \right)^{n_N}.$$

This gives the log-likelihood function expressed as:

$$\log L(\nu_{tot}, \theta) = -\nu_{tot} + \sum_{j=1}^N n_j \log \nu_j(\nu_{tot}, \theta),$$

where the terms not depending on the parameters were omitted [126].

By using the data  $\mathbf{n}$  and expected entries rates  $\boldsymbol{\nu}$  it is possible to construct a test statistic for a goodness-of-fit studies. Consider the ratio

$$\lambda = \frac{F(\mathbf{n}; \boldsymbol{\nu})}{F(\mathbf{n}; \mathbf{n})}, \quad (5.1)$$

which for Poisson distributed data can be brought to the form:

$$\lambda = e^{n_{tot} - \nu_{tot}} \prod_{j=1}^N \left( \frac{\nu_j}{n_j} \right)^{n_j}.$$

From that one can obtain a quantity:

$$-2 \log \lambda = 2 \sum_{j=1}^N \left( n_j \log \frac{n_j}{\nu_j} + \nu_j - n_j \right), \quad (5.2)$$

which, according to Wilks' theorem, follows a chi-square distribution for  $N - m$  degrees of freedom, where  $m$  is the number of estimated parameters [127, 128]. Note that the  $F(\mathbf{n}; \mathbf{n})$  term in Eq. 5.1 does not depend on parameters of interest. Thus the ratio  $\lambda$  can serve as a likelihood function itself.

### 5.2.3. Likelihood fit implementation

The fit is based on treweighting MC signal events in each bin of the *true phase-space*:

$$N_i^{signal} = c_i N_i^{MC\ signal},$$

where  $i$  runs over the *true phase-space* (PS) bins (which is 2-dimensional in  $\mu^+$  kinematical variables as reported in Tab. 5.9),  $N_i^{signal}$  is the number of selected signal events (proportional to the reported cross section),  $N_i^{MC\ signal}$  is the number of selected signal events in prior nominal MC and  $c_i$  are the main free parameters of the fit, so-called *template parameters*.

The rate of events in *true PS* bins is determined by the *unfolding* method. It uses information from the nominal Monte Carlo where both simulated kinematics of a particle and detector response are generated. This allows to obtain a mapping from the *reconstructed PS* to the *true PS*. Thus the signal and background event rates for the nominal MC in *true PS* bins  $i$  can be expressed as:

$$N_i^{MC\ signal} = \sum_j^{reco} N_j^{MC\ signal} t_{ij}^{det},$$

$$N_i^{MC\ BKG} = \sum_j^{reco} N_j^{MC\ BKG} t_{ij}^{det},$$

where  $j$  runs over bins of reconstructed PS and  $t_{ij}^{det}$  is the transfer matrix. The total number of selected events in  $i$ -th bin is given by:

$$N_i = c_i N_i^{MC\ signal} + N_i^{MC\ BKG}.$$

If all interactions were modelled perfectly in Monte Carlo and there were no systematic uncertainties in the experiment the number of selected events in  $j$ -th bin of reconstructed PS could be calculated as:

$$N_j = \sum_i^{true} N_i (t_{ji}^{det})^{-1} = \sum_i^{true} \left[ c_i N_i^{MC\ signal} + N_i^{MC\ BKG} \right] (t_{ji}^{det})^{-1}.$$

This quantity could be compared to the actual observed number of event  $N_j^{obs}$  and the best agreement between MC predictions and data would be obtained by optimising template parameters  $c_i$ . In reality a set of additional parameters is needed to address the systematic uncertainties. These are so-called *nuisance parameters* which are divided into three groups:

- model parameters  $\vec{s}$  - related to specific interaction and FSI modelling in the nominal MC,

- flux parameters  $f_n$  - normalising flux of different (anti)neutrino flavours in energy bins,
- detector systematic parameters  $r_j^{det}$  - related to detector systematic uncertainty in each bin of reconstructed PS.

Eventually, the fully parametrised number of events in  $j$ -th bin of reconstructed PS is expressed as:

$$N_j = \sum_i^{true} \left[ c_i \left( \prod_s^{model} \omega(s)_i^{signal} \right) N_i^{MC\ signal} + \sum_k^{BKG\ modes} \left( \prod_s^{model} \omega(s)_i^k \right) N_i^{MC\ BKG\ k} \right] r_j^{det} (t_{ji}^{det})^{-1} \sum_n^{E_{\bar{\nu}_\mu} \text{ bins}} w_{in} f_n, \quad (5.3)$$

where  $\omega(s)_i^k$  is the weight function dependent of model parameter  $s$  for the specific interaction topology  $k$  in the  $i$ -th bin of *true PS*,  $w_{in}$  is the weight mapping *true PS* bin to a  $\bar{\nu}_\mu$  energy bin.

One can see that the selected event rate changes proportionally to the values of detector systematic  $r_j^{det}$  and flux  $f_n$  nuisance parameters (nominal value of these parameters is 1). The impact of the model parameters  $\vec{s}$  is not as straightforward.

In principle, one could consider an arbitrary variation of a model parameter and reweight each relevant event in the sample in order to find the new event rate. This approach is however time-consuming if a large number of variations is considered. A solution is to use splines generated with T2KReWeight package [130] prior to the fit. Splines are divided with respect to 9 final state topologies, 10 types of neutrino level interaction and 16 four-momentum transfer  $Q^2$  regions. Thus for each model parameter 1440 splines are prepared. This allows to obtain weight function  $\omega(s)_i^k$  for a specific  $\vec{s}$  variation. An example is presented in Fig. 5.7. In this case the spline is computed for resonant axial mass *MARES*, the topology of interest is a final state with single  $\mu^+$  and single  $\pi^-$ , the relevant type of interaction is  $\bar{\nu}_\mu$  CC resonant and the low  $Q^2$  region is chosen. The spline value indicates how much this particular type of event should be reweighted for a specific value of the model parameter. The exact weight calculation is done for 31 values of the parameter (the nominal one, 15 lower values and 15 higher values). Between these points the weight is linearly interpolated.

The main Fitter mechanism is to fit nominal MC predictions to data by minimising

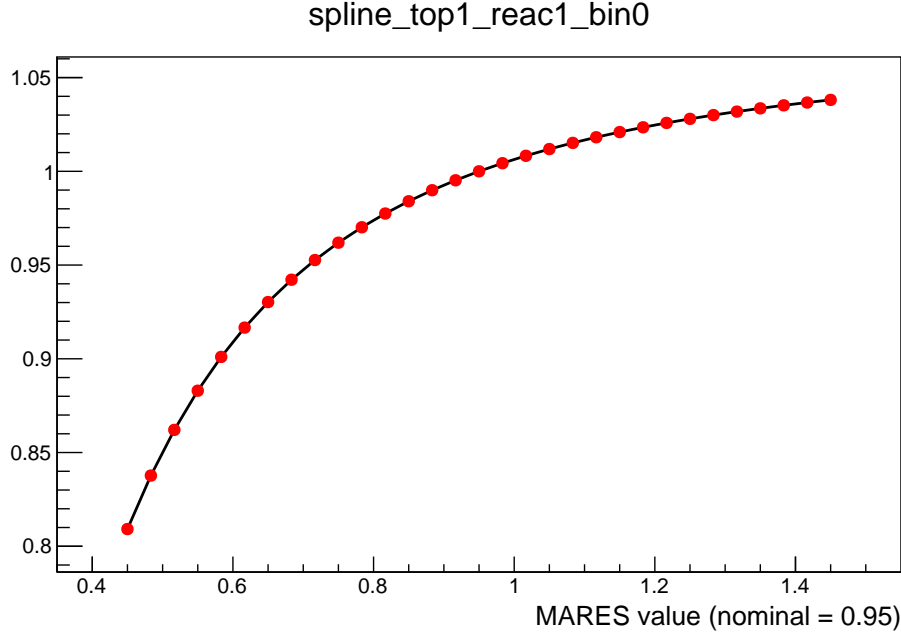


Figure 5.7: One of the splines computed for resonant axial mass *MARES* parameter.

the following likelihood:

$$\chi^2 = \chi_{stat}^2 + \chi_{syst}^2 = \sum_j^{reco} 2 \left( N_j - N_j^{obs} + N_j^{obs} \log \frac{N_j^{obs}}{N_j} \right) + \chi_{syst}^2, \quad (5.4)$$

where  $N_j$  is defined as in Eq. 5.3 and  $N_j^{obs}$  refers to the event rate measured in the experiment. (Note that the statistical term  $\chi_{stat}^2$  has the same form as in Eq. 5.2 and therefore follows chi-square distribution.) The penalty term  $\chi_{syst}^2$  is increasing when nuisance parameters are pulled away from their prior values:

$$\begin{aligned} \chi_{syst}^2 = & (\vec{r}^{det} - \vec{r}_{prior}^{det})(V_{cov}^{det})^{-1}(\vec{r}^{det} - \vec{r}_{prior}^{det}) \\ & + (\vec{f} - \vec{f}_{prior})(V_{cov}^{flux})^{-1}(\vec{f} - \vec{f}_{prior}) \\ & + (\vec{s} - \vec{s}_{prior})(V_{cov}^{model})^{-1}(\vec{s} - \vec{s}_{prior}), \end{aligned} \quad (5.5)$$

where  $V_{cov}^a$  are prior covariance matrices provided as the input for the fit. Assuming that nuisance parameters are described by N-dimensional Gaussian probability density functions the penalty term follows chi-square distribution for N degrees of freedom [131].

### Detector systematic covariance matrix

Model, flux and detector systematic covariance matrices are necessary inputs for the fit. Two of them were already introduced in previous chapters. Model and flux covariance matrices are presented in Fig. 4.8 and 4.9, respectively. The detector systematic

covariance matrix is reported in the *reconstructed phase-space* binning for all analysis samples and has dimensions  $143 \times 143$ . Only the total detector systematic uncertainty (described in subsection 4.1.4) is taken into account. The matrix is presented in Fig. 5.8. One can notice that bins within CC1FGD $\pi^-$  signal sample are strongly correlated to one another. This feature arises from the fact that the detector systematic uncertainty is mostly impacted by the pion SI systematic (see Table 4.2). For CC1FGD $\pi^-$  sample the volume of interest is constant (see subsection 4.1.3) and pion track properties are similar regardless of  $\mu^+$  kinematics. Hence, variations of pion SI cross sections will have similar impact in different phase-space bins.

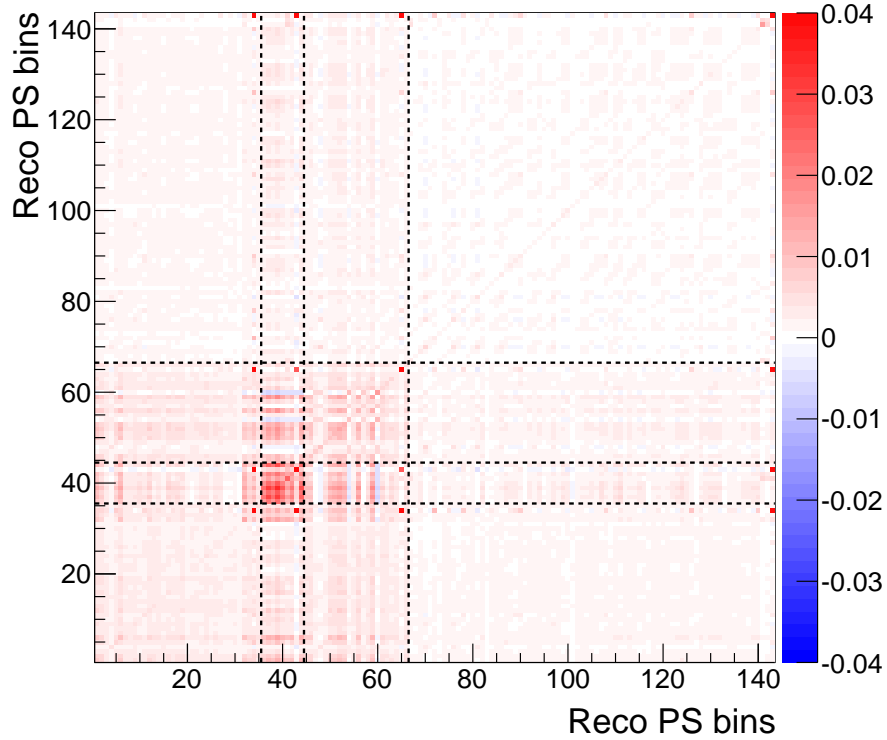


Figure 5.8: Detector systematic covariance matrix. Dashed lines indicate samples boundaries: CC1TPC $\pi^-$  signal sample (bins 1-35), CC1FGD $\pi^-$  signal sample (bins 36-44), Reversed Z-range cut background sample (bins 45-66), CC-other background sample (bins 67-143). In several bins the systematic uncertainty exceeds 20%. Color scale constrained for better visualisation.

## Minuit2

The fit is done with the Minuit2 minimiser [132] and MIGRAD algorithm in order to find minimum of the likelihood function defined in Eq. 5.4. This provides the best fit

for the template and nuisance parameters. Next the Hessian matrix<sup>2</sup> is calculated with HESSE algorithm<sup>3</sup>. The covariance matrix for the postfit parameters is obtained by inverting the Hessian matrix.

#### 5.2.4. Cross section calculation and error propagation

As an output of the fit the postfit values of template and nuisance parameters are obtained as well as the postfit covariance matrix. This provides modified MC event rate distribution. The next step is the calculation of the cross section in the  $i$ -th bin of *true phase-space* as:

$$\left( \frac{d^2\sigma^{signal}}{dp_\mu d\cos\theta_\mu} \right)_i = \frac{S_i}{\epsilon_i \cdot \Phi \cdot T \cdot (\Delta p_\mu)_i (\Delta \cos\theta_\mu)_i}, \quad (5.6)$$

where  $S_i$  - number of selected signal events in  $i$ -th bin,  $\epsilon_i$  - selection efficiency in  $i$ -th bin,  $\Phi$  denotes  $\bar{\nu}_\mu$  flux integrated over the energy spectrum,  $T$  - number of nucleons in FGD1 fiducial volume (FV),  $(\Delta p_\mu)_i$ ,  $(\Delta \cos\theta_\mu)_i$  - bin width in momentum and angle, respectively. The efficiency  $\epsilon_i$  is calculated with the postfit event rates and thus it may slightly differ from the nominal efficiency. The number of nucleons in FGD1 FV is estimated from the elemental composition of an XY module [133] (see Appendix C) and is found to be  $(5.537 \pm 0.037) \times 10^{29}$ . The number of nucleons is proportional to the FGD mass and the FGD mass uncertainty is already included in the detector systematic uncertainties (see subsection 4.1.2) so no additional error propagation is needed. The integrated  $\bar{\nu}_\mu$  flux  $\Phi$  is obtained from the T2K flux simulation prepared by the T2K beam group (see Fig. 5.9). For the collected data sample of  $8.46 \times 10^{20}$  POT the nominal  $\bar{\nu}_\mu$  flux is equal to:

$$\Phi = (1.258 \pm 0.062) \times 10^{13} \frac{1}{\text{cm}^2}.$$

This value is corrected with the postfit  $\bar{\nu}_\mu$  flux nuisance parameters. Each parameter reweights certain energy region of the  $\bar{\nu}_\mu$  flux (see Tab. 4.5, bins 6-16).

Finally, the cross section error is estimated with the toy Monte Carlos method. In order to generate toys the postfit covariance matrix is Cholesky decomposed to lower-triangular matrix  $L$  with the TDecompChol ROOT package. This matrix is multiplied by a vector of Gaussian random numbers  $\vec{b}$  with mean 0 and variance 1. In each toy MC the postfit parameters vector  $\vec{u}_{toy}$  is calculated as:

$$\vec{u}_{toy} = \vec{u}_{bestfit} + L\vec{b},$$

<sup>2</sup>That is, the matrix of second derivatives of likelihood in parameters space.

<sup>3</sup>Both MIGRAD and HESSE algorithms are included in the ROOT Minuit2 libraries.

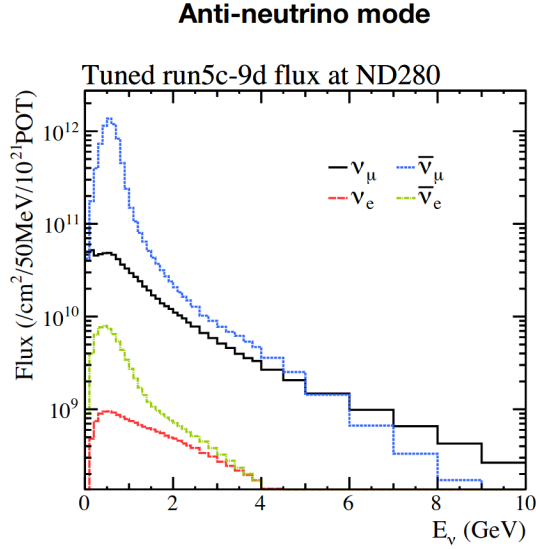


Figure 5.9: Simulated energy distribution of neutrino flux at ND280 for RHC beam mode. Plot taken from [134].

which provides new signal event rate  $S_i^{toy}$ , efficiency  $\epsilon_i^{toy}$  and the integrated flux  $\Phi_{toy}$ . Thus for each toy MC the cross section  $\sigma_{toy}$  is calculated according to Eq. 5.6 and the cross section covariance matrix  $C_\sigma^{ij}$  is computed as:

$$C_\sigma^{ij} = \frac{1}{\text{number of toys}} \sum_{toy} (\sigma_{toy} - \sigma_{bestfit})_i (\sigma_{toy} - \sigma_{bestfit})_j,$$

where  $i, j$  indicate *true phase-space* bins.

### 5.3. Fake data studies

Before fitting Monte Carlo to the real data it is necessary to check that the Fitter is working correctly. Multiple fits were performed during Author's analysis to ensure the stability and robustness of the Fitter. Most important of them are described in this section. Additional checks are reported in Appendix B.

#### 5.3.1. Asimov fit

The most basic test is to fit nominal Monte Carlo sample to itself. This is so-called *Asimov fit* which must result in parameters' postfit values equal to prefit values. This test allows to check the treatment of parameters' error for the nominal Monte Carlo sample, in particular statistical error for the template parameters. In Figure 5.10 the Asimov fit results for template parameters are presented. All parameters were fitted to

their nominal value 1. For this fit the MC sample was not normalised to data POT and thus the scale of the errors is smaller than what one could expect in the measurement.

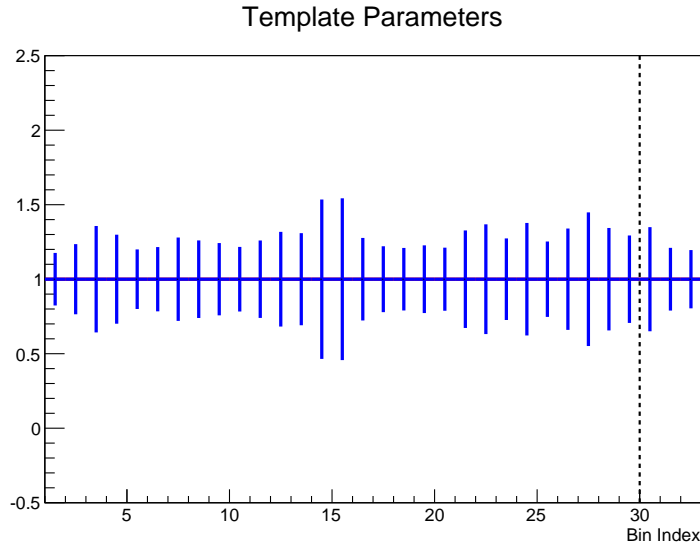


Figure 5.10: Asimov fit: postfit template parameters' values and errors. Dashed line separates out of phase-space region.

The Asimov fit results for nuisance parameters are presented in Figures 5.11 (model parameters), 5.12 (flux parameters), 5.13 (detector systematic parameters). As expected, the postfit parameters' values are the same as nominal values before the fit. Note that the postfit parameters' errors are in general different than the prefit errors. The postfit error (both for template and nuisance parameters) is determined by checking how  $\chi^2 = \chi_{stat}^2 + \chi_{syst}^2$  (Eq. 5.4) varies around the parameter's best fit point. Large

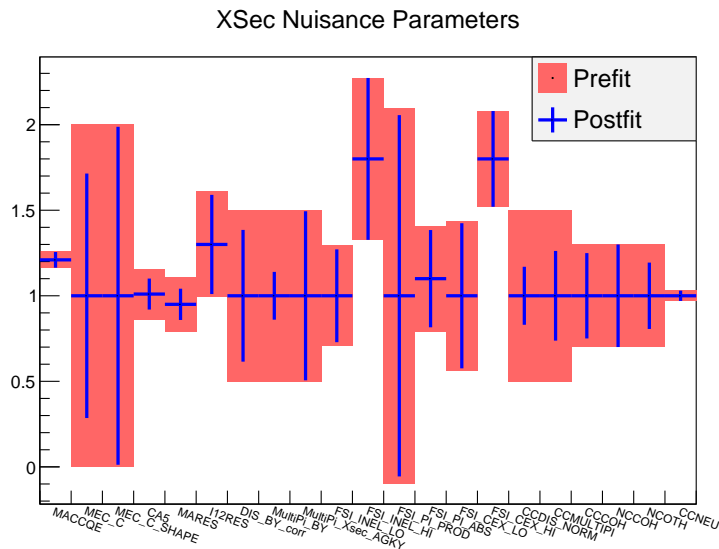


Figure 5.11: Asimov fit: postfit nuisance model parameters' values and errors.

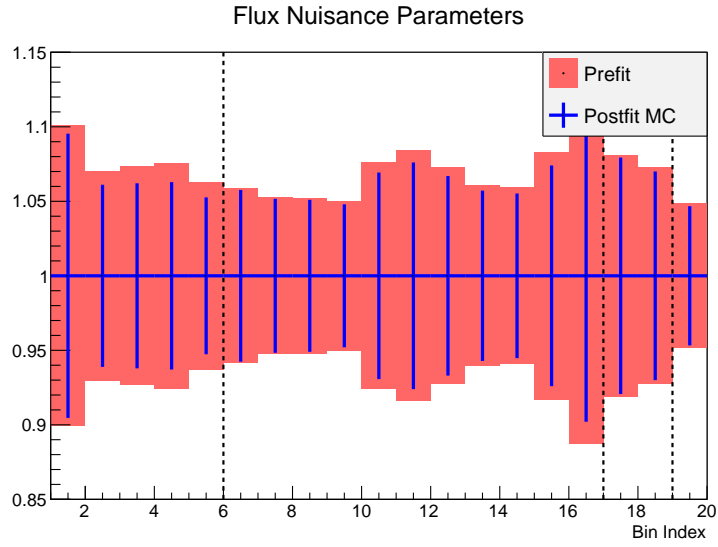


Figure 5.12: Asimov fit: postfit nuisance flux parameters' values and errors. Dashed lines separate parameters corresponding to different neutrino flavours:  $\nu_\mu$  (bins 1-5),  $\bar{\nu}_\mu$  (bins 6-16),  $\nu_e$  (bins 17-18),  $\bar{\nu}_e$  (bin 19).

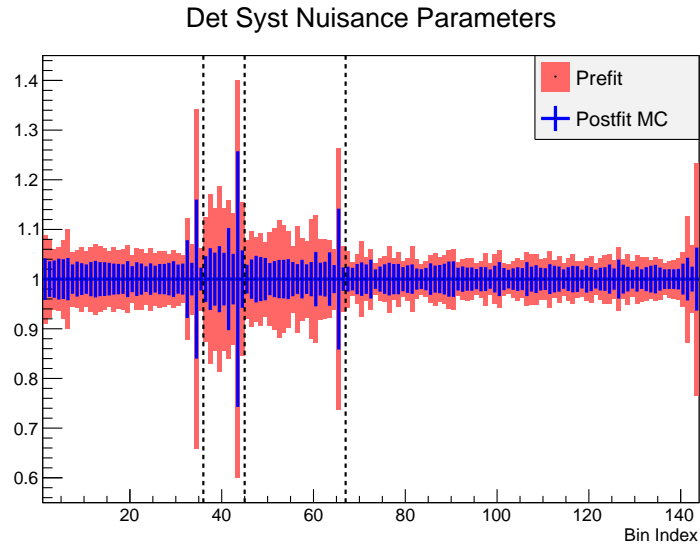


Figure 5.13: Asimov fit: postfit nuisance detector systematic parameters' values and errors. Dashed lines separate parameters corresponding to different analysis samples: CC1TPC $\pi^-$  signal sample (bins 1-35), CC1FGD $\pi^-$  signal sample (bins 36-44), Reversed Z-cut background sample (bins 45-66), CC-other background sample (bins 67-143).

$\chi^2$  increase for small parameter shift indicates that the parameter is well constrained and the corresponding postfit error is small. On the other hand, a small change in  $\chi^2$  indicates that the parameter is not well constrained and its uncertainty must be bigger.

Since the scale of  $\chi_{stat}^2$  contribution increases with the sample statistics one can expect that after normalising MC samples to data POT the  $\chi_{stat}^2$  contribution will be smaller and the postfit errors will be larger.

The extracted differential cross section for Asimov fit results is presented in Fig. 5.15. The reported values span through several orders of magnitude due to very different bin sizes (see Table 5.9). This cross section will be treated later on as the nominal NEUT prediction and compared with other fit results. The error propagation was done for 500 toy Monte Carlo experiments. The corresponding covariance matrix is presented in Fig. 5.15.

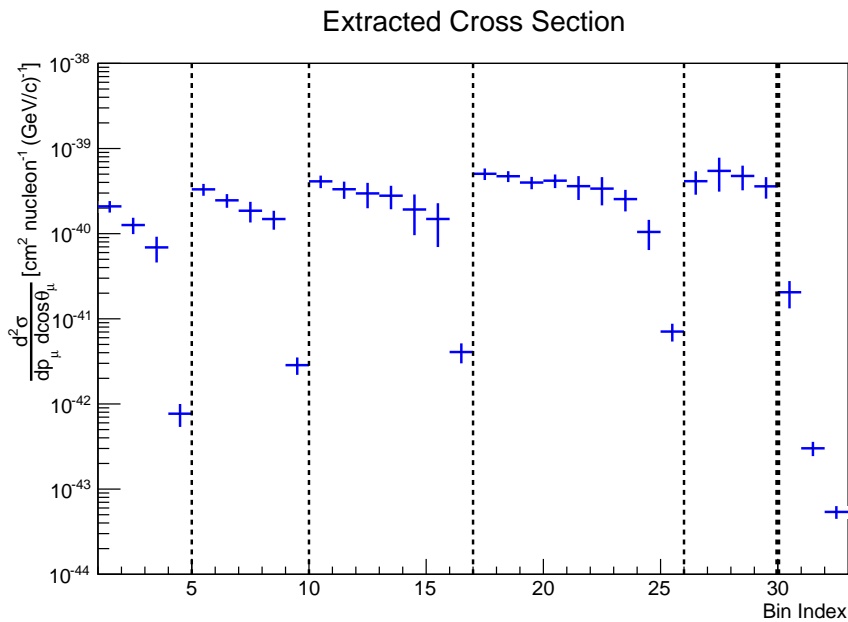


Figure 5.14: Asimov fit: Extracted cross section reported in *true phase-space* bins (see Table 5.9). Thin dashed lines separate different angular regions of the phase space:  $0.74 < \cos \theta_\mu < 0.88$  (bins 1-4),  $0.88 < \cos \theta_\mu < 0.94$  (bins 5-9),  $0.94 < \cos \theta_\mu < 0.97$  (bins 10-16),  $0.97 < \cos \theta_\mu < 1$  (bins 17-25),  $0.99 < \cos \theta_\mu < 1$  (bins 26-29). Within each angular region higher bin index corresponds to higher momentum  $p_\mu$ . Thick dashed line separates out of phase-space region.

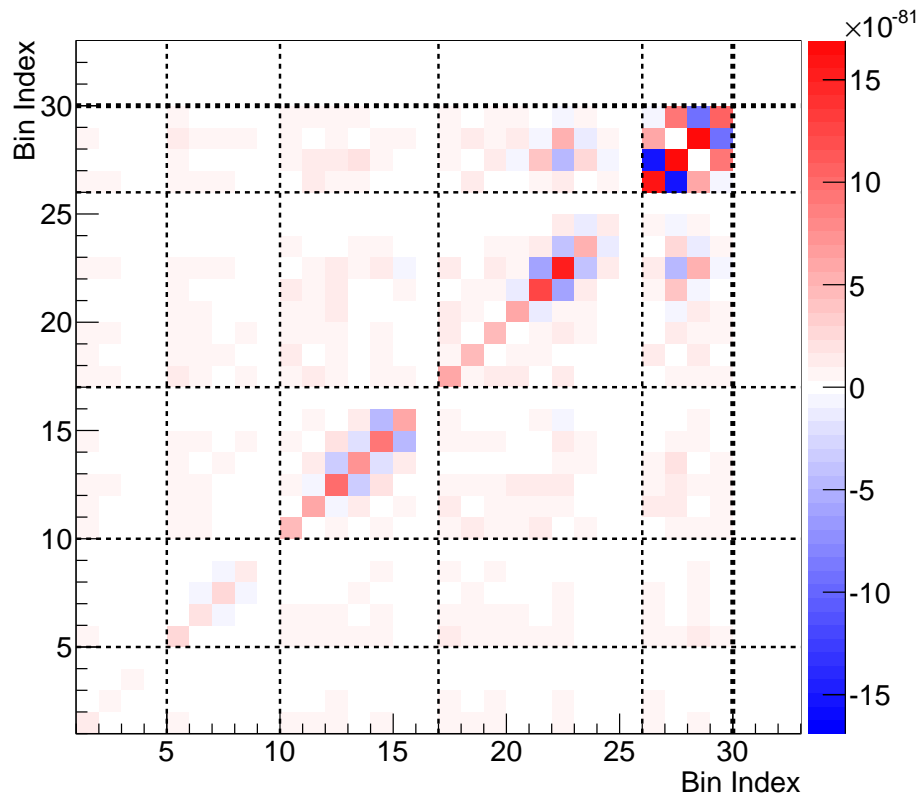


Figure 5.15: Asimov fit: Covariance matrix for the extracted cross section. Thin dashed lines separate different angular regions of the phase space:  $0.74 < \cos \theta_\mu < 0.88$  (bins 1-4),  $0.88 < \cos \theta_\mu < 0.94$  (bins 5-9),  $0.94 < \cos \theta_\mu < 0.97$  (bins 10-16),  $0.97 < \cos \theta_\mu < 1$  (bins 17-25),  $0.99 < \cos \theta_\mu < 1$  (bins 26-29). Within each angular region higher bin index corresponds to higher momentum  $p_\mu$ . Thick dashed lines separate out of phase-space region. Color scale constrained for better visualisation.

### 5.3.2. Enhanced signal fit

In order to check that the template parameters are sensitive to the signal, the following fake data test was performed. NEUT MC sample was scaled to data POT by reweighting each event by the ratio:

$$\frac{\text{POT}(data)}{\text{POT}(MC)} = \frac{8.46 \times 10^{20}}{1.1362 \times 10^{22}} \approx 0.0745.$$

Then each signal event in NEUT MC sample was reweighted by a factor of 1.2. In this way a fake data sample was obtained, with the signal contribution enhanced by 20%. It was expected that fitting nominal MC to such fake data sample would result in template parameters equal to 1.2. The results presented in Fig. 5.16 confirm this expectation. Note that due to the POT scaling the statistical errors are significantly bigger than for Asimov fit. The impact of statistical fluctuations on postfit template parameters is discussed in Appendix B.

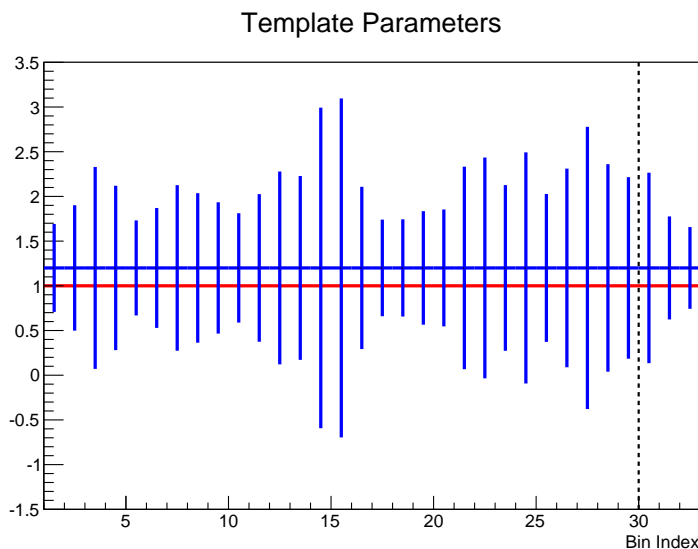


Figure 5.16: Enhanced signal fit: postfit template parameters' values and errors. Dashed line separates out of phase-space region.

Postfit nuisance parameters are presented in Figs. 5.17-5.19. All parameters are fitted almost exactly to their nominal values. The initial and final  $\chi^2$  quantity (Eq. 5.4), which is minimised in the fit, is reported in Table 5.11. As intended, the signal samples are much more sensitive to signal reweighting than the background samples which is manifested in higher initial  $\chi^2$  contribution.

The extracted differential cross section for the discussed fit is presented in Fig. 5.20. In each bin the cross section is, as expected, 20% higher than the nominal one. The error propagation was done for 500 toy Monte Carlo experiment. The corresponding covariance matrix is presented in Fig. 5.21.

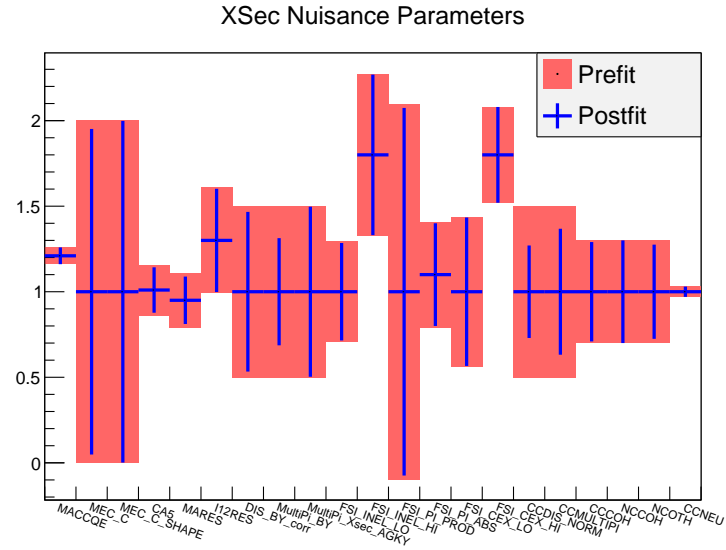


Figure 5.17: Enhanced signal fit: postfit nuisance model parameters' values and errors.

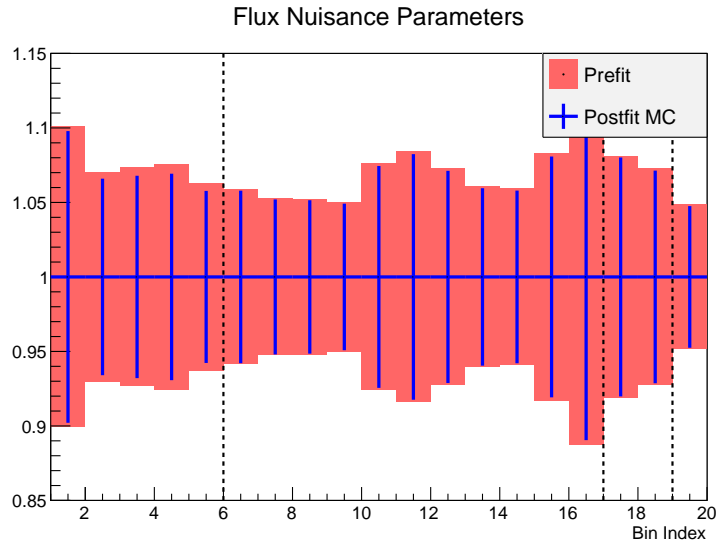


Figure 5.18: Enhanced signal fit: postfit nuisance flux parameters' values and errors. Dashed lines separate parameters corresponding to different neutrino flavours:  $\nu_\mu$  (bins 1-5),  $\bar{\nu}_\mu$  (bins 6-16),  $\nu_e$  (bins 17-18),  $\bar{\nu}_e$  (bin 19).

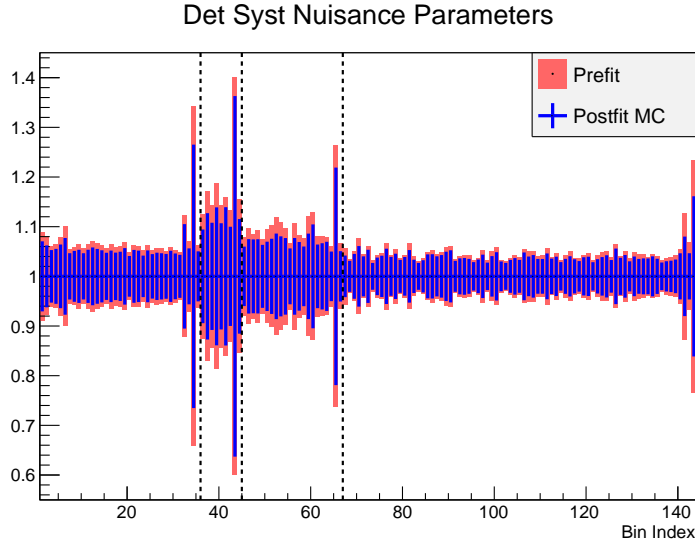


Figure 5.19: Enhanced signal fit: postfit nuisance detector systematic parameters' values and errors. Dashed lines separate parameters corresponding to different analysis samples: CC1TPC $\pi^-$  signal sample (bins 1-35), CC1FGD $\pi^-$  signal sample (bins 36-44), Reversed Z-cut background sample (bins 45-66), CC-other background sample (bins 67-143).

$\chi^2$ contribution	Initial	Final
Total $\chi^2$	7.5505	$< 10^{-6}$
$\chi_{stat}^2$	7.5505	$< 10^{-6}$
per CC1TPC $\pi^-$ sample	5.4916	$< 10^{-6}$
per CC1FGD $\pi^-$ sample	1.4343	$< 10^{-6}$
per Reversed Z-cut sample	0.2387	$< 10^{-6}$
per CC-other sample	0.3859	$< 10^{-6}$
$\chi_{syst}^2$	0	$< 10^{-6}$

Table 5.11: Enhanced signal fit. Comparison of  $\chi^2$  value before and after the fit.

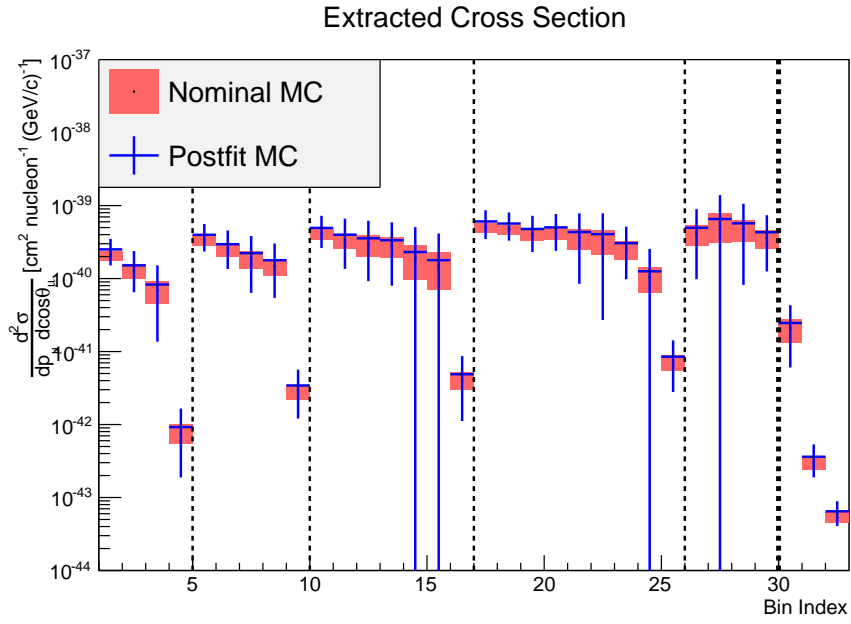


Figure 5.20: Enhanced signal fit: Extracted cross section reported in *true phase-space* bins (see Table 5.9). Thin dashed lines separate different angular regions of the phase space:  $0.74 < \cos \theta_\mu < 0.88$  (bins 1-4),  $0.88 < \cos \theta_\mu < 0.94$  (bins 5-9),  $0.94 < \cos \theta_\mu < 0.97$  (bins 10-16),  $0.97 < \cos \theta_\mu < 1$  (bins 17-25),  $0.99 < \cos \theta_\mu < 1$  (bins 26-29). Within each angular region higher bin index corresponds to higher momentum  $p_\mu$ . Thick dashed line separates out of phase-space region.

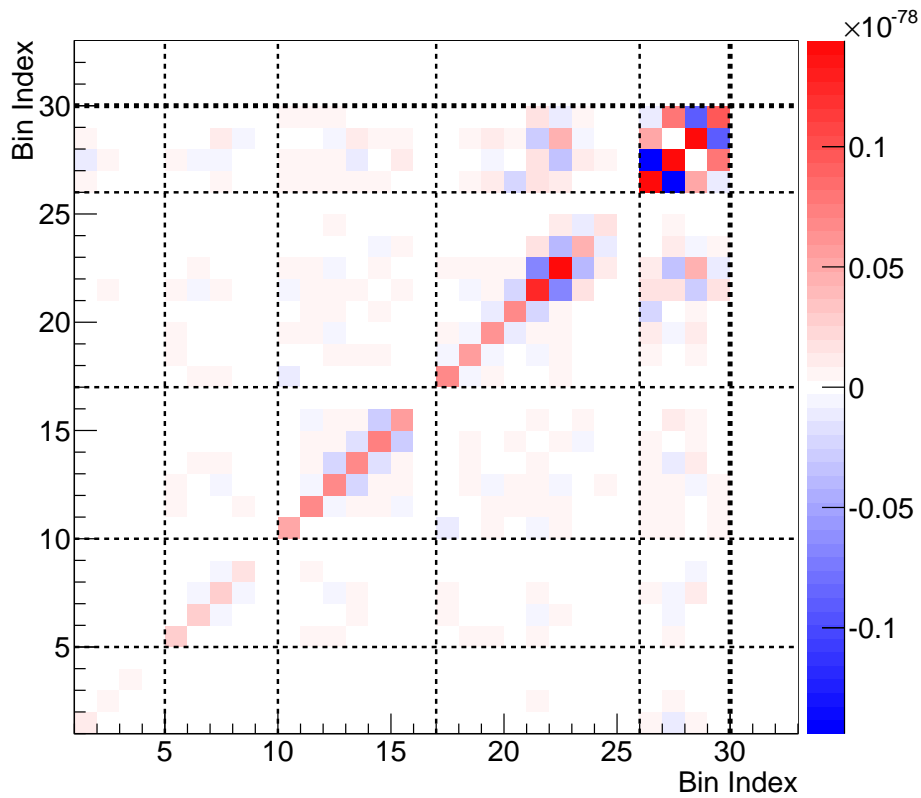


Figure 5.21: Enhanced signal fit: Covariance matrix for the extracted cross section. Thin dashed lines separate different angular regions of the phase space:  $0.74 < \cos \theta_\mu < 0.88$  (bins 1-4),  $0.88 < \cos \theta_\mu < 0.94$  (bins 5-9),  $0.94 < \cos \theta_\mu < 0.97$  (bins 10-16),  $0.97 < \cos \theta_\mu < 1$  (bins 17-25),  $0.99 < \cos \theta_\mu < 1$  (bins 26-29). Within each angular region higher bin index corresponds to higher momentum  $p_\mu$ . Thick dashed lines separate out of phase-space region. Color scale constrained for better visualisation.

### 5.3.3. Statistical and systematic fluctuations

The  $\chi^2$  quantity in Eq. 5.4 is expected to follow a chi-square distribution. In order to check that two sets of fits were performed with statistical and systematic fluctuations.

At first, only statistical fluctuations were considered. The Poisson variations were applied to the nominal MC sample in each bin of the *reconstructed phase-space* and the nominal distribution was fitted to the fluctuated one. This was repeated 500 times. For such fits only template parameters were allowed to change (nuisance parameters were fixed at nominal values). The distribution of the postfit  $\chi^2$  values is presented in Fig. 5.22-left. Since in the fit procedure the event rate is compared in 143 bins and 32 template parameters are fitted, it was expected that the  $\chi^2$  quantity will follow the chi-square distribution for 111 degrees of freedom. Thus the distribution of the postfit  $\chi^2$  values should have mean around 111 and RMS close to  $\sqrt{222} \approx 14.9$ . As it can be seen in Fig. 5.22-left, the actual mean value is 113.6 and RMS is 15.55. The uncertainty of the mean value can be estimated as RMS of the distribution divided by square root of the number of repeated fits, which in this case is approximately equal to 0.7. One must conclude that it is statistically unlikely that obtained histogram follows chi-square distribution for 111 degrees of freedom.

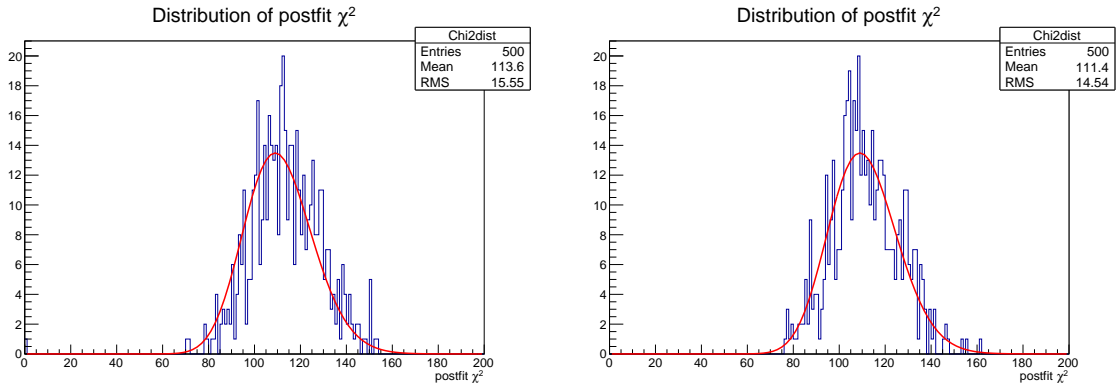


Figure 5.22: Postfit  $\chi^2$  distribution. Left: Only statistical fluctuations with nuisance parameters fixed. Right: Statistical and systematic fluctuations combined. In both plots the red line represents the chi-square distribution for 111 degrees of freedom.

Next, the statistical fluctuations were combined with systematic fluctuations of nuisance parameters. For each nuisance parameter Gaussian variations were applied with the correlations provided by the input covariance matrices and the nominal distribution was fitted to the fluctuated one. This procedure was also repeated 500 times. In this case both template and nuisance parameters were fitted. The distribution of the postfit  $\chi^2$  values is presented in Fig. 5.22-right. The penalty term introduced in Eqs. 5.4-5.5 should follow the chi-square distribution for  $N$  degrees of freedom, where  $N$  is

the number of nuisance parameters. If nuisance parameters were fixed this additional term should on average increase the postfit  $\chi^2$  value by  $N$ . However, since the nuisance parameters are being fitted the number of degrees of freedom in the fit must decrease by  $N$ . Eventually, in this case the  $\chi^2$  quantity is also expected to follow the chi-square distribution for 111 degrees of freedom. As can be seen in Fig. 5.22-right, the mean postfit  $\chi^2$  value is 111.4 and RMS is 14.54. In this case the obtained histogram agrees quite well with the expected distribution.

In conclusion, fits with statistical fluctuations and only template parameters seem to follow chi-square distribution for the number of degrees of freedom higher than expected 111. This might indicate that some template parameters are strongly correlated or there's a problem in their treatment. However, this effect cannot be significant since for the fits with statistical and systematic fluctuations (both template and nuisance parameters included) the postfit  $\chi^2$  distribution is close to the expected one.

### 5.3.4. NEUT to Genie fit

Before unblinding data the final Fitter validation was done by fitting nominal NEUT v5.4.0 MC to GENIE v2.8.0 [135] MC sample corresponding to  $2.74 \times 10^{21}$  POT. The ND280 detector and flux models were the same for both samples, however there are some differences between NEUT and GENIE generators at neutrino interaction level.

In GENIE generator a different value for the CCQE axial mass of  $0.99 \text{ GeV}/c^2$  is used (compared to  $1.21 \text{ GeV}/c^2$  in NEUT). Also, a different nuclear model based on relativistic Fermi gas with Bodek and Ritchie corrections [136] is applied. For resonant interactions both NEUT and GENIE use Rein-Sehgal model, however in case of GENIE different form factors are used [137]. The resonant axial mass of  $1.12 \text{ GeV}/c^2$  is applied (compared to  $0.95 \text{ GeV}/c^2$  for NEUT). Genie simulates DIS similarly to NEUT but with different Bodek-Yang corrections [138]. In case of coherent interaction both generators are based on Rein-Sehgal model, however in GENIE the corrections from Berger-Sehgal model are not used. FSI interactions are simulated in GENIE with different predictions for the cross sections. For more detailed comparison of NEUT and GENIE see [139].

The NEUT to Genie fit results for template parameters are presented in Fig. 5.23. For this fit GENIE MC sample was normalised to data POT to get the scale of the errors similar to what one could expect in the measurement. The purity of the signal selection for GENIE MC was found to be 52.4% in joint CC1TPC $\pi^-$ +CC1FGD $\pi^-$  signal samples (compared to 47.2% for NEUT). It was checked that GENIE predicted more signal than NEUT both for events with high angle and forward-going  $\mu^+$  tracks. Thus one could expect that in general the postfit template parameters will be higher

than 1. This is indeed the case for 13 out of first 16 parameters corresponding to high angle bins of the *true phase-space* ( $0.74 < \cos \theta_\mu < 0.97$ ) as well as for out of phase-space (OOPS) region. Contrary to expectations, most postfit parameters in the phase-space region corresponding to forward-going  $\mu^+$  tracks (bins 17-29) are lower than 1, however their decrease is within the margin of uncertainty.

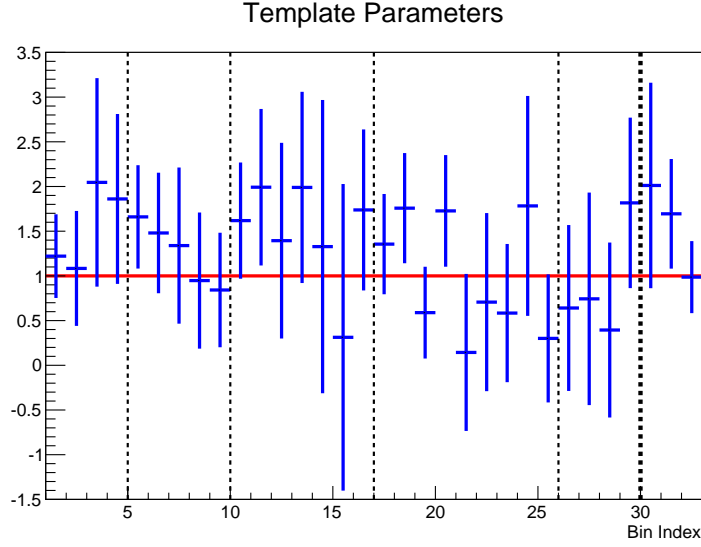


Figure 5.23: NEUT to Genie fit: postfit template parameters' values and errors. Thin dashed lines separate different angular regions of the phase space:  $0.74 < \cos \theta_\mu < 0.88$  (bins 1-4),  $0.88 < \cos \theta_\mu < 0.94$  (bins 5-9),  $0.94 < \cos \theta_\mu < 0.97$  (bins 10-16),  $0.97 < \cos \theta_\mu < 1$  (bins 17-25),  $0.99 < \cos \theta_\mu < 1$  (bins 26-29). Within each angular region higher bin index corresponds to higher momentum  $p_\mu$  (see Table 5.9). Thick dashed line separates out of phase-space region.

Postfit nuisance model parameters are presented in Fig. 5.24. In most cases the postfit parameter's value is close to the prefit value - the difference is smaller than  $\frac{1}{2}$  of the prior error. Following parameters have been changed more significantly than that:

- $C_5^A, M_A^{RES}$  - Due to different form factors used in resonant interactions modelling in GENIE the shift of these parameters was to some extent expected.
- $MultiPi_{BY}$  - Since GENIE uses different Bodek-Yang corrections the change of this parameter is acceptable.
- $CCMULTIPI$  - This parameter together with  $CCDIS_{norm}$  normalise contribution of CC DIS interaction (see section 4.2) and are noticeably decreased in the fit. This agrees quite well with the fact that contribution of  $\nu_\mu/\bar{\nu}_\mu$  CC DIS in-

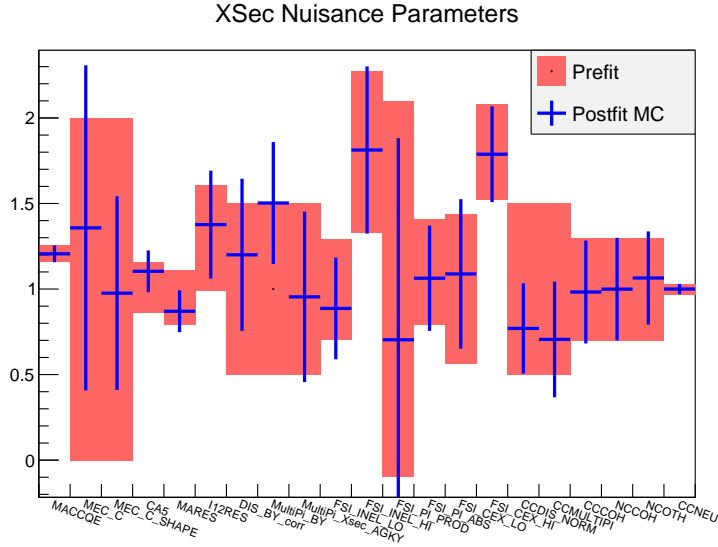


Figure 5.24: NEUT to Genie fit: postfit nuisance model parameters' values and errors.

teractions in all analysis samples is about 49% for NEUT samples and only 41% for GENIE samples.

One could have expected CCQE axial mass to be decreased due to smaller prior value in GENIE, however it must be noted that CCQE interaction contributes marginally to the selected event rate and thus the fit is not very sensitive to this parameter.

Postfit nuisance flux and detector systematic parameters are presented in Figs. 5.25-5.26. In most cases the postfit values of these parameters are close to the prefit values

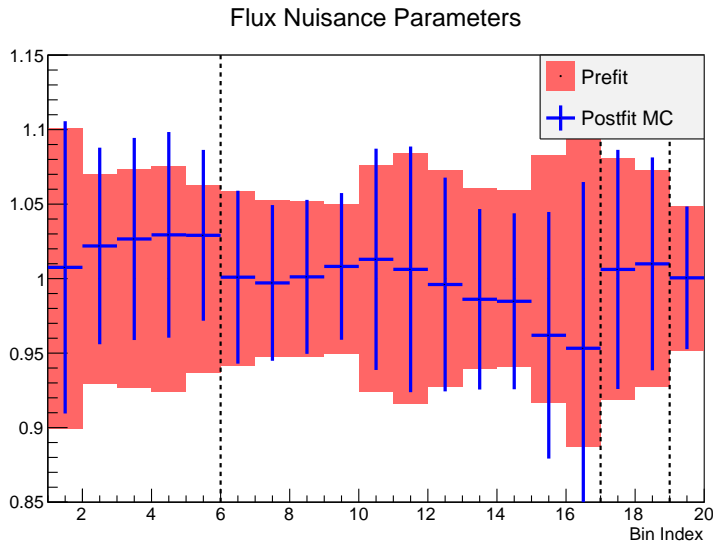


Figure 5.25: NEUT to Genie fit: postfit nuisance flux parameters' values and errors. Dashed lines separate parameters corresponding to different neutrino flavours:  $\nu_\mu$  (bins 1-5),  $\bar{\nu}_\mu$  (bins 6-16),  $\nu_e$  (bins 17-18),  $\bar{\nu}_e$  (bin 19).

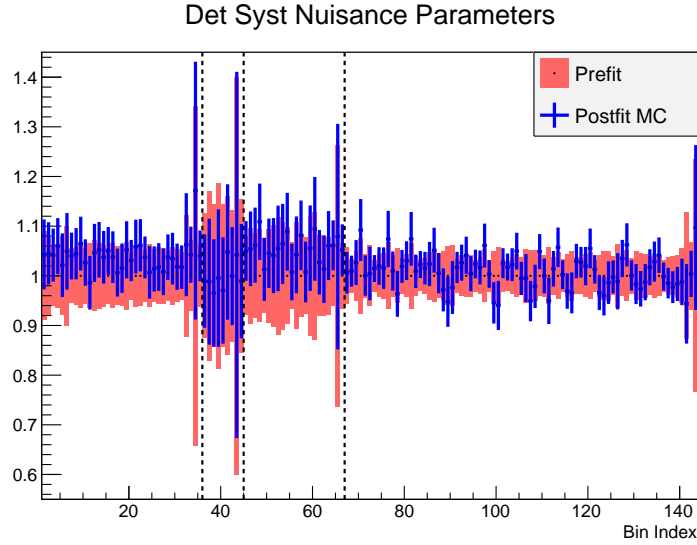


Figure 5.26: NEUT to Genie fit: postfit nuisance detector systematic parameters' values and errors. Dashed lines separate parameters corresponding to different analysis samples: CC1TPC $\pi^-$  signal sample (bins 1-35), CC1FGD $\pi^-$  signal sample (bins 36-44), Reversed Z-cut background sample (bins 45-66), CC-other background sample (bins 67-143).

within the margin of uncertainty. One can note however that for CC1TPC $\pi^-$  signal sample and the reversed Z-cut background sample the detector nuisance parameters are pulled up throughout the phase-space. For the CC1TPC $\pi^-$  sample this might be related to the bigger event rate predicted by GENIE than by NEUT as shown in Table 5.12. For the reversed Z-cut sample the increase of detector systematic parameters might be a compensation for lowered CC DIS contribution.

The initial and final  $\chi^2$  quantity, which is minimised in the fit, is reported in Table 5.13. The postfit  $\chi^2$  value is smaller than in the fluctuation tests (Fig. 5.22-right), because the flux and detector models are the same for NEUT and GENIE. The systematic fluctuations on flux and detector nuisance parameters introduce a bigger

sample	NEUT (restricted PS)	GENIE (restricted PS)
CC1TPC $\pi^-$ signal	634 (531.9)	743.5 (628.8)
CC1FGD $\pi^-$ signal	107.4 (89.4)	122.3 (95.8)
Reversed Z-cut bkg	571 (341.7)	630.4 (351.2)
CC-other bkg	2065 (1750)	2009 (1705)

Table 5.12: Total event rates in NEUT MC predictions and GENIE MC predictions. Values normalised to data POT.

$\chi^2$ contribution	Initial	Final
Total $\chi^2$	140.69	61.795
$\chi_{stat}^2$	140.69	53.824
per CC1TPC $\pi^-$ sample	46.056	4.5597
per CC1FGD $\pi^-$ sample	10.703	4.3848
per Reversed Z-cut sample	22.743	11.452
per CC-other sample	61.187	33.428
$\chi_{syst}^2$	0	7.9709
$\chi_{flux}^2$	0	0.7001
$\chi_{model}^2$	0	2.9364
$\chi_{detsyst}^2$	0	4.3344

Table 5.13: NEUT to GENIE fit. Comparison of  $\chi^2$  value before and after the fit. Contribution from different systematic sources is included.

discrepancy between fluctuated NEUT and nominal NEUT MC than between nominal NEUT and nominal GENIE MC.

The extracted differential cross section for the NEUT to GENIE fit is presented in Fig. 5.27. The error propagation was done for 500 toy Monte Carlo experiments. The corresponding covariance matrix is presented in Fig. 5.28.

In order to compare the postfit cross section distribution  $\sigma_i^{postfit}$  with the fake data cross section distribution  $\sigma_i^{fake\ data}$  one can calculate  $\chi_{fake\ data}^2$  as:

$$\chi_{fake\ data}^2 = \sum_{i,j}^{true\ PS} (\sigma_i^{postfit} - \sigma_i^{fake\ data})(C_\sigma)_{ij}^{-1}(\sigma_j^{postfit} - \sigma_j^{fake\ data}),$$

where  $i, j$  indices run over *true phase-space* bins and  $C_\sigma$  is the postfit cross section covariance matrix. This quantity is found to be equal to:

$$\chi_{fake\ data}^2 = \begin{cases} 16.178 & \text{per 32 bins (including OOPS)} \\ 15.687 & \text{per 29 bins (without OOPS)} \end{cases}$$

which indicates that the postfit cross section distribution is in a good agreement with the fake data GENIE sample.

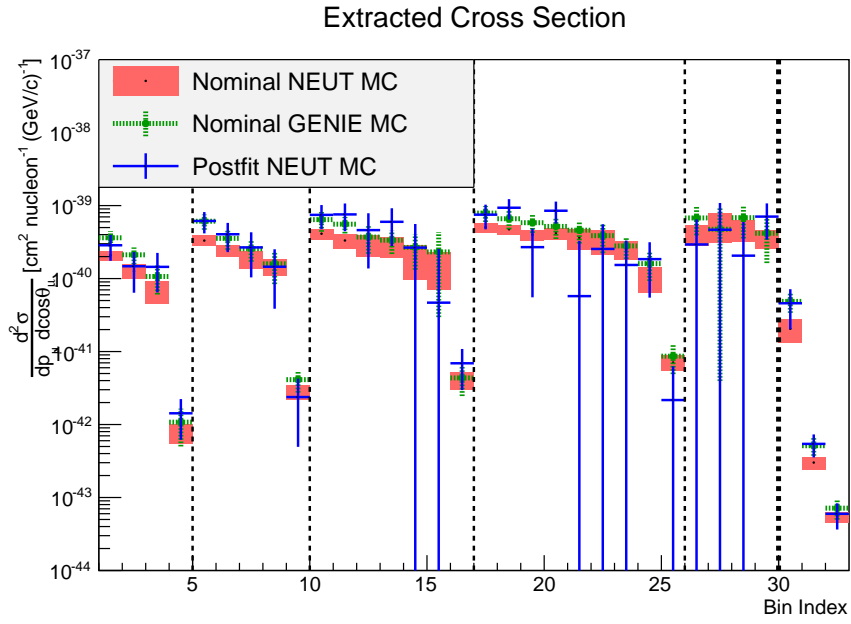


Figure 5.27: NEUT to GENIE fit: Extracted cross section reported in *true phase-space* bins (see Table 5.9). Thin dashed lines separate different angular regions of the phase space:  $0.74 < \cos \theta_\mu < 0.88$  (bins 1-4),  $0.88 < \cos \theta_\mu < 0.94$  (bins 5-9),  $0.94 < \cos \theta_\mu < 0.97$  (bins 10-16),  $0.97 < \cos \theta_\mu < 1$  (bins 17-25),  $0.99 < \cos \theta_\mu < 1$  (bins 26-29). Within each angular region higher bin index corresponds to higher momentum  $p_\mu$ . Thick dashed line separates out of phase-space region.

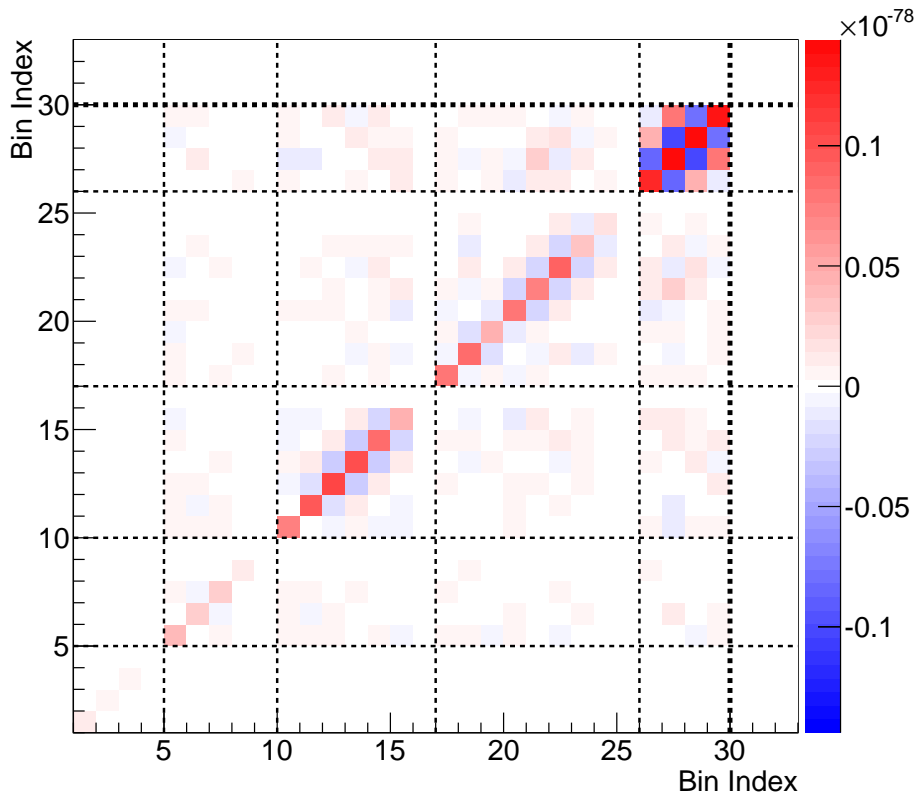


Figure 5.28: NEUT to GENIE fit: Covariance matrix for the extracted cross section. Thin dashed lines separate different angular regions of the phase space:  $0.74 < \cos \theta_\mu < 0.88$  (bins 1-4),  $0.88 < \cos \theta_\mu < 0.94$  (bins 5-9),  $0.94 < \cos \theta_\mu < 0.97$  (bins 10-16),  $0.97 < \cos \theta_\mu < 1$  (bins 17-25),  $0.99 < \cos \theta_\mu < 1$  (bins 26-29). Within each angular region higher bin index corresponds to higher momentum  $p_\mu$ . Thick dashed lines separate out of phase-space region. Color scale constrained for better visualisation.

# Chapter 6

## Data results

In this chapter the final results obtained with unblinded data are presented. The  $\bar{\nu}_\mu$  CC1 $\pi^-$  cross section is measured with the likelihood fit method described in Chapter 5. The cross section is reported as double differential in  $\mu^+$  kinematic variables  $d^2\sigma/dp_\mu d\cos\theta_\mu$ , one dimensional projections  $d\sigma/dp_\mu$ ,  $d\sigma/d\cos\theta_\mu$  and total cross section integrated over the restricted phase-space.

### 6.1. Events distribution in the phase-space

Data event rates in the analysis samples together with the **prefit** NEUT Monte Carlo predictions normalised to data POT are presented in Table 6.1. Values for both unrestricted and restricted phase-space are shown. There is an overall good agreement between data and Monte Carlo. For the CC1TPC $\pi^-$  signal samples the measured event rate is quite smaller than MC, but this difference is within limits of double statistical uncertainty. For the CC-other background sample without phase-space restrictions the Monte Carlo predictions are however significantly smaller than the actual data. Such discrepancy is unlikely to be just a result of statistical fluctuations. In particular it was found that within CC-other sample there are 371 data events with multiple reconstructed  $\pi^-$ , while normalised Monte Carlo predicts only 273 events with such signature. Among those 273 MC events 88% are caused by deep inelastic scattering (DIS). This observation indicates that DIS might be underestimated in NEUT Monte Carlo. In the entire CC-other sample DIS contributes to about 58% of events (23% with  $W < 2 \text{ GeV}/c^2$  and 35% with  $W > 2 \text{ GeV}/c^2$ ).

Data events distribution together with the **prefit** NEUT Monte Carlo are presented in Figs. 6.1-6.4 for all analysis samples, broken down by the true topology composition.

sample	MC (restricted PS)	data (restricted PS)
CC1TPC $\pi^-$ signal	634 (531.9)	604 (499)
CC1FGD $\pi^-$ signal	107.4 (89.4)	101 (86)
Reversed Z-cut bkg	571 (341.7)	562 (340)
CC-other bkg	2065 (1750)	2223 (1817)

Table 6.1: Total event rates in MC predictions and data. Values in parentheses refer to the restricted phase-space.

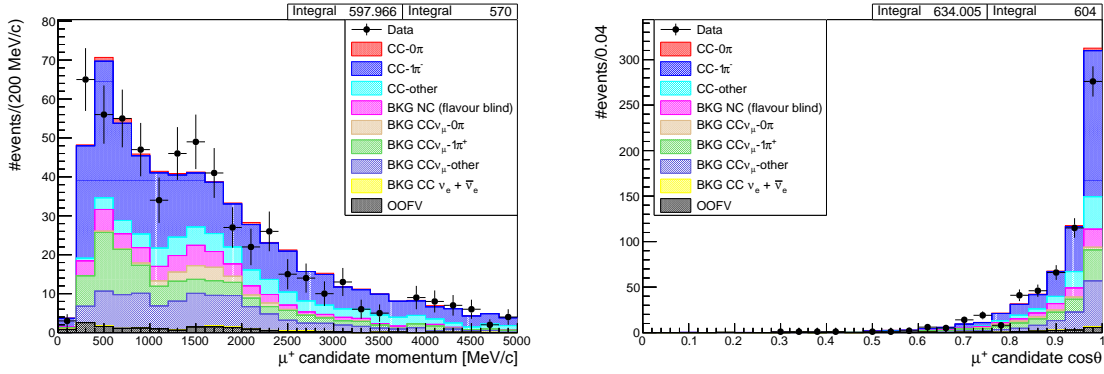


Figure 6.1: **CC1TPC $\pi^-$  signal selection.** Data and MC distribution of reconstructed kinematic variables (left - momentum, right -  $\cos\theta$ ) of the reconstructed  $\mu^+$  candidate. Colors indicate the true topology of the event.

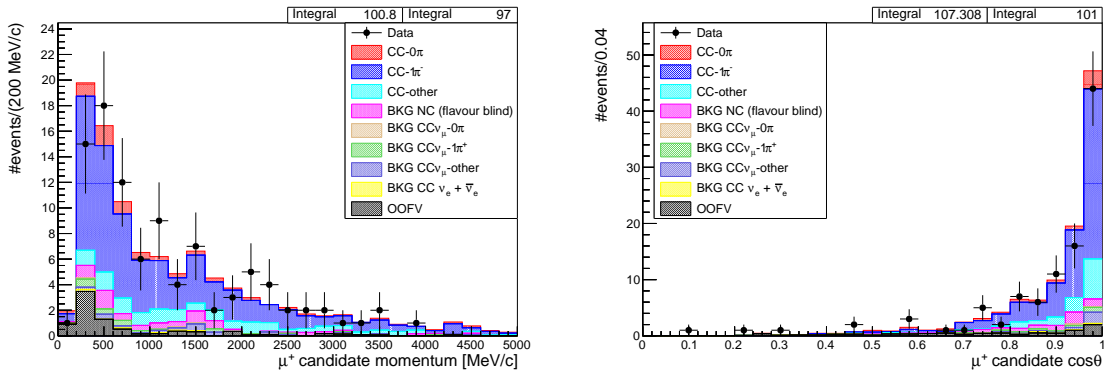


Figure 6.2: **CC1FGD $\pi^-$  signal selection.** Data and MC distribution of reconstructed kinematic variables (left - momentum, right -  $\cos\theta$ ) of the reconstructed  $\mu^+$  candidate. Colors indicate the true topology of the event.

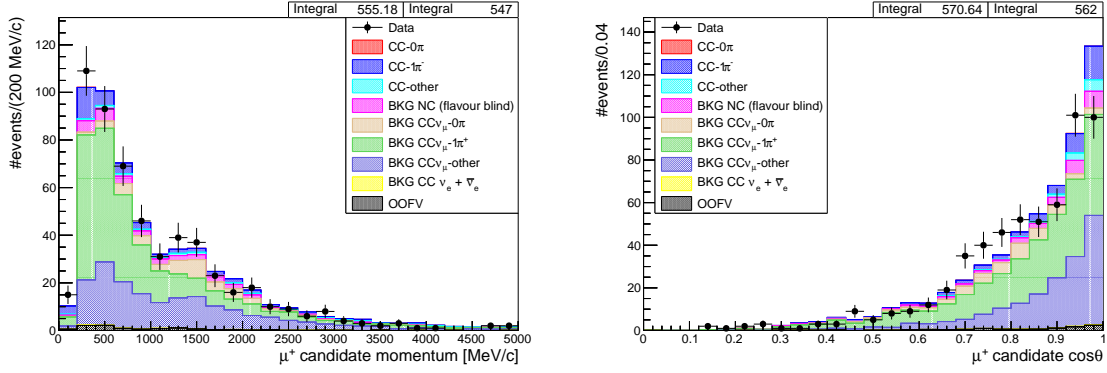


Figure 6.3: **Reversed Z-range cut background selection.** Data and MC distribution of reconstructed kinematic variables (left - momentum, right -  $\cos\theta$ ) of the reconstructed  $\mu^+$  candidate. Colors indicate the true topology of the event.

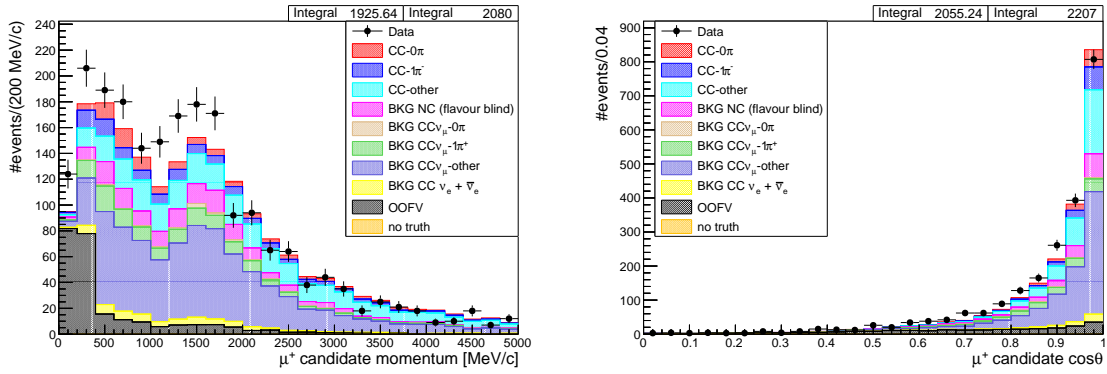


Figure 6.4: **CC-other background selection.** Data and MC distribution of reconstructed kinematic variables (left - momentum, right -  $\cos\theta$ ) of the reconstructed  $\mu^+$  candidate. Colors indicate the true topology of the event.

Data events distributions together with the **prefit and postfit** NEUT Monte Carlo predictions in the *reconstructed phase-space* binning are presented in Figs. 6.5-6.8. One can see that for the CC1TPC $\pi^-$  signal sample the discrepancy between data and MC after the fit is significantly smaller than before the fit. This is also the case (although less apparent) for background samples. For the reversed Z-range cut background sample there is a distinct deficit of data events in the phase-space region corresponding to forward going reconstructed  $\mu^+$  track and excess of data events for high angle  $\mu^+$  tracks. This feature is seen both for nominal and postfit MC. Similarly for CC-other sample specific phase-space regions seem to have systematic excess or deficit of data with respect to Monte Carlo. Bins with significant data deficit correspond rather to forward going  $\mu^+$  tracks, while bins with the highest data excess correspond to high angle  $\mu^+$  tracks. For the CC1FGD $\pi^-$  signal sample there is a general good agreement

between MC and data within the restricted phase-space, but the data event rate is noticeably smaller in OOPS region. More quantitative comparison in terms of  $\chi_{stat}^2$  is given in the next section.

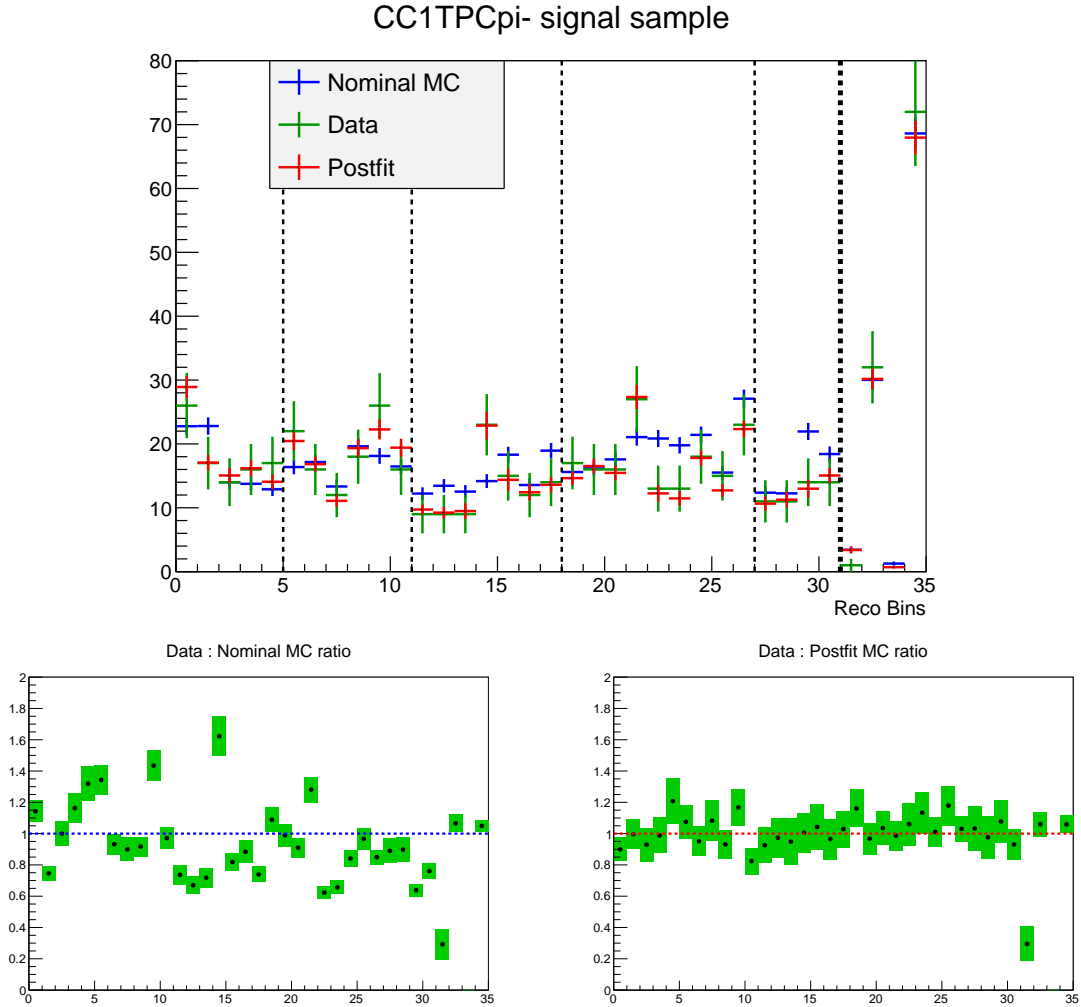


Figure 6.5: **CC1TPC $\pi^-$  signal selection.** Top: Data and NEUT MC distribution in the *reconstructed phase-space* binning (see Tables 5.2-5.3, pp. 118-119). Thin dashed lines separate different angular regions of the phase space:  $0.74 < \cos \theta_\mu < 0.88$  (bins 0-4),  $0.88 < \cos \theta_\mu < 0.94$  (bins 5-10),  $0.94 < \cos \theta_\mu < 0.97$  (bins 11-17),  $0.97 < \cos \theta_\mu < 1$  (bins 18-26),  $0.99 < \cos \theta_\mu < 1$  (bins 27-30). Thick dashed line separates out of phase-space region. Bottom left: data to postfit MC ratio. Bottom right: data to nominal MC ratio.

As can be seen in bottom plots of Figs. 6.5-6.7 the penultimate bin has zero data event rate  $N_j^{obs} = 0$ . This bin corresponds to out of phase-space region of reconstructed  $\mu^+$  momentum  $p_\mu > 30$  GeV/c. Zero event rate is not a problem for the Fitter which for this bin uses the limit of expression in Eq. 5.4:

$$\lim_{N_j^{obs} \rightarrow 0} \left( N_j - N_j^{obs} + N_j^{obs} \log \frac{N_j^{obs}}{N_j} \right) = N_j$$

as a contribution to  $\chi_{stat}^2$ .

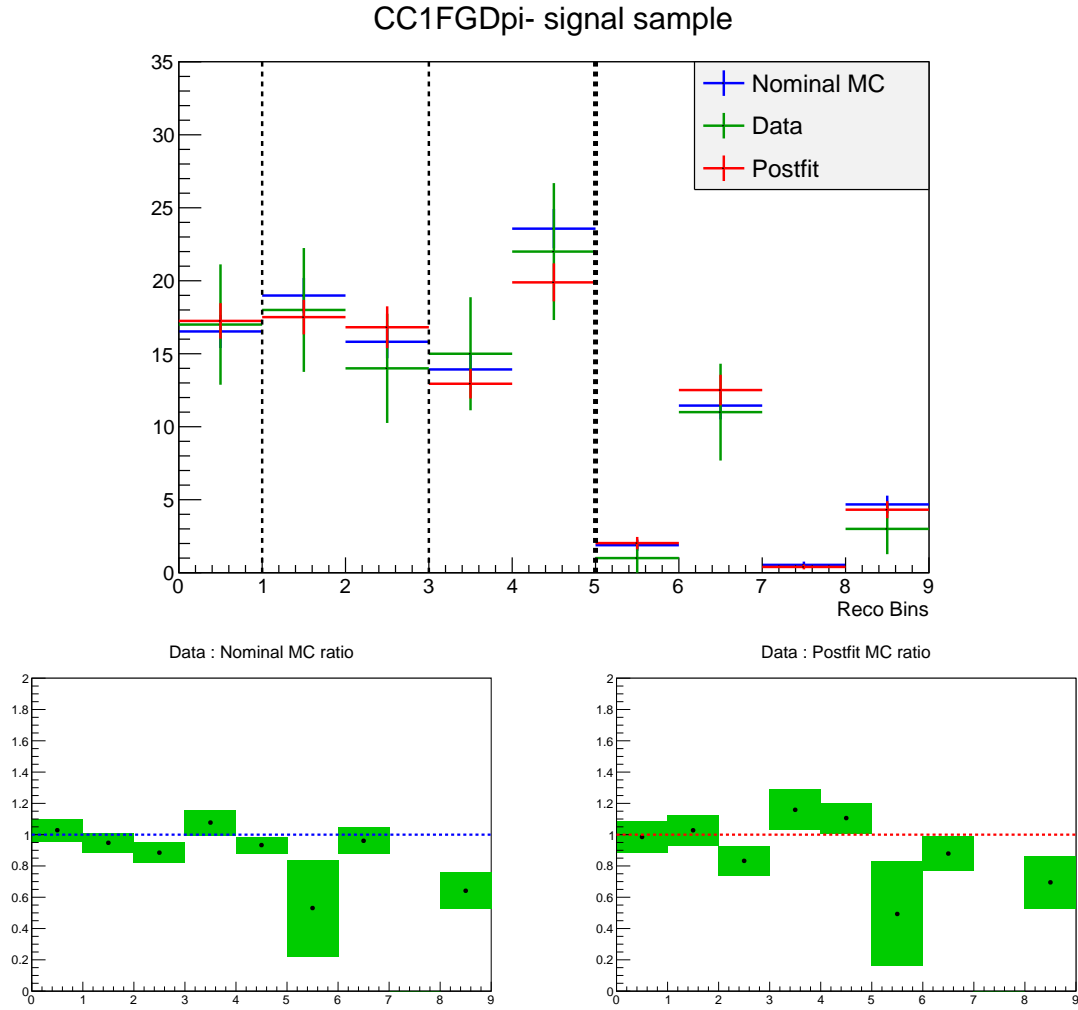


Figure 6.6: **CC1FGD $\pi^-$  signal selection.** Top: Data and NEUT MC distribution in the *reconstructed phase-space* binning (see Table 5.4, p. 120). Thin dashed lines separate different angular regions of the phase space:  $0.74 < \cos\theta_\mu < 0.88$  (bin 0),  $0.88 < \cos\theta_\mu < 0.97$  (bins 1-2),  $0.97 < \cos\theta_\mu < 1$  (bins 3-4). Thick dashed line separates out of phase-space region. Bottom left: data to prefit MC ratio. Bottom right: data to postfit MC ratio.

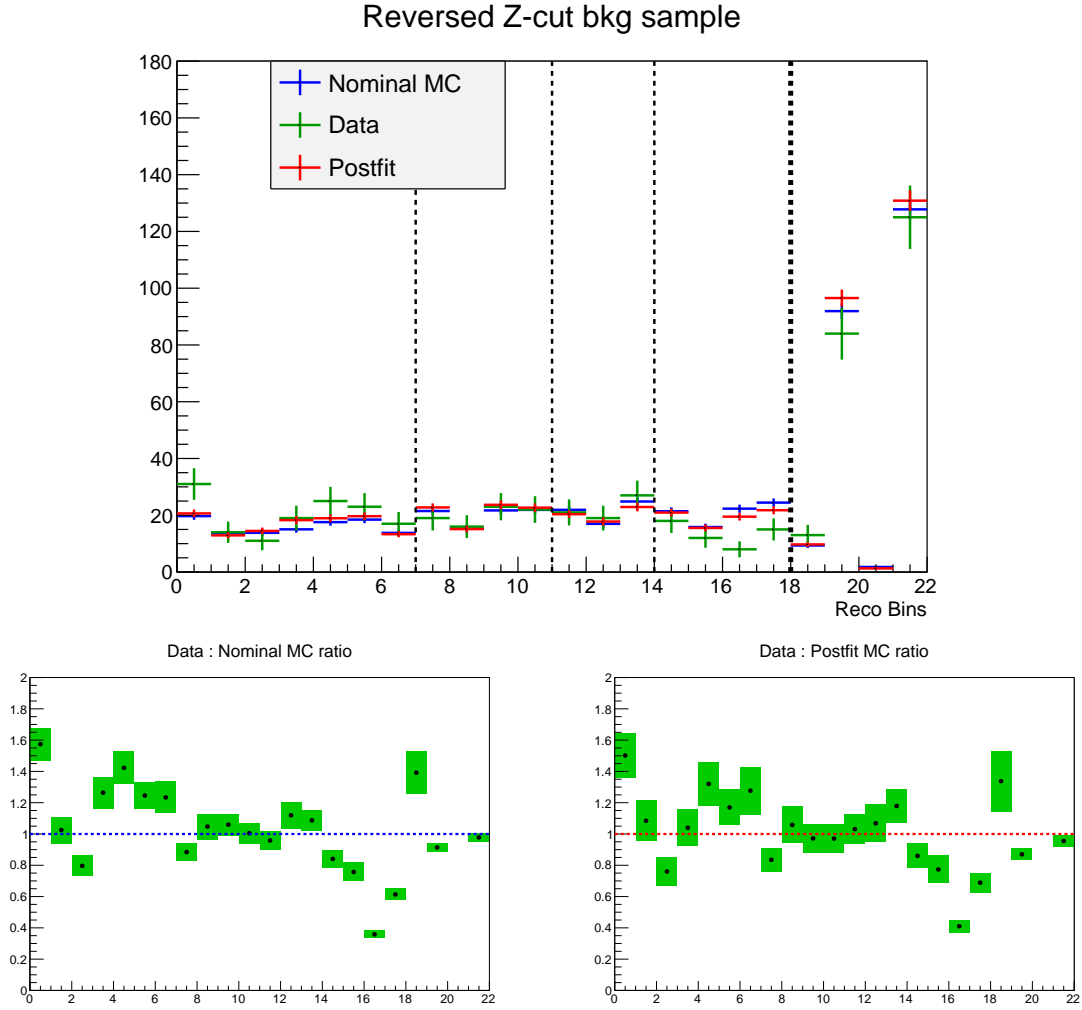


Figure 6.7: **Reversed Z-range cut background selection.** Top: Data and NEUT MC distribution in the *reconstructed phase-space* binning (see Table 5.5, p. 121). Thin dashed lines separate different angular regions of the phase space:  $0.74 < \cos \theta_\mu < 0.88$  (bins 0-6),  $0.88 < \cos \theta_\mu < 0.94$  (bins 7-10),  $0.94 < \cos \theta_\mu < 0.97$  (bins 11-13),  $0.97 < \cos \theta_\mu < 1$  (bins 14-17). Thick dashed line separates out of phase-space region. Bottom left: data to prefit MC ratio. Bottom right: data to postfit MC ratio.

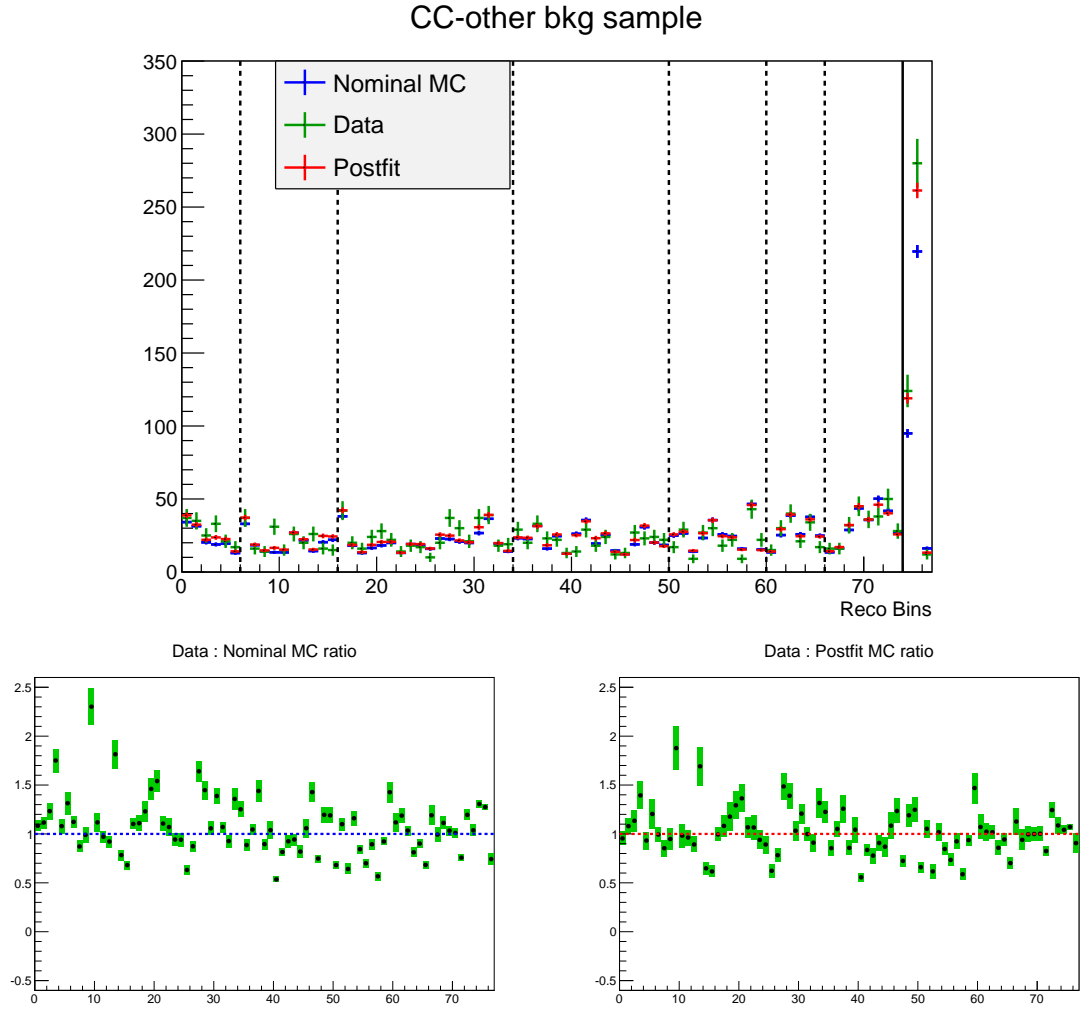


Figure 6.8: **CC-other background selection.** Top: Data and NEUT MC distribution in the *reconstructed phase-space* binning (see Tables 5.6-5.8, pp. 123-125). Thin dashed lines separate different angular regions of the phase space:  $0.74 < \cos \theta_\mu < 0.82$  (bins 0-5),  $0.82 < \cos \theta_\mu < 0.88$  (bins 6-15),  $0.88 < \cos \theta_\mu < 0.94$  (bins 16-33),  $0.94 < \cos \theta_\mu < 0.97$  (bins 34-49),  $0.97 < \cos \theta_\mu < 1$  (bins 50-59),  $0.97 < \cos \theta_\mu < 1$  (bins 60-65),  $0.97 < \cos \theta_\mu < 1$  (bins 66-73). Solid line separates out of phase-space region. Bottom left: data to prefit MC ratio. Bottom right: data to postfit MC ratio.

## 6.2. Fit output

The fit results for template parameters are presented in Fig. 6.9. The template parameters correspond to the *true phase-space* bins reported in Table 5.9 in Chapter 5. In this fit five template parameters were fitted to negative values (bins: 12, 14, 21, 22 and 28). Naturally, the negative cross section is unphysical, but if the assigned uncertainty is large enough then the measurement still might be correct. In this case all negative postfit parameters agree with positive cross section within the margin of error. Note that the bins with negative template parameters are located next to the bins with very high template parameters i.e. 13, 15 and 27 (bins 22 and 27 correspond to the same momentum region and neighbouring angular regions). Some of those bins, especially bin 27 are characterised by relatively bad momentum reconstruction resolution (see Table 5.10, p. 128) which may cause strong anticorrelations between bordering bins. The cross section will be reported both in this binning and in a coarser one, where a number of bins are merged.

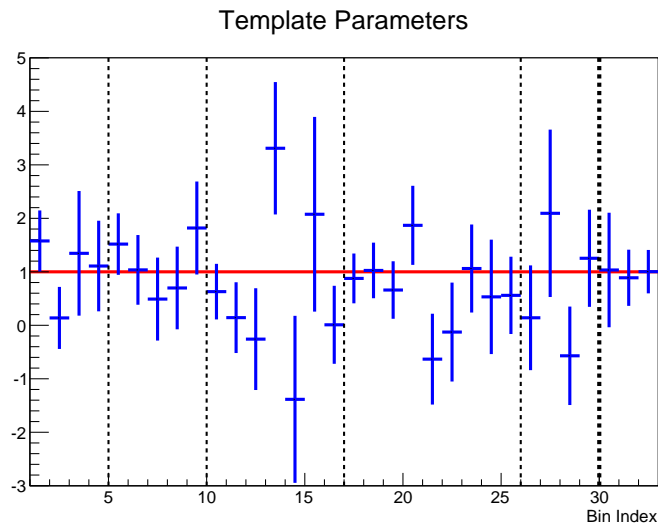


Figure 6.9: NEUT to data fit: postfit template parameters' values and errors. Thin dashed lines separate different angular regions of the phase space:  $0.74 < \cos \theta_\mu < 0.88$  (bins 1-4),  $0.88 < \cos \theta_\mu < 0.94$  (bins 5-9),  $0.94 < \cos \theta_\mu < 0.97$  (bins 10-16),  $0.97 < \cos \theta_\mu < 1$  (bins 17-25),  $0.99 < \cos \theta_\mu < 1$  (bins 26-29). Within each angular region higher bin index corresponds to higher momentum  $p_\mu$  (see Table 5.9, p. 126). Thick dashed line separates the out of phase-space region.

The fit results for nuisance model parameters are presented in Fig. 6.10. There is an overall very good agreement between prefit and postfit parameters' values (better than in case of NEUT to GENIE fit). The difference between prefit and postfit value is smaller than  $\frac{1}{2}$  of corresponding postfit error for all but two parameters:  $CCDIS_{norm}$

and  $NCOTH$ .  $CCDIS_{norm}$  normalises CC DIS interactions for  $W > 2$  GeV/c<sup>2</sup> and  $NCOTH$  normalises NC interactions other than coherent (see section 4.2). These two modes of interaction contribute to about 45% of predicted event rate in CC-other sample for nominal NEUT MC. Both  $CCDIS_{norm}$  and  $NCOTH$  parameters are pulled up in the fit due to the excess of data event rate in CC-other sample. In order to better understand this effect, additional NEUT to data fit was done without CC-other sample (see Appendix B).

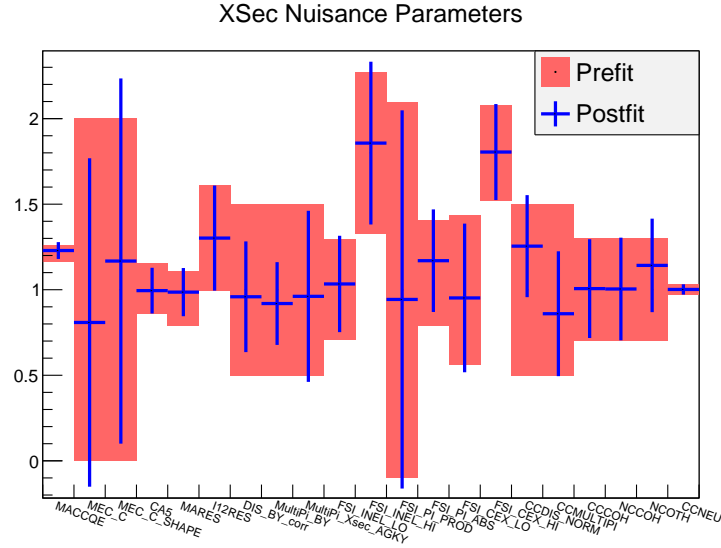


Figure 6.10: NEUT to data fit: postfit nuisance model parameters' values and errors.

The fit results for nuisance flux and detector systematic parameters are presented in Figs. 6.11-6.12. In most cases postfit values of these parameters agree with prefit values within the margin of uncertainty, although some detector systematic nuisance parameters were changed quite significantly. The latter feature is caused by the usage of CC-other sample (see Appendix B for fit results without CC-other sample).

The initial and final  $\chi^2$  quantity, which is minimised in the fit, is reported in Table 6.2. The postfit  $\chi^2$  value is bigger than in most fluctuation tests in Chapter 5 (namely, for the statistical+systematic fluctuations the postfit  $\chi^2$  is bigger in only 9 out of 500 fits - see Fig. 5.22-right). This is caused by high  $\chi^2_{stat}$  contribution from reversed Z-cut sample ( $\chi^2_{stat} = 28.198$  per 22 reconstructed  $PS$  bins) and CC-other sample (90.288 per 77 reconstructed  $PS$  bins).

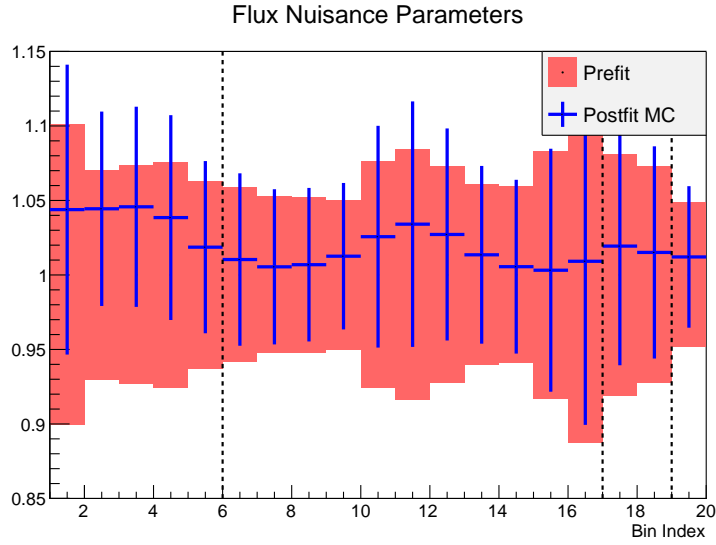


Figure 6.11: NEUT to data fit: postfit nuisance flux parameters' values and errors. Dashed lines separate parameters corresponding to different neutrino flavours:  $\nu_\mu$  (bins 1-5),  $\bar{\nu}_\mu$  (bins 6-16),  $\nu_e$  (bins 17-18),  $\bar{\nu}_e$  (bin 19).

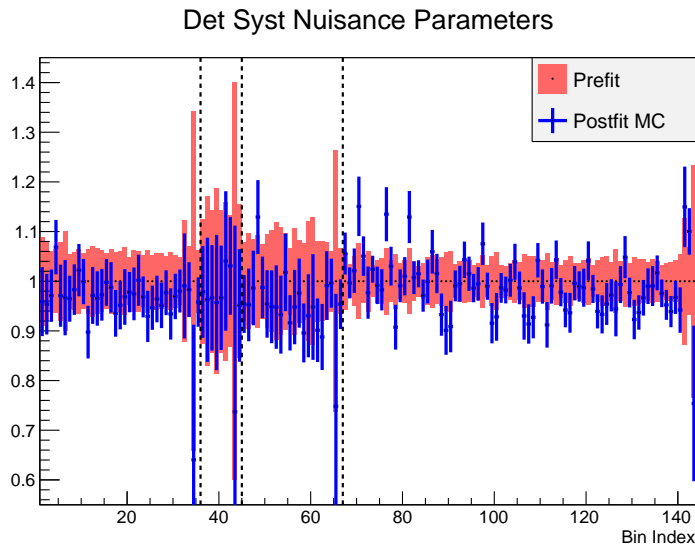


Figure 6.12: NEUT to data fit: postfit nuisance detector systematic parameters' values and errors. Dashed lines separate parameters corresponding to different analysis samples: CC1TPC $\pi^-$  signal sample (bins 1-35), CC1FGD $\pi^-$  signal sample (bins 36-44), Reversed Z-cut background sample (bins 45-66), CC-other background sample (bins 67-143).

$\chi^2$ contribution	Initial	Final
Total $\chi^2$	218.20	141.58
$\chi_{stat}^2$	218.20	129.54
per CC1TPC $\pi^-$ sample	38.367	7.9441
per CC1FGD $\pi^-$ sample	2.7504	3.1129
per Reversed Z-cut sample	36.131	28.198
per CC-other sample	140.96	90.288
$\chi_{syst}^2$	0	12.038
$\chi_{flux}^2$	0	0.5478
$\chi_{model}^2$	0	1.0068
$\chi_{detsyst}^2$	0	10.484

Table 6.2: NEUT to data fit. Comparison of  $\chi^2$  value before and after the fit. Contribution of different systematic sources is included.

### 6.3. Cross section extraction

The extracted differential cross section for the NEUT v5.4.0 MC fitted to data is presented in Fig. 6.13. Plots with logarithmic and linear scale are shown in order to better visualise differences in all bins. GENIE MC v2.8.0 is also included for a reference. The error propagation was done for 500 toy Monte Carlo experiments. Corresponding covariance matrix is presented in Fig. 6.14. One can notice anticorrelations between cross section in bin 27 and cross section in bins 26, 28. As indicated in section 6.2 this may be related to momentum reconstruction resolution which is worse in bin 27 than in other bins.

In order to compare the postfit cross section distribution  $\sigma_i^{postfit}$  with the nominal NEUT and GENIE cross section distributions  $\sigma_i^{NEUT/GENIE}$  one can calculate  $\chi_{NEUT/GENIE}^2$  as:

$$\chi_{NEUT/GENIE}^2 = \sum_{i,j}^{true\ PS} (\sigma_i^{postfit} - \sigma_i^{NEUT/GENIE})(C_\sigma)_{ij}^{-1}(\sigma_j^{postfit} - \sigma_j^{NEUT/GENIE}),$$

where  $i, j$  indices run over *true phase-space* bins and  $C_\sigma$  is the postfit cross section covariance matrix. This quantity is found to be equal to:

$$\chi_{NEUT}^2 = \begin{cases} 26.071 & \text{per 32 bins (including OOPS)} \\ 25.23 & \text{per 29 bins (without OOPS)} \end{cases}$$

$$\chi_{GENIE}^2 = \begin{cases} 60.996 & \text{per 32 bins (including OOPS)} \\ 55.699 & \text{per 29 bins (without OOPS)} \end{cases}$$

which shows that the postfit cross section distribution is closer to nominal NEUT rather than nominal GENIE predictions.

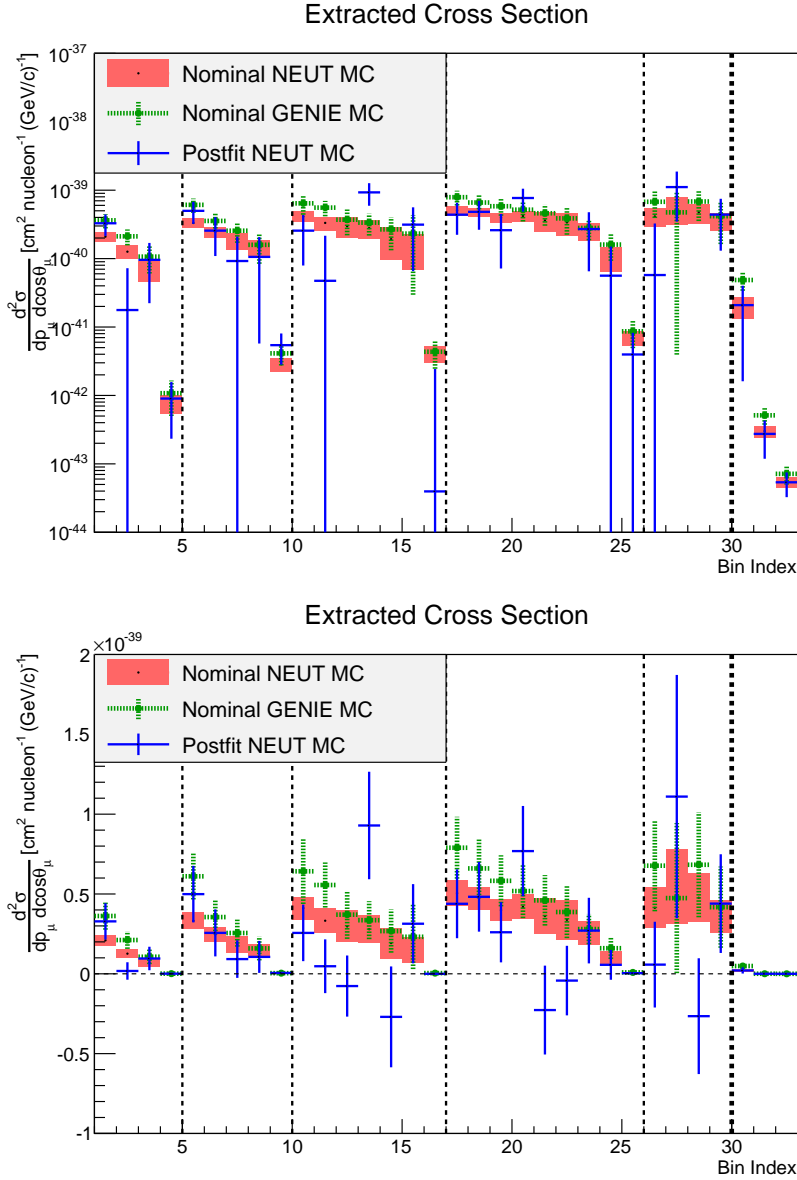


Figure 6.13: NEUT to data fit: Extracted cross section reported in *true phase-space* bins (see Table 5.9, p. 126). Thin dashed lines separate different angular regions of the phase space:  $0.74 < \cos\theta_\mu < 0.88$  (bins 1-4),  $0.88 < \cos\theta_\mu < 0.94$  (bins 5-9),  $0.94 < \cos\theta_\mu < 0.97$  (bins 10-16),  $0.97 < \cos\theta_\mu < 1$  (bins 17-25),  $0.99 < \cos\theta_\mu < 1$  (bins 26-29). Within each angular region higher bin index corresponds to higher momentum  $p_\mu$ . Thick dashed line separates the out of phase-space region. Top plot: logarithmic scale. Bottom plot: linear scale.

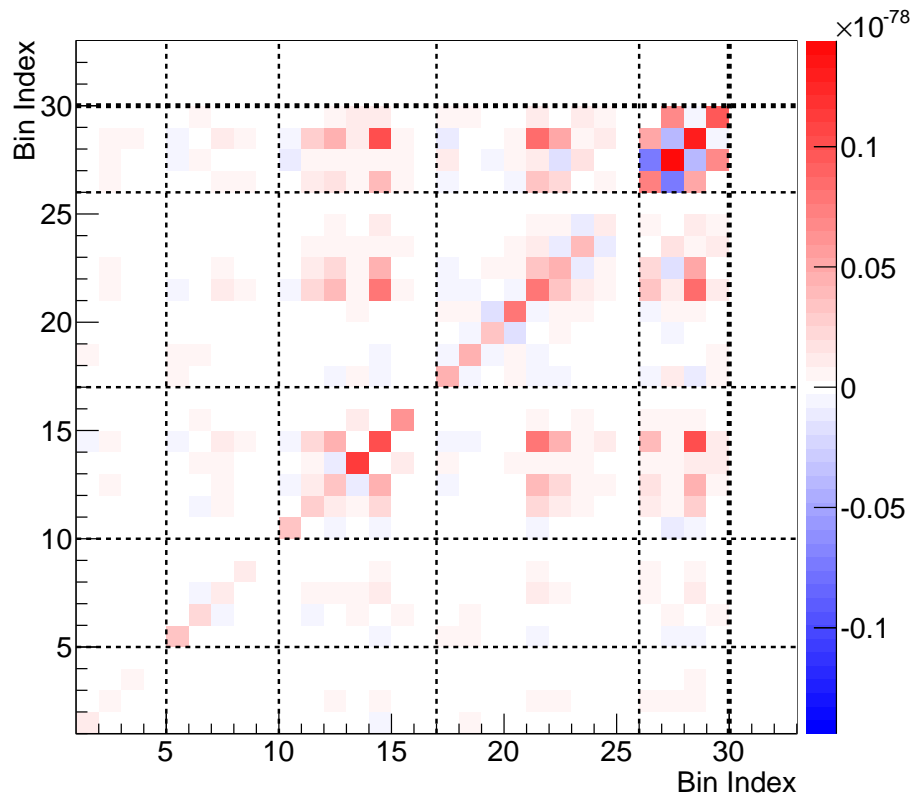


Figure 6.14: NEUT to data fit: Covariance matrix for the extracted cross section. Thin dashed lines separate different angular regions of the phase space:  $0.74 < \cos \theta_\mu < 0.88$  (bins 1-4),  $0.88 < \cos \theta_\mu < 0.94$  (bins 5-9),  $0.94 < \cos \theta_\mu < 0.97$  (bins 10-16),  $0.97 < \cos \theta_\mu < 1$  (bins 17-25),  $0.99 < \cos \theta_\mu < 1$  (bins 26-29). Within each angular region higher bin index corresponds to higher momentum  $p_\mu$ . Thick dashed lines separate out of phase-space region. Color scale constrained for better visualisation.

As mentioned in section 1.5 the cross section is reported also in coarser binning defined in Table 5.1, p. 117. For clarity the relation between fine *true phase-space* binning (applied in the aforementioned plots) and the coarse binning is given in Table 6.3. Some of the coarse bins correspond to the merged clusters of the fine bins. OOPS region is omitted in the coarse binning.

Coarse binning	Fine binning
1	1
⋮	⋮
7	7
8	8+9
9	10
10	11
11	12
12	13+14+15+16
13	17
14	18
15	19
16	20+...+29

Table 6.3: *True phase-space* binning. Relation between coarse binning and fine binning. Bins 1-7 are identical in both schemes. For exact definitions see Tables 5.1 (p. 117) and 5.9 (p. 117).

The extracted differential cross section in the coarse *true phase-space* binning and the corresponding covariance matrix are presented in Fig. 6.15. One can see that in bins 9-11 (kinematic region of  $0.94 < \cos\theta_\mu < 0.97$ ,  $200 \text{ MeV}/c < p_\mu < 1100 \text{ MeV}/c$ ) the postfit cross section is significantly smaller than the nominal prediction of both NEUT and GENIE. In the coarse binning scheme bin 11 is the only one for which the extracted cross section has a negative value whereas in the fine binning scheme there were five such bins. This suggests that negative values of template parameters shown in Fig. 6.9 are a result of fluctuations at low event rate. Additional plots with the double differential cross section shown as a function of momentum in different angular regions are presented in Fig. 6.16.

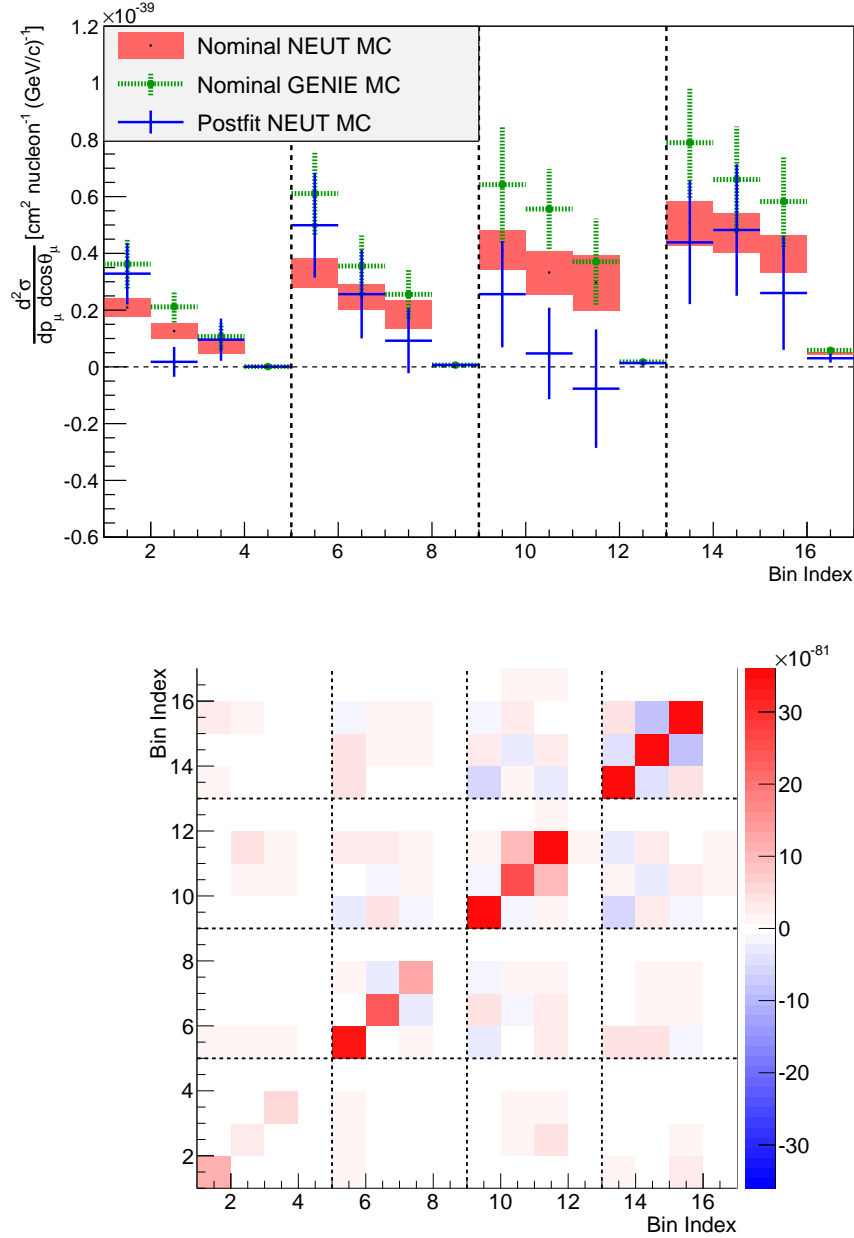


Figure 6.15: NEUT to data fit. Top: Extracted cross section reported in **coarse true phase-space** bins (see Table 5.1). Bottom: Cross section covariance matrix. The dashed lines separate different angular regions of the phase space:  $0.74 < \cos\theta_\mu < 0.88$  (bins 1-4),  $0.88 < \cos\theta_\mu < 0.94$  (bins 5-8),  $0.94 < \cos\theta_\mu < 0.97$  (bins 9-12),  $0.97 < \cos\theta_\mu < 1$  (bins 13-16). Within each angular region higher bin index corresponds to higher momentum  $p_\mu$ .

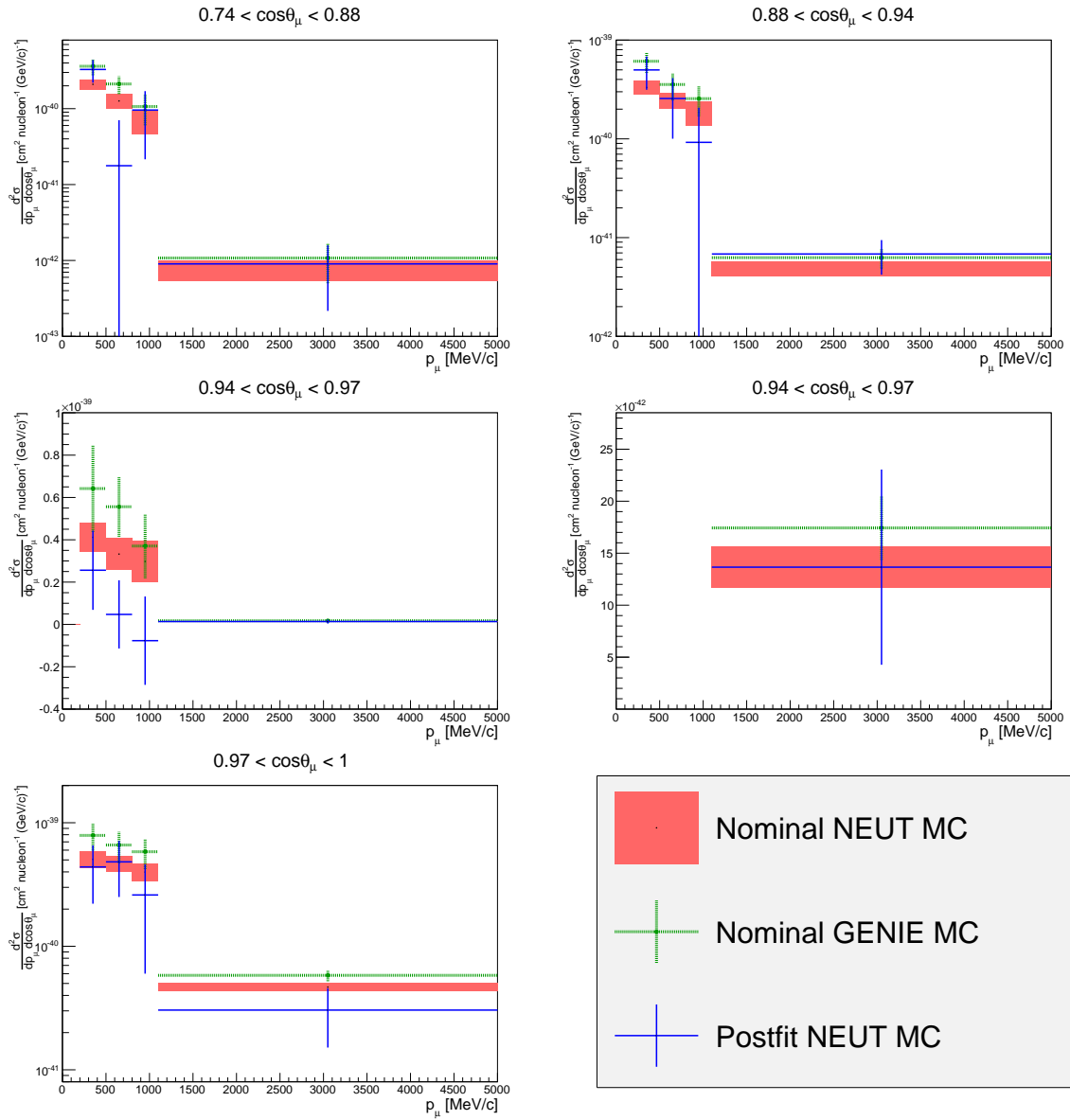


Figure 6.16: NEUT to data fit. Extracted cross section as a function of  $p_\mu$  for different  $\cos\theta_\mu$  regions. Momentum bins in range 1.1-30  $\text{GeV}/c$  were drawn in the plots as 1.1-5  $\text{GeV}/c$  bins for better visualisation. The middle right plot shows the same part of phase space as the middle left plot, but is zoomed in order to present results in high momentum bin.

Next the cross section is integrated over the  $\mu^+$  emission angle and reported in 4  $p_\mu$  bins: 200-500 MeV/c, 500-800 MeV/c, 800-1100 MeV/c and 1100-30000 MeV/c. The result is presented in Fig. 6.17 together with the corresponding covariance matrix. One can see that in low momentum bin 200-500 MeV/c the postfit cross section is slightly higher than the nominal NEUT and lower than the nominal GENIE prediction. For

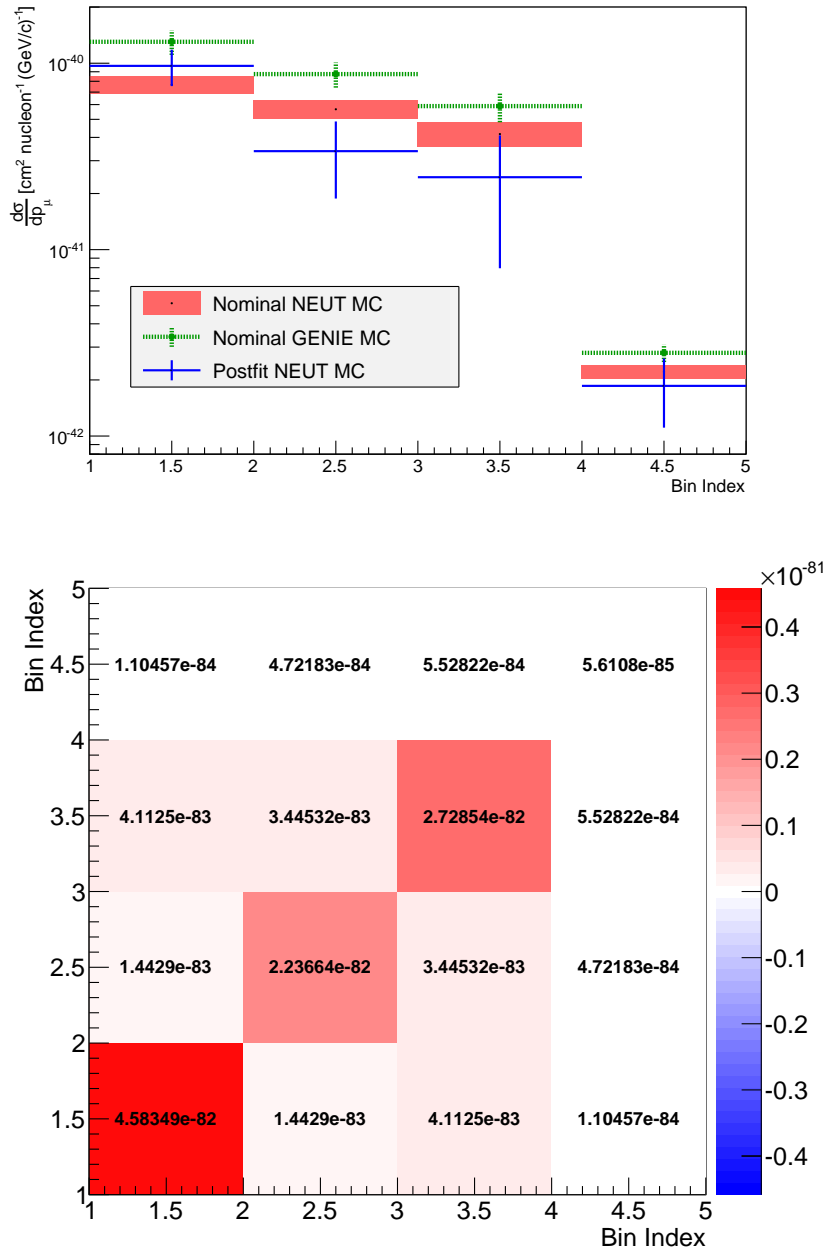


Figure 6.17: NEUT to data fit. Top: Extracted cross section reported in true  $\mu^+$  momentum bins: 200-500 MeV/c, 500-800 MeV/c, 800-1100 MeV/c and 1100-30000 MeV/c. Bottom: Cross section covariance matrix.

$p_\mu > 500$  MeV/c the fit favours cross section lower than in both generators.

Next the cross section is reported in 4  $\cos\theta_\mu$  bins:  $0.74 < \cos\theta_\mu < 0.88$ ,  $0.88 < \cos\theta_\mu < 0.94$ ,  $0.94 < \cos\theta_\mu < 0.97$  and  $0.97 < \cos\theta_\mu < 1$ , integrated over the  $\mu^+$  momentum. The result is presented in Fig. 6.18 together with the corresponding covariance matrix. In the first two bins (kinematic region of  $0.74 < \cos\theta_\mu < 0.94$ )

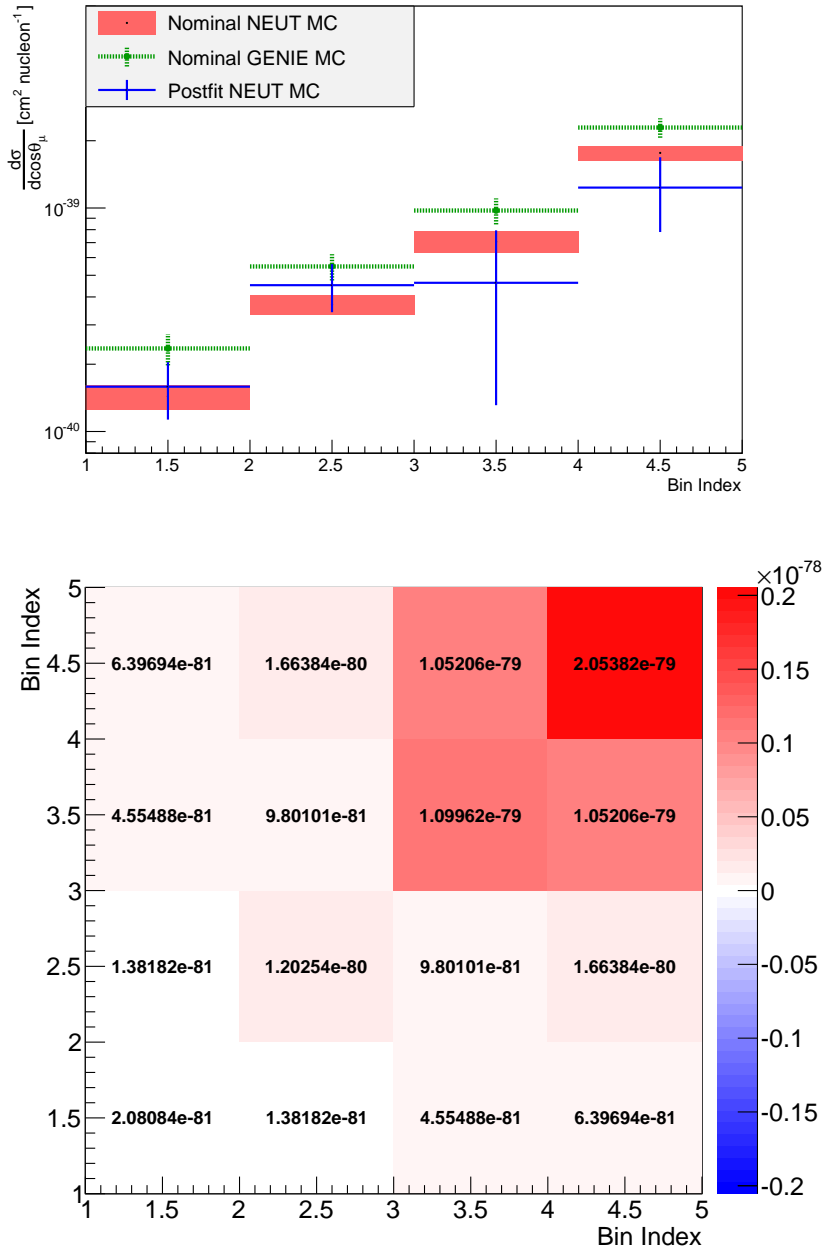


Figure 6.18: NEUT to data fit. Top: Extracted cross section reported in true  $\mu^+$   $\cos\theta$  bins:  $0.74 < \cos\theta_\mu < 0.88$ ,  $0.88 < \cos\theta_\mu < 0.94$ ,  $0.94 < \cos\theta_\mu < 0.97$  and  $0.97 < \cos\theta_\mu < 1$ . Bottom: Cross section covariance matrix.

the postfit cross section is higher than the nominal NEUT and lower than the nominal GENIE prediction. For  $\cos\theta_\mu > 0.94$  the fit favours cross section lower than in both generators.

Equivalent plots with differential cross section  $d\sigma/dp_\mu$  as a function of  $p_\mu$ , and differential cross section  $d\sigma/d\cos\theta_\mu$  as a function of  $\cos\theta_\mu$  are presented in Fig. 6.19.

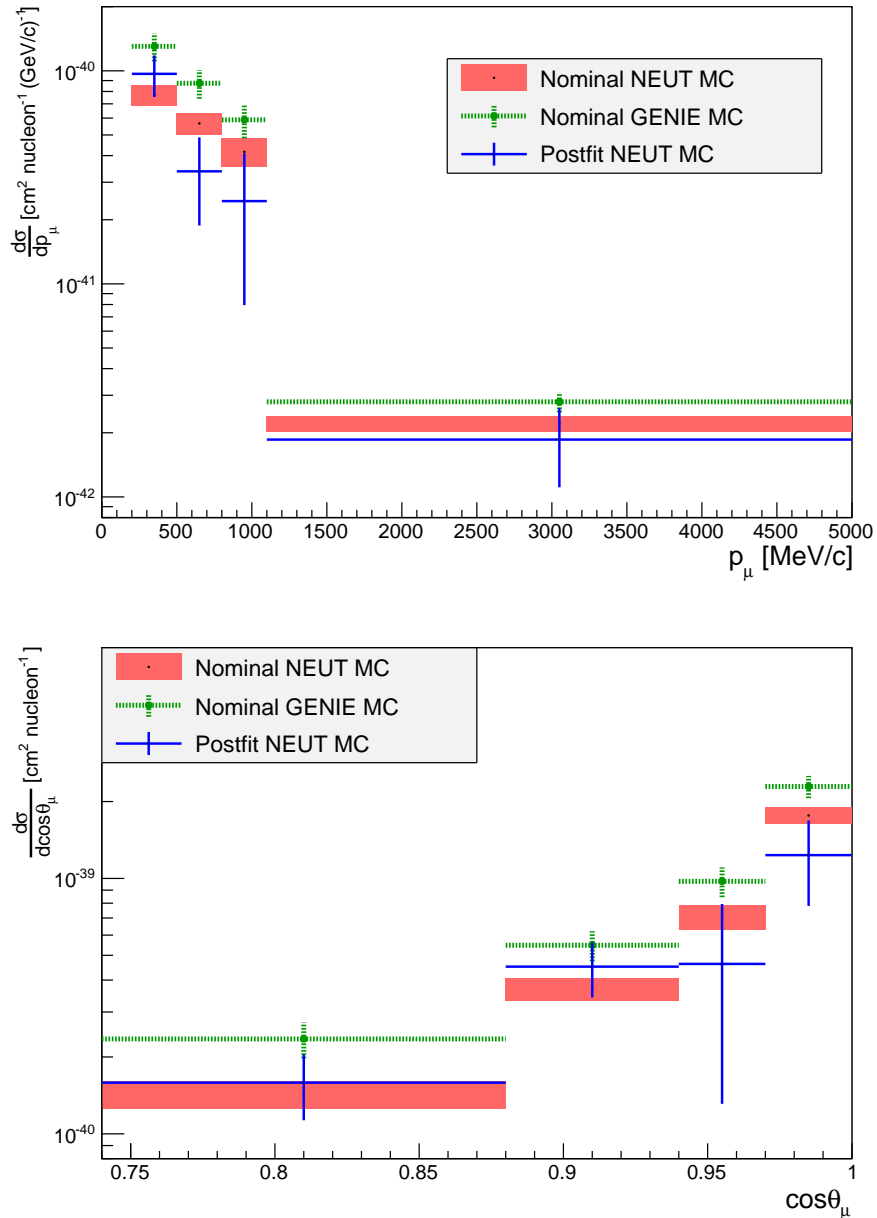


Figure 6.19: NEUT to data fit. Top: Extracted cross section reported in true  $\mu^+$  momentum. Momentum bin in range 1.1-30 GeV/c was drawn in the plot as 1.1-5 GeV/c bin for better visualisation. Bottom: Extracted cross section reported in true  $\mu^+$   $\cos\theta$ .

Finally the total postfit cross section  $\sigma_{total}$  integrated over the restricted phase-space is found to be:

$$\sigma_{total} = (1.002 \pm 0.277[\text{stat+syst}] \pm 0.123[\text{stat}]) \times 10^{-40} \text{ cm}^2 \text{ per nucleon.}$$

This result agrees within the margin of error with the cross section obtained from nominal NEUT v5.4.0 MC sample:  $\sigma_{NEUT} = (1.164 \pm 0.091) \times 10^{-40} \text{ cm}^2 \text{ per nucleon}$ . It is however significantly smaller than the cross section obtained from nominal GENIE v2.8.0 MC sample:  $\sigma_{GENIE} = (1.638 \pm 0.152) \times 10^{-40} \text{ cm}^2 \text{ per nucleon}$ . An important difference between these two generators is in Rein-Sehgal coherent model, which is used with Berger-Sehgal correction in NEUT, but without such correction in GENIE. Comparison between these results is presented in Fig. 6.20. One can conclude that data favours NEUT v5.4.0 over GENIE v2.8.0. This observation agrees with another T2K analysis [140] where measured  $\nu_\mu$  CC1 $\pi^+$  cross section favoured NEUT v5.3.3 scaled to the Berger-Sehgal coherent model over default NEUT v5.3.3 with Rein-Sehgal coherent model.

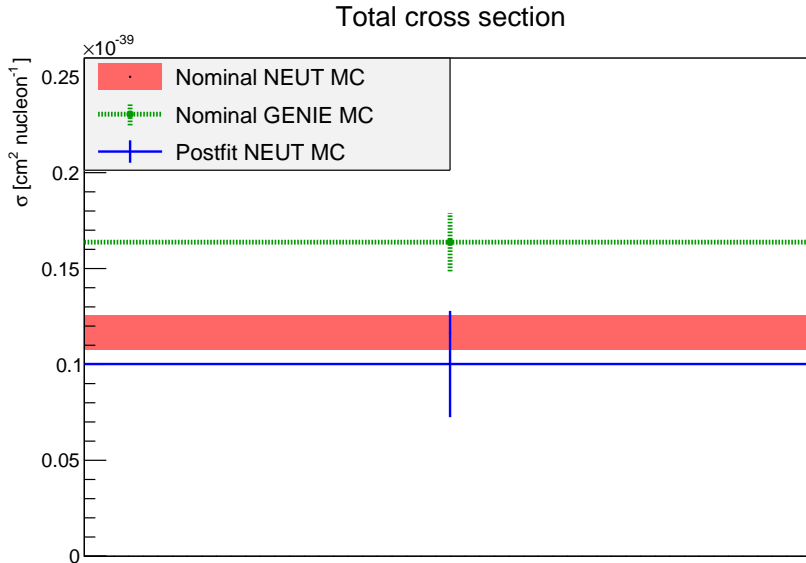


Figure 6.20: NEUT to data fit. Comparison of the total postfit cross section with nominal NEUT and GENIE results.

Despite overall good agreement between the extracted cross section and nominal NEUT v5.4.0, the results in kinematic region of ( $200 \text{ MeV}/c < p_\mu < 1100 \text{ MeV}/c$ ,  $0.94 < \cos\theta_\mu < 0.97$ ) indicates that nominal Monte Carlo predictions are overestimated in this part of the phase-space, as can be seen in Fig. 6.15-top for bins 9-11. Note however that bins 10 and 11 are correlated (Fig. 6.15-bottom), which makes the data-MC discrepancy less significant.

# Summary and outlook

In the presented Thesis the cross section measurement of single  $\pi^-$  production in  $\bar{\nu}_\mu$  CC interaction on hydrocarbon was reported. This interaction channel is an important one at T2K energy scale and it contributes to the background in the far detector event samples which are used in the oscillation analysis. In case of  $\pi^-$  misreconstruction the event may be classified as CCQE-like and change the measured event rate, thus affecting the extracted oscillation parameters. The cross section measurement allows to constrain the modelling of the background in the CCQE-like sample and to validate neutrino interaction models in general.

The measurement was done in T2K near detector ND280 with scintillator FGD1 subdetector used as the target for  $\bar{\nu}_\mu$  interactions. The cross section was measured as integrated over the energy spectrum of the incident neutrino beam (so-called *flux integrated* cross section). Data used in the measurement were collected in  $\bar{\nu}_\mu$  beam mode runs and correspond to about  $8.5 \times 10^{20}$  POT. Until the final stages of analysis Author followed *blind analysis* strategy and did not check the selected data event rates. The selection optimisation and detector systematic error estimation were done with NEUT v5.4.0 MC samples.

The signal selection is based on the reconstruction of  $\mu^+$  and  $\pi^-$  tracks. The separation of the signal events is difficult, due to high  $\nu_\mu$  flux contamination in the  $\bar{\nu}_\mu$  beam. In particular the interactions with single  $\pi^+$  production by  $\nu_\mu$  can be confused with signal if true  $\mu^-$  is misidentified as  $\pi^-$  and true  $\pi^+$  is misidentified as  $\mu^+$ . Both topologies look very similar in the detector: a pair of two track of different charge, with practically identical mean energy loss.

In order to suppress this background, Author introduced the so-called Z-range cut, where Z-coordinate  $Z_{\mu/\pi}$  of the ending positions of reconstructed  $\mu^+$  and  $\pi^-$  tracks are taken into account. A basic motivation for this cut was the fact that on average muons propagate in matter further than hadrons, which may strongly reinteract with the matter. Events with  $Z_\mu - Z_\pi > -10$  cm are selected as signal and those which fail this cut constitute the *reversed Z-cut background sample*. A set of efficiency studies was done in order to check that the Z-range cut does not introduce model dependency.

Altogether, two signal samples and two background samples were used. The leading detector systematic was related to pion secondary interactions. Author introduced an improvement in calculation of that uncertainty by applying dynamic volume of interest.

The cross section was extracted with the likelihood fit method. The nominal NEUT Monte Carlo predictions were parametrised by so-called *nuisance* parameters related to flux normalisation, neutrino interaction modelling and detector systematic effects, as well as *template parameters* which normalise the signal. Monte Carlo predictions in four analysis samples were simultaneously fitted to data event rate and the cross section was calculated based on best fit parameters' values. A number of fake data studies was performed to validate the procedure.

The cross section was reported as double differential in  $p_\mu$  and  $\cos\theta_\mu$ . The result was also given as differential cross section in  $p_\mu$  (integrated over angle) and differential cross section in  $\cos\theta_\mu$  (integrated over momentum), as well as the total cross section  $\sigma_{total}$  integrated over the restricted phase-space:

$$\sigma_{total} = (1.002 \pm 0.277) \times 10^{-40} \text{ cm}^2 \text{ per nucleon.}$$

This result agrees within the margin of error with nominal NEUT v5.4.0 predictions and favours them over GENIE v2.8.0.

Most of analysis presented in this thesis is also described by Author in the dedicated technical note for T2K collaboration. It is planned to prepare official T2K publication about single  $\pi^-$  production measurement after the technical note passes the collaboration review. There is also another ongoing T2K analysis where the same signal is measured as double differential cross section in  $\pi^-$  kinematic variables [141] - the preliminary results has not been reviewed by the collaboration yet. This complementary measurement is done with a different selection strategy and for a different phase-space restrictions.

In the future, one can think of improvements to the presented measurements. As it was mentioned, one of the leading systematic uncertainties in the measurement is related to pion secondary interactions. The improvement of this systematic could be done by introduction of a better pion SI modelling into the detector simulation or reweighting it to the external data.

The relatively large statistical error can be reduced by using new data collected by T2K near detector in  $\bar{\nu}_\mu$  mode. As an example, if  $5 \times 10^{21}$  POT in  $\bar{\nu}_\mu$  mode could be collected in the Phase 2 of T2K and early years of Hyper-Kamiokande experiment (in which the ND280 detector will still be used), one could expect about 2100 data events in the signal samples, assuming linear growth with the POT number (as stated in section 2.5 currently there are  $1.65053 \times 10^{21}$  POT collected for  $\bar{\nu}_\mu$  beam mode).

Additionally, starting with T2K Phase 2 the current in the horns is expected to reach 320 kA instead of 250, leading to about 10% increase in number of neutrinos produced per POT.

Moreover, thanks to the planned upgrades of the near detector ND280 [142] it would be possible to enlarge the phase-space of the measurement. The new ND280 design includes a scintillator detector Super-FGD, which will consist of about 2 millions optically independent scintillator cubes. The light signal will be read out by optic fibers in three orthogonal directions. Two additional TPCs (High-Angle TPCs) will be installed: one below and one above Super-FGD. The new design will allow for better angular acceptance and lower threshold for the particle reconstruction.

By combining future ND280 data with those already existing the extraction of the cross section will be possible with much smaller statistical error.

# Appendix A: additional efficiency studies

Plots in this appendix are related to the Z-range cut described in subsection 3.3.3. The impact of this cut on selection efficiency was discussed in section 3.4. Additional studies are presented here.

## Efficiency vs difference of longitudinal momenta

Distribution of ‘Z-cut survival ratio’ was presented for  $\mu^+$  and  $\pi^-$  kinematic observables in Fig. 3.18. Additional kinematic check was done for the difference of longitudinal  $\mu^+$  and  $\pi^-$  momenta  $p_\mu^{longitudinal} - p_\pi^{longitudinal}$ . The distribution of Z-range cut survival probability versus  $p_\mu^{longitudinal} - p_\pi^{longitudinal}$  is presented in Fig. 6.21. The distributions of events prior and after the cut are included in the plots. Note that bins have different widths and in each bin the absolute event rate is reported. Majority of events is in the region of  $p_\mu^{longitudinal} > p_\pi^{longitudinal}$  and the cut survival probability is flat in this part of the phase-space. This is not the case for events with  $p_\mu^{longitudinal} < p_\pi^{longitudinal}$ , where there is a distinctive fall in the considered probability. However, this effect is less significant for selection within the restricted phase-space.

2D distribution of Z-cut survival probability is presented in Fig. 6.22. The smallest probability is for events with  $p_\mu^{longitudinal}$  below 400 MeV/c. Contribution of those events is suppressed by phase-space restrictions, which exclude low momentum muons and high angle muons.

## 4D efficiency study

Following checks were done in order to show that the Z-range cut actually distinguishes muons and pions, not only positive and negative tracks of certain kinematic properties. The efficiencies of selecting  $\bar{\nu}_\mu$  CC1 $\pi^-$  and  $\nu_\mu$  CC1 $\pi^+$  topologies were compared in 4D phase-space (negative/positive particle true momentum/ $\cos\theta$ ). The distributions of true  $\bar{\nu}_\mu$  CC1 $\pi^-$  and true  $\nu_\mu$  CC1 $\pi^+$  events selected in CC1TPC $\pi^-$  signal sample without Z-cut are shown in Fig. 6.23. The binning is explained explicitly in Table 6.4.

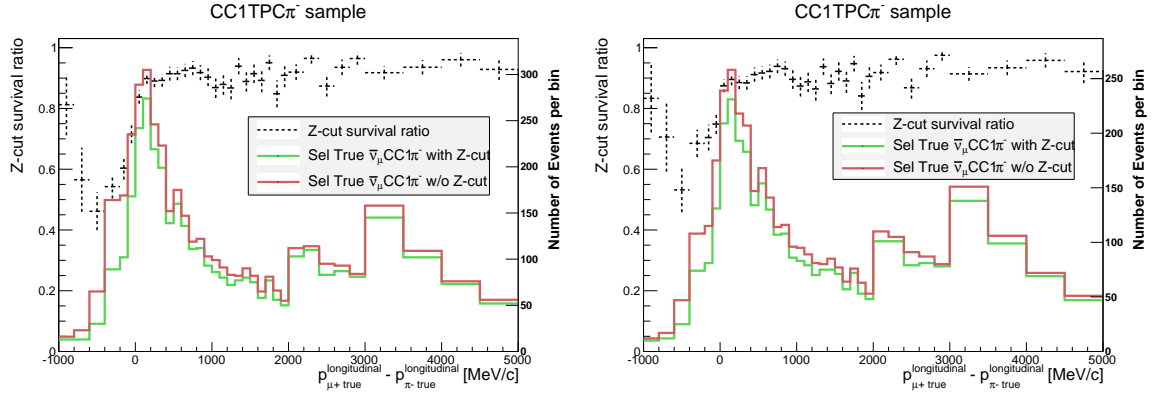


Figure 6.21: Impact of the Z-range cut on the selection efficiency - ratio of the number of signal events selected as CC1TPC $\pi^-$ +Z-range cut to those selected in the CC1TPC $\pi^-$  sample plotted as the function of the difference of true longitudinal momenta ( $p_{\mu^+}^{longitudinal} - p_{\pi^-}^{longitudinal}$ ). Left: all signal events. Right: restricted phase-space.

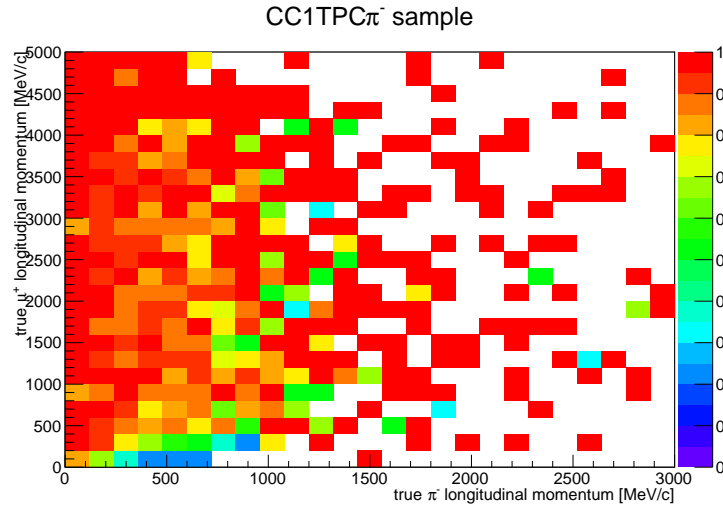


Figure 6.22: Impact of the Z-range cut on the selection efficiency - ratio of the number of signal events selected as CC1TPC $\pi^-$ +Z-range cut to those selected in the CC1TPC $\pi^-$  sample.

For the 4D efficiency study the total considered phase-space corresponds to momentum  $p < 5$  GeV/c and angle  $\cos \theta > 0.6$  for both negative and positive track. One can see that the signal  $\bar{\nu}_{\mu}$  CC1 $\pi^-$  topology and the background  $\nu_{\mu}$  CC1 $\pi^+$  topology are concentrated in very different phase-space regions. The bin most populated with the signal is (3, 3), which corresponds to events with low momentum  $\pi^-$  emitted at high angle  $\mu^+$  and high momentum forward going  $\mu^+$ . The bin most populated with the CC1 $\pi^+$  background is (7, 7), which corresponds to high momentum forward going  $\mu^-$  and low momentum high angle  $\pi^+$ .

cos $\theta$ bins		
bin number	neg particle cos $\theta$	pos particle cos $\theta$
1	[0.6; 0.85]	[0.6; 0.85]
2	[0.6; 0.85]	[0.85; 0.95]
3	[0.6; 0.85]	[0.95; 1]
4	[0.85; 0.95]	[0.6; 0.85]
5	[0.85; 0.95]	[0.85; 0.95]
6	[0.85; 0.95]	[0.95; 1]
7	[0.95; 1]	[0.6; 0.85]
8	[0.95; 1]	[0.85; 0.95]
9	[0.95; 1]	[0.95; 1]
momentum bins		
bin number	neg particle momentum [GeV/c]	pos particle momentum [GeV/c]
1	[0; 0.5]	[0; 0.5]
2	[0; 0.5]	[0.5; 1]
3	[0; 0.5]	[1; 5]
4	[0.5; 1]	[0; 0.5]
5	[0.5; 1]	[0.5; 1]
6	[0.5; 1]	[1; 5]
7	[1; 5]	[0; 0.5]
8	[1; 5]	[0.5; 1]
9	[1; 5]	[1; 5]

Table 6.4: Binning used in 4D efficiency studies.

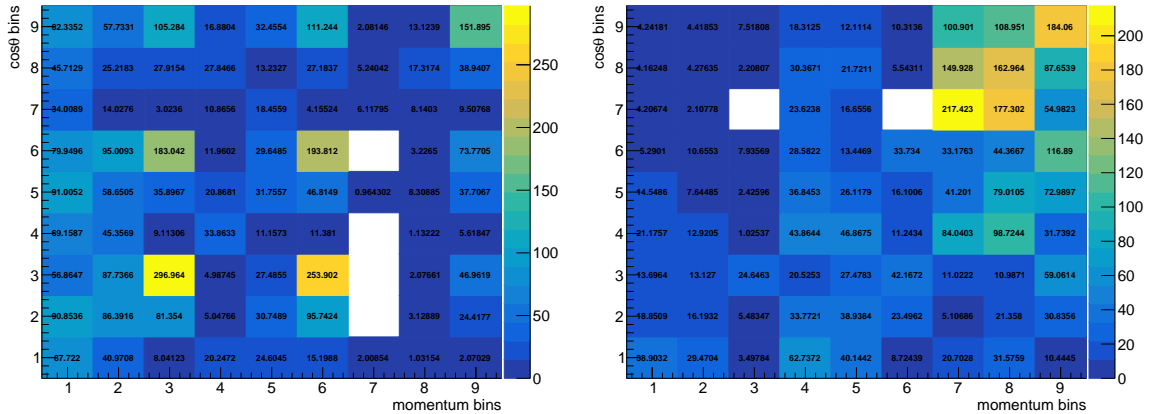


Figure 6.23: Distribution of events selected with CC1TPC $\pi^-$  selection (no Z-cut). Left: true CC1 $\pi^-$  topology. Right: true CC1 $\pi^+$  topology.

4D efficiency distributions are presented in Fig. 6.24. The total efficiency is 23.3% for  $CC1\pi^-$  and 15.5% for  $CC1\pi^+$ . The distribution of the efficiency is quite similar for both topologies. In 47 bins out of 81 the efficiency is bigger for  $CC1\pi^-$  selection, in 32 bins it is bigger for  $CC1\pi^+$  (2 bins are not populated by either topology prior to any selection so efficiencies cannot be compared).

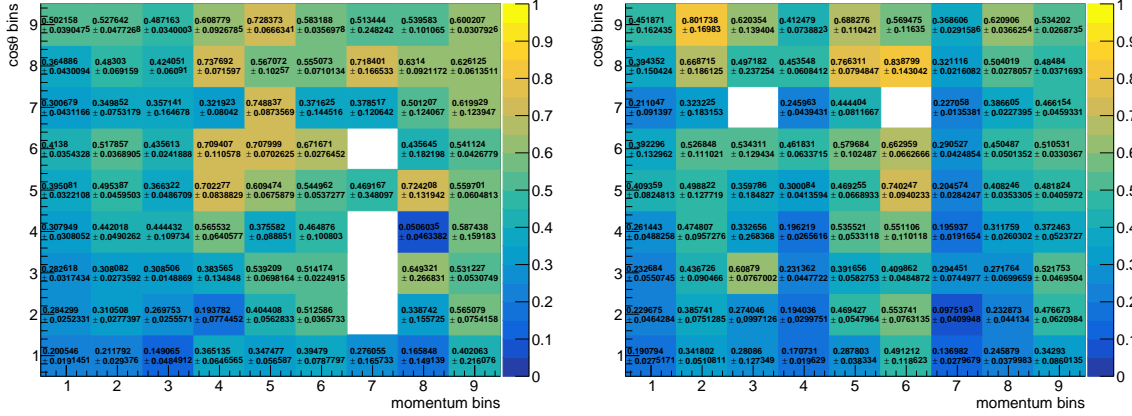


Figure 6.24: Efficiency of  $CC1\pi^-$  selection (no Z-cut). Left: true  $CC1\pi^-$  topology. Right: true  $CC1\pi^+$  topology.

The efficiency distributions for the selection with the Z-range cut are presented in Fig. 6.25. The total efficiency for  $CC1\pi^-$  decreased to 20.6%, while for  $CC1\pi^+$  it dropped to 4.1%. This effect is visible throughout the phase-space. To make the Z-range cut evaluation simpler the probability of surviving this cut (i.e. ratio of number of events in  $CC1\pi^-$  sample to events in ( $CC1\pi^- + Z$ -cut) sample) was plotted in

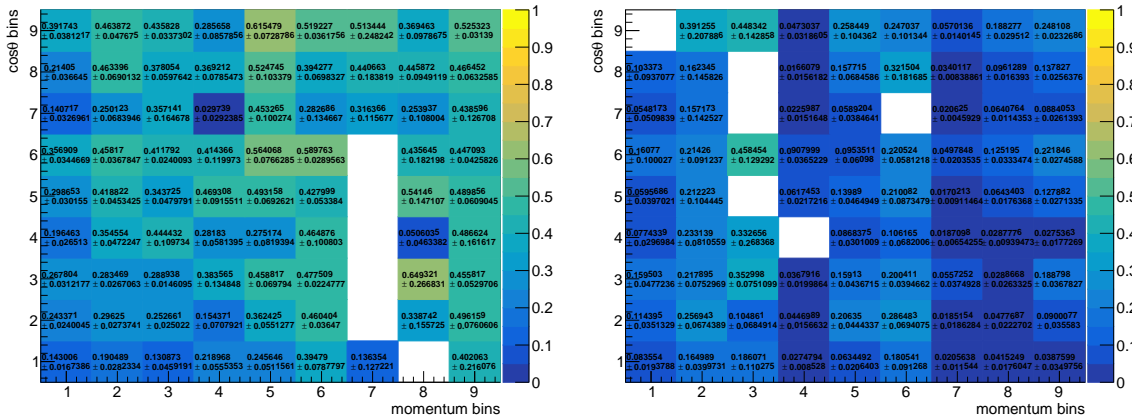


Figure 6.25: Efficiency of  $(CC1\pi^- + Z\text{-cut})$  selection. Left: true  $CC1\pi^-$  topology. Right: true  $CC1\pi^+$  topology.

4D as well (Fig. 6.26). This probability is bigger for  $CC1\pi^-$  topology in 69 out of 74 bins. (In 7 bins the number of true  $CC1\pi^-$  or  $CC1\pi^+$  events is zero for the  $CC1TPC\pi^-$  sample prior to the Z-cut.) Such advantage of  $CC1\pi^-$  topology indicates that the Z-range cut is not equivalent to momentum + direction cuts but it really distinguishes muons and pions.

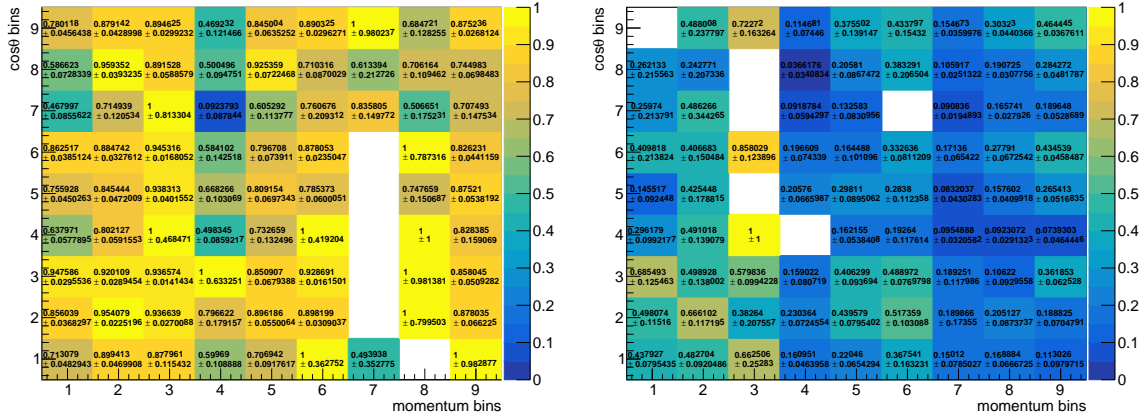


Figure 6.26: Probability of surviving the Z-range cut. Left: true  $CC1\pi^-$  topology. Right: true  $CC1\pi^+$  topology.

# Appendix B: additional Fitter studies

This appendix presents further likelihood fit studies that were not described in the main part of the thesis.

## Enhanced signal fit with statistical fluctuations

In subsection 5.3.2 the fit of nominal MC to fake data with enhanced signal contribution was discussed. Since all signal events were reweighted by a factor of 1.2, all postfit template parameters were equal to 1.2. In order to check the Fitter sensitivity to the signal in more realistic conditions this fit was repeated 500 hundred times with statistical fluctuations applied to the fake data sample in each bin of the *reconstructed phase-space*. The distributions of postfit template parameters  $c_i$  are presented in Figures 6.27-6.29 and summarised in Table 6.5.

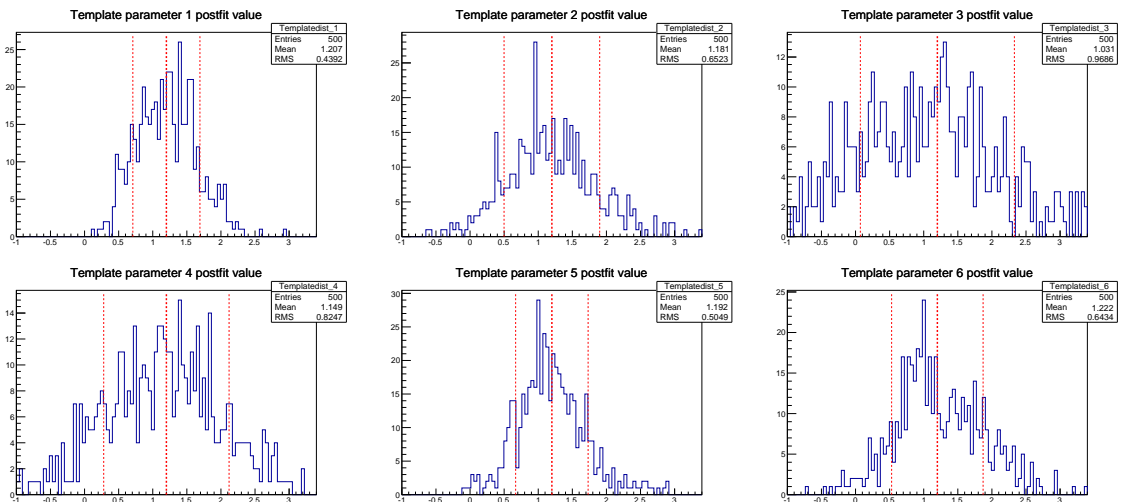


Figure 6.27: Enhanced signal fit with statistical fluctuations. Each histogram presents a distribution of postfit template parameter  $c_i$  value (**parameters from 1 to 6**). Red lines indicate the postfit value and error range obtained in the fit without fluctuations.

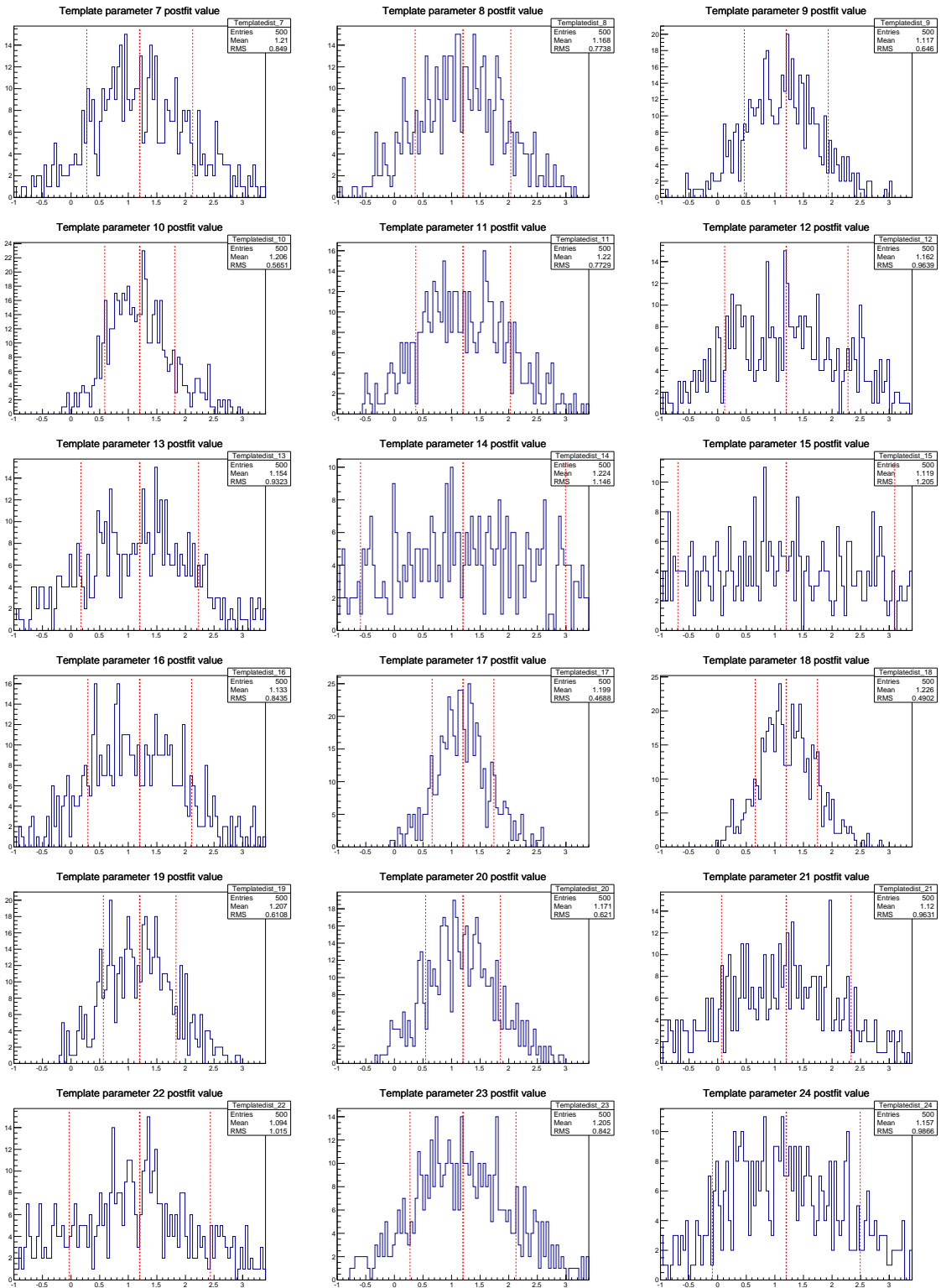


Figure 6.28: Enhanced signal fit with statistical fluctuations. Each histogram presents a distribution of postfit template parameter  $c_i$  value (**parameters from 7 to 24**). Red lines indicate the postfit value and error range obtained in the fit without fluctuations.

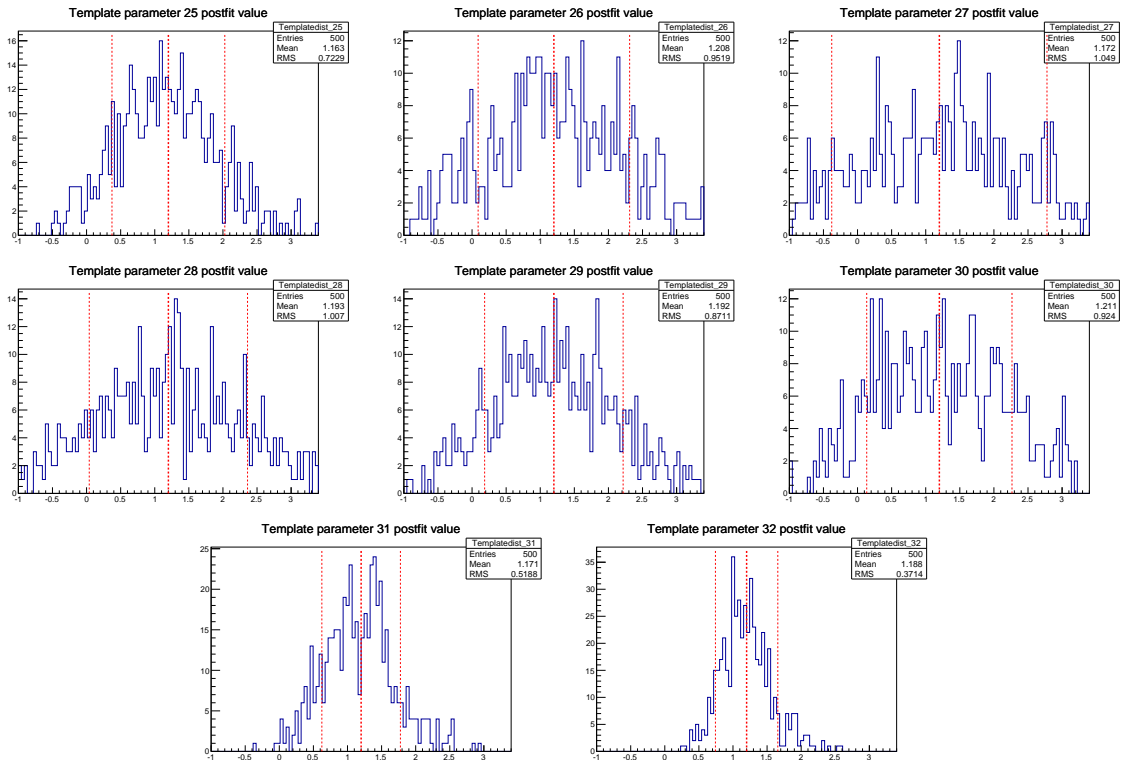


Figure 6.29: Enhanced signal fit with statistical fluctuations. Each histogram presents a distribution of a postfit template parameter  $c_i$  value (**parameters from 25 to 32**). Red lines indicate the postfit value and error range obtained in the fit without fluctuations.

For each histogram the mean  $c_i$  value should be close to 1.2. The uncertainty of the mean  $c_i$  can be estimated as RMS of  $c_i$  distribution divided by square root of the number of repeated fits. The difference between the nominal value 1.2 and the mean  $c_i$  should be smaller than the mean  $c_i$  uncertainty. This is indeed the case for majority of the template parameters (20 out of 32). For 9 parameters the difference is bigger than the mean  $c_i$  uncertainty but smaller than double mean  $c_i$  uncertainty. For 2 parameters the difference is bigger than double but smaller than triple mean  $c_i$  uncertainty. These proportions (20:9:2) are roughly in agreement with Gaussian distributed error and don't indicate anything wrong with the fit. However, for one template parameter -  $c_3$ , corresponding to bin 3 in *true phase-space* - the discrepancy is nearly four times bigger than the mean  $c_3$  uncertainty. It is therefore statistically unlikely that  $c_3$  is Gaussian distributed with mean value 1.2 and one must conclude that this template parameter is much less sensitive to the signal than other parameters. In principle, this should be fixed by reconfiguring the binning scheme, but since the problem was identified only for one parameter no modifications were applied.

Parameter index	Mean $c_i$	RMS/ $\sqrt{500}$	1.2 - mean $c_i$
1	1.207	0.020	-0.007
2	1.181	0.029	0.019
3	1.031	0.043	0.169
4	1.149	0.037	0.051
5	1.192	0.023	0.008
6	1.222	0.029	-0.022
7	1.21	0.038	-0.010
8	1.168	0.035	0.032
9	1.117	0.029	0.083
10	1.206	0.025	-0.006
11	1.22	0.035	-0.020
12	1.162	0.043	0.038
13	1.154	0.042	0.046
14	1.224	0.051	-0.024
15	1.119	0.054	0.081
16	1.133	0.038	0.067
17	1.199	0.021	0.001
18	1.226	0.022	-0.026
19	1.207	0.027	-0.007
20	1.171	0.028	0.029
21	1.12	0.043	0.080
22	1.094	0.045	0.106
23	1.205	0.038	-0.005
24	1.157	0.044	0.043
25	1.163	0.032	0.037
26	1.208	0.043	-0.008
27	1.172	0.047	0.028
28	1.193	0.045	0.007
29	1.192	0.039	0.008
30	1.211	0.041	-0.011
31	1.171	0.023	0.029
32	1.188	0.017	0.012

Table 6.5: Summary of enhanced signal fits with statistical fluctuations. Mean  $c_i$  values are compared with the postfit value 1.2 obtained without statistical fluctuations.

### NEUT to data fit without CC-other sample

In Chapter 6 the final results of  $\bar{\nu}_\mu$  CC1 $\pi^-$  cross section measurement are presented. They are obtained from fitting simultaneously the nominal NEUT MC samples to data event rate in four analysis samples: CC1TPC $\pi^-$  and CC1FGD $\pi^-$  signal samples, reversed Z-range cut and CC-other background samples. The biggest discrepancy between data and prior NEUT predictions was for the CC-other sample, where MC is underestimated with respect to data event rate (see Fig. 6.4 in Chapter 6). In order to better understand the impact of this discrepancy on the results, the fit was repeated for only three analysis samples, without CC-other.

The fit results for template parameters are presented in Figure 6.30. In general the postfit parameters' values are close to the results reported in Figure 6.9 in Chapter 6. In particular, the five template parameters which were fitted previously to negative values (bins: 12, 14, 21, 22 and 28) are again fitted to negative values (bins: 12, 14, 21, 28) or to a very low positive value (bin 22, where template parameter  $c_{22} \approx 0.066$ ; in the fit with CC-other sample it was  $c_{22} \approx -0.13$ ). One can conclude that the usage of CC-other sample has a minor impact on the postfit parameters' values.

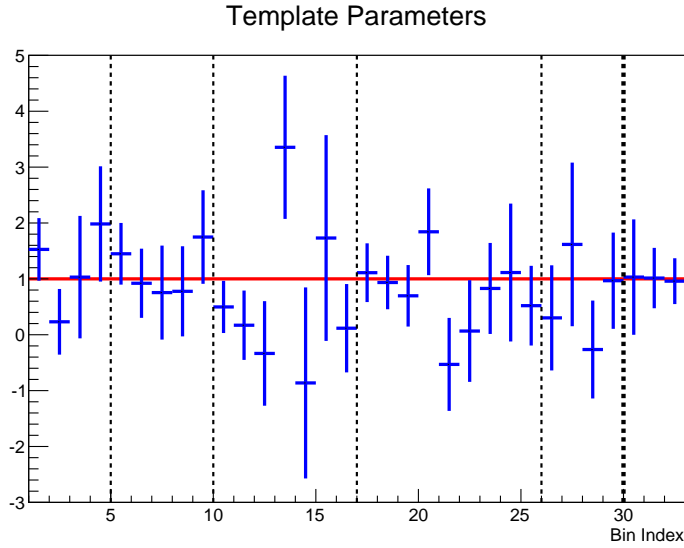


Figure 6.30: NEUT to data fit (without CC-other sample): postfit template parameters' values and errors. Thin dashed lines separate different angular regions of the phase space:  $0.74 < \cos \theta_\mu < 0.88$  (bins 1-4),  $0.88 < \cos \theta_\mu < 0.94$  (bins 5-9),  $0.94 < \cos \theta_\mu < 0.97$  (bins 10-16),  $0.97 < \cos \theta_\mu < 1$  (bins 17-25),  $0.99 < \cos \theta_\mu < 1$  (bins 26-29). Within each angular region higher bin index corresponds to higher momentum  $p_\mu$  (see Table 5.9). Thick dashed line separates out of phase-space region.

The fit results for nuisance model parameters are presented in Fig. 6.31. For all parameters the difference between prefit and postfit value is smaller than  $\frac{1}{2}$  of postfit

error. Note that the postfit values of  $CCDIS_{norm}$  and  $NCOTH$  are smaller than for the fit with CC-other sample as compared in Table 6.6 (see also Fig. 6.10). As mentioned in Chapter 6 these two parameters normalise modes of interaction that contribute to about 45% of predicted event rate in CC-other sample for nominal NEUT MC. The obtained results indicate that for the fit with all analysis samples the  $CCDIS_{norm}$  and  $NCOTH$  parameters are pulled up in order to increase MC predictions in CC-other sample.

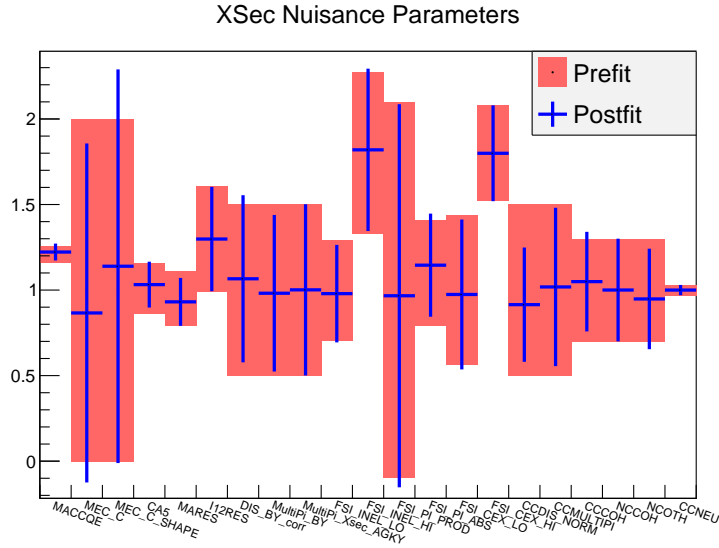


Figure 6.31: NEUT to data fit (without CC-other sample): postfit nuisance model parameters' values and errors.

parameter	postfit value	
	fit with all analysis samples	fit w/o CC-other sample
$CCDIS_{norm}$	$1.255 \pm 0.298$	$0.915 \pm 0.334$
$NCOTH$	$1.142 \pm 0.273$	$0.948 \pm 0.294$

Table 6.6: **NEUT to data fit.** Comparison of the postfit values of  $CCDIS_{norm}$  and  $NCOTH$  parameters for the fit with and without CC-other background sample.

The fit results for nuisance flux and detector systematic parameters are presented in Figs. 6.32-6.33. There is an overall very good agreement between prefit and postfit parameters' values. Three detector systematic parameters are noticeably pulled down (bins: 34, 43, 65). They correspond to the *reconstructed phase-space* OOPS bins where data event rate is zero (OOPS region of reconstructed  $\mu^+$  momentum above 30 GeV/c).

The initial and final  $\chi^2$  quantity, which is minimised in the fit, is reported in Table 6.7. One can see that the postfit  $\chi^2_{syst}$  is a few times smaller than for the fit with all

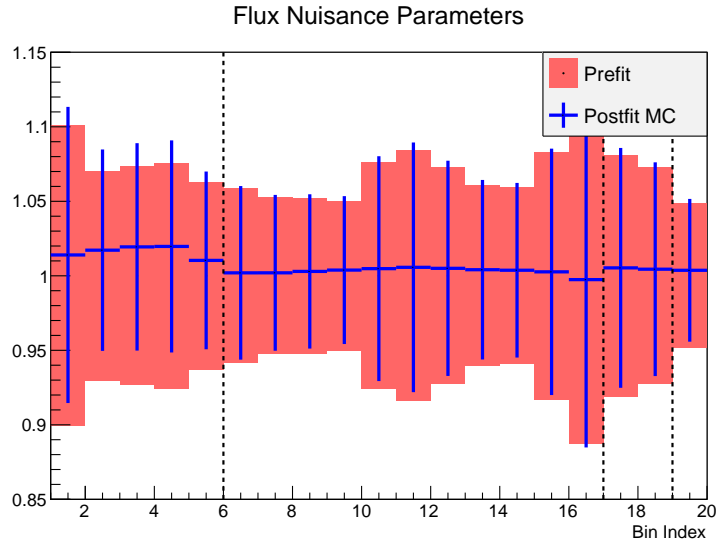


Figure 6.32: NEUT to data fit (without CC-other sample): postfit nuisance flux parameters' values and errors. Dashed lines separate parameters corresponding to different neutrino flavours:  $\nu_\mu$  (bins 1-5),  $\bar{\nu}_\mu$  (bins 6-16),  $\nu_e$  (bins 17-18),  $\bar{\nu}_e$  (bin 19).

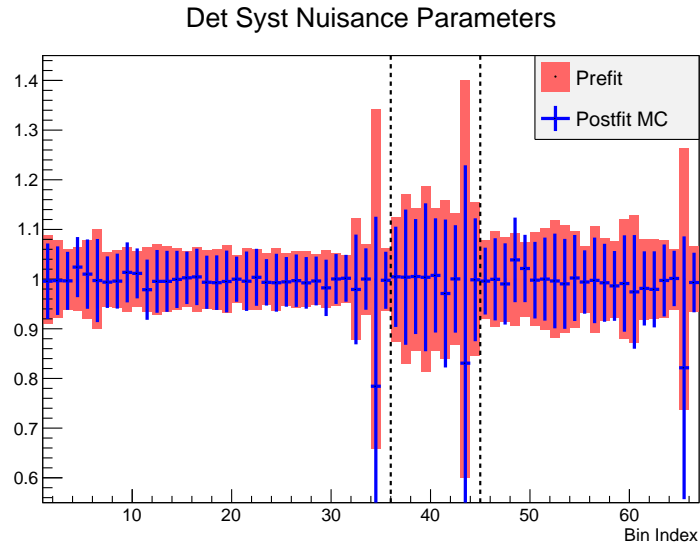


Figure 6.33: NEUT to data fit (without CC-other sample): postfit nuisance detector systematic parameters' values and errors. Dashed lines separate parameters corresponding to different analysis samples: CC1TPC $\pi^-$  signal sample (bins 1-35), CC1FGD $\pi^-$  signal sample (bins 36-44), Reversed Z-cut background sample (bins 45-66).

analysis samples. As explained in subsection 5.3.3 in case of combined statistical and systematic fluctuations the total postfit  $\chi^2$  value should follow chi-square distribution for  $M$  degrees of freedom, where  $M$  is the difference between number of *reconstructed*

*phase-space* bins and number of template parameters. In this case  $M = 66 - 32 = 34$ . The standard deviation for chi-square distribution is  $\sqrt{2M} \approx 8.2$ . The total postfit  $\chi^2$  for the fit without CC-other sample is about 40. The Fitter performance is therefore comparable with what one could expect for fluctuation studies.

$\chi^2$ contribution	Initial	Final
Total $\chi^2$	77.249	39.864
$\chi_{stat}^2$	77.249	38.148
per CC1TPC $\pi^-$ sample	38.367	7.6739
per CC1FGD $\pi^-$ sample	2.7504	2.5192
per Reversed Z-cut sample	36.131	27.955
$\chi_{syst}^2$	0	1.7163
$\chi_{flux}^2$	0	0.0800
$\chi_{model}^2$	0	0.2537
$\chi_{detsyst}^2$	0	1.3826

Table 6.7: NEUT to data fit (without CC-other sample). Comparison of  $\chi^2$  value before and after the fit. Contribution of different systematic sources is included.

# Appendix C: Elemental composition of FGD1 scintillator modules

Information in this Appendix is based on T2K Technical Note 91 [133].

As mentioned in subsection 5.2.4, the number of nucleons in FGD1 fiducial volume is estimated from the elemental composition of an XY module in FGD1. Each of the XY modules consist of an X and Y layer of scintillator bars. Scintillator material is polysterene (CH) doped with  $C_{15}H_{11}NO$ . The coating of the scintillator is made of  $TiO_2$  mixed with polystyrene. Scintillator bars are glued to G10 sheets which are made mostly of  $SiO_2$ . Additionally, the methacrylate-based adhesive is used to assemble XY modules. The elemental composition of an XY module is reported in Table 6.8 in terms of areal density.

Element	Areal density [g/cm <sup>2</sup> ]
C	$1.849 \pm 0.0092$
H	$0.1579 \pm 0.0021$
O	$0.0794 \pm 0.0048$
Ti	$0.0355 \pm 0.0059$
Si	$0.0218 \pm 0.0043$
N	$0.0031 \pm 0.0012$
Total	$2.147 \pm 0.0144$

Table 6.8: Elemental composition of an XY scintillator module.

The number of nucleons in FGD1 FV is calculated as:

$$N_{nucleons}^{total} = N_A \frac{\text{mol}}{\text{g}} \times \Delta X_{FV} \Delta Y_{FV} \times 14 \times \rho_{total},$$

where  $N_A$  is the Avogadro constant,  $\Delta X_{FV}, \Delta Y_{FV}$  denote dimensions of FGD1 fiducial volume, factor 14 is the number of XY modules in FGD1 FV and  $\rho_{total}$  is the total areal density of XY module. The result is

$$N_{nucleons}^{total} \approx 5.537 \times 10^{29}.$$

# Acronyms

**AGKY** Andreopoulos-Gallagher-Kehayias-Yang. 25

**CC** charged current. 13

**CCQE** CC quasielastic. 13

**COH** coherent. 21

**CP** Charge-parity. 17

**DAQ** Data Acquisition System. 46

**DIS** deep inelastic scattering. 21

**ECals** Electromagnetic Calorimeters. 39

**FEBS** Front-End Boards. 46

**FECs** Front-End Cards. 47

**FEE** Front-End Electronics. 46

**FEM** Front-End Mezzanine. 47

**FGDs** Fine Grained Detectors. 39

**FHC** Forward Horn Current. 33

**ID** Inner Detector. 47

**IH** inverted hierarchy. 19

**INGRID** Interactive Neutrino GRID. 38

**MC** Monte Carlo. 11

**MCM** Master Clock Module. 47

**MEC** meson exchange current. 21

**MSW** Mikheyev-Smirnov-Wolfenstein. 19

**NC** neutral current. 13

**NH** normal hierarchy. 19

**OD** Outer Detector. 47

**OOFV** out of fiducial volume. 57

**OOPS** out of phase-space. 116

**PID** particle identification. 49

**PMNS** Pontecorvo-Maki-Nakagawa-Sakata. 16

**POT** protons on target. 30, 175

**RES** resonant. 21

**RHC** Reversed Horn Current. 33

**SCM** Slave Clock Module. 47

**SI** secondary interactions. 94

**SK** Super-Kamiokande. 47

**SMRD** Side Muon Range Detector. 39

**TFBs** Trip-t Front-End Boards. 46

**TPCs** Time Projection Chambers. 39

# Bibliography

- [1] W. Pauli, Letter to the participants of the conference in Tübingen (dated 4 December 1930), published in: *Phys. Today* **31N9** (1978), 27
- [2] E. Fermi, *Tentativo di una teoria dell'emissione dei raggi beta*, Ric. Sci. **4** (1933), 491-495
- [3] C. L. Cowan, Jr., et al., *Science* **124**, 103 (1956).
- [4] S. H. Neddermeyer and C. D. Anderson, Phys. Rev. **51** (1937), 884-886
- [5] J. C. Street and E. C. Stevenson, Phys. Rev. **52** (1937), 1003-1004  
doi:10.1103/PhysRev.52.1003
- [6] Y. Nishina, M. Takeuchi and T. Ichimiya, Phys. Rev. **52** (1937), 1198-1199  
doi:10.1103/PhysRev.52.1198
- [7] C. M. G. Lattes, H. Muirhead, G. P. S. Occhialini and C. F. Powell, Nature **159** (1947), 694-697 doi:10.1038/159694a0
- [8] R. E. Marshak and H. A. Bethe, Phys. Rev. **72** (1947), 506-509  
doi:10.1103/PhysRev.72.506
- [9] B. Pontecorvo, Zh. Eksp. Teor. Fiz. **39** (1960), 1166
- [10] M. Schwartz, Phys. Rev. Lett. **4** (1960), 306-307 doi:10.1103/PhysRevLett.4.306
- [11] G. Danby, J. M. Gaillard, K. A. Goulianos, L. M. Lederman, N. B. Mistry, M. Schwartz and J. Steinberger, Phys. Rev. Lett. **9** (1962), 36-44  
doi:10.1103/PhysRevLett.9.36
- [12] M. L. Perl, G. S. Abrams, A. Boyarski, M. Breidenbach, D. Briggs, F. Bulos, W. Chinowsky, J. T. Dakin, G. J. Feldman and C. E. Friedberg, *et al.* Phys. Rev. Lett. **35** (1975), 1489-1492 doi:10.1103/PhysRevLett.35.1489

- [13] K. Kodama *et al.* [DONUT], Phys. Lett. B **504** (2001), 218-224 doi:10.1016/S0370-2693(01)00307-0
- [14] N. Agafonova *et al.* [OPERA], Phys. Lett. B **691** (2010), 138-145
- [15] Z. Li *et al.* [Super-Kamiokande], Phys. Rev. D **98** (2018) no.5, 052006
- [16] F. Perrin, *Possibilité d'émission de particules neutres de masse intrinsèque nulle dans les radioactivités beta*, Comptes-Rendus 197 (1933) 1625
- [17] P. A. Zyla *et al.* [Particle Data Group], PTEP **2020** (2020) no.8, 083C01, *Neutrino Masses, Mixing, and Oscillations*
- [18] Z. Maki, M. Nakagawa and S. Sakata, Prog. Theor. Phys. **28** (1962), 870-880 doi:10.1143/PTP.28.870
- [19] Y. Fukuda *et al.* [Super-Kamiokande], *Evidence for oscillation of atmospheric neutrinos*, Phys. Rev. Lett. **81** (1998), 1562-1567
- [20] Q. R. Ahmad *et al.* [SNO], *Direct evidence for neutrino flavor transformation from neutral current interactions in the Sudbury Neutrino Observatory*, Phys. Rev. Lett. **89** (2002), 011301
- [21] M. H. Ahn *et al.* [K2K], *Measurement of Neutrino Oscillation by the K2K Experiment*, Phys. Rev. D **74** (2006), 072003
- [22] K. Abe *et al.* [T2K], *Indication of Electron Neutrino Appearance from an Accelerator-produced Off-axis Muon Neutrino Beam*, Phys. Rev. Lett. **107** (2011), 041801
- [23] F. P. An *et al.* [Daya Bay], *Observation of electron-antineutrino disappearance at Daya Bay*, Phys. Rev. Lett. **108** (2012), 171803
- [24] P. Adamson *et al.* [NOvA], *First measurement of electron neutrino appearance in NOvA*, Phys. Rev. Lett. **116** (2016) no.15, 151806
- [25] *Foundations of Nuclear and Particle Physics*, Cambridge University Press 2017, p. 481.
- [26] E. Majorana, Nuovo Cim. **14** (1937), 171-184
- [27] M. S. Athar and S. K. Singh, *The Physics of Neutrino Interactions*, Cambridge University Press 2020, p. 24-25.

- [28] P. A. Zyla *et al.* [Particle Data Group], PTEP **2020** (2020) no.8, 083C01, *Neutrinoless Double- $\beta$  decay* revised by A. Piepke and P. Vogel.
- [29] G. Anton *et al.* [EXO-200], *Search for Neutrinoless Double- $\beta$  Decay with the Complete EXO-200 Dataset* Phys. Rev. Lett. **123** (2019) no.16, 161802
- [30] V. Alenkov, H. W. Bae, J. Beyer, R. S. Boiko, K. Boonin, O. Buzanov, N. Chanthima, M. K. Cheoun, D. M. Chernyak and J. S. Choe *et al.*, *First Results from the AMoRE-Pilot neutrinoless double beta decay experiment*, Eur. Phys. J. C **79** (2019) no.9, 791
- [31] D. Q. Adams *et al.* [CUORE], *Improved Limit on Neutrinoless Double-Beta Decay in  $^{130}\text{Te}$  with CUORE*, Phys. Rev. Lett. **124** (2020) no.12, 122501
- [32] M. Agostini *et al.* [GERDA], *Final Results of GERDA on the Search for Neutrinoless Double- $\beta$  Decay*, Phys. Rev. Lett. **125** (2020) no.25, 252502
- [33] P. A. Zyla *et al.* [Particle Data Group], PTEP **2020** (2020) no.8, 083C01, *CKM Quark-Mixing Matrix* revised by A. Ceccucci, Z. Ligeti and Y. Sakai.
- [34] I. Esteban, M. C. Gonzalez-Garcia, M. Maltoni, T. Schwetz and A. Zhou, JHEP **09** (2020), 178
- [35] M. Aker *et al.* [KATRIN], *Improved Upper Limit on the Neutrino Mass from a Direct Kinematic Method by KATRIN* Phys. Rev. Lett. **123** (2019) no.22, 221802
- [36] R. Barate *et al.* [ALEPH], *An Upper limit on the tau-neutrino mass from three-prong and five-prong tau decays* Eur. Phys. J. C **2** (1998), 395-406 doi:10.1007/s100520050149
- [37] V. N. Gribov and B. Pontecorvo, Phys. Lett. B **28** (1969), 493 doi:10.1016/0370-2693(69)90525-5
- [38] J. N. Bahcall and S. C. Frautschi, Phys. Lett. B **29** (1969), 623-625
- [39] B. Kayser, *Neutrino physics*, eConf **C040802** (2004), L004
- [40] A. D. Sakharov, Pisma Zh. Eksp. Teor. Fiz. **5** (1967), 32-35
- [41] L. Wolfenstein, Phys. Rev. D **17** (1978), 2369-2374
- [42] L. Wolfenstein, Phys. Rev. D **20** (1979), 2634-2635
- [43] S. P. Mikheyev and A. Y. Smirnov, Sov. J. Nucl. Phys. **42** (1985), 913-917

- [44] M. S. Athar and S. K. Singh, *The Physics of Neutrino Interactions*, p. 38.
- [45] J. Datta, M. Nizam, A. Ajmi and S. U. Sankar, *Matter vs vacuum oscillations in atmospheric neutrinos*, Nucl. Phys. B **961** (2020), 115251
- [46] S. Bharti, U. Rahaman and S. Uma Sankar, *Matter versus vacuum oscillations at long-baseline accelerator neutrino experiments*, Mod. Phys. Lett. A **36** (2021) no.13, 2150098
- [47] M. Maltoni and A. Y. Smirnov, Eur. Phys. J. A **52** (2016) no.4, 87
- [48] A. de Gouvea, [arXiv:hep-ph/0411274 [hep-ph]].
- [49] R. Acciarri *et al.* [DUNE], *Long-Baseline Neutrino Facility (LBNF) and Deep Underground Neutrino Experiment (DUNE): Conceptual Design Report, Volume 1: The LBNF and DUNE Projects*, [arXiv:1601.05471 [physics.ins-det]].
- [50] K. Abe *et al.* [Hyper-Kamiokande], *Hyper-Kamiokande Design Report*, [arXiv:1805.04163 [physics.ins-det]].
- [51] P. A. Zyla *et al.* [Particle Data Group], PTEP **2020** (2020) no.8, 083C01, *Neutrino Mixing*
- [52] Y. Hayato, Nucl. Phys. B Proc. Suppl. **112** (2002), 171-176 doi:10.1016/S0920-5632(02)01759-0
- [53] Y. Hayato, Acta Phys. Polon. B **40** (2009), 2477-2489
- [54] J. A. Formaggio and G. P. Zeller, Rev. Mod. Phys. **84** (2012), 1307-1341 doi:10.1103/RevModPhys.84.1307
- [55] A. de Gouvea and J. Jenkins, Phys. Rev. D **74** (2006), 033004
- [56] D. Casper, Nucl. Phys. B Proc. Suppl. **112** (2002), 161-170 doi:10.1016/S0920-5632(02)01756-5
- [57] J. L. Hewett, H. Weerts, R. Brock, J. N. Butler, B. C. K. Casey, J. Collar, A. de Gouvea, R. Essig, Y. Grossman and W. Haxton, *et al.*
- [58] *Foundations of Nuclear and Particle Physics*, p. 514.
- [59] P. A. Zyla *et al.* [Particle Data Group], PTEP **2020** (2020) no.8, 083C01, *Baryon Summary Tables*
- [60] K. M. Graczyk and J. T. Sobczyk, Phys. Rev. D **77** (2008), 053003

- [61] M. S. Athar and S. K. Singh, *The Physics of Neutrino Interactions*, pp. 527-533.
- [62] M. Glück, E. Reya and A. Vogt, *Eur. Phys. J. C* **5** (1998), 461-470
- [63] A. Bodek and U. K. Yang, [arXiv:hep-ex/0308007 [hep-ex]]
- [64] T. Yang, C. Andreopoulos, H. Gallagher and P. Kehayias, *A hadronization model for the MINOS experiment*, *AIP Conf. Proc.* **967** (2007) no.1, 269-275
- [65] T. Sjostrand, *Comput. Phys. Commun.* **82** (1994), 74-90
- [66] D. Rein and L. M. Sehgal, *Annals Phys.* **133** (1981), 79-153
- [67] D. Rein and L. M. Sehgal, *Nucl. Phys. B* **223** (1983), 29-44
- [68] C. Berger and L. M. Sehgal, *Phys. Rev. D* **76** (2007), 113004
- [69] R. A. Smith and E. J. Moniz, *Nucl. Phys. B* **43** (1972), 605 [erratum: *Nucl. Phys. B* **101** (1975), 547]
- [70] S. Dolan, *Probing nuclear effects in neutrino-nucleus scattering at the T2K off-axis near detector using transverse kinematic imbalances*, PhD thesis, University of Oxford (2017), <https://ora.ox.ac.uk/objects/uuid:16cef4e8-b52b-48c4-a954-81fba0b7536b>
- [71] S. K. Singh and E. Oset, *Phys. Rev. C* **48** (1993), 1246-1258
- [72] O. Benhar and A. Fabrocini, *Phys. Rev. C* **62** (2000), 034304
- [73] J. W. Van Orden and T. W. Donnelly, *Phys. Rev. C* **100** (2019) no.4, 044620
- [74] C. Ciofi degli Atti and C. B. Mezzetti, *Phys. Rev. C* **79** (2009), 051302
- [75] J. Nieves, J. E. Amaro and M. Valverde, *Phys. Rev. C* **70** (2004), 055503 [erratum: *Phys. Rev. C* **72** (2005), 019902]
- [76] T. Katori, *AIP Conf. Proc.* **1663** (2015) no.1, 030001
- [77] M. B. Barbaro, J. E. Amaro, J. A. Caballero, A. De Pace, T. W. Donnelly, G. D. Megias and I. Ruiz Simo, *Nucl. Theor.* **35** (2016), 60-71
- [78] K. Abe *et al.* [T2K], *Phys. Rev. D* **103** (2021) no.11, 112008
- [79] R. Gran, J. Nieves, F. Sanchez and M. J. Vicente Vacas, *Neutrino-nucleus quasi-elastic and 2p2h interactions up to 10 GeV*, *Phys. Rev. D* **88** (2013) no.11, 113007

- [80] S. Bolognesi *et al.*, *NIWG model and uncertainties for 2017 oscillation analysis*, T2K Technical Note 315
- [81] L. L. Salcedo, E. Oset, M. J. Vicente-Vacas and C. Garcia-Recio, *Computer Simulation of Inclusive Pion Nuclear Reactions*, Nucl. Phys. A **484** (1988), 557-592
- [82] K. Nakamura *et al.* [Particle Data Group], *Review of particle physics*, J. Phys. G **37** (2010), 075021
- [83] T. Feusels *et al.*, *Tuning of the NEUT Cascade Model using  $\pi^\pm$ -A Scattering External Data to Improve Final State Interaction and Secondary Interaction Systematic Uncertainties*, T2K Technical Note 325
- [84] T. Le *et al.* [MINERvA], Phys. Rev. D **100** (2019) no.5, 052008
- [85] R. Acciarri *et al.* [ArgoNeuT], Phys. Rev. D **98** (2018) no.5, 052002
- [86] K. Abe *et al.* [T2K Collaboration], Nucl. Instrum. Meth. A **659** (2011) 106.
- [87] K. M. Tsui [T2K], *Recent Cross-section Results from the T2K Experiment*, PoS **ICHEP2020** (2021), 184
- [88] K. Suzuki *et al.* [T2K], PTEP **2015** (2015) no.5, 053C01
- [89] T. Sekiguchi *et al.* [T2K], Nucl. Instrum. Meth. A **789** (2015), 57-80
- [90] K. T. McDonald, arXiv:hep-ex/0111033 [hep-ex]
- [91] M. Otani, *Measurement of Neutrino Oscillation in the T2K Experiment*, PhD thesis, Kyoto University (2012)
- [92] K. Abe, N. Abgrall, Y. Ajima, H. Aihara, J. B. Albert, C. Andreopoulos, B. Andrieu, M. D. Anerella, S. Aoki and O. Araoka, *et al.*, *Measurements of the T2K neutrino beam properties using the INGRID on-axis near detector*, Nucl. Instrum. Meth. A **694** (2012), 211-223
- [93] S. Assylbekov *et al.* Nucl. Instrum. Meth. A **686** (2012), 48-63
- [94] P. A. Amaudruz *et al.* [T2K ND280 FGD Collaboration], Nucl. Instrum. Meth. A **696** (2012) 1
- [95] N. Abgrall *et al.* [T2K ND280 TPC Collaboration], Nucl. Instrum. Meth. A **637** (2011) 25
- [96] D. Allan *et al.* [T2K UK], JINST **8** (2013), P10019

- [97] S. Aoki *et al.* Nucl. Instrum. Meth. A **698** (2013), 135-146  
doi:10.1016/j.nima.2012.10.001
- [98] J. Altegoer *et al.* [NOMAD], Nucl. Instrum. Meth. A **404** (1998), 96-128
- [99] L. Magaletti, *Measurement of  $\bar{\nu}_\mu$  CC interactions with the ND280 detector of the T2K experiment*, PhD thesis, University of Bari (2014)
- [100] M. Ravonel Salzgeber [T2K], *Measurement of the  $\nu_\mu$  flux and inclusive charged current cross section at T2K's near detector*, PoS **ICHEP2012** (2013), 378
- [101] N. Abgrall *et al.* [T2K ND280 TPC], *Time Projection Chambers for the T2K Near Detectors*, Nucl. Instrum. Meth. A **637** (2011), 25-46
- [102] A. A. García Soto, *Study of the  $\nu_\mu$  interactions via charged current in the T2K near detector*
- [103] Image from: <http://www-flc.desy.de/pet/>
- [104] M. Yokoyama *et al.* Nucl. Instrum. Meth. A **610** (2009), 362-365
- [105] M. Yokoyama *et al.* Nucl. Instrum. Meth. A **622** (2010), 567-573
- [106] M. Thorpe *et al.*, *The T2K near detector data acquisition systems*, doi:10.1109/RTC.2010.5750358
- [107] A. Vacheret *et al.* doi:10.1109/NSSMIC.2007.4436543
- [108] Y. Fukuda *et al.* [Super-Kamiokande], Phys. Rev. Lett. **82** (1999), 2430-2434
- [109] M. H. Ahn *et al.* [K2K], Phys. Rev. D **74** (2006), 072003
- [110] Y. Ashie *et al.* [Super-Kamiokande], Phys. Rev. D **71** (2005), 112005
- [111] J. Hosaka *et al.* [Super-Kamiokande], Phys. Rev. D **74** (2006), 032002
- [112] H. Nishino *et al.* [Super-Kamiokande], Phys. Rev. Lett. **102** (2009), 141801
- [113] P. A. Cherenkov, Dokl. Akad. Nauk SSSR **2** (1934) no.8, 451-454
- [114] C. Simpson [Super-Kamiokande], PoS **ICHEP2018** (2019), 008
- [115] Benno List, *Why and When to Optimize Efficiency Times Purity*, <https://www.desy.de/~blist/notes/whyeffpur.ps.gz>

- [116] K. Abe *et al.* [T2K], Phys. Rev. D **87** (2013) no.9, 092003  
doi:10.1103/PhysRevD.87.092003
- [117] P. Bartet *et al.*,  $\nu_\mu$  CC event selections in the ND280 tracker using Run 2+3+4 data, T2K Technical Note 212
- [118] C. Licciardi, M. Barbi, *Particle identification with the Fine Grained Detectors*, T2K Technical Note 103
- [119] Y. Petrov, A. Hillairet, *ND280 TPC Track Reconstruction Efficiency*, T2K Technical Note 163
- [120] D. Brailsford *et al.*, *Study of the tracker ECal systematic uncertainties*, T2K Technical Note 279
- [121] J. Kim, B. Kirby, M. Wilking, *Michel Electron Tagging in FGD1*, T2K Technical Note 104
- [122] L. Monfregola, *Muon neutrino charged current quasi-elastic interactions in the T2K off-axis near detector*, PhD thesis, University of Valencia (2015), <https://inspirehep.net/files/001018d6a1d8f0e70a2466fb1ed7d84d>
- [123] P. de Perio *et al.*, *Implementation of the NIWG Cross Section Parametrization*, T2K Technical Note 113
- [124] E. T. Atkin *et al.*, *NIWG model and uncertainties for 2019-2020 oscillation analysis*, T2K Technical Note 344
- [125] G. Cowan, *Statistical data analysis*, Oxford 1998, p. 70
- [126] *Ibid.*, p. 87-89
- [127] *Ibid.*, p. 90-91
- [128] L. Lista, *Statistical Methods for Data Analysis in Particle Physics*, Lect. Notes Phys. **909** (2016), published by Springer, pp.184-185
- [129] <https://cuddandr.gitlab.io/xsLLhFitter/>
- [130] C. Andreopoulos, J. Dobson, S. Dytman, *Handling Neutrino Interaction Uncertainties using Event Reweighting*, T2K Technical Note 7
- [131] G. Cowan, *Statistical data analysis*, Oxford 1998, p. 36

- [132] F. James and M. Winkler, *Minuit 2*,  
<https://root.cern.ch/root/html/doc/guides/minuit2/Minuit2.pdf>
- [133] S. Oser, *Elemental Composition of the FGD XY Modules*, T2K Technical Note 91
- [134] Internal T2K presentation by L. Berns, <https://t2k.org/beam/NuFlux/FluxRelease/21b-replica/21bv2/slides-accompanying-21bv2-release>
- [135] C. Andreopoulos *et al.*, *The GENIE Neutrino Monte Carlo Generator*, Nucl. Instrum. Meth. A **614** (2010), 87-104
- [136] A. Bodek and J. L. Ritchie, *Further Studies of Fermi Motion Effects in Lepton Scattering from Nuclear Targets*, Phys. Rev. D **24** (1981), 1400
- [137] K. S. Kuzmin, V. V. Lyubushkin and V. A. Naumov, *Axial masses in quasielastic neutrino scattering and single-pion neutrino production on nucleons and nuclei*, Acta Phys. Polon. B **37** (2006), 2337-2348
- [138] A. Bodek and U. k. Yang, *A Unified model for inelastic  $e - N$  and  $\nu - N$  cross-sections at all  $Q^2$* , AIP Conf. Proc. **792** (2005) no.1, 257-260
- [139] K. Abe *et al.* [T2K], *Measurement of inclusive double-differential  $\nu_\mu$  charged-current cross section with improved acceptance in the T2K off-axis near detector*, Phys. Rev. D **98** (2018), 012004
- [140] J. Schwehr, *Measurement of the differential charged current single pion cross section using muon momentum and muon angle in the pi zero detector of the T2K experiment*, PhD thesis, Colorado State University (2018)
- [141] L. O'Sullivan, *Measurement of the  $\bar{\nu}_\mu CCl\pi^-$  cross-section on water and hydrocarbon with ND280*, PhD thesis, University of Sheffield (2021)
- [142] K. Abe *et al.* [T2K], *T2K ND280 Upgrade - Technical Design Report*, arXiv:1901.03750